THE ANALYSIS OF MICROSTRIP WIRE-GRID ANTENNA ARRAYS

by

Louis Trichardt Hildebrand

Submitted in partial fulfilment of

the requirements for the degree

MEng

in the Faculty of Engineering

University of Pretoria

November 1992

DIE ANALISE VAN MIKROSTROOK DRAADROOSTER-ANTENNESAMESTELLINGS

deur

Louis Trichardt Hildebrand

Voorgelê ter gedeeltelike vervulling

van die vereistes vir die graad

MIng

in die Fakulteit Ingenieurswese

Universiteit van Pretoria

November 1992

The analysis of microstrip wire-grid antenna arrays

by: Louis Trichardt Hildebrand

Supervisor: Prof. D.A. McNamara

Department: Electrical and Electronic Engineering

Degree: MEng

The design of antenna arrays involves, amongst others, the selection of the array elements and geometry, as well as the element excitations. The feeding network to obtain the desired excitations can become quite complex, and hence expensive. One possible alternative would be to make use of microstrip wire-grid antenna arrays. These arrays are composed of staggered interconnected rectangular loops of dimensions a half-wavelength by a wavelength (in the presence of the dielectric). It is because the short sides are considered to be discrete elements fed via microstrip transmission lines, that these antennas are viewed as arrays. While considerable success has been achieved in the design of these antennas, published work has been either of an entirely experimental nature or based on approximate (albeit clever) network models which do not allow for fine control of the array element excitations or off-centre-frequency computations generally. It is the purpose of this thesis to perform an almost rigorous numerical analysis of these arrays in order to accurately predict their element excitations.

Models used to study microstrip antennas range from simplified ones, such as transmission-line models up to more sophisticated and accurate integral-equation models. The *mixed-potential integral equation formulation* is one of these accurate models which allows for the analysis of arbitrarily shaped microstrip antennas with any combination of frequency and dielectric thickness. The model treats the antenna as a single entity so that

physical effects such as radiation, surface waves, mutual coupling and losses are automatically included. According to this formulation, the microstrip antenna is modelled by an integral equation which is solved using the method of moments. By far the most demanding part of the integral equation analysis is its actual numerical implementation. For this reason a complete description of the numerical implementation of the formulation is given in this thesis. To verify the accuracy of the implementation, rectangular microstrip patch antennas were analysed and surface current distributions were shown to compare favourably with published results. The formulation is then applied to the analysis of microstrip wire-grid antenna arrays which makes it possible to accurately predict surface current distributions on these arrays. Radiation patterns are determined directly from computed current distributions in the presence of the dielectric substrate and groundplane, and are essentially exact except for finite groundplane effects. To verify theoretically predicted results for wire-grid antenna arrays, several arrays were fabricated and actual radiation patterns were measured. Good correspondence between measured and predicted co-polar radiation patterns was found, while the overall cross-polarization behaviour in cases with large groundplanes could also be predicted.

The fact that numerical experimentation can be performed on wire-grid antenna arrays to examine element excitations, means that it is now possible to carefully design for some desired aperture distribution.

Die analise van mikrostrook draadrooster-antennesamestellings

deur: Louis Trichardt Hildebrand

Studieleier: Prof. D.A. McNamara

Departement Elektriese en Elektroniese Ingenieurswese

Graad: MIng

Die ontwerp van antennesamestellings behels, onder andere, die keuse van stralingselemente, die geometrie van die antennestruktuur, asook die onderskeie elementaandrywings. In sommige gevalle is die voernetwerk om die verlangde aandrywings te verkry, egter ingewikkeld en daarom duur. 'n Antennestruktuur met 'n relatief eenvoudige voernetwerk is die sogenaamde draadrooster-antennesamestelling. Hierdie samestellings bestaan uit dun geëtste interverbinde reghoekige draadlusse waarvan die sye afmetings van 'n halwe golflengte en 'n golflengte in die teenwoordigheid van die diëlektrikum het. Omdat die afsonderlike kort sye van elke draadlus beskou word as diskrete stralers wat gevoer word deur mikrostrooklyne, word die antennes beskou as samestellings. Alhoewel heelwat sukses in die verlede behaal is in die ontwerp van dié antennes, is gepubliseerde resultate of eksperimenteel van aard of gebaseer op benaderde analise-metodes. Dit is die doel van hierdie verhandeling om draadrooster-antennesamestellings akkuraat en nougeset te analiseer met die doel om elementaandrywings akkuraat te kan voorspel.

Metodes wat gebruik word om mikrostrookantennes te analiseer strek van eenvoudige transmissielynmodelle tot meer ingewikkelde en akkurate integraalvergelyking-metodes. Die gemengde-potensiaal integraalvergelyking-formulering is een van hierdie akkurate metodes wat dit moontlik maak om arbitrêre vorme van mikrostrookantennes te

analiseer, met enige kombinasie van frekwensie en diëlektriese substraatdikte. Die metode neem ook die effekte van verliese, oppervlakstrome en wedersydse koppeling tussen verskillende elemente van 'n samestelling in ag. Volgens dié formulering word die mikrostrookantenne met 'n integraalvergelyking gemodelleer wat dan met die momente-metode opgelos word. Die mees veeleisende deel van die integraalvergelyking-metode is die numeriese implementering van die metode self en daarom word baie aandag in hierdie verhandeling daaraan geskenk. Om die akkuraatheid van die implementering te bevestig, is oppervlakstroomverspreidings op reghoekige geëtste stralingsvlakantennes bereken, en met reeds-gepubliseerde berekende resultate vergelyk. Goeie ooreenkoms is verkry. Die akkurate integraalvergelyking-metode is hierna gebruik om draadrooster-antennesamestellings te analiseer. Die metode maak dit moontlik om die stroomverpreidings (in effek die elementaandrywings) op dié strukture akkuraat te bereken. Stralingspatrone word direk van hierdie strome, in die teenwoordigheid van die diëlektrikum en grondvlak, bereken, en is in effek eksak behalwe vir eindige-grondvlak effekte. Om teoretiese resultate wat met behulp van die analise-metode verkry is, te verifieer, is draadrooster-antennesamestellings vervaardig en gemete en berekende stralingspatrone vergelyk. Goeie ooreenkoms tussen die berekende en voorspelde ko-polêre stralingspatrone is gevind, terwyl selfs die kruis-polarisasie gedrag in gevalle met groot grondvlakke, redelik goed voorspel kan word.

Die feit dat "numeriese eksperimentering" nou op mikrostrook draadrooster-antennesamestellings uitgevoer kan word om elementaandrywings te bereken, bring mee dat daar nou doelgerig ontwerp kan word vir verlangde stralingseienskappe van sodanige antennes.

" Nie met mag en krag sal jy slaag nie,

maar deur my Gees,

sê die Here die Almagtige. "

Sagaria 4:6

ACKNOWLEDGEMENTS

I would like to express my gratitude to the following people:

- My supervisor, Prof. D.A. McNamara for his outstanding guidance.

- Prof. J.R. Mosig of the Ecole Polytechnique Federale de Lausanne, Switzerland, for valuable advice given throughout the duration of this work.

- Thanks are also due to Prof. J.H. Cloete of the University of Stellenbosch, and

- Mr. D. Janse Van Rensburg of the compact range at the University of Pretoria.

- To my family: thank you for giving me this opportunity and the moral support throughout my studies.

- Finally, a special word of appreciation to Karen for her understanding encouragement and support.

TABLE OF CONTENTS

PREFACE

The purpose of this preface is not to replace the introductory chapter, but rather intended briefly to point out to the reader the structure of the thesis. The principal contributions contained in the thesis are stated in Section 3.8, Section 4.5 and Chapter 5. Chapter 1 introduces the topic of the thesis and outlines its aims. Detail on the contents of any chapter is given in the introductory section of that chapter. Chapter 2 can be considered background information, with details of the author's contributions contained in Chapters 3 and 4.

CHAPTER 1

MICROSTRIP WIRE-GRID ANTENNA ARRAYS

An *antenna* is a device that (depending on one's viewpoint) uses currents and voltages from a transmission line, or the E and H fields from a waveguide, to launch an electromagnetic wavefront into free space or into the local environment. The antenna acts as a transducer to match the transmission line or waveguide to the medium surrounding the antenna. The launching process is known as *radiation*, and the transmitting antenna is the launcher. If a wavefront is intercepted by an antenna, some power is absorbed from the wavefront, and the antenna acts as a receiving antenna. To obtain certain radiation characteristics (for example, high directivity, narrow beamwidths, low side lobes or steerable beams), several antennas can be arranged in space and interconnected by a feeding network. Such a configuration of multiple radiating elements is referred to as an *antenna array*. The design of an array involves the selection of the array elements and geometry, as well as the element excitations. The feeding network to obtain the desired excitations can become quite complex, and hence expensive. One possible alternative is to make use of *microstrip antenna arrays*. Microstrip antennas are thin and lightweight radiating elements, formed by a substrate which is backed by a metallic sheet, referred to as the groundplane. Thin metallic conductors are then deposited on the substrate by printed circuit techniques.

Microstrip patch arrays, however, have restricted bandwidth and can sometimes

exhibit undesirable polarization characteristics. Microstrip wire-grid[1] antenna arrays, on the other hand, combine all the usual benefits of patch-type radiators with adequate cross-polarization control and good bandwidth. Wire-grid arrays, examples of which are shown in Figures 1.1 and 1.2, are composed of staggered interconnected rectangular loops of dimensions a half-wavelength by a wavelength (in the presence of the dielectric). It is because of its appearance that these arrays are often referred to as brick-wall arrays. It is argued that the excitation is such that the radiation due to currents on the short segments (the vertical segments in Figure 1.1) combine constructively, while that due to currents on the longer segments cancel. The wavelength-long segments are considered to act as transmission lines. It is because of this that the short sides are regarded as discrete elements of an array, fed via microstrip transmission lines. Element excitations may be controlled by varying the widths of the short elements, thereby obtaining a desired aperture distribution. While considerable success has been achieved in the design of these antennas, published work has been either of an entirely experimental nature or based on approximate network models. It is the purpose of this thesis to perform an almost rigorous numerical analysis of these microstrip wire-grid antenna arrays. The analysis will be done using a moment method solution of an integral equation formulation of the problem, due to Mosig and Gardiol [2,3,4]. A detailed exposition of this method is given in Section 2.3. By far the most demanding part of the integral equation analysis is its actual numerical implementation. Published information on the latter, in order to satisfy the space restrictions associated with journal articles, essentially takes the form of suggestions on how to overcome numerical difficulties. There are

[1] The wire-grid antenna array principle was derived some years ago by Kraus [1].

usually insufficient details for a direct implementation of the analysis. Therefore, Chapter 3 (which along with Chapter 4 contain the principal contributions of this thesis) presents a very complete description of the numerical implementation developed by the present author. It has purposefully been illustrated with various graphs, and can be considered a pictorial "tour" of the work in [2,3,4]. Chapter 4 applies the integral equation technique to the analysis of microstrip wire-grid arrays, the aim being the theoretical determination of the excitations, and hence radiation patterns of such arrays. Finally, some general concluding remarks on the work are given in Chapter 5. Several appendices, in which derivations which provide increased insight are given, are also included.

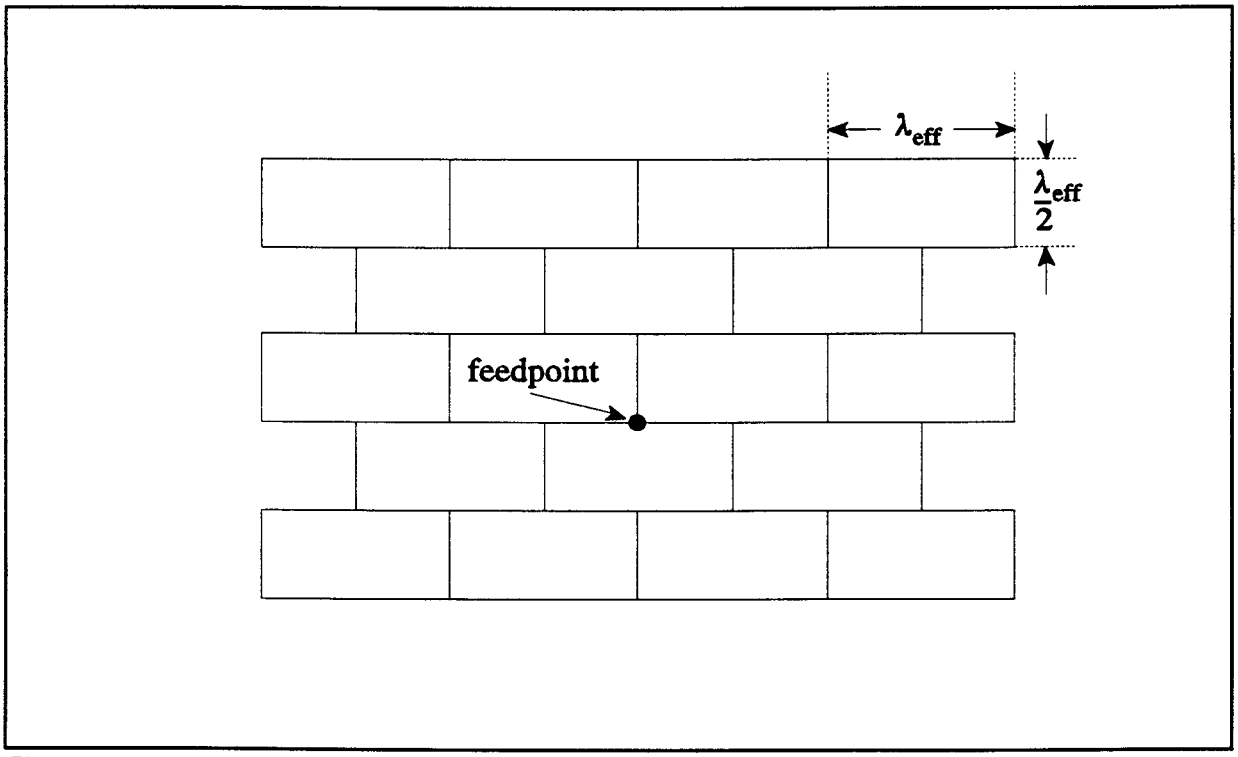

Figure 1.1 *Example of a microstrip wire-grid antenna array. λ_{eff} is the wavelength in the presence of the dielectric.*

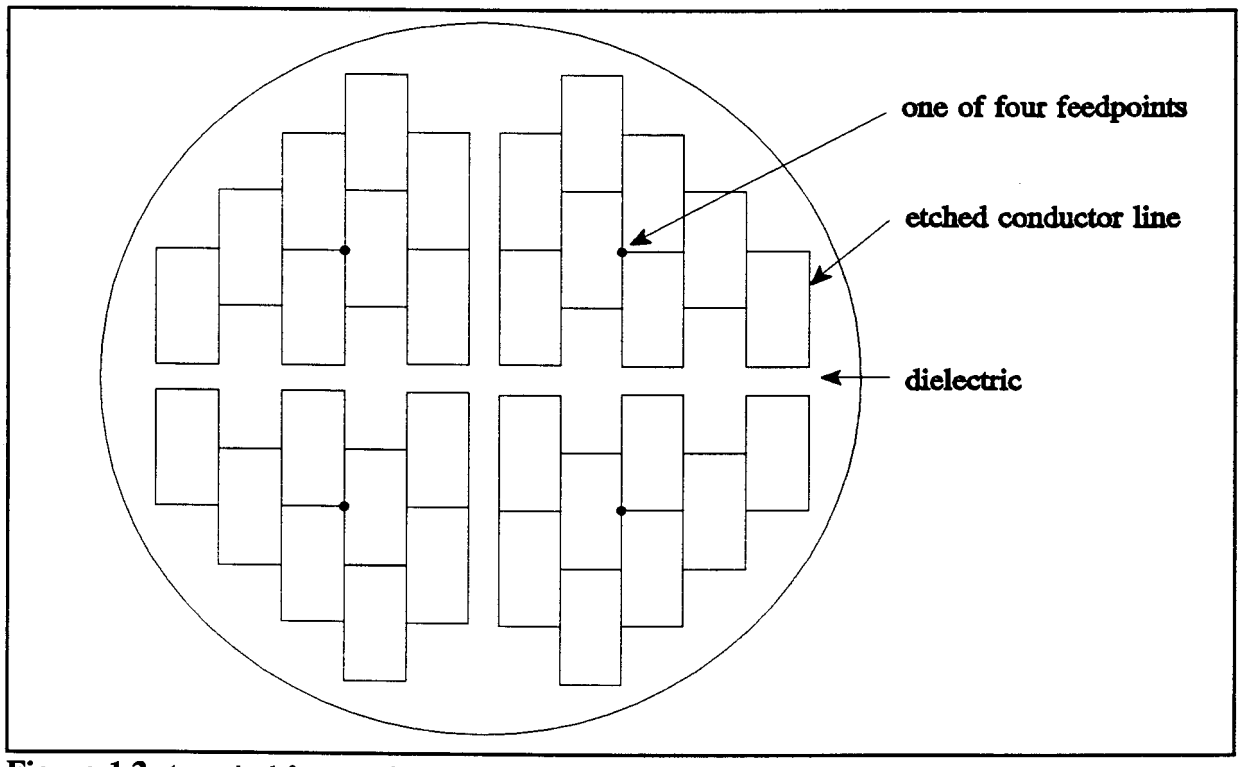

Figure 1.2 *An etched four-quadrant wire-grid antenna array.*

CHAPTER 2

REVIEW OF EXISTING ANALYSIS TECHNIQUES FOR MICROSTRIP ANTENNAS

2.1 INTRODUCTION

In this chapter we will give a review of existing analysis techniques for microstrip antennas. Widely used approximate models and some of their shortcomings are discussed in Section 2.2, leading to a review of the more accurate integral equation methods. A discussion of the formulation used in this thesis will then be given in Section 2.3. However, details of numerical algorithms and other computational aspects are deferred to Chapter 3. The present chapter describes existing formulations and can be considered the technical background to the thesis work.

2.2 CLASSIFICATION OF EXISTING TECHNIQUES FOR THE ANALYSIS OF MICROSTRIP ANTENNAS

To date, several models for the analysis of microstrip antennas have been developed. Some of these models are restricted to geometries such as rectangular or circular patches, while others are restricted in terms of structure size or attainable accuracy. These models range from simplified ones, such as *transmission-line network models* [5] where the antenna is divided into components (eg. T-junctions, hybrid junctions) and the effects of their individual network

models are combined using conventional scattering matrix theory. This method can provide reasonable radiation pattern predictions for simplified structures, however, network models for the individual components can be rather difficult to compute and therefore this method is not easily extendable to complicated geometries. Furthermore, a detailed analysis is needed in any case to include phenomena such as radiation and surface waves into these individual network models.

Widespread use is also made of the *cavity model* [6]. Hereby, the model used in the study of resonators is extended to study radiation, the antenna radiating at the resonant frequency of the equivalent cavity. This model may be expanded to include the complete set of cavity modes (multimode cavity theory) and dielectric losses by placing a lossy equivalent dielectric in the cavity. The effects of surface waves may also be included, albeit approximately. The cavity model provides a means of predicting, with reasonable accuracy, impedances and radiation characteristics of thin separable structures. This model however, cannot be used to consider the effects of external mutual coupling between different elements of an array of such antennas and falls short of accurately predicting behaviour in the case of electrically thick substrates.

In the more accurate and sophisticated approaches, the microstrip antenna is modelled by an integral equation which is derived using appropriate Green's functions and the boundary conditions on the electromagnetic fields. The *method of moments* [7] is then used in solving for the unknowns (surface current and/or associated surface charge densities) in these integral equations. In the moment

method application to these integral equations one arrives at expressions for the determination of the impedance matrix elements. As pointed out by Pozar [8], it is here that one has the choice of two approaches. The associated Green's functions (i.e. those for an electric current element radiating in the presence of a dielectric slab backed by a groundplane) are usually derived in the Fourier transform domain. The spectral domain approach uses the Green's functions in this transform domain directly. The spatial domain approach uses the Green's functions after these have been transformed to the spatial domain. In either case the moment method solution yields the coefficients of the spatially distributed current/charge densities. A very clear comparison of the two approaches can be found in [8,Sect.IV.B]. From the solutions of these integral equations, the radiated fields can be determined using radiation integrals (in terms of the same Green's functions used to formulate the integral equations). There are many different forms of integral equations; the most common being the electric field integral equation (EFIE) and magnetic field integral equation (MFIE). The EFIE enforces the boundary conditions on the tangential electric field, while the MFIE enforces the boundary conditions on the tangential magnetic field. When both vector and scalar potentials are used in the formulation of especially the EFIE, it has become customary to refer to it as the mixed-potential integral equation (MPIE).

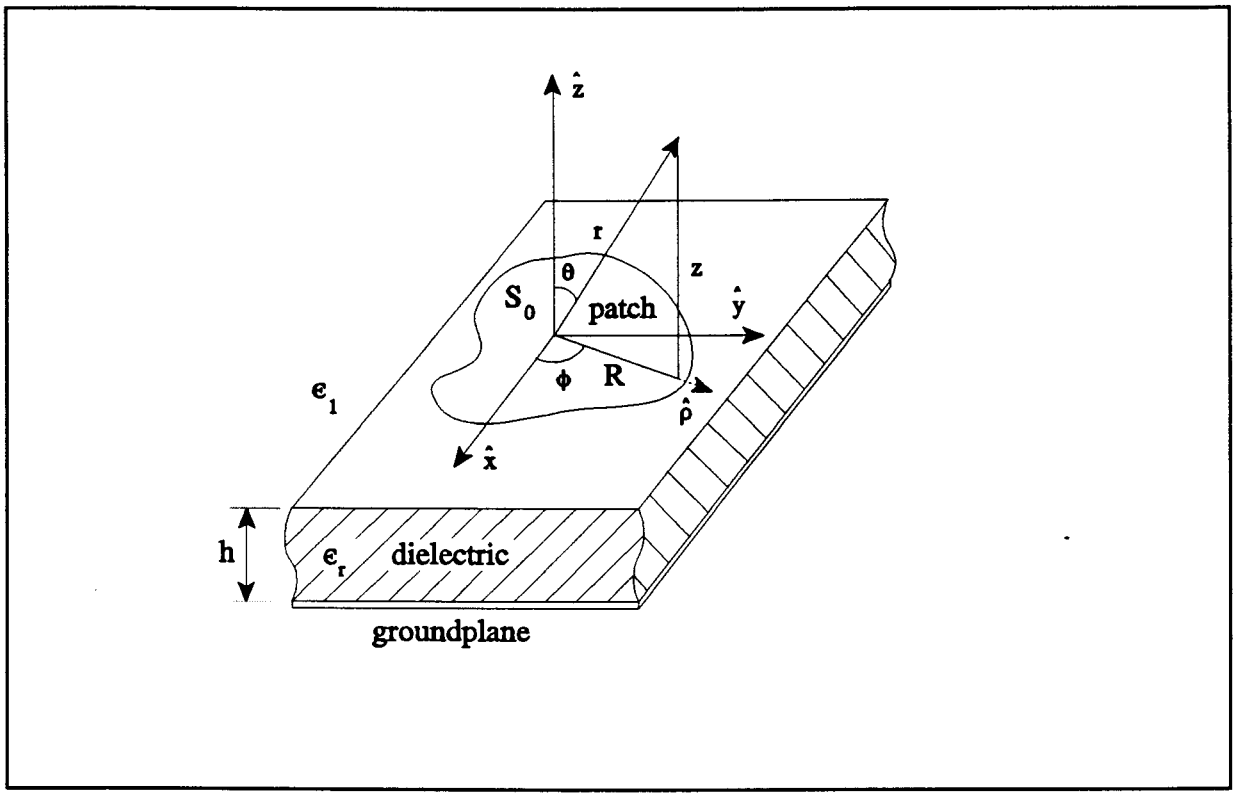

Figure 2.1 *Geometry of an arbitrarily shaped microstrip patch.*

2.3 DETAILED EXPOSITION OF THE FORMULATION USED IN THIS THESIS

There has been little information published on the relative advantages/disadvantages of the spectral-domain approach over the spatial-domain approach, and vice versa. Numerical difficulties associated with one approach are not entirely avoided through use of the other, but simply manifest themselves in another form [8]. It is true, however, that the spectral-domain approach applications have been limited to a few simple shapes. Especially for more general shapes, it has recently been concluded that [9] "unless a breakthrough is achieved in the acceleration of the slowly converging double spectral integrals that arise - the spectral domain approach is not competitive in terms of efficiency with the state-of-the-art space domain methods". This view is

perhaps further strengthened by the improvements in the "analytical forms" of the spatial domain approach [10]. At any rate, the spatial domain formulation of Mosig and Gardiol [5] has been used in this thesis. The method allows for the analysis of arbitrarily shaped patches (Figure 2.1) with no intrinsic limitations on frequency and dielectric thickness. Mutual coupling between different elements of an array is automatically taken into account, while the effects of surface waves as well as dielectric and ohmic losses are included. The groundplane and dielectric slab, however, are assumed to extend to infinity in the transverse directions, and the formulation expects the substrate to be non-magnetic, isotropic and homogeneous. The microstrip antenna is modelled by an integral equation, where the unknown is the electric surface current distribution. The Green's functions forming the kernel of this equation are that for an electric current element radiating in the presence of a dielectric slab backed by a conducting groundplane, the element being located at the surface of the slab.

2.3.1 The mixed-potential integral equation

The integral equation is formulated in the spatial domain using vector and scalar potentials, hence the term mixed-potential integral equation (MPIE). Introducing expressions for the potentials in an equation relating the total tangential electric field to the electric surface current, yields the following expression for the MPIE [3]:

$$\hat{z} \times \left(j\omega \int_{S_0} \overline{G}_A \cdot J_s dS' + \nabla \int_{S_0} G_V \, q_s dS' + Z_s \, J_s \right) = \hat{z} \times E^e \qquad (2.1)$$

where the patch extends over the part of the z=0 plane denoted by S_0. $\mathbf{E}^e$ denotes the excitation electric field, while $\overline{\mathbf{G}}_A$[1] and G_V represent the Green's functions associated with the vector and scalar potentials, respectively. The unknowns in this integral equation are the surface current $\mathbf{J}_s$ and the surface charge q_s. They are, however, not independent and are related through the continuity equation [11] $\nabla.\mathbf{J}_s + j\omega q_s = 0$. Z_s is a surface impedance accounting for the finite conductivity of the patch. An accurate value for the surface impedance can only be obtained through measurement since Z_s includes effects such as surface roughness and finite thickness of the metallic patch. In practice however, most patches are thick compared to the skin depths, and the classical expression

$$Z_s = \frac{1 + j}{\sigma^* \delta} \quad \Omega \qquad (2.2)$$

still offers a good approximation. σ^* is an effective conductivity that includes roughness effects, and can be several times lower than values found in standard tables (typically one fourth); δ represents skin depth and is approximated by $[2/(\omega\mu\sigma^*)]^{1/2}$ where ω is the working frequency and μ the permeability.

[1] In this thesis **bold** overlined characters denote dyadics while vectors will be represented by bold characters.

2.3.2 Green's functions

$\bar{G}_A$ is a three-dimensional dyadic Green's function with $G_A^{st}(r/r')$ giving the s-component of the vector potential existing at point r created by a t-directed Hertz dipole at r'. The Green's function, G_V, associated with the scalar potential, must be carefully defined and the uniqueness thereof is only guaranteed if

$$\nabla . \bar{G}_A(r/r') = \mu \epsilon \nabla G_V(r/r') = -\mu \epsilon \nabla' G_V(r/r') \tag{2.3}$$

where ∇' acts on the primed co-ordinates [3]. The validity of the integral equation depends therefore, on whether (2.3) holds. Appendix B derives expressions for the potentials (A and V) created by a horizontal electric dipole on the air-dielectric interface of a microstrip structure; from these expressions the components of the dyadic Green's function can be written as follows:

$$G_A^{xx}(r/r') = \frac{\mu_0}{2\pi} \int_0^\infty J_0(\lambda R) \frac{\lambda}{D_{TE}} e^{-u_0 z} d\lambda \tag{2.4}$$

$$G_A^{yx}(r/r') = 0 \tag{2.5}$$

$$G_A^{zx}(r/r') = -\frac{\mu_0}{2\pi} (\epsilon_r - 1) \cos\phi \int_0^\infty J_1(\lambda R) \frac{\lambda^2}{D_{TE} D_{TM}} e^{-u_0 z} d\lambda \tag{2.6}$$

where $\mu_0 = 4\pi \cdot 10^{-7}$ is the permeability of free space, J_n is the Bessel function

of n'th order and first kind, $D_{TE} = u_0 + u \coth uh$ and $D_{TM} = \epsilon_r \mu_0 + u \tanh uh$, $u_0 = (\lambda^2 - k_0^2)^{1/2}$, $u = (\lambda^2 - \epsilon_r k_0^2)^{1/2}$, k_0 is the free space wavenumber, h the substrate thickness and $R = |\mathbf{r} - \mathbf{r}'|$. Angle ϕ is defined in Figure 2.1. If both source and observation points are located on the air-dielectric interface ($z=0$), then of course $\mathbf{r} = x\hat{x} + y\hat{y}$ and thus $\phi = \tan^{-1}\{(y - y')/(x - x')\}$. For the case of a lossy dielectric, $\epsilon_r = \epsilon_r'(1 - j\tan\delta)$ where[2] $\tan\delta$ is the loss tangent. Likewise, since a microstrip substrate exhibits rotational symmetry about the z-axis, it follows that:

$$G_A^{yy}(r/r') = G_A^{xx}(r/r') \tag{2.7}$$

$$G_A^{xy}(r/r') = 0 \tag{2.8}$$

$$G_A^{xy}(r/r') = -\frac{\mu_0}{2\pi}(\epsilon_r - 1)\sin\phi \int_0^\infty J_1(\lambda R)\frac{\lambda^2}{D_{TE} D_{TM}} e^{-u_0 z} d\lambda \tag{2.9}$$

Since only horizontal currents are considered, components G_A^{xz}, G_A^{yz} and G_A^{zz} need not be evaluated. Mosig and Gardiol [3] have shown that (2.3) holds for a scalar potential Green's function defined by

$$G_V(r/r') = \frac{1}{2\pi\epsilon_0}\int_0^\infty J_0(\lambda R)\frac{\lambda N}{D_{TE} D_{TM}} e^{-u_0 z} d\lambda \tag{2.10}$$

[2] δ in this expression should not be mistaken with skin depth also denoted by δ.

where ϵ_0 is the permittivity of free space and $N = u_0 + u \tanh uh$. In solving for the surface current distribution, we are interested in the case where both source and observer are located on the air-dielectric interface ($z=0$). The term $\exp(-u_0 z)$ appearing in the above expressions is then set to unity. For far-field radiation computation, on the other hand, this will not be the case and this term has to be retained in the Green's function expressions. Note that (2.4), (2.6), (2.9) and (2.10) show that the Green's functions themselves must be evaluated numerically; this in addition to the numerical integration needed in the evaluation of the impedance matrix elements (which contain these Green's functions) when the moment method is used.

Closer inspection[3] of the Green's function integrands, reveals the existence of three distinct integration difficulties which will be discussed shortly. However, by writing the integrals as

$$\int_0^{\infty} F(\lambda)\,d\lambda = \int_0^{k_0} F(\lambda)\,d\lambda + \int_{k_0}^{k_0\sqrt{\epsilon_r'}} F(\lambda)\,d\lambda + \int_{k_0\sqrt{\epsilon_r'}}^{\infty} F(\lambda)\,d\lambda \qquad (2.11)$$

it is possible to address these problems separately. Firstly, in the interval $[0\ ,\ k_0]$ the square root, $(\lambda^2 - k_0^2)^{1/2}$, appearing in the denominator of the integrands, introduces a discontinuity in the derivative at $\lambda = k_0$. This corresponds to a *branch point*[4] on the complex plane k_ρ where $k_\rho = \lambda + j\upsilon$. Numerical difficulties

[3] Section 3.2 gives graphical illustrations.

[4] Section 3.2.1 discusses branch points.

encountered here can be overcome by the substitution $\lambda = k_0 \cos t$ resulting in a smoother function which can easily be integrated numerically. Secondly, it can be shown [11] that $D_{TE}=0$ and $D_{TM}=0$ are the characteristic equations of the surface waves existing on the dielectric substrate. It can, however, also be shown [4] that D_{TE} has no zeros and D_{TM} has only one (corresponding to the zero-cutoff TM_0 surface wave) if $f[GHz] \leq 75/\{h[mm](\epsilon_r'-1)^{1/2}\}$. In this thesis it will be assumed that this inequality holds; this is true in most practical applications of the type to be considered. Therefore, if the integrand contains D_{TM} in the denominator (as is the case for G_V, G_A^{zx}, and G_A^{zy}), it can be shown [4] that the singularity is bounded to the interval $[k_0 , k_0(\epsilon_r')^{1/2}]$ which justifies the subdivision proposed in (2.11). For lossy cases, this singularity lies just below the λ-axis on the complex plane k_ρ; in the lossless case this singularity lies on the λ-axis itself. Two techniques are commonly utilized to deal with such singularities. These are the *folding around the pole* technique [12] and *pole extraction* [13], the latter being particularly suitable for application in this analysis. According to this technique, a singularity in the Green's function integrand at $\lambda_p + j\nu_p$ can be extracted by writing the integral as

$$\int_{k_0}^{k_0\sqrt{\epsilon_r'}} F(\lambda)\,d\lambda = \int_{k_0}^{k_0\sqrt{\epsilon_r'}} [F(\lambda) - F_{sing}(\lambda)]\,d\lambda + \int_{k_0}^{k_0\sqrt{\epsilon_r'}} F_{sing}(\lambda)\,d\lambda \qquad (2.12)$$

where

$$F_{sing}(\lambda) = \frac{Res}{\lambda - (\lambda_p + j\nu_p)} \tag{2.13}$$

Numerical root-finding techniques yield $\lambda_p + j\nu_p$ while Res is the residue of F at this pole. The function F_{sing} can be integrated analytically, i.e.

$$\int_{k_0}^{k_0\sqrt{\epsilon_r'}} F_{sing}(\lambda)\, d\lambda = \frac{Res}{2} \ln\left[\frac{(k_0\sqrt{\epsilon_r'} - \lambda_p)^2 + \nu_p^2}{(\lambda_p - k_0)^2 + \nu_p^2}\right] + j\, Res \tan^{-1}\left[\frac{k_0\sqrt{\epsilon_r'} - \lambda_p}{\nu_p}\right] + j\, Res \tan^{-1}\left[\frac{\lambda_p - k_0}{\nu_p}\right] \tag{2.14}$$

while $[F(\lambda) - F_{sing}(\lambda)]$, being a well-behaved function (call it the *difference term*), is numerically integrable. An infinite derivative in the difference term integrand at $\lambda = k_0$ may be eliminated by the substitution $\lambda = k_0 \cosh t$.

The integrands of G_A^{xx} and G_A^{yy} do not contain D_{TM} in the denominator and therefore do not require application of the pole extraction technique. In these cases, the substitution $\lambda = k_0 \cosh t$ may be performed to obtain smooth integrands at $\lambda = k_0$.

Thus far we have discussed the evaluation of the Green's functions in the intervals $[0 , k_0]$ and $[k_0 , k_0(\epsilon_r')^{1/2}]$. Finally, in the interval $[k_0(\epsilon_r')^{1/2} , \infty]$ the oscillatory integrands (for both lossless and lossy dielectric cases) have envelopes which converge very slowly, or even diverge at infinity. A technique based on the concept of a weighted average between half-cycle integrals, the *method of*

averages [14], can be used to numerically evaluate these integrals. This method will be the subject of Section 3.2.3.

The development of accurate numerical techniques for the evaluation of the Green's functions is an essential (and by far the most demanding) part of the overall process.

2.3.3 Basis and testing functions

By expanding the unknown surface current distribution over a set of basis functions and testing the integral equation against a set of testing functions, the MPIE may be solved with the method of moments [7]. Careful consideration should be given when choosing these basis and testing functions since correct choices are essential to the accuracy of final results. When no *a priori* assumptions about the surface current distribution on the microstrip antenna can be made, *subsectional basis functions* (as opposed to entire-domain basis functions) have been found to offer best results; in particular, rooftop basis functions have been used successfully [15]. The surface of the arbitrarily shaped microstrip antenna is divided into elementary cells called *charge cells* (Figure 2.2); two adjacent charge cells forming a *current cell* on which one rooftop basis function (Figure 2.3) is supported. Although equal cell size is not a condition, computation time increases for cases of unequal cell size. The components of the surface current are then expanded over basis functions T_x and T_y as follows:

$$J_{sx} = \frac{1}{b} \sum_{j=1}^{M} I_{xj} T_x(r - r_{xj}) \tag{2.15}$$

$$J_{sy} = \frac{1}{a} \sum_{j=1}^{N} I_{yj} T_y(r - r_{yj}) \tag{2.16}$$

where

$$T_x(r) = \begin{cases} 1 - |x|/a & ; \quad |x| < a \ , \quad |y| < b/2 \\ 0 & ; \quad \textit{elsewhere} \end{cases} \tag{2.17}$$

and a similar expression holds for $T_y(\mathbf{r})$. I_{xj} and I_{yj} are the unknown surface current coefficients with M and N the number of x- and y-directed current cells, respectively. The surface charge density associated with the expanded surface current density is obtained through substitution of (2.15) and (2.16) into the continuity equation, yielding

$$\rho_s = \frac{1}{j\omega ab} \left\{ \sum_{j=1}^{M} I_{xj} [\Pi(r - r_{xj}^{+}) - \Pi(r - r_{xj}^{-})] + \sum_{j=1}^{N} I_{yj} [\Pi(r - r_{yj}^{+}) - \Pi(r - r_{yj}^{-})] \right\} \tag{2.18}$$

where $\Pi(\mathbf{r})$ is a two-dimensional unit pulse function defined over a rectangle of dimensions a and b centred at $\mathbf{r} = (0,0)$. Figure 2.3 gives a graphical illustration of the charge distribution on an x-directed current cell. For testing functions, unidimensional rectangular pulses, being compatible with rooftop basis functions,

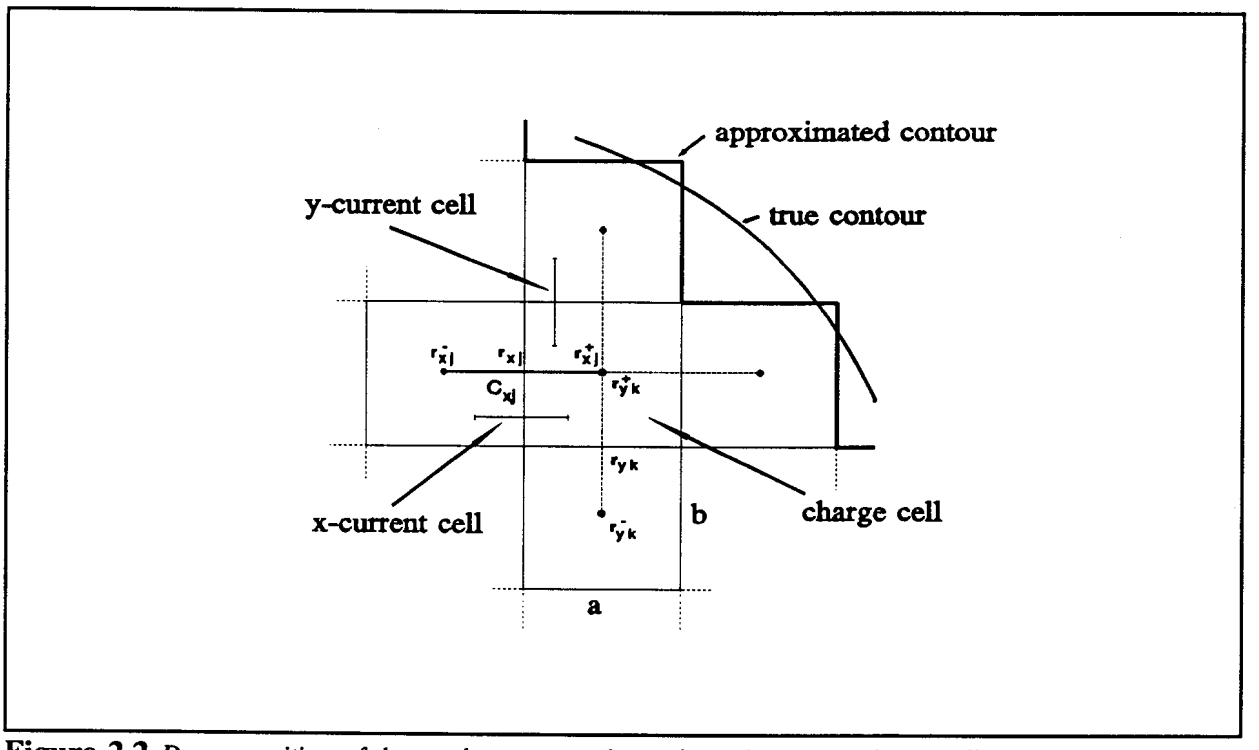

Figure 2.2 *Decomposition of the patch upper conductor into elementary charge cells.*

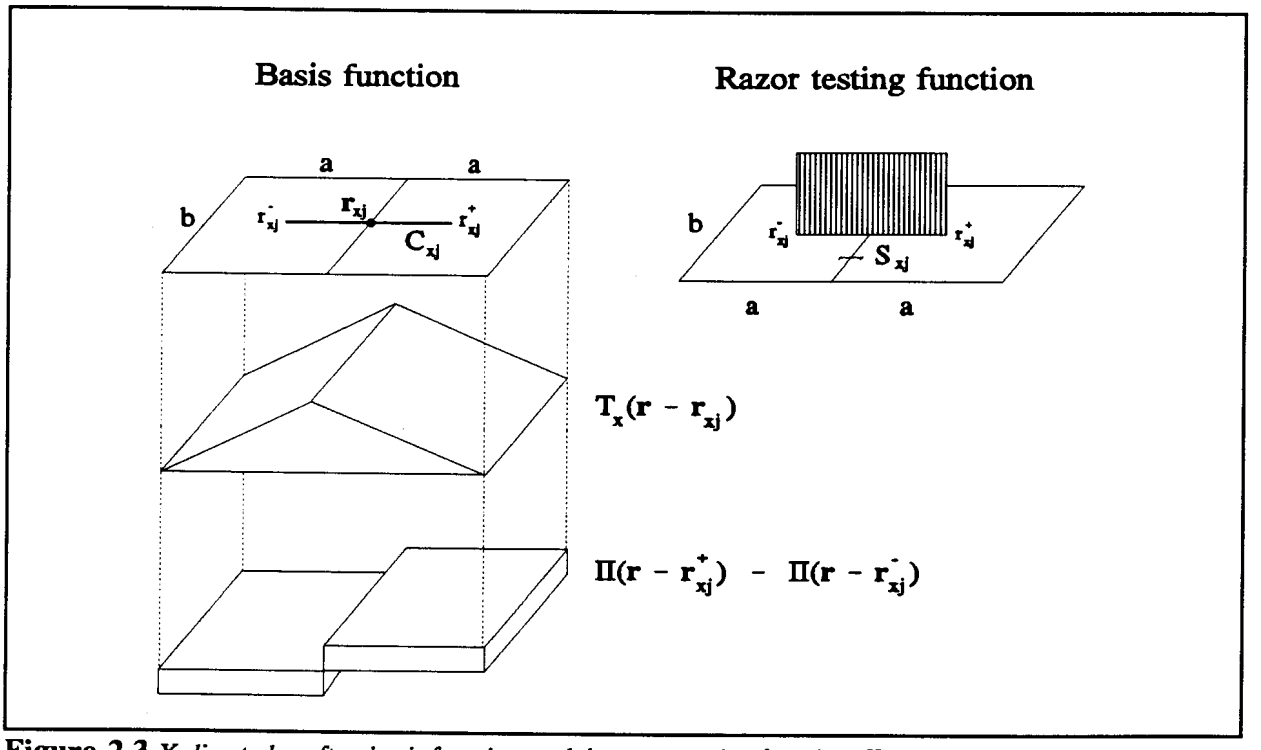

Figure 2.3 *X-directed rooftop basis function and the razor testing function. The associated charge distribution over the x-directed current cell is also shown.*

have been shown [4] to be most suitable. These testing functions, also called razor functions, extend along the segments linking the centres of adjacent charge cells as shown in Figure 2.3. The centre of test segment C_{xj} associated with the j'th x-directed current cell will be denoted by $\mathbf{r}_{xj}$ with its ends at $\mathbf{r}_{xj}^-$ and $\mathbf{r}_{xj}^+$.

2.3.4 Discrete Green's functions

The notation and computational task can be simplified by introducing *discrete Green's functions* (not to be confused with the Green's functions themselves) which have as sources complete basis functions as opposed to conventional elementary point sources. $\Gamma_A^{xx}(\mathbf{r}/\mathbf{r}_j)$ is then the x-component of the vector potential at $\mathbf{r}$ created by an x-directed rooftop distribution of surface current at $\mathbf{r}_j$, whereas $\Gamma_V(\mathbf{r}/\mathbf{r}_{oj})$ is the scalar potential at the same observation point resulting from a rectangular distribution of unit surface charge at $\mathbf{r}_{oj}$. The discrete Green's functions are now defined by the following dimensionless expressions [3]:

$$\Gamma_V(r/r_{oj}) = \int_{S_{oj}} \frac{\epsilon_0}{k_0} G_V(r/r') \Pi(r' - r_{oj}) k_o^2 \, dS' \qquad (2.19)$$

$$\Gamma_A^{xx}(r/r_{xj}) = \int_{S_{xj}} \frac{1}{\mu_0 k_0} G_A^{xx}(r/r') T_x(r' - r_{xj}) k_0^2 \, dS' \qquad (2.20)$$

A similar expression holds for Γ_A^{yy}. S_{xj} represents the surface of the current source cell centred at $\mathbf{r}_{xj}$ while the charge source cell centred at $\mathbf{r}_{oj}$ extends over S_{oj}. When the observation point $\mathbf{r}$ for the potential due to a particular source cell falls

within its own source cell boundaries, then the integrands for the discrete Green's functions are singular at **r** due to the Green's functions (one of the factors in the integrands) becoming singular. We will call any evaluation of the potential due to a given source cell at any point in its own source cell a "selfterm"; their evaluation is discussed in Section 3.3. We will use the term "scalar potential discrete Green's function" and "cell scalar potential" interchangeably.

2.3.5 The matrix equation

Through introduction of the basis and testing functions into the MPIE, we are able to transform the integral equation into a matrix algebraic equation which can be solved numerically. The use of discrete Green's functions yields the following matrix equation [2]

$$\begin{pmatrix} C^{xx} & C^{xy} \\ C^{yx} & C^{yy} \end{pmatrix} \begin{pmatrix} I_x \\ I_y \end{pmatrix} = \frac{1}{jZ_0} \begin{pmatrix} V_x^{(e)} \\ V_y^{(e)} \end{pmatrix} \tag{2.21}$$

where the elements of the submatrices are given by (note that the scalar potential due to any source cell is only required to be evaluated at the *centre* of its own cell and that of each of the other cells)

$$C_{ij}^{xx} = \frac{1}{k_0 a\, k_0 b}\Big[- \Gamma_V(r_{xi}^{+}/r_{xj}^{-}) - \Gamma_V(r_{xi}^{-}/r_{xj}^{+}) + \Gamma_V(r_{xi}^{+}/r_{xj}^{+}) + \Gamma_V(r_{xi}^{-}/r_{xj}^{-}) \Big] - \frac{1}{k_0 b}\int_{C_{xi}} \Gamma_A^{xx}(r/r_{xj})\, k_0\, dx + j\frac{Z_s}{Z_0}\frac{a}{b}\delta_{ij} \qquad (2.22)$$

$$i = 1 \ldots M \,,\; j = 1 \ldots M$$

and

$$C_{ij}^{xy} = \frac{1}{k_0 a\, k_0 b}\Big[- \Gamma_V(r_{xi}^{+}/r_{yj}^{-}) - \Gamma_V(r_{xi}^{-}/r_{yj}^{+}) + \Gamma_V(r_{xi}^{+}/r_{yj}^{+}) + \Gamma_V(r_{xi}^{-}/r_{yj}^{-}) \Big] \qquad (2.23)$$

$$i = 1 \ldots M \,,\; j = 1 \ldots N$$

δ_{ij} is the Kronecker delta, $V^{(e)}$ the excitation vector and Z_0 the free space characteristic impedance. An expression for C_{ij}^{yy} is obtained by interchanging couples (x,y), (a,b) and (M,N) within the expression for C_{ij}^{xx}; reciprocity, furthermore requires that for cells of equal size, $C_{ij}^{yx} = C_{ji}^{xy}$. We therefore have a matrix C of dimensions (M+N) × (M+N). Since construction of matrix C is a time-consuming task suitable approximations are sought to decrease computation time without sacrificing accuracy. In this regard, numerical tests performed by Mosig and Gardiol have shown [2] that for distances $|\, r_{xi} - r_{xj} \,|$ much greater than the dimensions of a charge cell, the following approximation for the integral

term in (2.22) may be considered:

$$\int_{C_{xi}} \Gamma_A^{xx}(r/r_{xj})\, k_0\, dx \simeq k_0\, a\, \Gamma_A^{xx}(r_{xi}/r_{xj}) \tag{2.24}$$

As a matter of fact, this approximation may be used everywhere, *even on the diagonal terms* [16]. Secondly, for large source-observer distances, the discrete Green's functions may be approximated by the following analytical expressions[5]:

$$\Gamma_V(r/r_{oj}) \simeq \frac{\epsilon_0}{k_0} G_V(r/r_{oj})\,(k_0 a)\,(k_0 b) \tag{2.25}$$

$$\Gamma_A^{xx}(r/r_{xj}) \simeq \frac{1}{\mu_0 k_0} G_A^{xx}(r/r_{xj})\,(k_0 a)\,(k_0 b) \tag{2.26}$$

The evaluation of the discrete Green's functions involves a large amount of computation; therefore it has been suggested [2] that an interpolation scheme be used to evaluate the Green's functions. Notice that for a given case, the Green's functions appearing in the integrands of expressions (2.19) and (2.20) are only dependent on the *distance* between source and observer[6]. It is therefore possible to tabulate the values for a small number of distances, ranging from zero to the maximum linear dimension of the etched radiator, and to interpolate between the tabulated values. Different tabulation schemes may be considered and some

[5] Sections 3.3.1 and 3.3.2 illustrate the validity of these approximations.

[6] On the other hand, *discrete Green's functions* are also dependent on source-observer orientation.

possibilities are discussed in Section 3.6. Interpolation allows a great reduction in computation time, while maintaining sufficient accuracy.

Finally, for the excitation vector, a coaxial probe feed will be considered for which a simple, yet sufficiently accurate model was introduced in [2]. This model assumes that the current on the coaxial probe is constant and is therefore only accurate for thin substrates[7]; more complex feed models valid for thick substrates are discussed in [17] and [18]. According to this model the excitation current spreads over a single charge cell (this model requires the coaxial probe to be located at the centre of a charge cell) as described by the following expression:

$$\boldsymbol{J}_e = \hat{x}\,\frac{I}{4b}\,sgn(x)\left(1 - \frac{2|x|}{a}\right) + \hat{y}\,\frac{I}{4a}\,sgn(y)\left(1 - \frac{2|y|}{b}\right) \qquad (2.27)$$

The associated excitation surface charge distribution over the charge cell is given by a rectangular pulse of value I/jωab where I is the total current carried by the inner coaxial conductor. Figure 2.4 gives an illustration of the electric surface current and charge distributions associated with the coaxial probe feed model. Note that only the x-directed component is featured for the sake of pictorial clarity; in actual fact, a similar distribution holds for the y-directed component as seen from (2.27). It has been found [16] that the contribution of the excitation *current* (as opposed to the *charge*) to $\mathbf{V}^{(e)}$ can usually be neglected, otherwise it

[7] Up to about λ/10 thick. This model is used in this thesis since we are primarily interested in computing the relative distribution of current on the structure (and hence array aperture distribution) rather than accurate input impedance computations which require considerably more computational intensive excitation models.

must be computed from the expression for Γ_A^{xx} (Γ_A^{yy}) with J_{ex} (J_{ey}) replacing T_x (T_y). This model was developed to be compatible with the basis functions, and thus, the elements of the excitation vector may be obtained from the matrix elements with the little additional (that is, if the contribution of the excitation current to $\mathbf{V}^{(e)}$ cannot be neglected) computation mentioned above [2]. If we recognise that the matrix elements according to (2.23) represent the effect of a charge doublet (Figure 2.3) integrated along a test segment, then since with the above coaxial probe model the excitation is a single pulse of charge (Figure 2.4), the elements of the excitation vector may be seen to be approximated by [16]

$$V_{xi}^{(e)} \approx \frac{Z_0}{j k_0 a k_0 b} \left[\Gamma_V(r_{xi}^+/r) - \Gamma_V(r_{xi}^-/r) \right]$$

$$V_{yi}^{(e)} \approx \frac{Z_0}{j k_0 a k_0 b} \left[\Gamma_V(r_{yi}^+/r) - \Gamma_V(r_{yi}^-/r) \right] \qquad (2.28)$$

where feedpoint r is located at the centre of a charge cell. In (2.28) it is assumed that the contribution of the excitation current to $\mathbf{V}^{(e)}$ is negligible. The matrix equation can now be solved for the unknown surface current coefficients I_x and I_y appearing in expressions (2.15) and (2.16). Matrix C is ill-conditioned, so that a careful evaluation of its elements is needed to obtain accurate final results. Once the surface current distribution is known, other antenna parameters of interest may be calculated; the radiation pattern for instance, may be obtained directly from the computed surface current distribution.

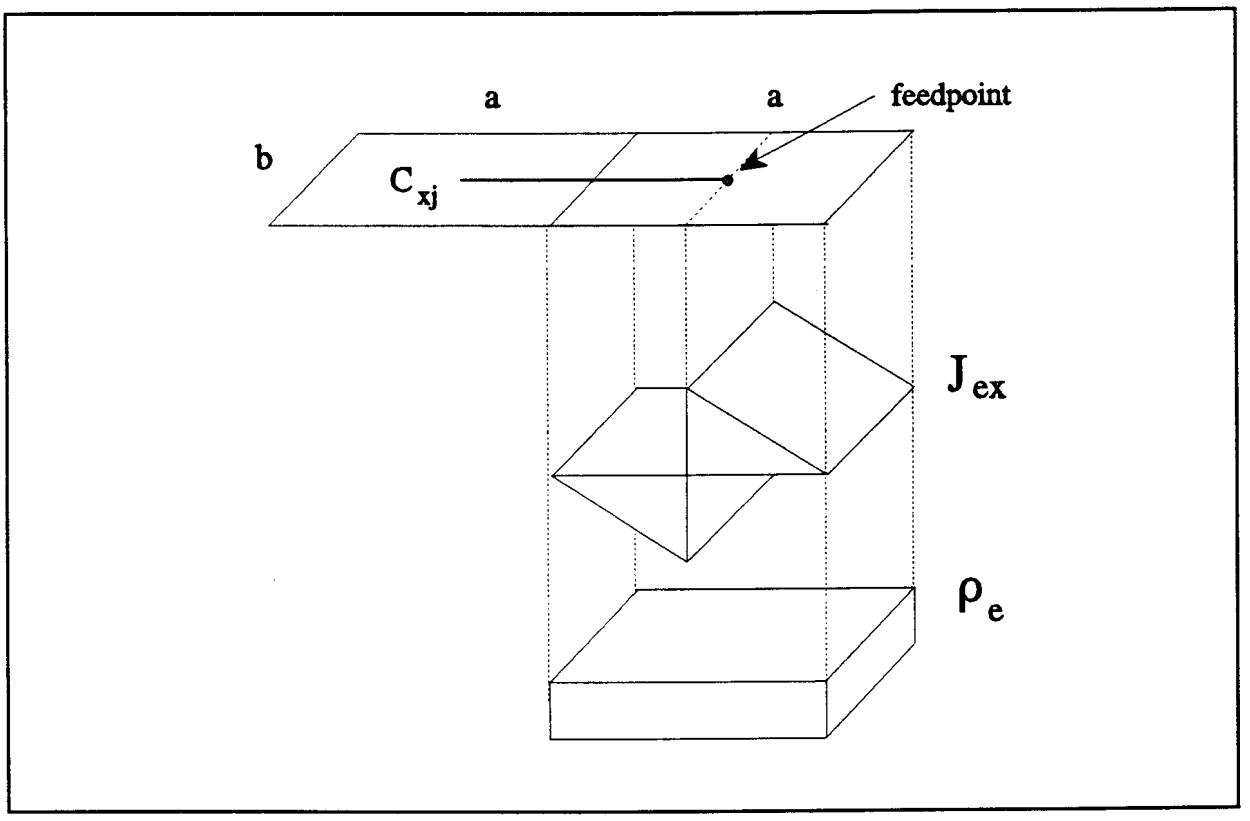

Figure 2.4 *Electric surface current and charge distributions associated with coaxial probe excitation.*

2.4 SUMMARY

In this chapter a review of existing analysis techniques for microstrip antennas was given. The transmission-line model was mentioned, from which it was concluded that a more accurate analysis technique would be needed to include effects such as surface waves and radiation. The cavity model, including effects such as surface waves and dielectric losses, was also discussed. This model, however, does not include mutual coupling effects and falls short of predicting behaviour in the case of electrically thick dielectrics. More accurate and sophisticated integral equation approaches, by which the microstrip antenna is modelled by an integral equation, were then considered. A thorough treatment

of the spatial domain mixed-potential integral equation formulation of Mosig and Gardiol [4] was then given. This formulation enables us to do an almost (except for finite groundplane effects) rigorous analysis of microstrip antennas. It permits for the analysis of complex-shaped microstrip radiators with any combination of dielectric thickness and permittivity; dielectric and ohmic losses as well as surface wave effects are also automatically included. There are in principle no limitations on frequency and the analysis remains accurate at frequencies other than some centre-frequency at which a particular design is done. However, to obtain quantitative results this formulation has to be implemented numerically; such numerical aspects form the subject of Chapter 3.

CHAPTER 3

COMPUTATIONAL ASPECTS OF THE SPATIAL DOMAIN FORMULATION IMPLEMENTED

3.1 INTRODUCTION

It was pointed out in Chapter 1 that the actual numerical implementation of the integral equation analysis of microstrip radiators requires substantial effort. Since relatively few details are available elsewhere, the present chapter is devoted to this aspect.

Numerical techniques needed in the construction of the Green's functions will receive close attention in Section 3.2, while discrete Green's functions defined in Chapter 2 will be discussed in Section 3.3 regarding selfterm evaluation and the possible use of approximations. The construction and solution of the moment method matrix equation will be the subject of Section 3.4, while Section 3.5 is concerned with routines used in numerical integration. Interpolation, used in the evaluation of the discrete Green's functions in order to reduce computation time, is discussed in Section 3.6. In particular, the tabulation scheme and interpolation itself will receive attention. Integrals in far-field radiation computation are not suited to standard numerical integration routines, necessitating the use of the asymptotic techniques discussed in Section 3.7.

An effort has been made in this chapter to graphically illustrate why numerical difficulties arise and how these are remedied. All computations performed for such illustrative purposes in this chapter were done at 1.206 GHz for

$\epsilon_r = (4.34, -0.0868)$. The effective conductivity (σ^*) was taken as $\sigma_{Cu}/4$ where $\sigma_{Cu} = 5.76 \times 10^7$ mhos/m.

3.2 CONSTRUCTION OF THE REQUIRED GREEN'S FUNCTIONS

The construction of the Green's functions require the determination of the potentials (both **A** and V, since this is a mixed-potential formulation) created by a horizontal electric dipole (HED) located on the air-dielectric interface of the microstrip structure. Appendix B derives expressions for these potentials, as well as the Green's functions needed for the solution of the surface current distribution. These expressions are repeated here for the sake of this discussion.

$$G_A^{xx}(r/r') = G_A^{yy}(r/r') = \frac{\mu_0}{2\pi}\int_0^\infty J_0(\lambda R)\frac{\lambda}{D_{TE}}d\lambda \tag{3.1}$$

$$G_V(r/r') = \frac{1}{2\pi\epsilon_0}\int_0^\infty J_0(\lambda R)\frac{\lambda\, N}{D_{TE}D_{TM}}d\lambda \tag{3.2}$$

where:

$$D_{TE} = \sqrt{\lambda^2 - k_0^2} + \sqrt{\lambda^2 - \epsilon_r k_0^2}\coth\left(h\sqrt{\lambda^2 - \epsilon_r k_0^2}\right) \tag{3.3}$$

$$D_{TM} = \epsilon_r\sqrt{\lambda^2 - k_0^2} + \sqrt{\lambda^2 - \epsilon_r k_0^2}\tanh\left(h\sqrt{\lambda^2 - \epsilon_r k_0^2}\right) \tag{3.4}$$

$$N = \sqrt{\lambda^2 - k_0^2} + \sqrt{\lambda^2 - \epsilon_r k_0^2}\tanh\left(h\sqrt{\lambda^2 - \epsilon_r k_0^2}\right) \tag{3.5}$$

Note that we have set $z=0$ in these Green's function expressions since we are (until Section 3.7) interested in surface current computation on this plane. Figure 3.1[1] shows the integrand of $2\pi/\mu_0\, G_A^{xx}$ as a function of λ/k_0 at 1.206 GHz for $\epsilon_r=(4.34,-0.0868)$, and the particular circumstances $h/\lambda_0=0.07$ and $R/\lambda_0=0.5$. λ_0 is the free space wavelength and should not be confused with the variable λ in $k_\rho=\lambda + j\upsilon$. The scalar potential counterpart, i.e. the integrand of $2\pi\epsilon_0\, G_V$ as a function of λ/k_0, is shown in Figure 3.2. As seen from these figures, and discussed briefly in Section 2.3.2, discontinuities, singularities and oscillations in the Green's function integrands pose distinct problems, complicating the use of numerical integration techniques. Mosig and Gardiol [14] therefore suggested that the semi-infinite integration interval be subdivided, allowing these problems to be addressed separately. As mentioned in Section 2.3.2, this subdivision allows the integral to be written as

$$\int_0^\infty F(\lambda)\,d\lambda = \int_0^{k_0} F(\lambda)\,d\lambda + \int_{k_0}^{k_0\sqrt{\epsilon_r'}} F(\lambda)\,d\lambda + \int_{k_0\sqrt{\epsilon_r'}}^\infty F(\lambda)\,d\lambda \qquad (3.6)$$

In the remainder of this section the problematic behaviour of the Green's function integrands in each of these sub-intervals will be illustrated, and proposed solutions will be discussed.

[1] All figures in this chapter were generated by the author and are original.

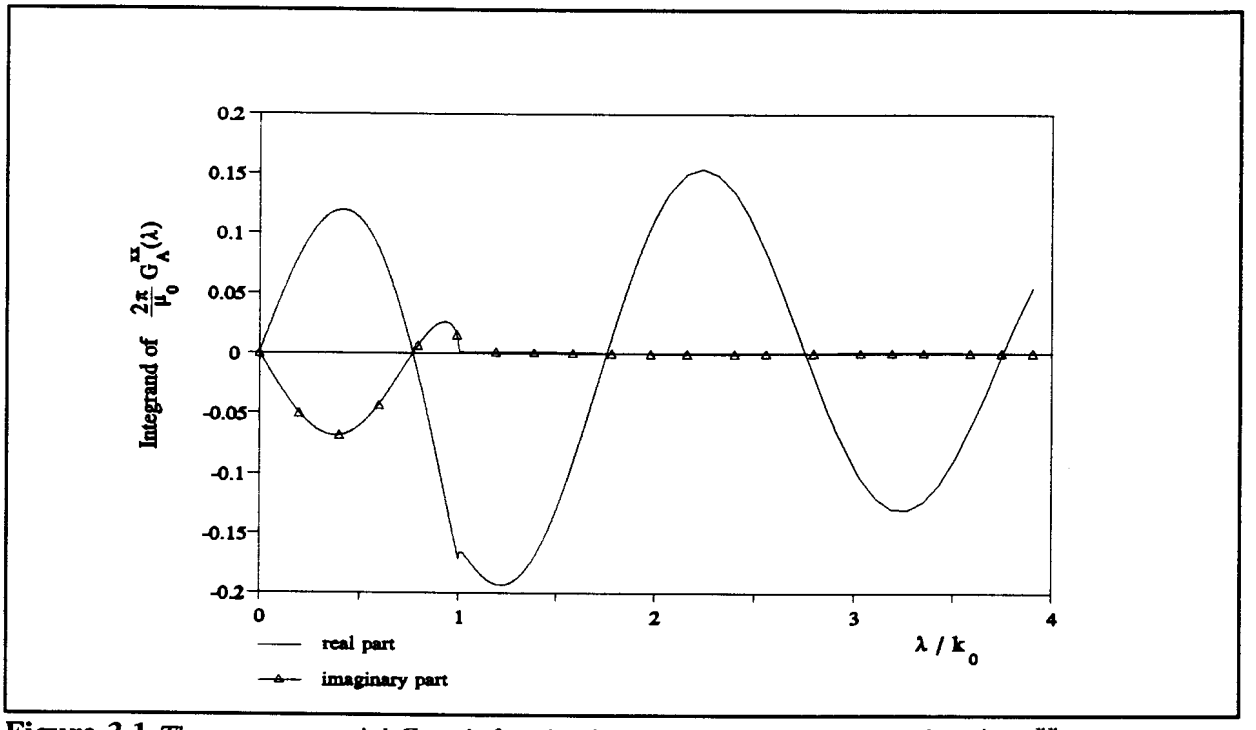

Figure 3.1 *The vector potential Green's function integrand, i.e. the integrand of* $2\pi/\mu_0 G_A^{xx}$ *for* $\varepsilon_r = (4.34, -0.0868)$, $h/\lambda_0 = 0.07$ *and* $R/\lambda_0 = 0.5$.

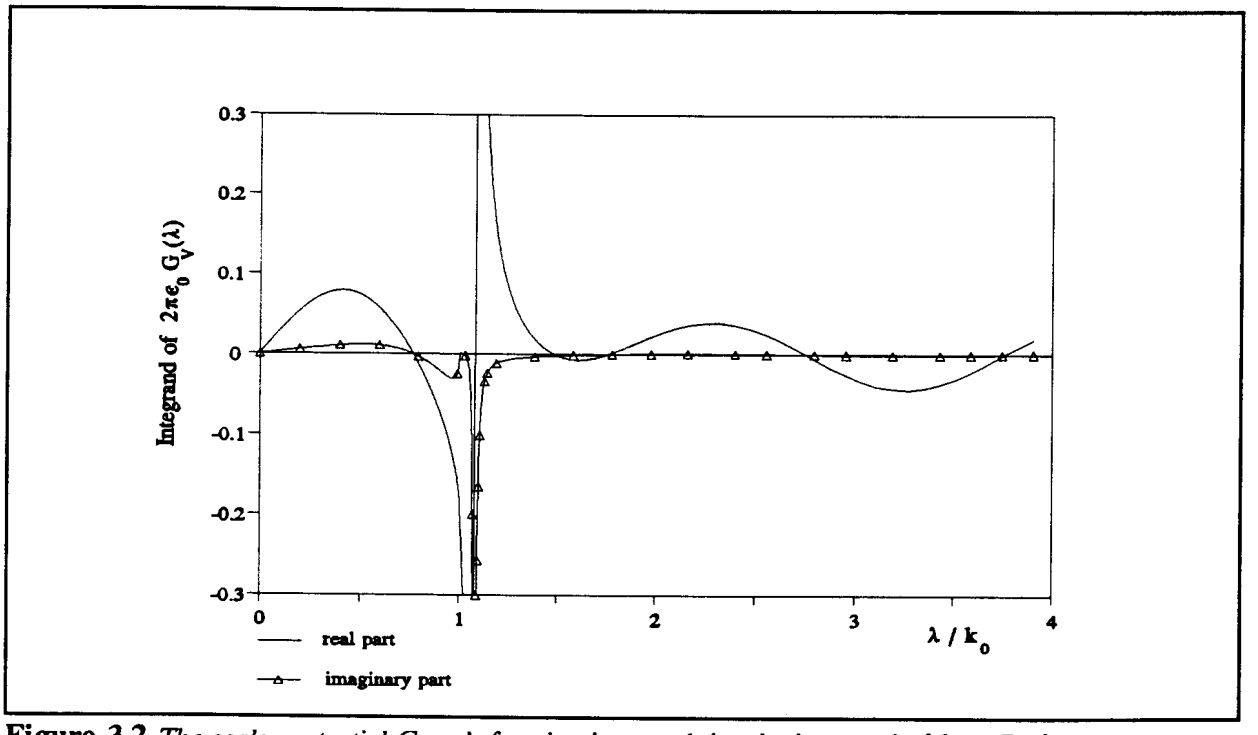

Figure 3.2 *The scalar potential Green's function integrand, i.e. the integrand of* $2\pi\varepsilon_0 G_V$ *for* $\varepsilon_r = (4.34, -0.0868)$, $h/\lambda_0 = 0.07$ *and* $R/\lambda_0 = 0.5$ *at* $f = 1.206$ *GHz.*

3.2.1 Interval [0 , k_0]

The term $u_0 = (\lambda^2 - k_0^2)^{1/2}$ appearing in the expressions for D_{TE}, D_{TM} and N introduces a branch point at $\lambda = k_0$. To define the term "branch point", let us consider a complex plane k_ρ where $k_\rho = \lambda + j\nu$. From Appendix B we recall that integration along the λ-axis (as in (3.1) and (3.2), for instance) is a special case of the complex integral along a path C on the k_ρ-plane. Therefore, u_0 transforms to

$$\sqrt{k_\rho^2 - k_0^2} \tag{3.7}$$

on this plane. We will now attempt to illustrate that the square root of a complex number is a multi-valued function. Consider for the moment a general complex number k_ρ. Now let us take the square root of k_ρ: $k_\rho^{1/2} = |k_\rho|^{1/2} e^{j\phi}$, where $\phi = (\theta_1/2 + m\pi) = \theta/2$ and $\theta = \arg(k_\rho)$; θ_1 being one possible value of θ. Examine the behaviour of $k_\rho^{1/2}$ as k_ρ attains values moving around the origin on a circle of unit radius. For $\theta = 0$ we have $k_\rho^{1/2} = 1$, since $|k_\rho|^{1/2} = 1$. Now if θ increases along the unit circle, we arrive back at the starting point after one revolution, where $\theta_1 = 0$, $m = 1$ and $k_\rho^{1/2} = -1$!. Therefore $k_\rho^{1/2}$ has two possible values (+1 and -1) for $k_\rho = (1,0)$, illustrating the multi-valuedness of the square root[2] of a complex number. *The origin whose encirclement produces the multi-valuedness is defined as the branch point.* Hence, $k_\rho = 0$ represents the branch point for $k_\rho^{1/2}$ whereas application of this theory to (3.7) leads to the conclusion that

[2] In similar fashion it may be shown that multi-valuedness occurs for general fractional powers.

$k_\rho = \pm k_0$ represents it's branch points. Since this root appeared in both Green's function expressions (i.e. in both (3.1) and (3.2)), branch points can be seen in both these integrands. Manifestations thereof are the discontinuities in the derivatives seen at $\lambda = k_0$. Standard numerical integration routines may be inefficient in the integration of functions with such discontinuous derivatives. To obtain accurate numerically integrated estimates for the Green's functions over the first interval, Mosig and Gardiol [3] have proposed the substitution $\lambda = k_0 \cos t$. Suppose the integrands may be written as $F(\lambda)$, then this substitution implies that

$$\int_0^{k_0} F(\lambda)\, d\lambda = \int_{1.5\pi}^{2\pi} F(k_0 \cos t)(-k_0 \sin t)\, dt \qquad (3.8)$$

Figures 3.3 and 3.4 give graphical illustrations of the integrands in Figures 3.1 and 3.2, respectively, after substitution in the interval $[0\ ,\ k_0]$. In other words, Figures 3.3 and 3.4 show $F(k_0 \cos t)(-k_0 \sin t)$ as functions of t, with $F(\lambda)$ representing the integrands of $2\pi/\mu_0 G_A^{xx}$ and $2\pi\epsilon_0 G_V$, respectively. The integrands are found to be smooth and easily integrable. In this way then, it is possible to deal with the effect of the branch point at $\lambda = k_0$.

3.2.2 Interval $[k_0\ ,\ k_0(\epsilon_r')^{1/2}]$

Since the integrand of G_V contains D_{TM} in the denominator (3.2), a singularity due to the existence of the dominant TM_0 surface wave mode, appears in the interval $[k_0\ ,\ k_0(\epsilon_r')^{1/2}]$, as discussed in Section 2.3.2 and seen from Figure 3.2

(Note that the amplitude of the integrand at the singularity has been limited in this figure for the sake of pictorial clarity). This singularity lies slightly below the real λ-axis on the complex plane k_ρ for cases of moderate dielectric loss, while it lies on the λ-axis for the lossless case ($\tan\delta = 0$). Strong variations of the integrand are caused by the pole, even in the lossy case. Following a pole extraction technique described in [3], the $2\pi\epsilon_0 G_V$ integrand may be expanded as follows: $J_0(\lambda R)\lambda N/(D_{TE}D_{TM}) = F(\lambda) = [F(\lambda) - F_{sing}(\lambda)] + F_{sing}(\lambda)$ where $F_{sing}(\lambda) = Res / [\lambda - (\lambda_p + j\nu_p)]$; Res is the residue of $F(k_\rho)$ at pole $k_{\rho p} = \lambda_p + j\nu_p$. This leaves $k_{\rho p}$ and Res to be determined. The present author has used Müller's method [19] with deflation to determine $k_{\rho p}$ - a root of the univariate complex function $D_{TM}(k_\rho)$; this method is numerically implemented in the IMSL routine ZANLY [20]. We also mention two methods whereby the residue may be determined.

Firstly,

$$Res = Res\left\{F(k_\rho), k_{\rho p}\right\} = \frac{1}{2\pi j}\oint_C F(k_\rho)\,dk_\rho \qquad (3.9)$$

where C is *any closed path* around the pole at $k_{\rho p}$. A condition, however, is that function $F(k_\rho)$ must be *analytic* inside C except at $k_{\rho p}$ [21]; a function $F(k_\rho)$ is said to be analytic in a domain D if $F(k_\rho)$ is defined and differentiable at all points of D [21]. The residue in (3.9) is written in the form of a complex line integral, and it may also be written in parametrised form as,

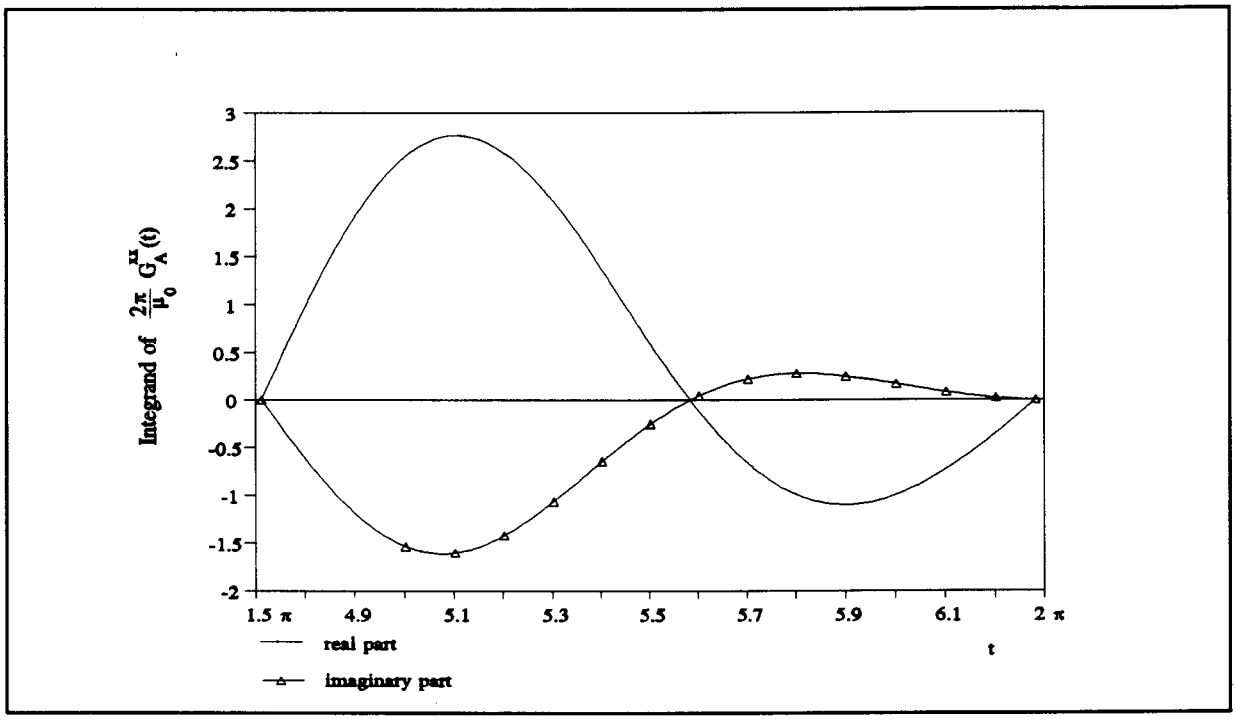

Figure 3.3 *Integrand of $2\pi/\mu_0 G_A^{xx}$ for $\lambda \in [0,k_0]$ after substitution $\lambda = k_0 \cos t$.*

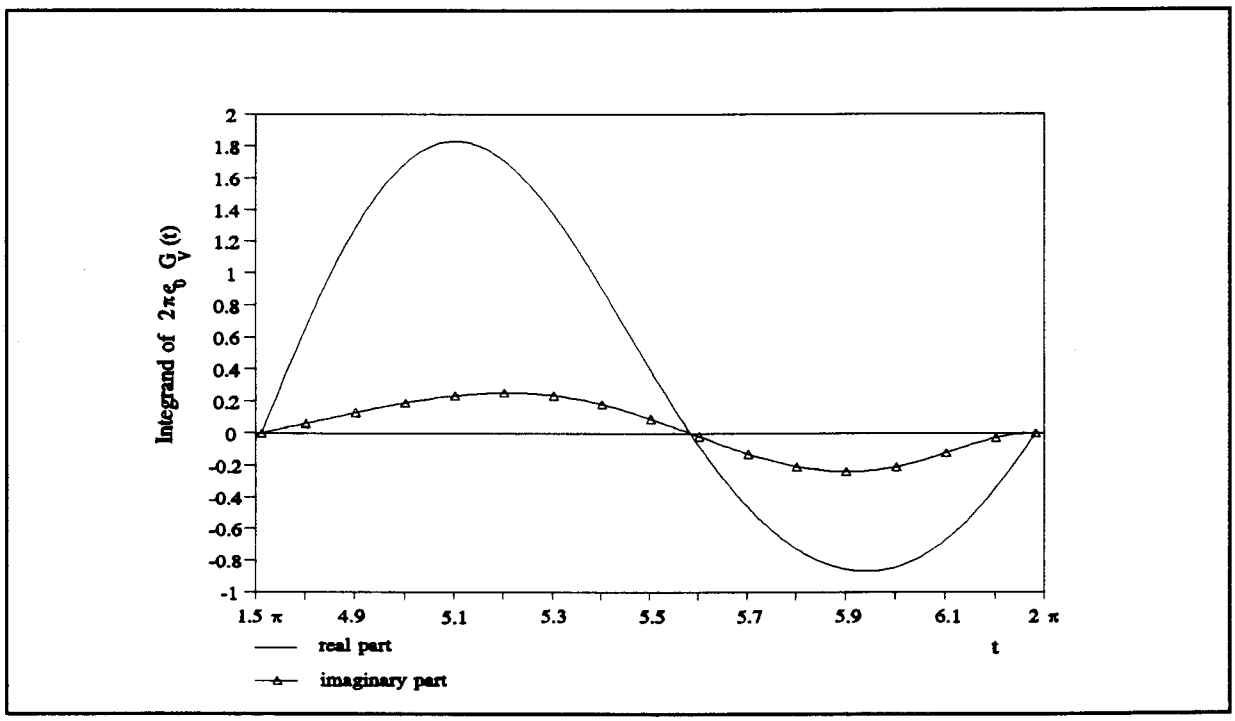

Figure 3.4 *Integrand of $2\pi\epsilon_0 G_V$ in the interval $\lambda \in [0,k_0]$ after substitution $\lambda = k_0 \cos t$.*

$$Res = Res\left\{F(k_\rho), k_{\rho p}\right\} = \frac{1}{2\pi j}\int_a^b F(k_\rho(t))\frac{dk_\rho(t)}{dt}dt \qquad (3.10)$$

where $k_\rho(t) = \lambda(t) + j\nu(t)$, $t \in [a,b]$. Since C may be represented by *any* closed path around $k_{\rho p}$, it is convenient to choose a circle. Then we have $\lambda(t) = r\cos t$ and $\nu(t) = r\sin t$ as the parametric equations; $t \in [0,2\pi)$ and r is the radius of the circle. The value of r is not important, provided F is analytic inside the borders of the circle except at $k_{\rho p}$. Figure 3.5 now shows the normalised distance $|k_{\rho p}/k_0 - 1|$ between pole $k_{\rho p}$ and the branch point at $\lambda = k_0$ (discussed in the previous section) as a function of dielectric thickness (h/λ_0). It can be seen that in the case of electrically thin substrates, the pole due to the surface wave is very close to the branch point. In such cases, radius r must be chosen carefully to avoid the inclusion of the branch point into the borders of the circle - inclusion thereof violating the analyticity of $F(k_\rho)$. With the use of (3.10) and careful selection of r, it is now possible to numerically determine a value for Res. For instance, at 1.206 GHz ($k_0 = 25.2753$) for $h/\lambda_0 = 0.07$, $R/\lambda_0 = 0.5$ and $\epsilon_r = (4.34, -0.0868)$, we have (for $r = 1.0153\ m^{-1}$) $Res = (0.47323, -0.01815)$ where $k_{\rho p} = (27.3059, -0.052039)$.

A second method which may be used numerically in the determination of the residue is:

$$Res = Res\left\{F(k_\rho), k_{\rho p}\right\} = \lim_{k_\rho \to k_{\rho p}} (k_\rho - k_{\rho p})F(k_\rho) \qquad (3.11)$$

Once $k_{\rho p}$ and the residue are known, the pole in the G_V integrand may be extracted according to the technique described above; i.e.:

$$\int_{k_0}^{k_0\sqrt{\epsilon_r'}} F(\lambda)\,d\lambda = \int_{k_0}^{k_0\sqrt{\epsilon_r'}} [F(\lambda) - F_{sing}(\lambda)]\,d\lambda + \int_{k_0}^{k_0\sqrt{\epsilon_r'}} F_{sing}(\lambda)\,d\lambda \qquad (3.12)$$

F_{sing} is analytically integrable as shown in (2.14), while the difference term, which is a well-behaved function, may be integrated numerically. Although the difference term itself is well-behaved, the terms $F(\lambda)$ and $F_{sing}(\lambda)$ become singular at $k_{\rho p}$. In the lossless case, to numerically evaluate the respective terms at $k_{\rho p}$ before subtraction, a small increment is added to the argument λ at the singularity. In this way the difference term is evaluated at $k_{\rho p}+\delta$ where $\delta \to 0$. An infinite derivative in the difference term integrand at $\lambda = k_0$ may be eliminated by the substitution $\lambda = k_0 \cosh t$. The real and imaginary parts of the G_V difference term integrand, after substitution, are shown in Figure 3.6; the singularity which has been extracted is visible in Figure 3.2. If the integrand does not contain D_{TM} in the denominator, the substitution may nevertheless be performed to obtain a smooth integrand at $\lambda = k_0$. This is the case for the Green's function $G_A^{xx}(\mathbf{r}/\mathbf{r}')$ (and $G_A^{yy}(\mathbf{r}/\mathbf{r}')$ for that matter), for which Figure 3.7 gives an illustration, after substitution, of the integrand shown in Figure 3.1.

At this point, we are able to accurately determine the integrals in (3.1) and (3.2) for $0 \le \lambda \le k_0(\epsilon_r')^{1/2}$. This leaves the interval $\lambda > k_0(\epsilon_r')^{1/2}$ which is the subject of Section 3.2.3.

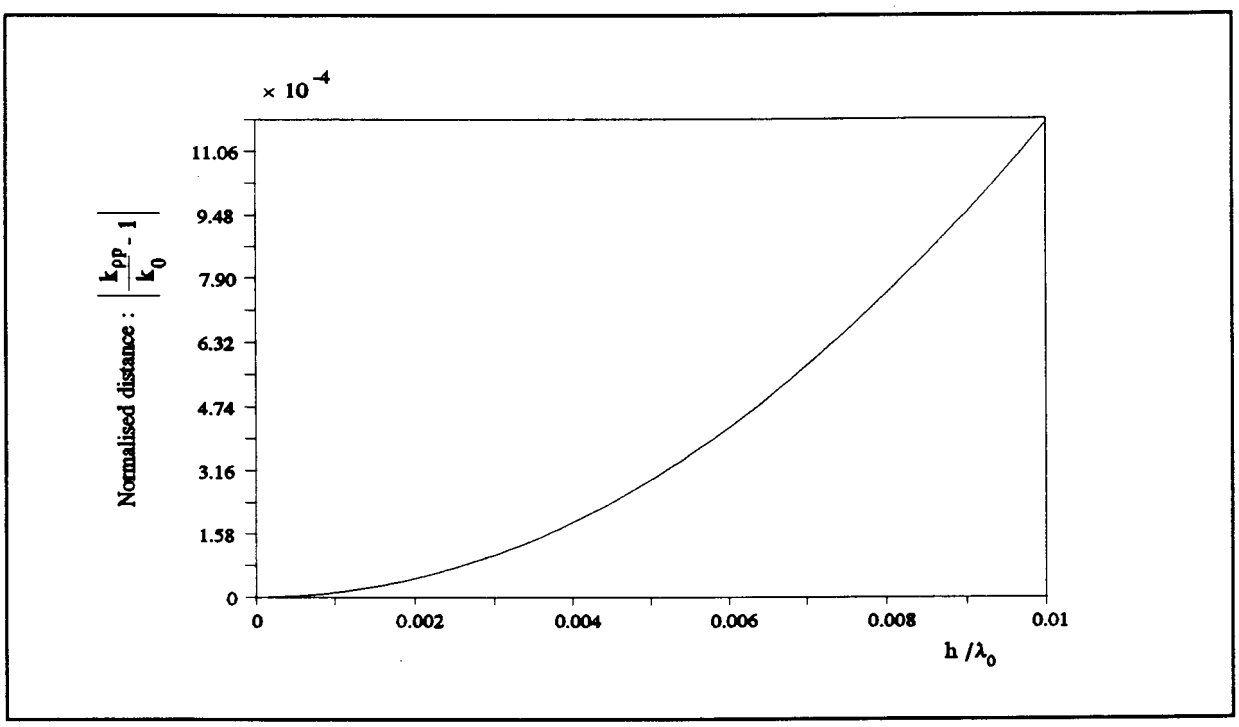

Figure 3.5 *Normalised distance between the pole (due to D_{TM}) and the branch point (due to u_0) as a function of dielectric thickness, i.e. $|k_{\rho p}/k_0 - 1|(h/\lambda_0)$.*

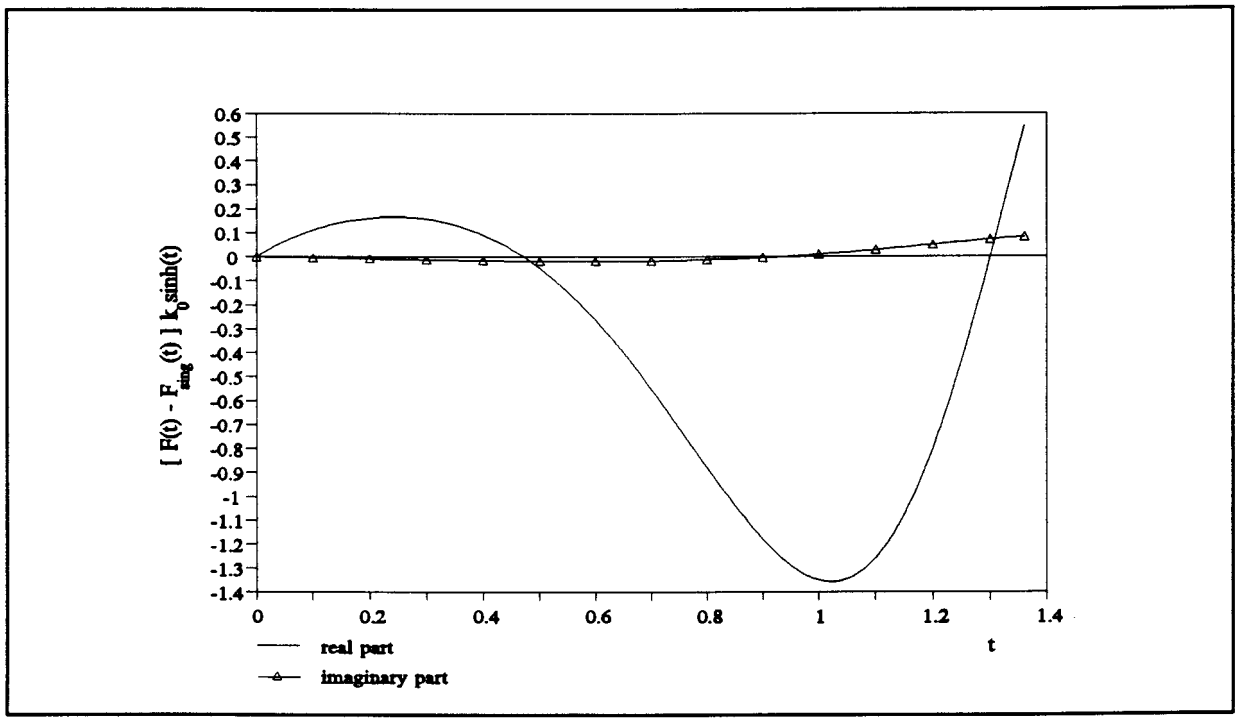

Figure 3.6 *$2\pi\epsilon_0 G_V$ difference term integrand after substitution $\lambda = k_0 \cosh t$. $F(\lambda)$ and $F_{sing}(\lambda)$ are defined in Section 3.2.2.*

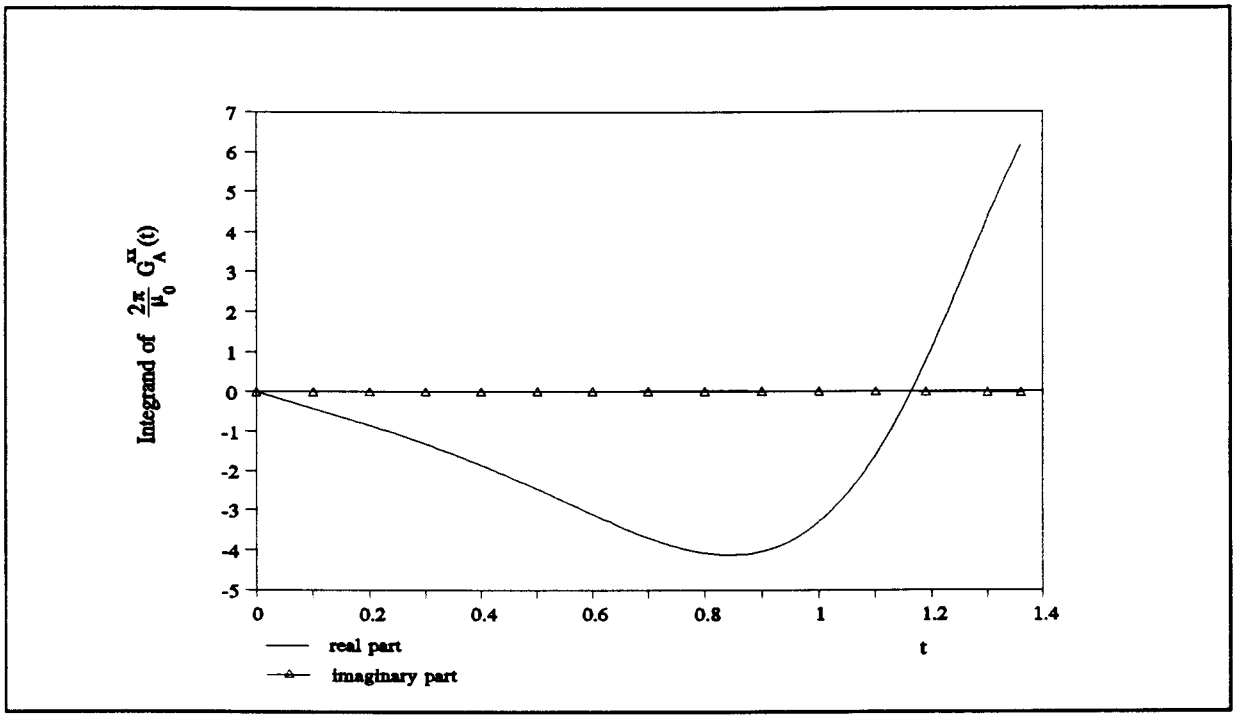

Figure 3.7 *Integrand of $2\pi/\mu_0\ G_A^{xx}$, shown in Figure 3.1, after substitution $\lambda = k_0 \cosh t$ in the interval $\lambda \in [k_0, k_0\sqrt{\epsilon_r'}]$.*

3.2.3 Method of averages in the interval $[k_0(\epsilon_r')^{1/2}, \infty]$

As seen from Figures 3.1 and 3.2 the Green's function integrands show oscillatory behaviour in this interval. Figures 3.8 and 3.9, furthermore, show that these integrands have envelopes which converge very slowly. Standard integration routines (such as the trapezium rule and Gauss quadrature) prove to be very inefficient in the integration of such functions, since a large number of integration points is required to achieve reasonable accuracy. Mosig and Gardiol [14] have found a technique known as the *method of averages*, introduced by Hurwitz and Zweifel [22], to be suitable for application to Sommerfeld integrals appearing in microstrip problems. This method is based on the decomposition

$$\int_a^\infty g(\xi R) f(\xi)\, d\xi = \sum_{n=0}^{\infty} \int_{a+np/2}^{a+(n+1)p/2} g(\xi R) f(\xi)\, d\xi \qquad (3.13)$$

where $g(\xi R)$ is an oscillating function with period p and $f(\xi)$ a smooth, non-oscillating function which behaves asymptotically as $O(\xi^{\alpha})$; the integrand therefore diverges for $\alpha > 0$. The integration over each half cycle is performed prior to the series summation. Although Bessel functions of the first kind - appearing in the Green's function expressions - are not strictly periodic, the method of averages may still be applied. However, since the zero's of Bessel functions are not known off-hand, the use of numerical techniques would be required, thereby considerably increasing computation time. Instead, Mosig and Gardiol [14] suggested the use of the large-argument approximation $J_n(\lambda R) \approx [2/(\pi\lambda R)]^{1/2}\cos(\lambda R - \pi/4 - n\pi/2)$ to estimate the zero's of the Bessel functions. Now we have

$$\xi_m \sim \left[(m-1) + 0.75 + \frac{n}{2}\right]\frac{\pi}{R} \tag{3.14}$$

where ξ_m approximates the m'th zero of $J_n(\lambda R)$. Table 3.1 indicates the accuracy of this approximation in comparing ξ_m ($m = 1,2,3...$) with the actual zero's of $J_0(\lambda)$ determined with the IMSL routine ZREAL [20]. A question about the validity of this approximation for small R values (source and observation points close to each other) might well arise at this point. In an attempt to answer this question, definite integrals for which the answers are known, were evaluated by the author

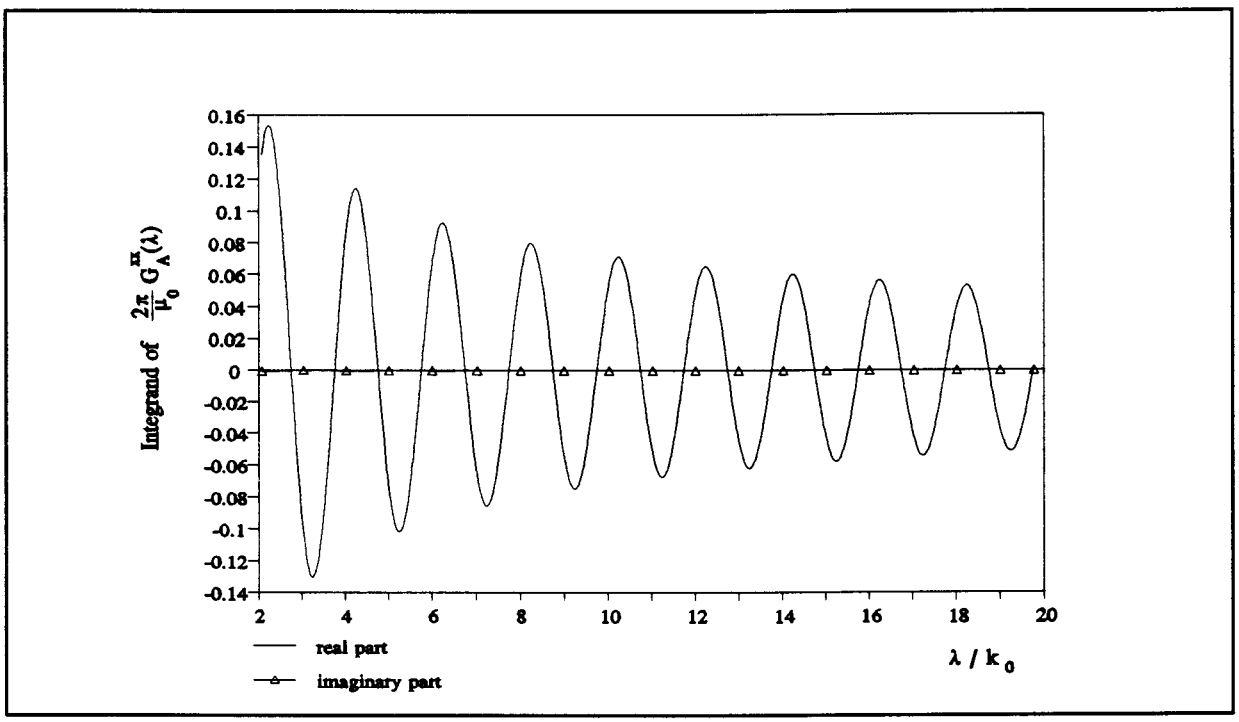

Figure 3.8 *Integrand of $2\pi/\mu_0 G_A^{xx}$ for $\lambda \in [k_0\sqrt{\epsilon_r}, 20k_0]$ showing the oscillating integrand with the slowly converging envelope.*

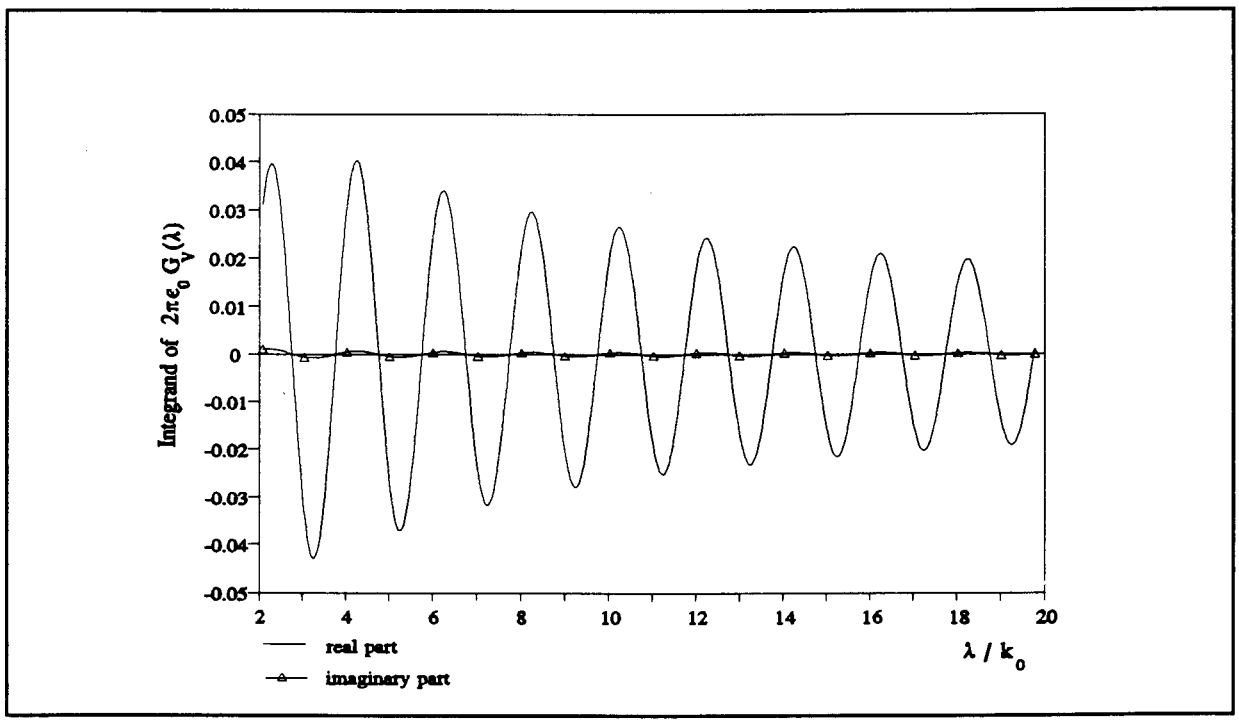

Figure 3.9 *$2\pi\epsilon_0 G_V$ integrand, illustrating the slowly converging envelope for $\lambda > k_0\sqrt{\epsilon_r}$.*

m	m'th ZERO OF $J_0(\lambda)$	APPROXIMATION: ξ_m	% ERROR
1	2.4048255576	2.3561944901	2.0222
2	5.5200781103	5.4977871437	0.4038
3	8.6537279129	8.6393797974	0.1658
4	11.791534439	11.780972450	0.08957
5	14.930917708	14.922565104	0.05594
6	18.071063968	18.064157758	0.03822
7	21.211636629	21.205750411	0.02775
8	24.352471531	24.347343065	0.02105

Table 3.1: Zero's of $J_0(\lambda)$ determined with ZREAL [20] and (3.14), respectively.

using (3.14) in the method of averages. We know from [23] that

$$\int_0^\infty J_n(\lambda R)\, d\lambda = \frac{1}{R} \tag{3.15}$$

for n > -1. This identity was confirmed for R values ranging from 2.0×10^{-6} to 2.0 and for both n = 0 and n = 1:

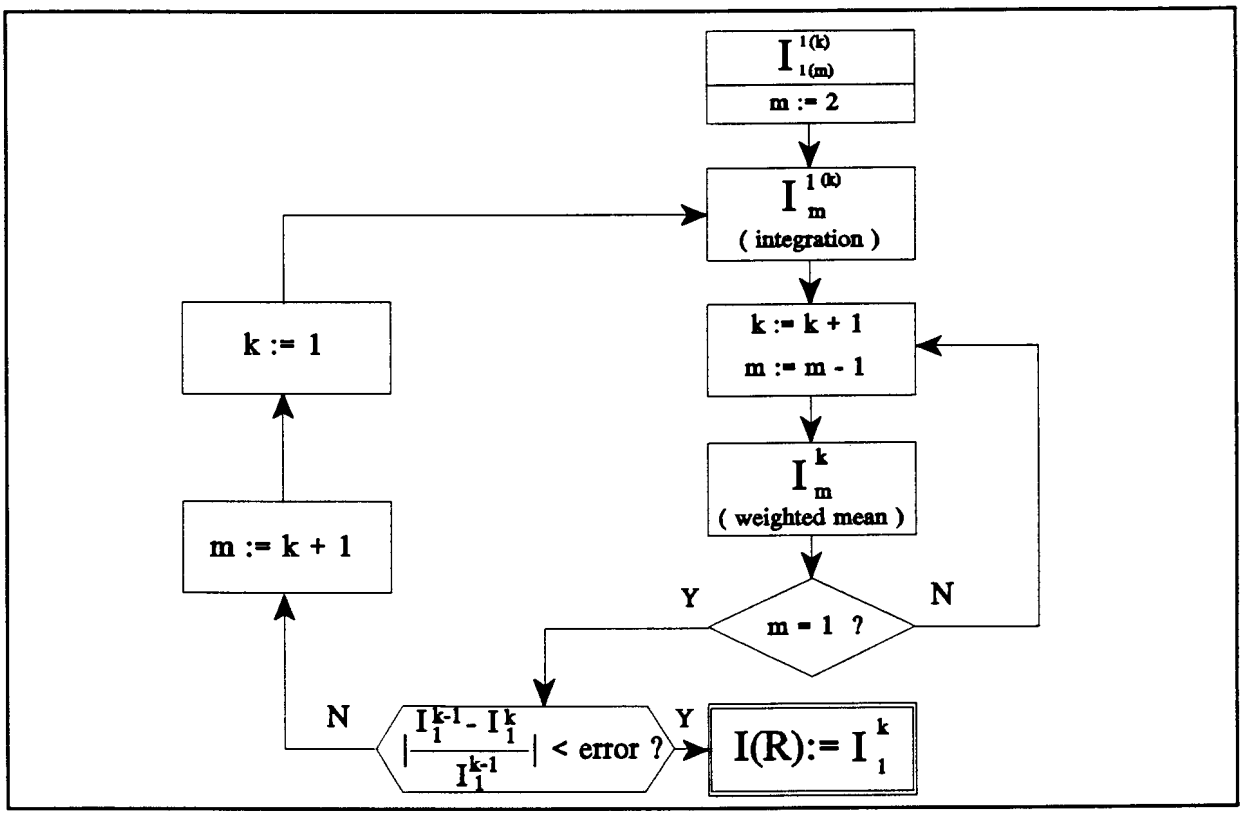

Figure 3.10 *Flowchart for the method of averages. Integration is performed according to (3.17) while the weighted mean expression is given in (3.19).*

$$\int_0^\infty J_n(\lambda R)\,d\lambda = \begin{cases} 0.500 & ;\ R = 2 \\ 5.00 & ;\ R = 0.2 \\ 5.00\times 10^{2} & ;\ R = 2\times 10^{-3} \\ 5.00\times 10^{5} & ;\ R = 2\times 10^{-6} \end{cases} \tag{3.16}$$

Further tests performed on such identities lead to the conclusion that (3.14) will not introduce a significant error, even for small values of R, when used in the method of averages.

Figure 3.10 gives the method of averages in the form of a flowchart. The first step is to perform an integration over a half cycle to determine I^1_m.

$$I_m^1 = \begin{cases} \int_a^{\xi_m} g(\xi R) f(\xi) d\xi & \text{for } m = 1 \\ I_{m-1}^1 + \int_{\xi_{m-1}}^{\xi_m} g(\xi R) f(\xi) d\xi & \text{for } m > 1 \end{cases} \tag{3.17}$$

where ξ_m is the m'th successive zero of the oscillating function g, with $\xi_m > a$. I_{m-1}^2 is then determined through the use of a *weighted mean*

$$I_{m-1}^2 = \frac{w_{m-1}^1 I_{m-1}^1 + w_m^1 I_m^1}{w_{m-1}^1 + w_m^1} \tag{3.18}$$

with both I_m^1 and I_{m-1}^1 having been determined previously through integration and with the weights given by $w_m^k = (\xi_1/\xi_m)^{(\alpha+1-k)}$. In general, (3.18) is given by

$$I_m^k = \frac{w_m^{k-1} I_m^{k-1} + w_{m+1}^{k-1} I_{m+1}^{k-1}}{w_m^{k-1} + w_{m+1}^{k-1}} \tag{3.19}$$

Repeated application of (3.19), with m decreasing towards 1 and k increasing simultaneously, leads to a value for I_1^k, which will give an approximation of the actual value, I(R), despite the fact that no additional integrations were performed. If the error criterion is not met, I_m^1 (where $m = k+1$) may be determined through integration, (3.17), and I_1^{k+1} through repeated application of (3.19). In this way, an estimate for I(R) may be obtained.

In the determination of the discrete Green's function[3] selfterms, the situation arises where the distance between source and observer (R) tends to zero. The effect of this, according to (3.14), is that the zero's of the oscillating Green's function integrand move further out from the origin along the λ-axis. In the method of averages, weights are determined according to the zero's of the oscillating function, i.e. $w_m^k = (\xi_1/\xi_m)^{(\alpha+1-k)}$. Now it is apparent that, for $\xi_m >> \xi_1$ and k a positive integer which may be large, the weight w_m^k could become a very large real number, creating possible numerical difficulties (numeric overflow or round-off errors, for instance). The present author has addressed this problem by firstly writing (3.19) as

$$I_m^k = \frac{10^{\log_{10}(w_m^{k-1})}\, 10^{\log_{10}(I_m^{k-1})} + 10^{\log_{10}(w_{m+1}^{k-1})}\, 10^{\log_{10}(I_{m+1}^{k-1})}}{10^{\log_{10}(w_m^{k-1})} + 10^{\log_{10}(w_{m+1}^{k-1})}} \qquad (3.20)$$

To ease mathematical manipulation, let

$a = (\alpha+2-k)\log_{10}(\xi_1/\xi_m)+\log_{10}(I_m^{k-1})$;[4]

$b = (\alpha+2-k)\log_{10}(\xi_1/\xi_{m+1})+\log_{10}(I_{m+1}^{k-1})$

$c = (\alpha+2-k)\log_{10}(\xi_1/\xi_m)$ and

$d = (\alpha+2-k)\log_{10}(\xi_1/\xi_{m+1})$. Then it follows that

$$I_m^k = \frac{10^a + 10^b}{10^c + 10^d} = \frac{10^a}{10^c}\left(\frac{1 + 10^{b-a}}{1 + 10^{d-c}}\right) = 10^{a-c}\left(\frac{1 + 10^{b-a}}{1 + 10^{d-c}}\right) \qquad (3.21)$$

---

[3] To be defined in Section 3.3.

[4] $\log_{10}(w_m^{k-1}) = (\alpha+2-k)\log_{10}(\xi_1/\xi_m)$ since $w_m^{k-1} = (\xi_1/\xi_m)^{(\alpha+2-k)}$

Therefore

$$I_m^k = 10^{\log_{10}(I_m^{k-1})}\left(\frac{1+10^{(\alpha+2-k)\left\{\log_{10}\left(\frac{\xi_1}{\xi_{m+1}}\right)-\log_{10}\left(\frac{\xi_1}{\xi_m}\right)\right\}}\,10^{\log_{10}(I_{m+1}^{k-1})-\log_{10}(I_m^{k-1})}}{1+10^{(\alpha+2-k)\left\{\log_{10}\left(\frac{\xi_1}{\xi_{m+1}}\right)-\log_{10}\left(\frac{\xi_1}{\xi_m}\right)\right\}}}\right) \tag{3.22}$$

where $10\exp\{(\alpha+2\text{-}k)[\log_{10}(\xi_1/\xi_{m+1})\text{-}\log_{10}(\xi_1/\xi_m)]\} = \beta$ is now a manageable real number even though w_m^{k-1} and/or w_{m+1}^{k-1} may be very large. Consider a situation where $\xi_1=200$, $\xi_{50}=8\times10^3$, $\xi_{51}=8.1\times10^3$, $k=50$ and $\alpha=0$; then we have: $w_{50}^{49}=7.923\times10^{76}$ and $w_{51}^{49}=1.438\times10^{77}$ whilst $\beta = 1.815$!. Therefore, to avoid numerical difficulties which may be encountered in a straightforward application of (3.19), we propose (3.22) as a means to determine I_m^k.

Figure 3.11 illustrates the effect of the distance between source and observer on the Green's function integrands; the real part of the G_A^{xx} integrand is shown for $R=0.5\lambda_0$ and $0.05\lambda_0$. It can be seen that when the observer ($\mathbf{r}$) approaches the source point ($\mathbf{r}'$), the zero's of the integrand move away from the origin. In the limiting case ($R=|\mathbf{r}-\mathbf{r}'|\to 0$) the first zero tends to infinity, producing a non-oscillating, non-zero function to be integrated over a semi-infinite interval. This produces the singularity in the Green's function at the source point. Figure 3.8 shows the real and imaginary parts of the G_A^{xx} integrand over the interval $[k_0(\epsilon_r')^{1/2}, 20k_0]$ for $R/\lambda_0=0.5$. As seen from this figure, the amplitude of the oscillation shown by the imaginary part of this integrand is negligible compared to the amplitude of the real part. A similar illustration is given in Figure 3.9 for

the scalar potential integrand; the imaginary part of this integrand, on the other hand, shows oscillations almost comparable in amplitude to that shown by the real part. A comparison between the imaginary parts of the respective Green's function integrands can be drawn from Figure 3.12 - note the strong oscillations shown by the imaginary part of the G_V integrand compared to that shown by its vector potential counterpart. This observation will be referred to again in Section 3.3.2 on discrete Green's functions. The effect of dielectric substrate thickness on the G_A^{xx} integrand is shown in Figure 3.13. For a very thin substrate ($h=0.001\lambda_0$), the integrand diverges over part of the interval; however, convergence as the argument moves out to infinity can be seen on Figure 3.14, which illustrates the G_A^{xx} integrand for $h=0.01\lambda_0$[5].

[5] The same is observed for $h=0.001\lambda_0$.

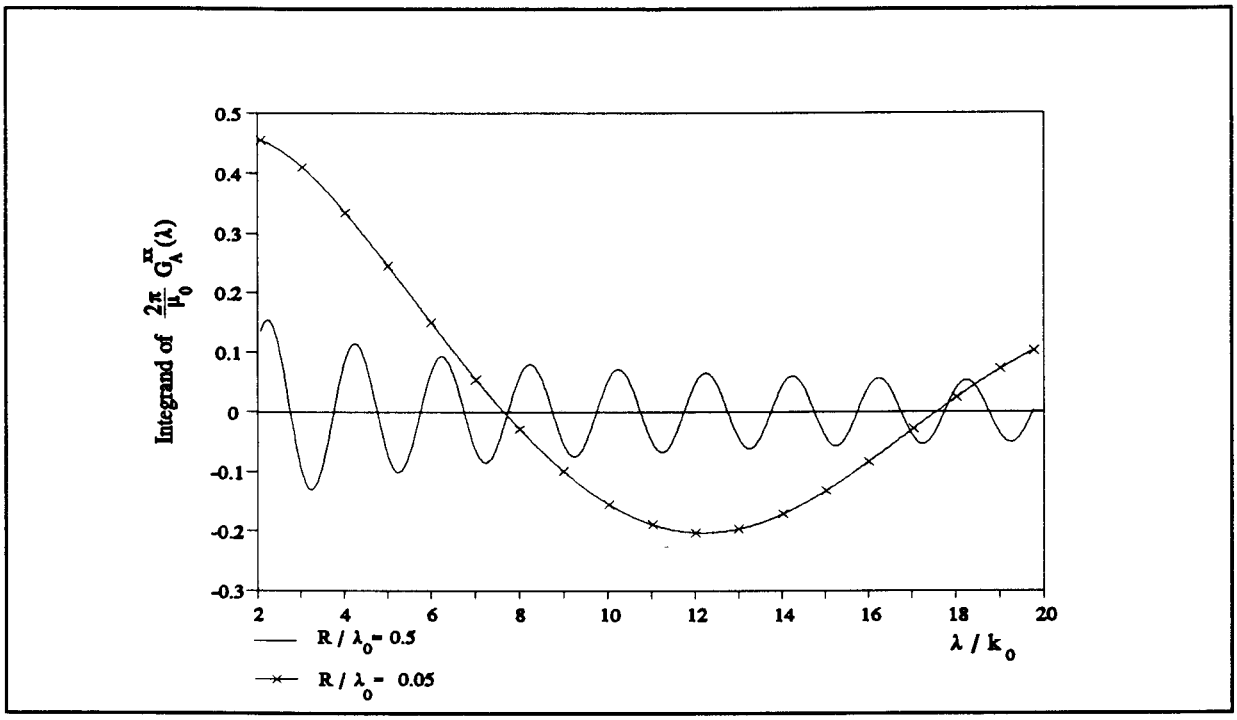

Figure 3.11 *Normalised integrand of $G_A^{xx}(r/r')$ for source-observer distances of $R/\lambda_0=0.5$ and $R/\lambda_0=0.05$. ($h/\lambda_0=0.07$ at f = 1.206 GHz)*

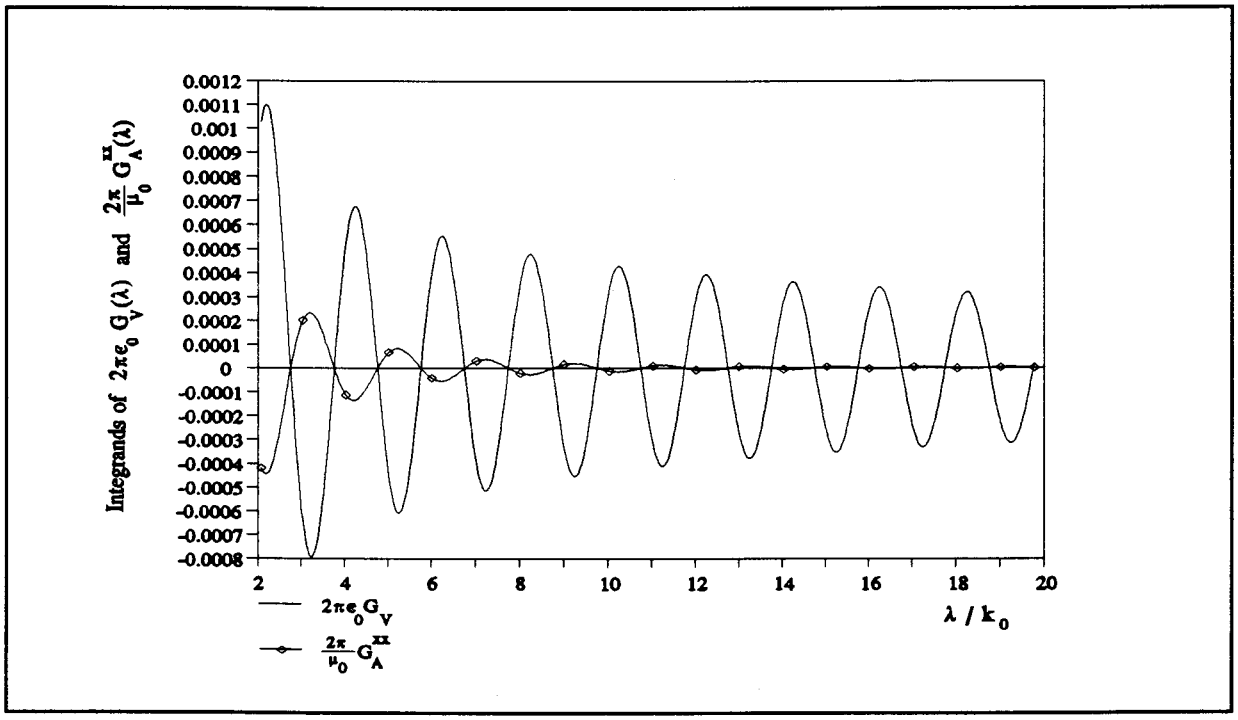

Figure 3.12 *Imaginary parts of both normalised Green's function integrands for $k_0\sqrt{\epsilon_r'} \leq \lambda \leq 20k_0$ and $R/\lambda_0=0.5$.*

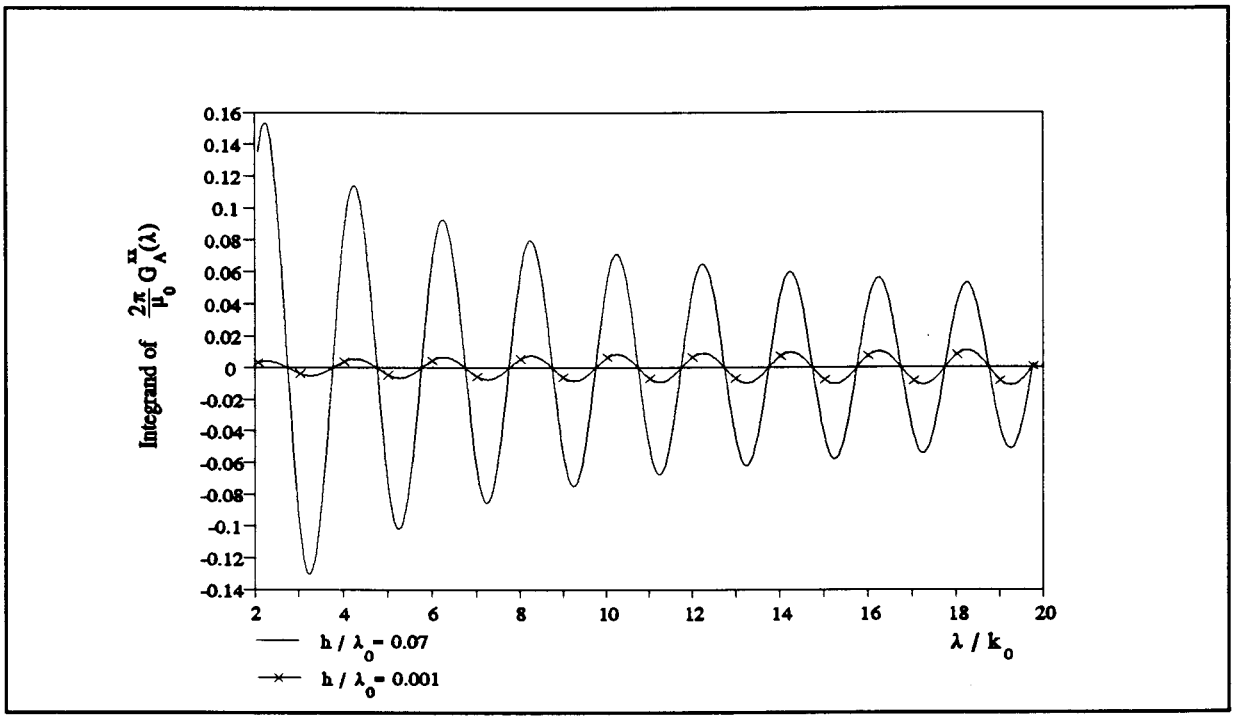

Figure 3.13 *Normalised integrand of $G_A^{xx}(r/r')$ for $h/\lambda_0=0.07$ and $h/\lambda_0=0.001$ with $R/\lambda_0=0.5$.*

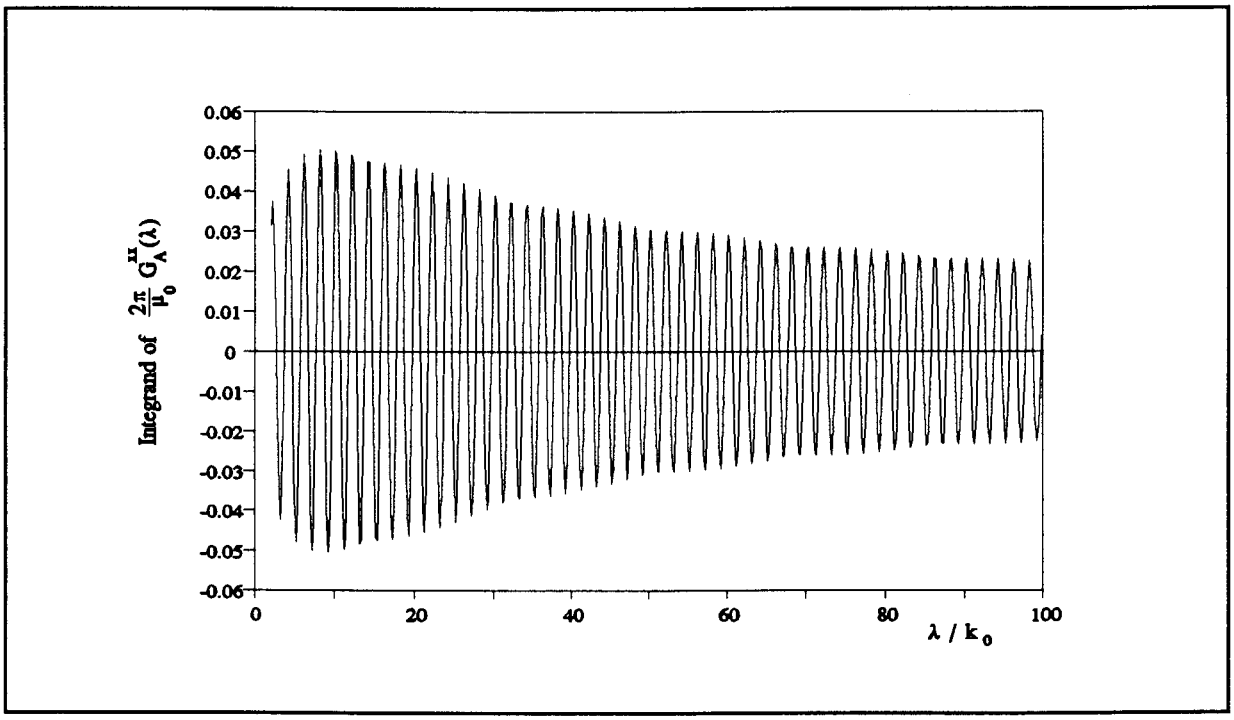

Figure 3.14 *Normalised integrand of $G_A^{xx}(r/r')$ over an extended interval for $h/\lambda_0=0.01$ and $R/\lambda_0=0.5$.*

3.3 DISCRETE GREEN'S FUNCTIONS

At this point we assume that the Green's functions (3.1) and (3.2) are available, evaluated using the methods of Section 3.2. Now as observed by Mosig and Gardiol [3], the notation and computational task can be simplified by introducing the idea of *discrete Green's functions*, which have as sources complete basis functions instead of elemental sources. For the basis functions selected in Chapter 2, we let Γ_A denote the vector potential created by a rooftop distribution of current, while the scalar potential resulting from a rectangular distribution of charge is represented by Γ_V. Numerical aspects concerning these discrete Green's functions will be the subject of this section. As mentioned in Section 3.1, all numerical experiments performed for illustrative purposes were done for ϵ_r=(4.34,-0.0868) at f=1.206 GHz. In addition, in the present section, the standard values h=0.8 mm and a=b=6.666 mm are utilised in illustrations.

3.3.1 Scalar potential discrete Green's function

The scalar potential discrete Green's function $\Gamma_V(\mathbf{r}/\mathbf{r}_{oj})$ is the scalar potential due to the j'th source cell and is defined by the dimensionless expression [3]

$$\Gamma_V(r/r_{oj}) = \int_{S_{oj}} \frac{\epsilon_0}{k_0} G_V(r/r') \Pi(r'-r_{oj}) k_0^2 \, dS' \qquad (3.23)$$

where S_{oj} is the surface occupied by the charge cell centred at $\mathbf{r}_{oj}$, and $\Pi(\mathbf{r}'-\mathbf{r}_{oj})$ a two-dimensional unit pulse function defined over S_{oj}. Expression (3.23) gives the scalar potential at $\mathbf{r}$ created by a rectangular distribution of charge centred at $\mathbf{r}_{oj}$

on the air-dielectric interface of a microstrip structure.

We consider first the scalar potential discrete Green's function selfterms. When the observation point **r** is located within its own source charge cell (in which case we are dealing with the "selfterms" as defined in Section 2.3.4), the Green's function G_V (and hence the Γ_V integrand) becomes singular at **r**, as follows from the discussion in Section 3.2.3. In order to illustrate this graphically, consider the integrand for $\Gamma_V(\mathbf{r}/\mathbf{r}_{oj})$ in (3.23); with $\mathbf{r}_{oj}=\mathbf{0}$ and $\mathbf{r}=\mathbf{0}$, this integrand becomes $\epsilon_0/k_0\ G_V(\mathbf{0}/\mathbf{r}')\ \Pi(\mathbf{r}'-\mathbf{0})\ k_0^2$ which is a function of $\mathbf{r}'=(x',y',0)$. The real and imaginary parts of this integrand are plotted in Figures 3.15 and 3.16, respectively, which shows clearly the singularity at observation point $\mathbf{r}=\mathbf{0}$. A pole extraction technique whereby the singular part of the Green's function is extracted before surface integration has been suggested by Mosig and Gardiol [3]. This singular part, corresponding to the dominant term of the static scalar Green's function, is given by [2]

$$G_{Vs} = \frac{1}{2\pi(\epsilon_r+1)\epsilon_0 \mid r-r' \mid} \tag{3.24}$$

Since the Green's function G_V becomes singular in both its real and imaginary parts[6], the static function behaves similarly in that ϵ_r is complex. Now by writing the Green's function under the surface integral in (3.23) as $G_V=(G_V-G_{Vs})\ +\ G_{Vs}$, the singularity may be extracted yielding a difference term

[6] This does not come as a surprise when considering the oscillations shown by the imaginary part (Figure 3.12) and keeping in mind the mechanism whereby these Green's functions become singular at the source point.

which is well-behaved and numerically integrable. Although the difference term is well-behaved, the terms G_V and G_{Vs} both become singular at the source point. The numerical evaluation of these terms before subtraction is done as discussed in Section 3.2.2. Figure 3.17 shows the real parts of the actual and static Green's functions as the observer approaches the source, while Figure 3.18 features the imaginary parts. The difference term integrand is shown in Figures 3.19 and 3.20 from which it is clear that the singularity in the selfterm[7] integrand has been extracted. The singular part (G_{Vs}) can be analytically integrated over the cell surface as done in [3] to give

$$\Gamma_{Vs}(r_{oj}/r_{oj}) = \frac{1}{2\pi(\epsilon_r+1)}\left[2k_0 a \ln\tan\left(\frac{\alpha}{2}+\frac{\pi}{4}\right) - 2k_0 b \ln\tan\left(\frac{\alpha}{2}\right)\right] \quad (3.25)$$

where $\alpha = \tan^{-1}(b/a)$, with a and b the charge cell dimensions. Note that, as mentioned in Section 2.3.5, the moment method matrix elements given in expression (2.22) require scalar potential discrete Green's function values only at the cell centre (this is not true in general for the vector potential discrete Green's function values) - this fact has already been incorporated in (3.25). An expression for the scalar potential discrete Green's function selfterm is thus given by

$$\Gamma_V(r_{oj}/r_{oj}) = \epsilon_0 k_0 \int_{S_{0j}} \left[G_V(r_{oj}/r') - G_{Vs}(r_{oj}/r')\right] dS' + \Gamma_{Vs}(r_{oj}/r_{oj}) \quad (3.26)$$

[7] Recall that by "selfterm" we mean those for which the observation point for a potential due to a specific source cell lies within the source cell itself.

Having dealt with the selfterms of the discrete Green's function associated with the scalar potential, we next consider the off-diagonal ones. The moment method matrix (C) is diagonally dominant [2]; therefore less stringent accuracy requirements apply to the off-diagonal elements and approximations for the scalar potential discrete Green's functions may then be considered [3]. In this regard we have

$$\Gamma_V(r/r_{oj}) \simeq \frac{\epsilon_0}{k_0} G_V(r/r_{oj})\,(k_0 a)\,(k_0 b) \tag{3.27}$$

The validity of this approximation is illustrated in Figures 3.21 and 3.22 for the case f = 1.206 GHz, a = b = 6.666 mm, h = 0.8 mm and $\epsilon_r = (4.34, -0.0868)$. For these figures a source cell was centred at the origin on the air-dielectric interface while an observer was moved along the y-axis - *it is important to keep in mind that the discrete Green's functions are not only dependent on the source-observer distances, but also on their relative orientations.* It can be seen that the closed-form expression (3.27) offers a good approximation for the discrete Green's function when the observer is located several cells away along the y-axis. Similar conclusions can be drawn from graphs featuring $\Gamma_V(\hat{\rho}R/\mathbf{0})$ versus R, the observer being moved away from the source cell at the origin in any direction $\hat{\rho}$ along the air-dielectric interface, where $\hat{\rho}R = x\hat{x} + y\hat{y}$ and $R = (x^2+y^2)^{1/2}$.

As a further illustration, Figures 3.23 through 3.26 show the integrands for the scalar potential discrete Green's functions for source cells (over which the integrand is to be integrated) centred at $\mathbf{r}_{xj} = (0,0)$ and observation points at $\mathbf{r}_{xi} = (2a,0)$ and $\mathbf{r}_{xi} = (8a,0)$, respectively.

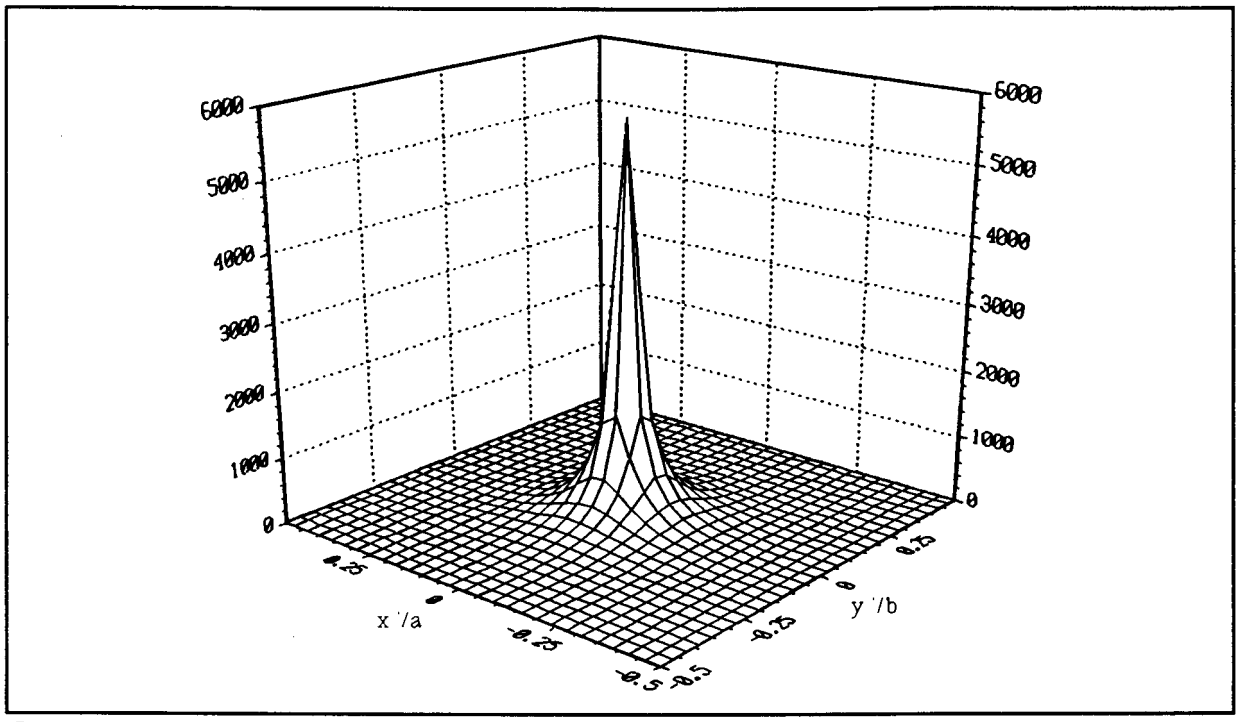

Figure 3.15 *Real part of the integrand, before pole extraction, in the expression for the Γ_V selfterms, as a function of r' over the region over which it is to be integrated. (Maximum value is infinite).*

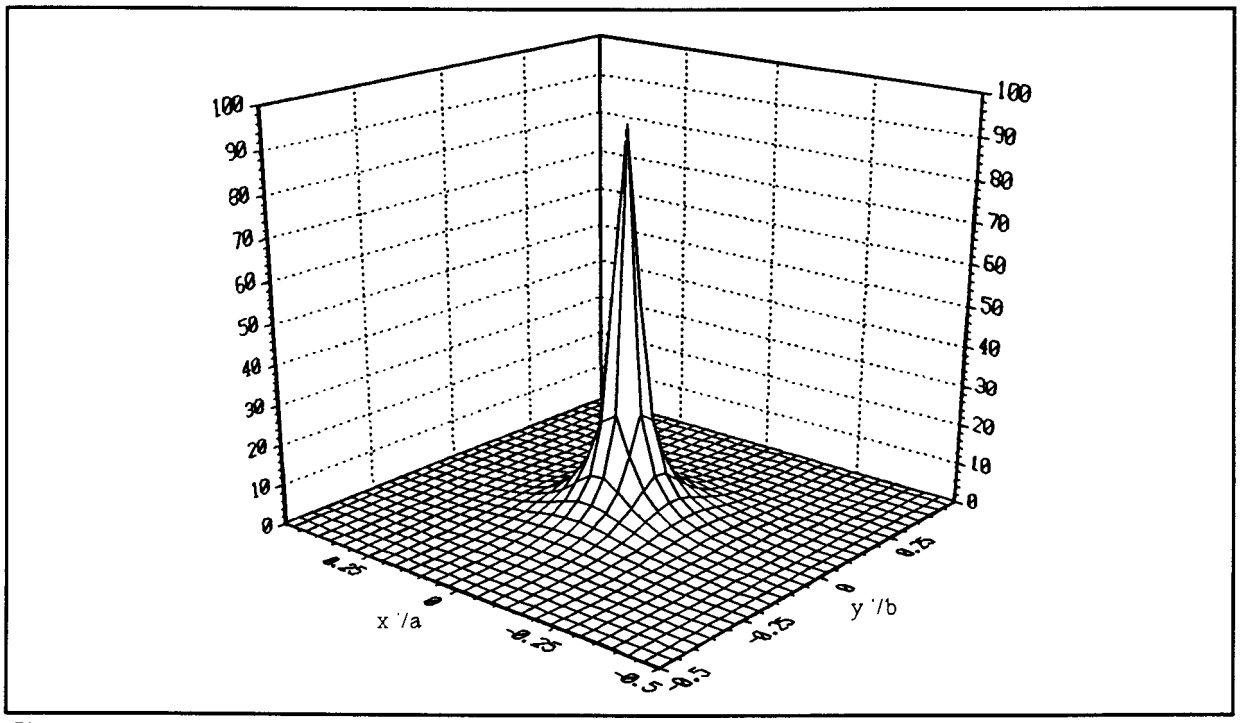

Figure 3.16 *Imaginary part of the Γ_V integrand corresponding to Figure 3.15. Note that the maximum value is infinite.*

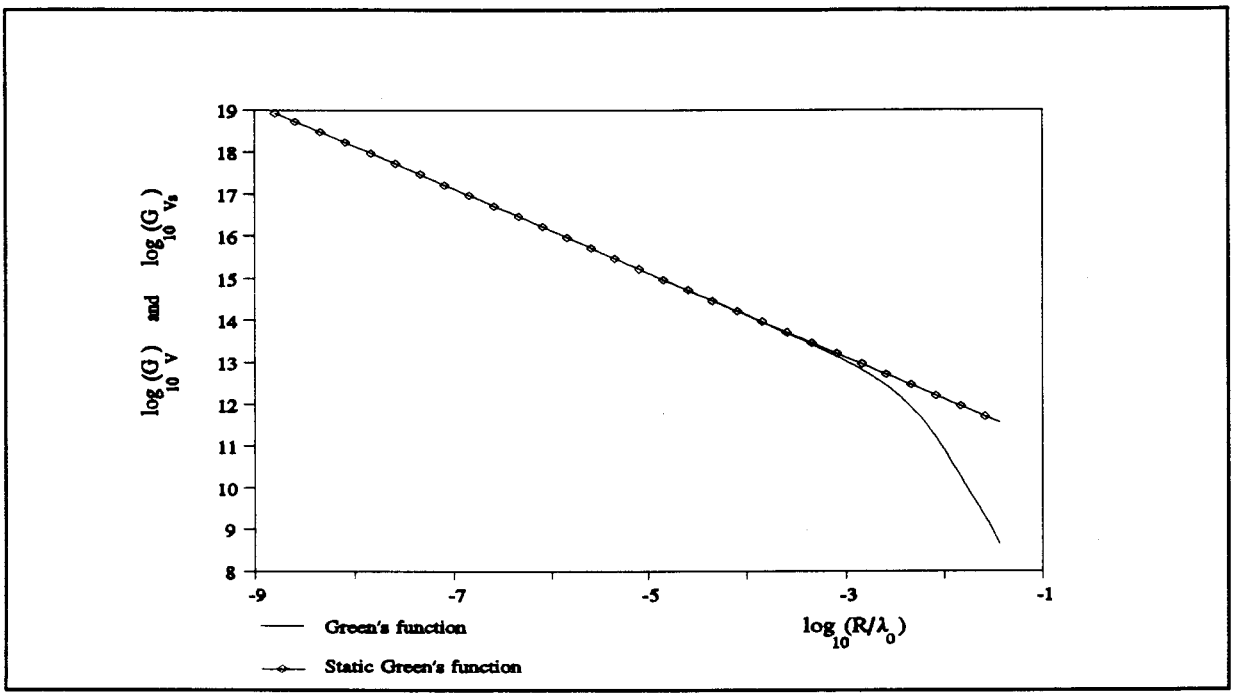

Figure 3.17 *Real parts of the Green's (G_V) and static Green's functions (G_{Vs}) as the observer approaches the source.*

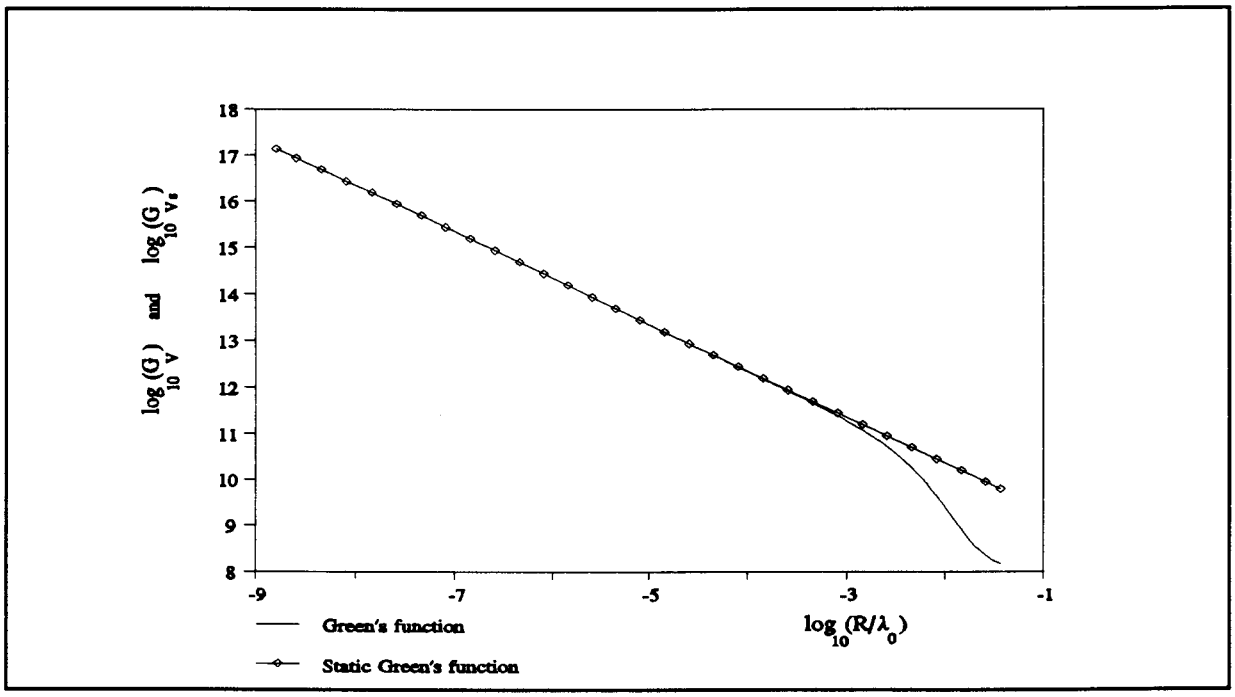

Figure 3.18 *Imaginary parts of the Green's and static Green's functions as the observer approaches the source.*

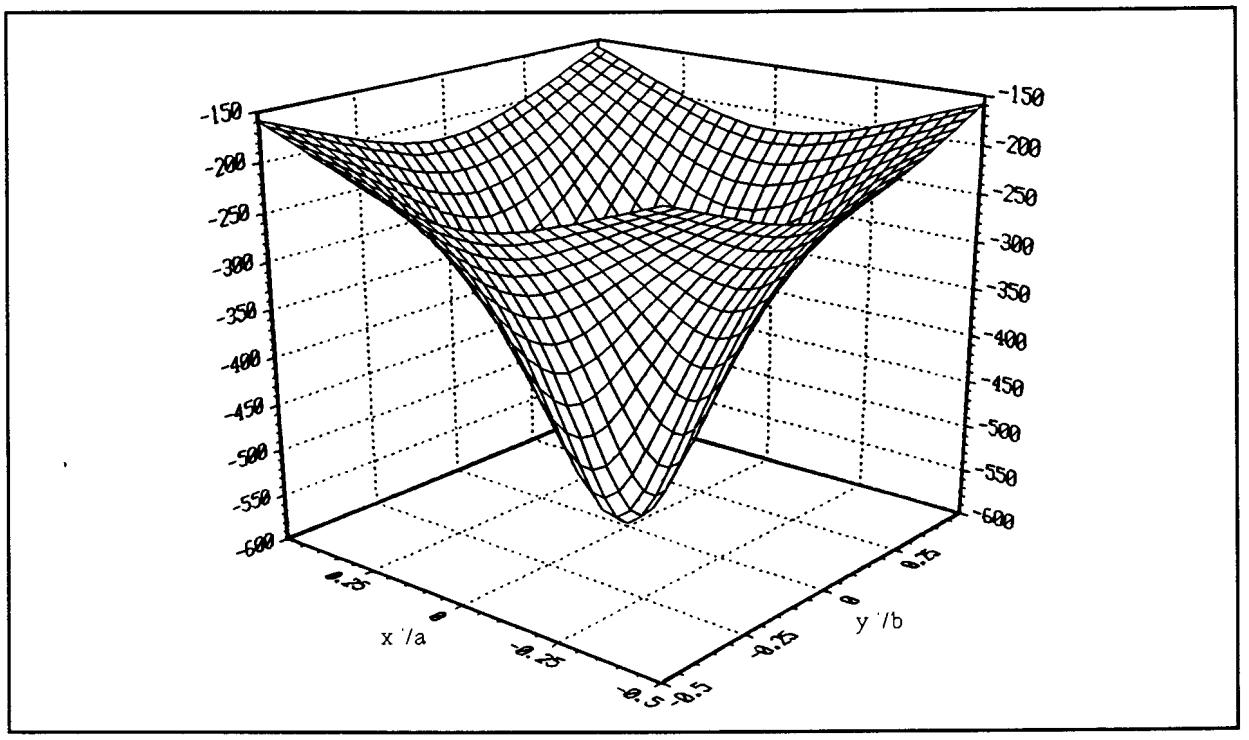

Figure 3.19 *Real part of the difference term integrand in the evaluation of the Γ_V selfterm.*

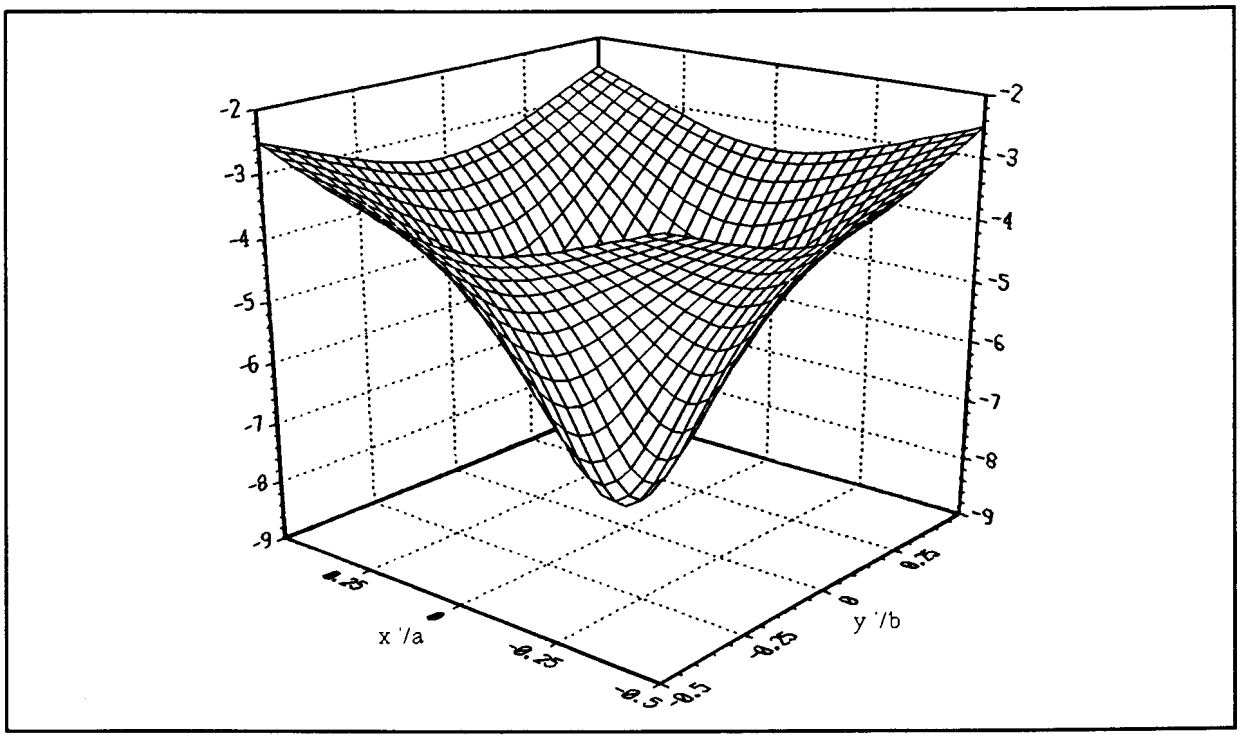

Figure 3.20 *Imaginary part of the difference term integrand corresponding to the real part shown in Figure 3.19.*

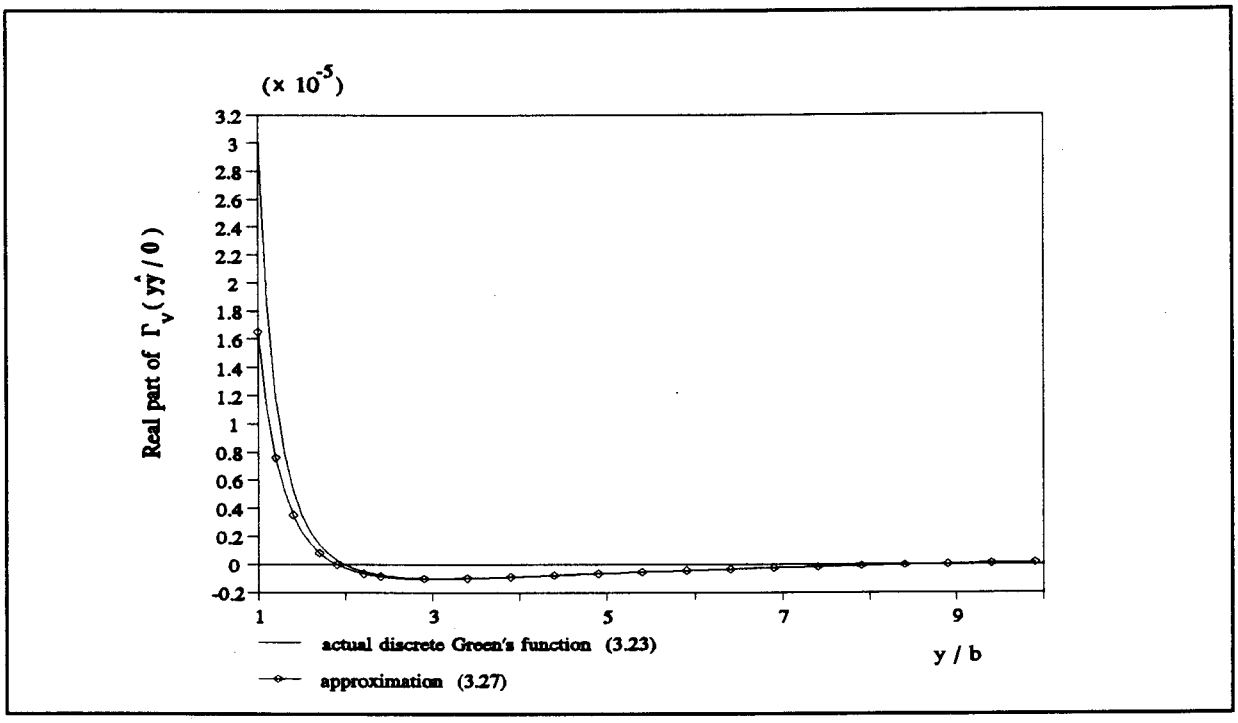

Figure 3.21 *Real parts of the actual and approximated scalar potential discrete Green's functions, for h=0.8 mm and a=b=6.666 mm. (discrete Green's functions are dimensionless quantities)*

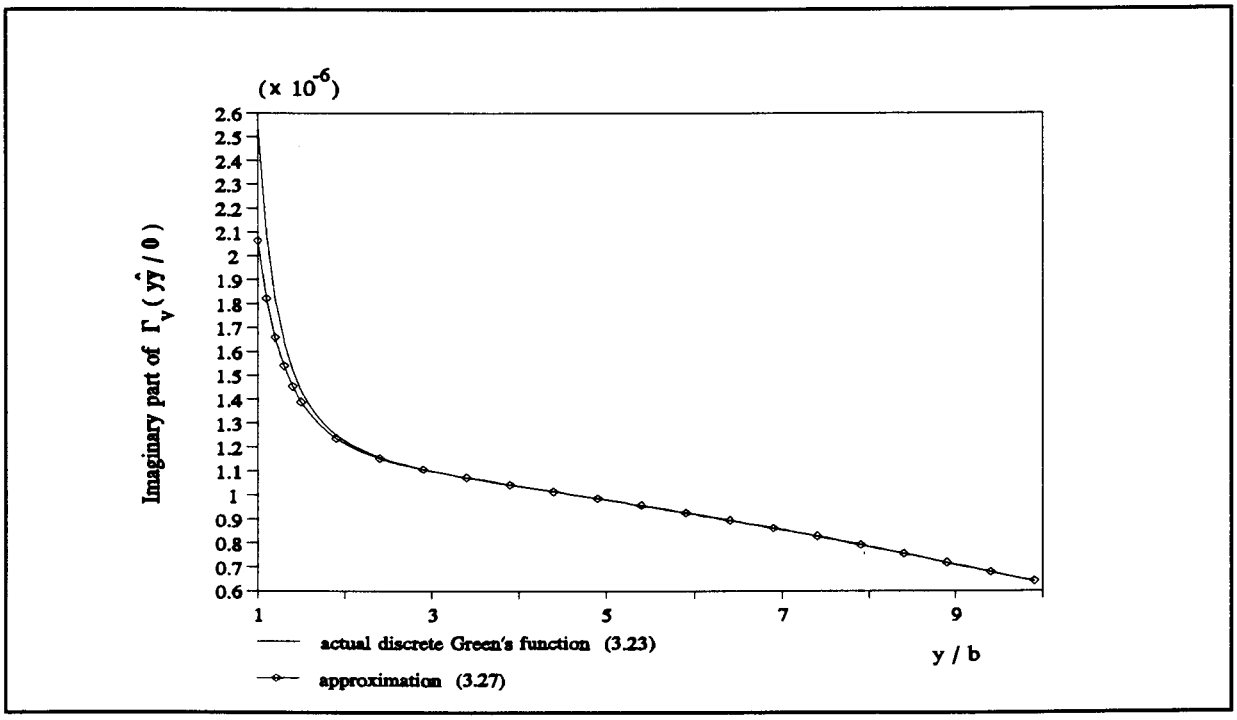

Figure 3.22 *Imaginary part corresponding to the real part shown in Figure 3.21.*

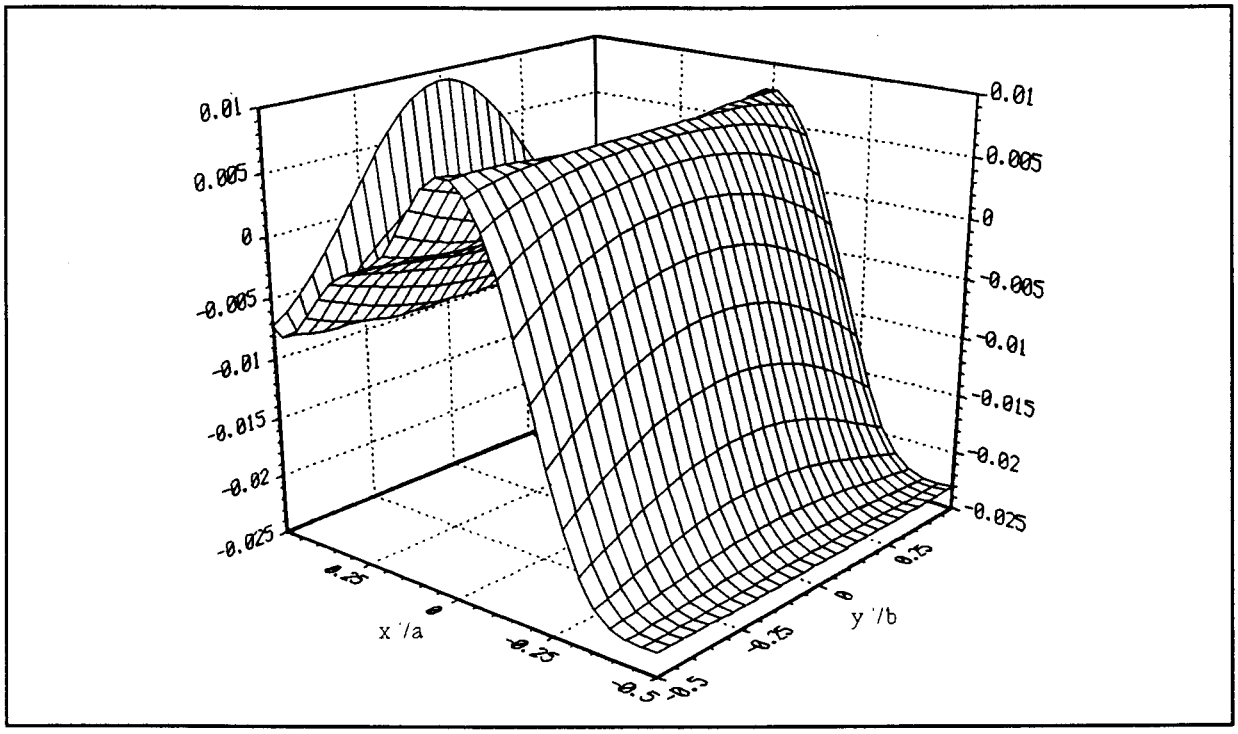

Figure 3.23 *Real part of the integrand of $\Gamma_V(r_{xi}/r_{xj})$ as a function of r' over the region over which it is to be integrated, with $r_{xi}=(2a,0)$ and $r_{xj}=(0,0)$.*

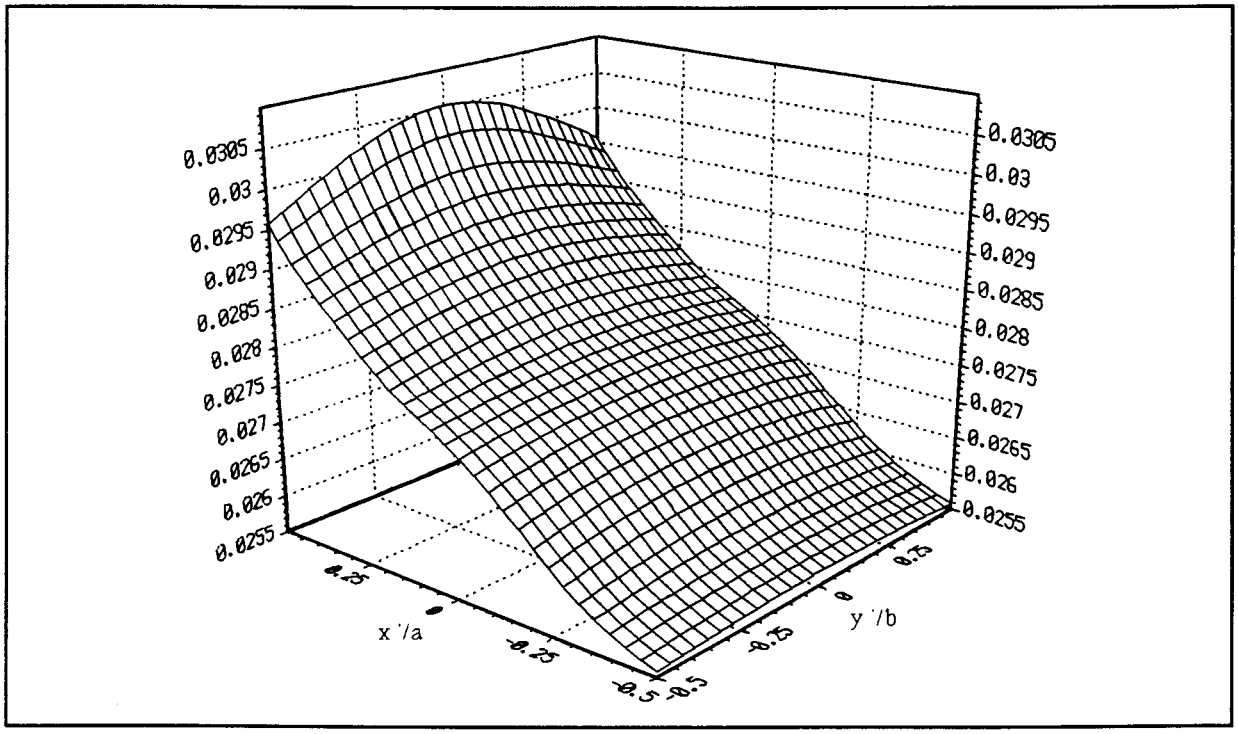

Figure 3.24 *Imaginary part of the Γ_V integrand corresponding to Figure 3.23.*

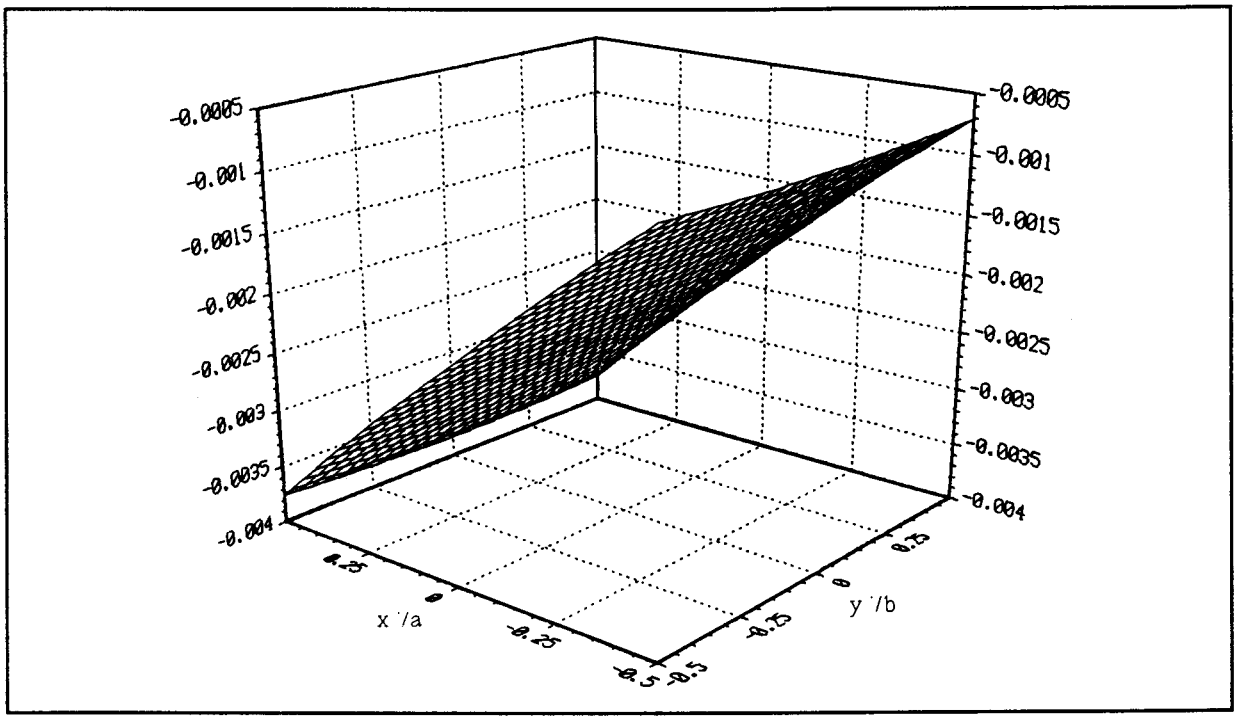

Figure 3.25 *Real part of the integrand of $\Gamma_V(r_{xi}/r_{xj})$ as a function of r' over the region over which it is to be integrated with $r_{xi}=(8a,0)$ and $r_{xj}=(0,0)$.*

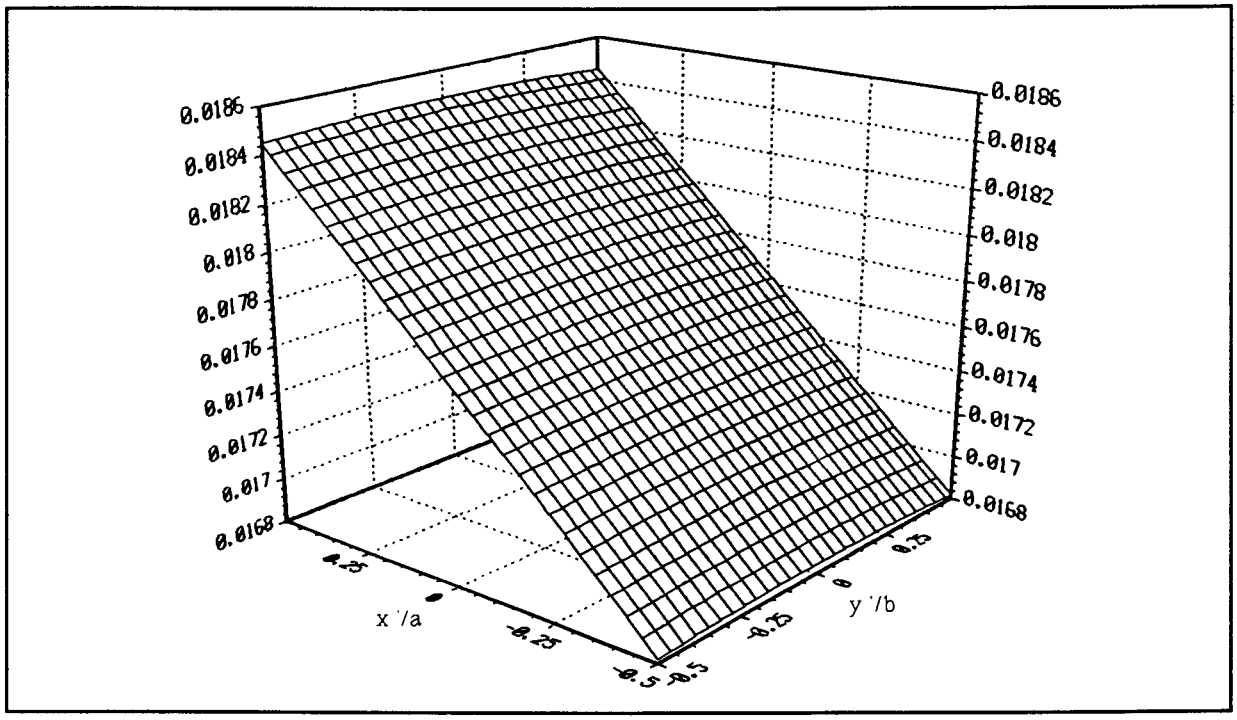

Figure 3.26 *Imaginary part of the Γ_V integrand corresponding to Figure 3.25.*

3.3.2 Vector potential discrete Green's functions

The vector potential discrete Green's functions will be discussed in this section. Although we will only consider Γ_A^{xx}, numerical techniques discussed here are directly applicable to Γ_A^{yy}. The vector potential discrete Green's function $\Gamma_A^{xx}(\mathbf{r}/\mathbf{r}_{xj})$ is the vector potential at $\mathbf{r}$ due to the j'th source current cell and is defined by the dimensionless expression [3]

$$\Gamma_A^{xx}(r/r_{xj}) = \int_{S_{xj}} \frac{1}{\mu_0 k_0} G_A^{xx}(r/r')\, T_x(r' - r_{xj})\, k_0^2\, dS' \qquad (3.28)$$

S_{xj} is the surface occupied by the current cell centred at $\mathbf{r}_{xj}$ while an x-directed rooftop basis function is denoted by $T_x(\mathbf{r})$ (Figure 2.3). We will first consider the vector potential discrete Green's function selfterms. The discrete Green's function integrand, or more specifically its factor G_A^{xx}, becomes singular when the observer and a source current cell coincide. Furthermore, in the computation of the moment method matrix elements, Γ_A^{xx} appears under an integral over a test segment C_{xi} (as seen in (2.22)). The singularity within current cell S_{xj} may thus appear at any point along C_{xi}. Figure 3.27 gives an illustration of the real part of the vector potential discrete Green's function integrand for an observer located at the centre of a source cell which is placed at the origin. The imaginary part of this integrand is shown in Figure 3.28 from which we observe that the imaginary part does not exhibit the same singular behaviour as that of the real part. This may be attributed to the fact that the imaginary part of G_A^{xx} stays very much bounded for $R \to 0$, or that is how it seems from Figure 3.29. This is not totally

surprising when considering the oscillations shown by the imaginary part of this integrand (Figure 3.12). For this reason the static Green's function term, used in the pole extraction technique (Section 3.3.1) is purely real and given by [2]

$$G_{As}^{xx} = \frac{\mu_0}{4\pi \left| r - r' \right|} \tag{3.29}$$

Figure 3.30 shows the real parts of the Green's function (G_A^{xx}) and it's static part (G_{As}^{xx}) as an observer approaches the source cell. From this figure it is apparent that a difference term would not become singular at the source point, and that the singularity can therefore be extracted by making use of (3.29) and expanding the Green's function under the integral in (3.28) as described in the previous section. Integration over the source cell is now performed in two parts: a difference term which is well-suited to numerical integration (Figure 3.31 shows the real part of this integrand) and the analytical integration of G_{As}^{xx} (singular part). Since this analytical integration could not be found in the literature, Appendix C derives an expression for (3.28) over an x-directed current cell centred at (0,0), with G_{As}^{xx} replacing G_A^{xx} in the integrand. The observer, and hence the singularity is situated at any point $\mathbf{r} = (r_x,0)$ along test segment C_{xi}. From this we have expression (3.30) where $\alpha_1 = \tan^{-1}[b/(2(a-r_x))]$, $\alpha_2 = \tan^{-1}[b/(2(a+r_x))]$ and $\alpha_3 = \tan^{-1}[b/(2r_x)]$. This expression was derived for an x-directed current cell centred at (0,0) with $r_x \geq 0$. The case of a y-directed current cell follows directly by interchanging a and b; in fact, when a = b the expressions for Γ_{As}^{xx} and Γ_{As}^{yy} are identical. Since the numerical values of Γ_{As}^{xx} and Γ_{As}^{yy} are independent of the current cell centre-

coordinates, (0,0) was chosen to simplify the closed-form expressions. For the case $r_x<0$, the vector potential discrete Green's function integrand with G_{As}^{xx} instead of G_A^{xx}, is simply a rotated version of the integrand for $r_x>0$ so that after integration $\Gamma_{As}^{xx}(-r_x/0) = \Gamma_{As}^{xx}(r_x/0)$. Expression (3.26) shows how the pole extraction technique was used to evaluate the Γ_V selfterms. Similarly now, it is possible to compute Γ_A^{xx} and Γ_A^{yy} for observers situated on source current cells. Having dealt with the vector potential discrete Green's functions selfterms, we next consider the terms appearing in the off-diagonal elements of the moment method matrix.

$$\Gamma_{As}^{xx}(r_x/0) = \frac{k_0}{2\pi}\left[(a-r_x)\ln\tan\left(\frac{\alpha_1}{2}+\frac{\pi}{4}\right)+\frac{b}{2}\ln\left[\frac{\tan\left(\frac{\pi}{2}-\frac{\alpha_2}{2}\right)}{\tan\left(\frac{\alpha_1}{2}\right)}\right]+(a+r_x)\ln\tan\left(\frac{\alpha_2}{2}+\frac{\pi}{4}\right)\right]$$

$$-\frac{k_0 a}{4\pi}\ln\tan\left(\frac{\alpha_2}{2}+\frac{\pi}{4}\right) + \frac{k_0 b^2}{16\pi a}\left[\operatorname{cosec}(\alpha_3)-\operatorname{cosec}(\alpha_2)\right]$$

$$-\frac{k_0 r_x^2}{4\pi a}\ln\tan\left(\frac{\alpha_2}{2}+\frac{\pi}{4}\right) + \frac{k_0 r_x b}{4\pi a}\ln\left[\frac{\tan\left(\frac{\alpha_3}{2}\right)}{\tan\left(\frac{\alpha_2}{2}\right)}\right]$$

$$-\frac{k_0}{4\pi a}(a-r_x)^2\ln\tan\left(\frac{\alpha_1}{2}+\frac{\pi}{4}\right) + \frac{k_0 b^2}{16\pi a}\left[\operatorname{cosec}(\alpha_3)-\operatorname{cosec}(\alpha_1)\right]$$

$$-\frac{k_0 r_x}{2\pi a}(a-r_x)\ln\tan\left(\frac{\alpha_1}{2}+\frac{\pi}{4}\right) - \frac{k_0 r_x b}{4\pi a}\ln\left[\frac{\operatorname{cotan}\left(\frac{\alpha_3}{2}\right)}{\tan\left(\frac{\alpha_1}{2}\right)}\right] \qquad \textbf{(3.30)}$$

As in the scalar potential case, an approximation for Γ_A^{xx} may be considered for large source-observer distances; in this regard

$$\Gamma_A^{xx}(r/r_{xj}) \approx \frac{1}{\mu_0 k_0} G_A^{xx}(r/r_{xj})\,(k_0 a)\,(k_0 b) \qquad (3.31)$$

The validity of this approximation is illustrated in Figures 3.32 and 3.33 from which it can be seen that the analytical expression (3.31) offers a good approximation for Γ_A^{xx} when the observer is located several cells from the source. As in the scalar potential case, these figures were generated by placing a source cell at the origin on the air-dielectric interface, and moving an observer along the y-axis. Similar conclusions can be drawn from graphs featuring $\Gamma_A^{xx}(\hat{\rho}R/0)$ versus R ($\hat{\rho}R = x\hat{x} + y\hat{y}$ and $R = (x^2+y^2)^{1/2}$), in other words, the observer being moved away from the source in any direction along the air-dielectric interface.

As a further illustration, Figures 3.34 through 3.37 show vector potential discrete Green's function integrands for source cells at $\mathbf{r}_{xj}=(0,0)$ and observation points at $\mathbf{r}=(2a,0)$ and $\mathbf{r}=(8a,0)$, respectively.

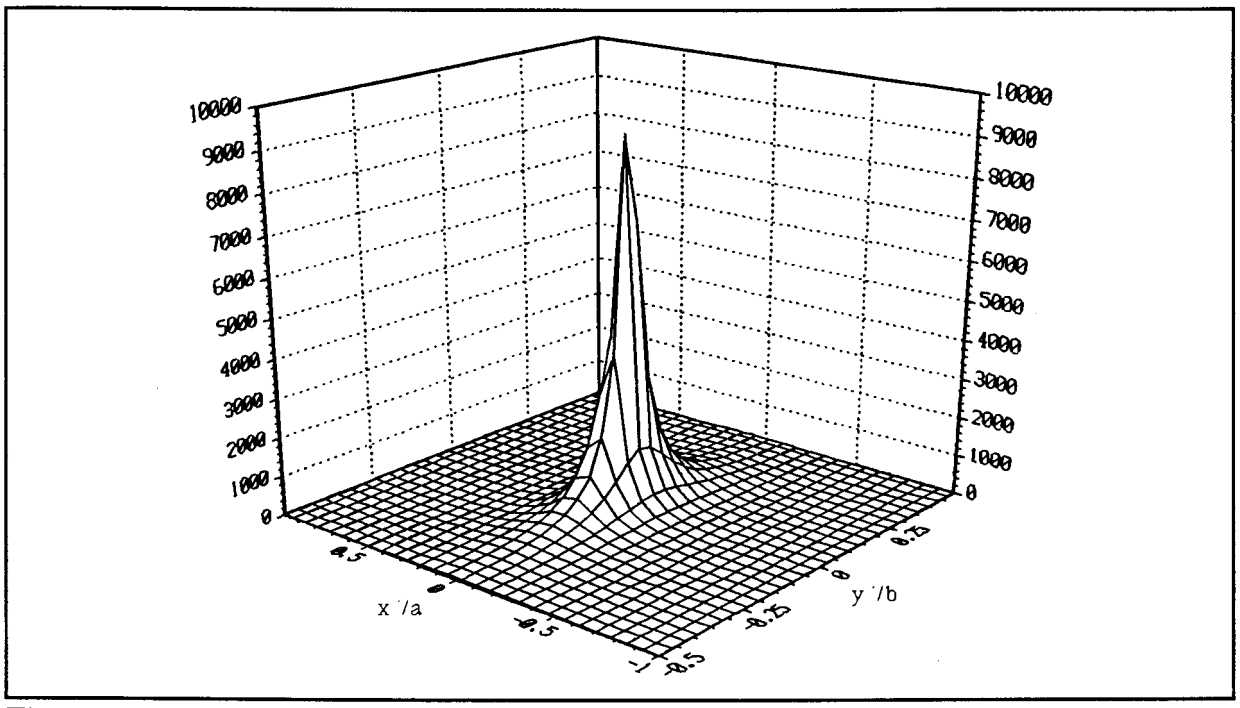

Figure 3.27 *Real integrand of $\Gamma_A^{*x}(0/0)$, before pole extraction, as a function of r′ over the cell over which it is to be integrated.*

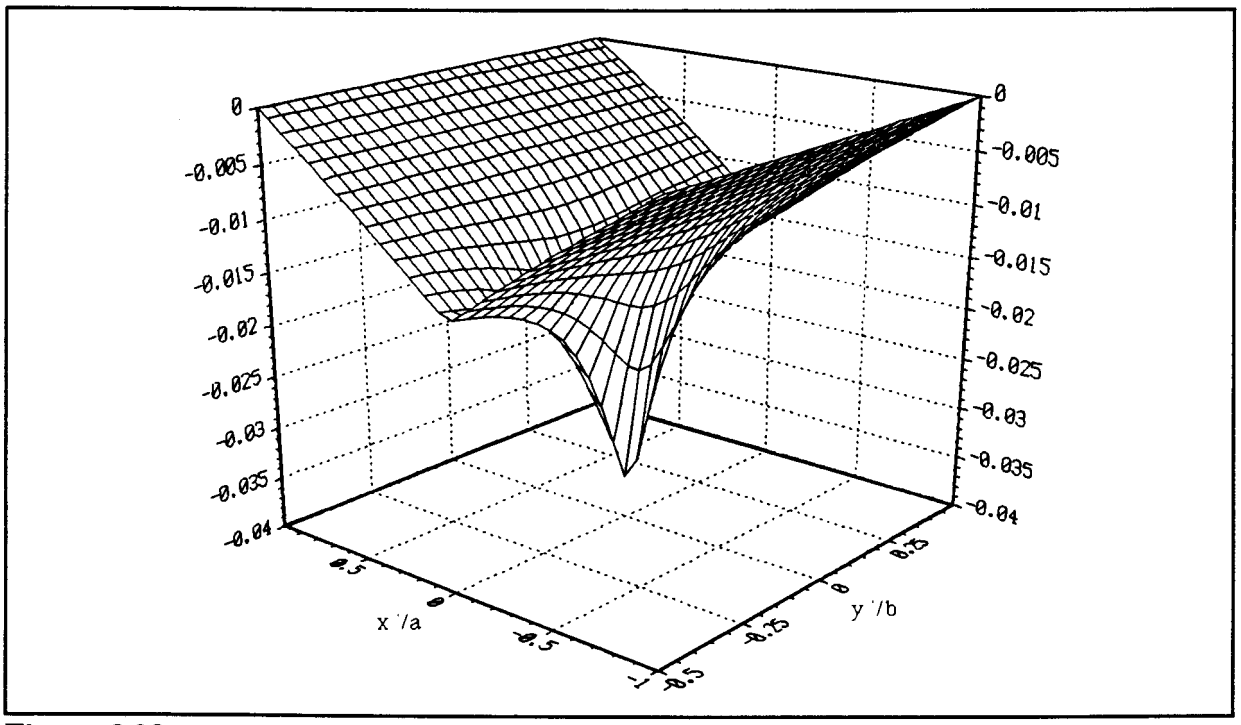

Figure 3.28 *Imaginary part of the integrand corresponding to the real part shown in Figure 3.27.*

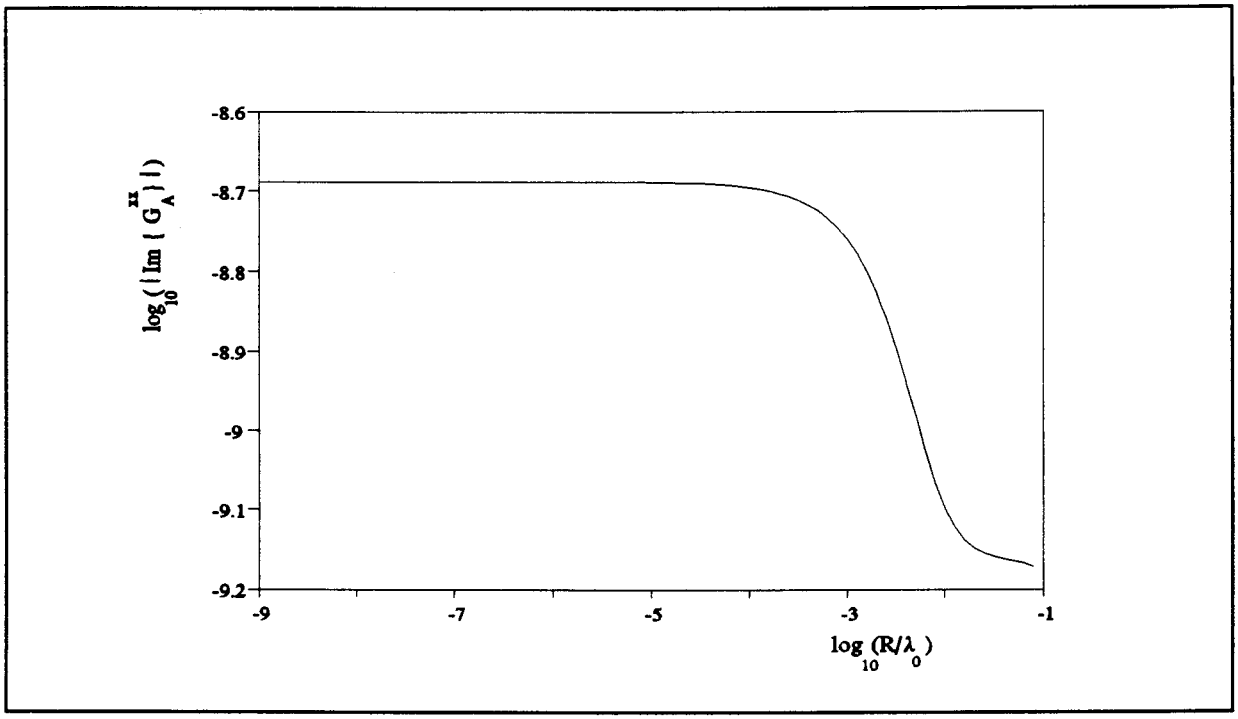

Figure 3.29 *Imaginary part of G_A^{xx} as an observer approaches the source; the real part is shown in Figure 3.30.*

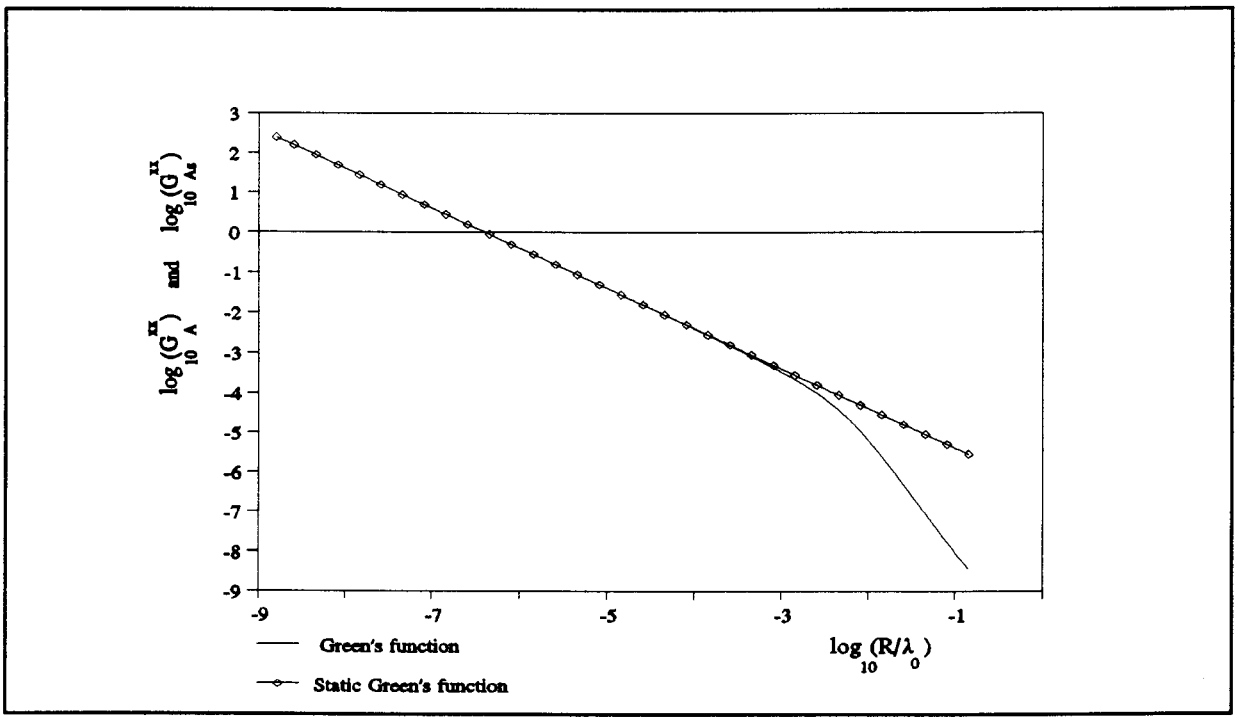

Figure 3.30 *Real parts of the Green's (G_A^{xx}) and static Green's functions (G_{As}^{xx}) associated with the vector potential.*

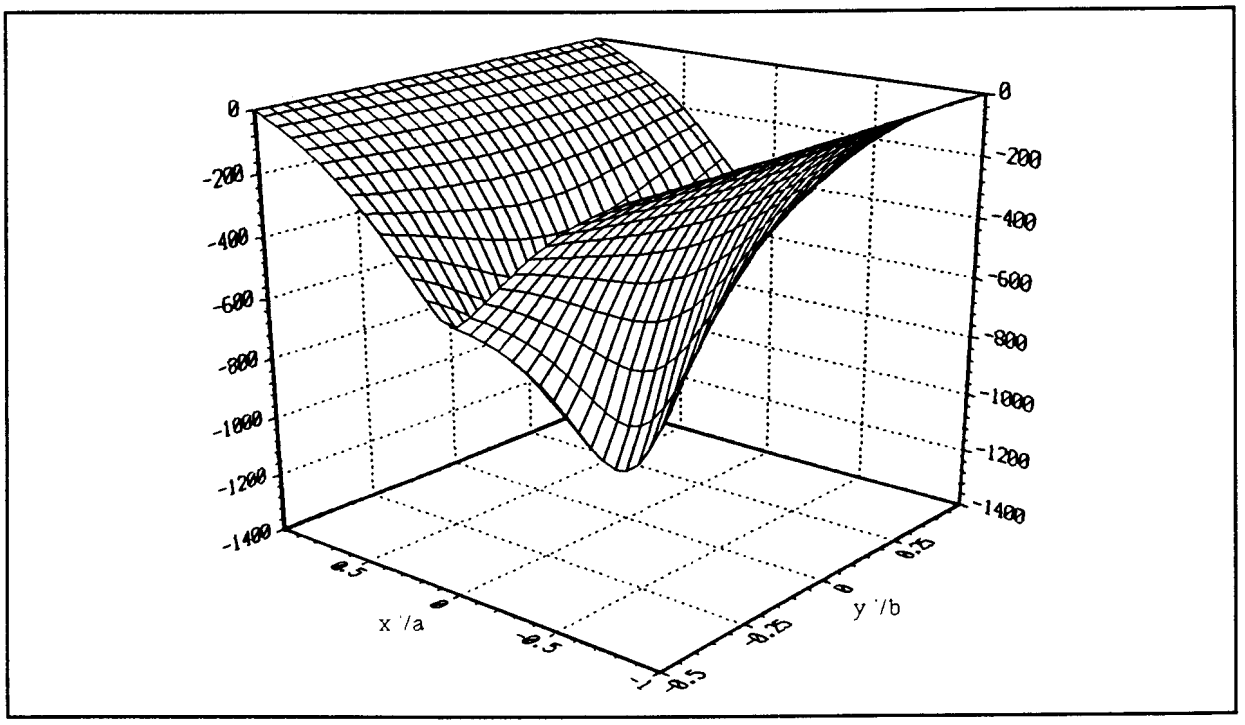

Figure 3.31 *Real part of the difference term integrand for the pole shown in Figure 3.27.*

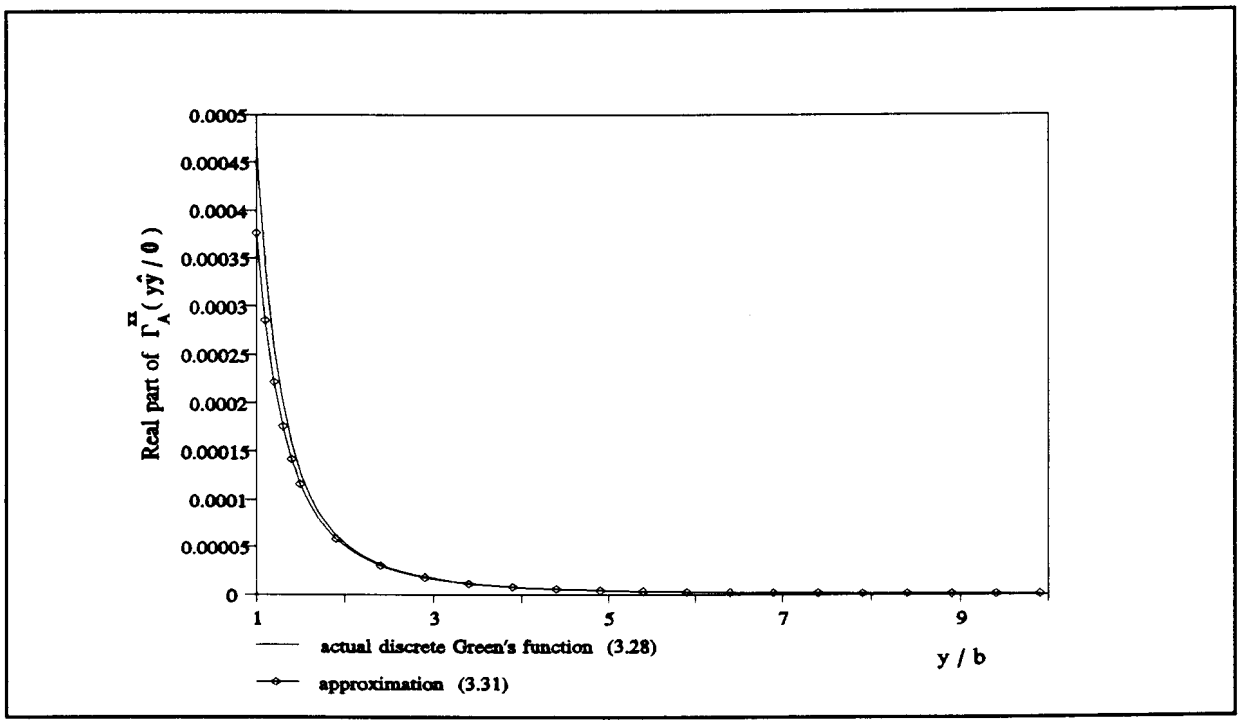

Figure 3.32 *Real parts of the actual and approximated vector potential discrete Green's functions for* $\varepsilon_r = (4.34, -0.0868)$, $h = 0.8$ *mm and* $a = b = 6.666$*mm at* $f = 1.206$ *GHz.*

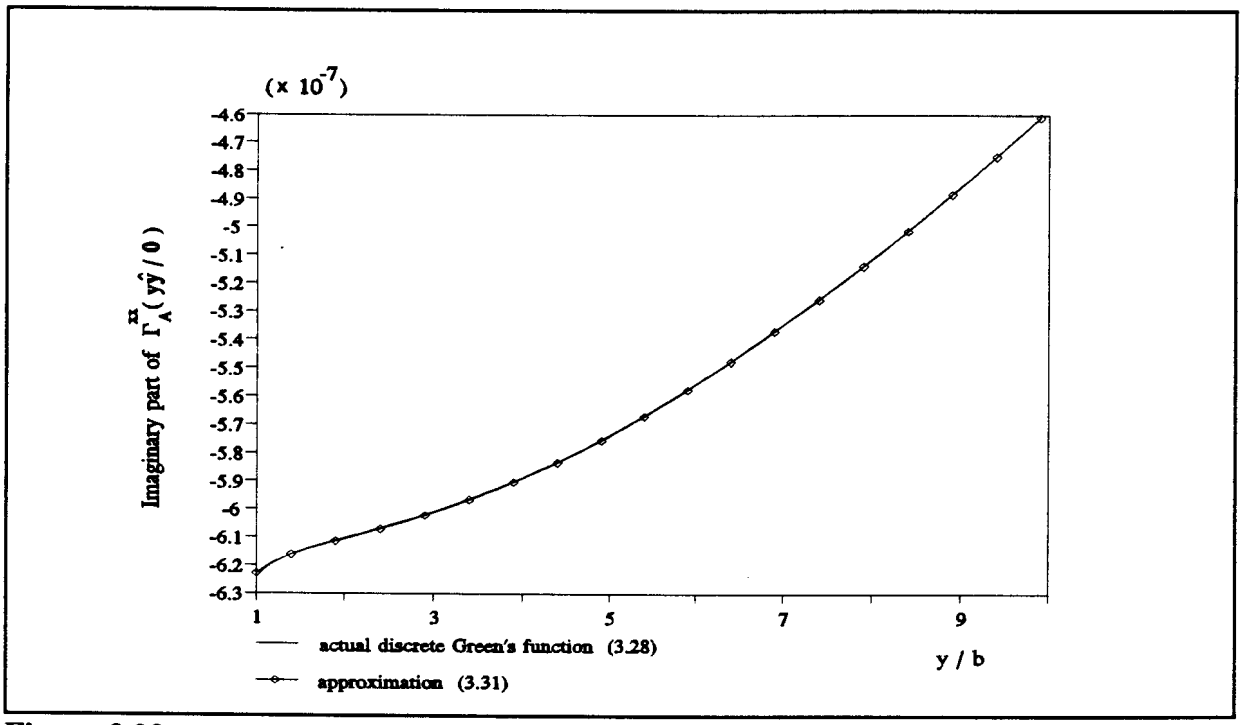

Figure 3.33 *Imaginary part accompanying the real part shown in Figure 3.32.*

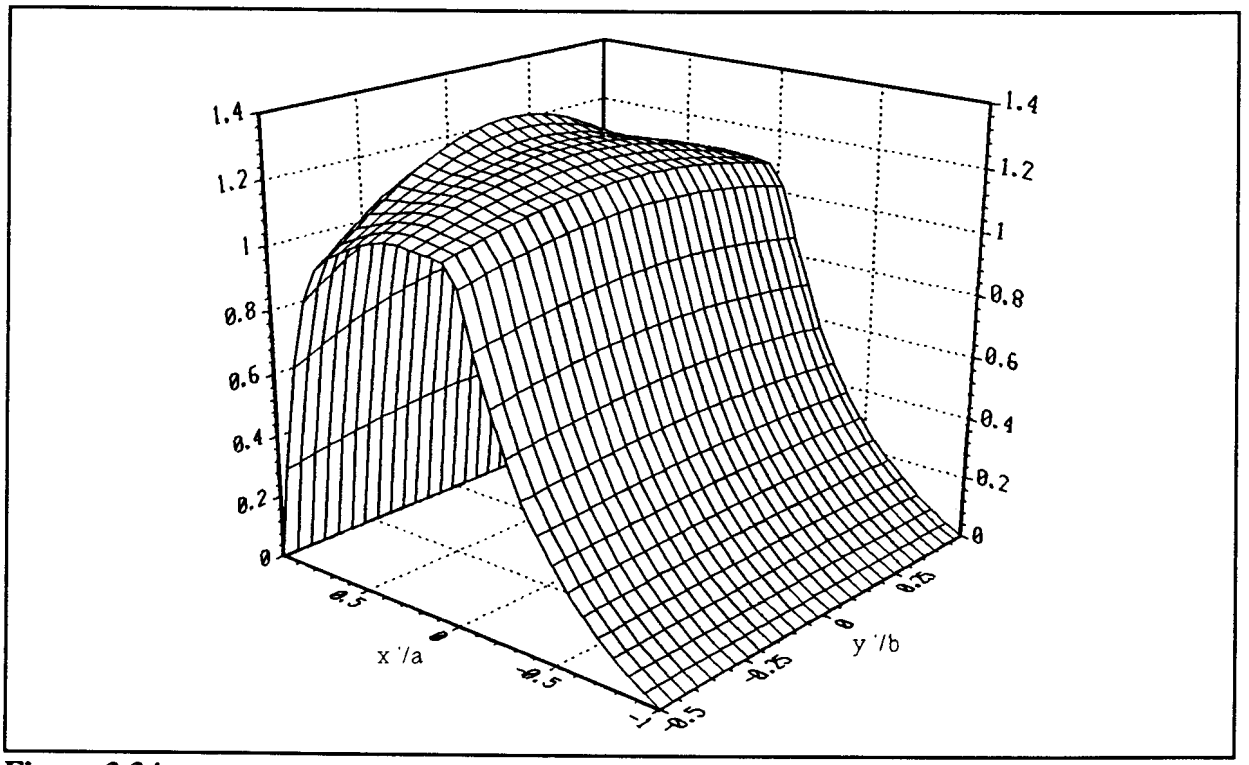

Figure 3.34 *Real integrand of $\Gamma_A^{xx}(\Omega 2a/0)$ as a function of $\mathbf{r}'$ over the region over which it is to be integrated.*

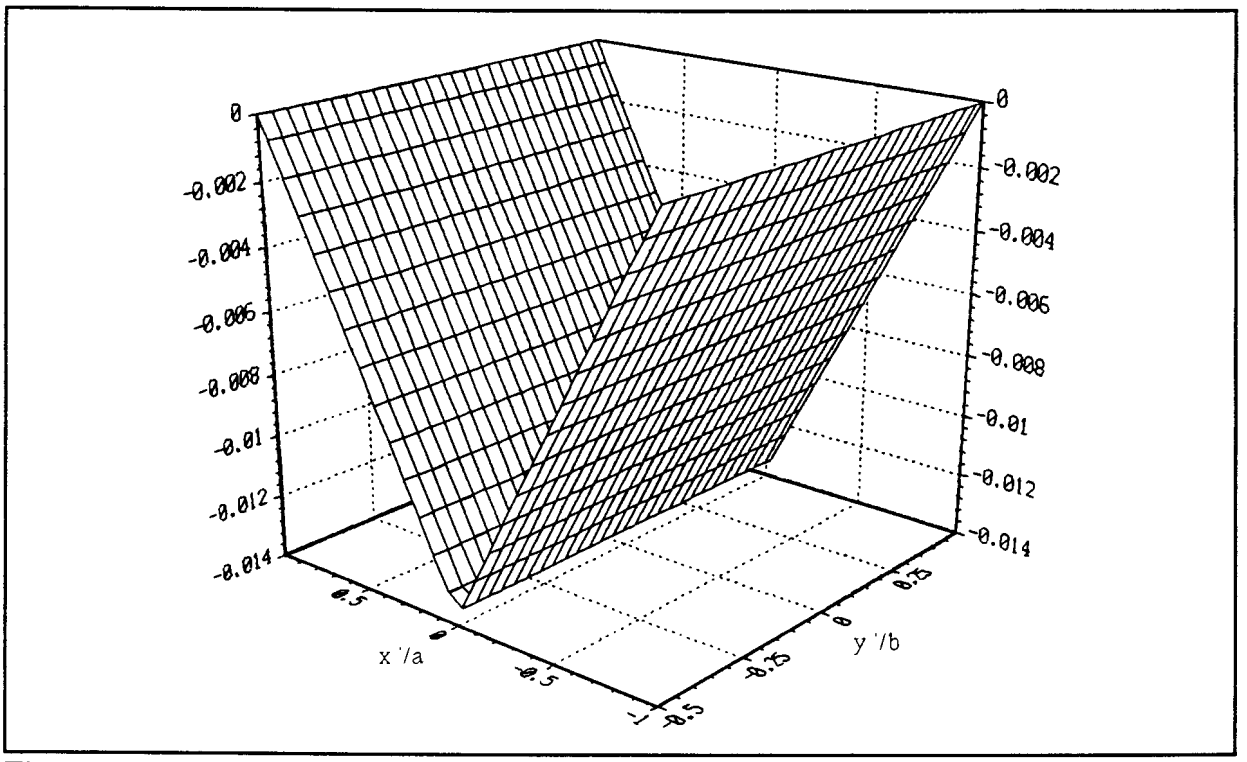

Figure 3.35 *Imaginary part of the integrand corresponding to the real part shown in Figure 3.34.*

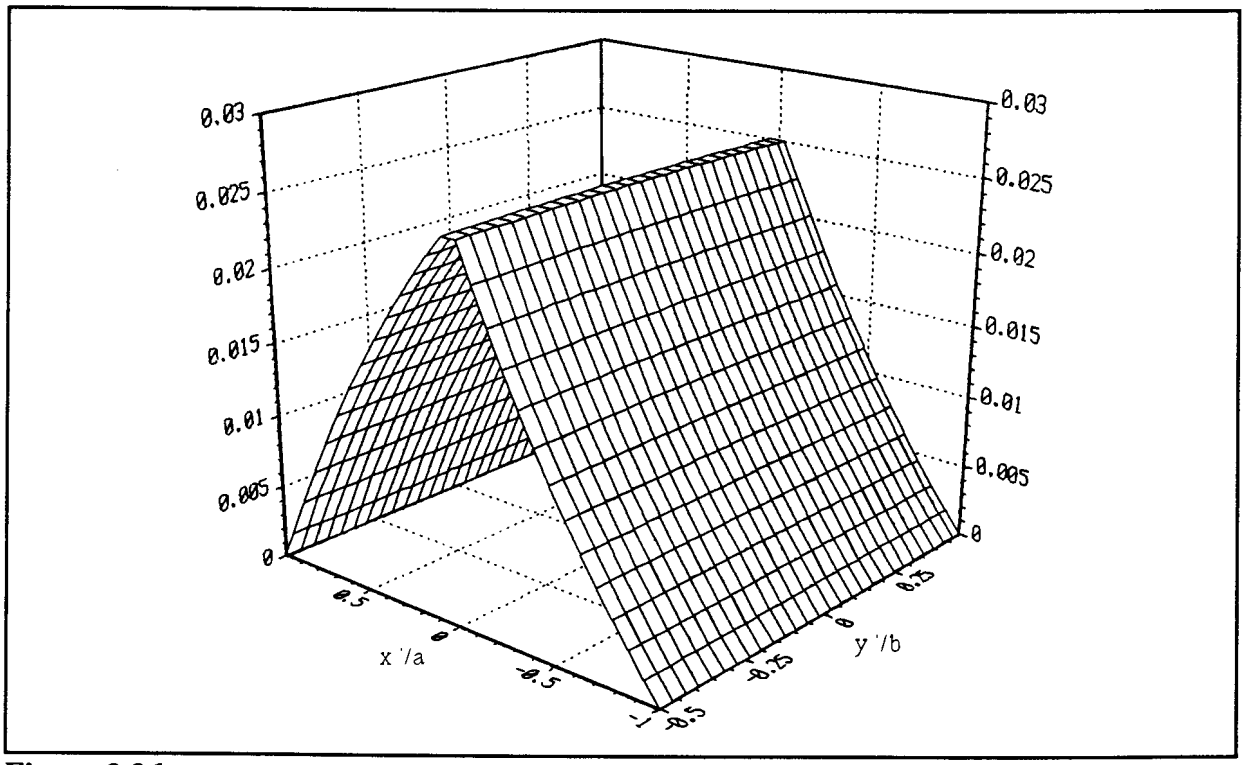

Figure 3.36 *Real integrand of $\Gamma_A^{xx}(\mathfrak{L}8a/0)$ as a function of $\mathbf{r}'$ over the region over which it is to be integrated.*

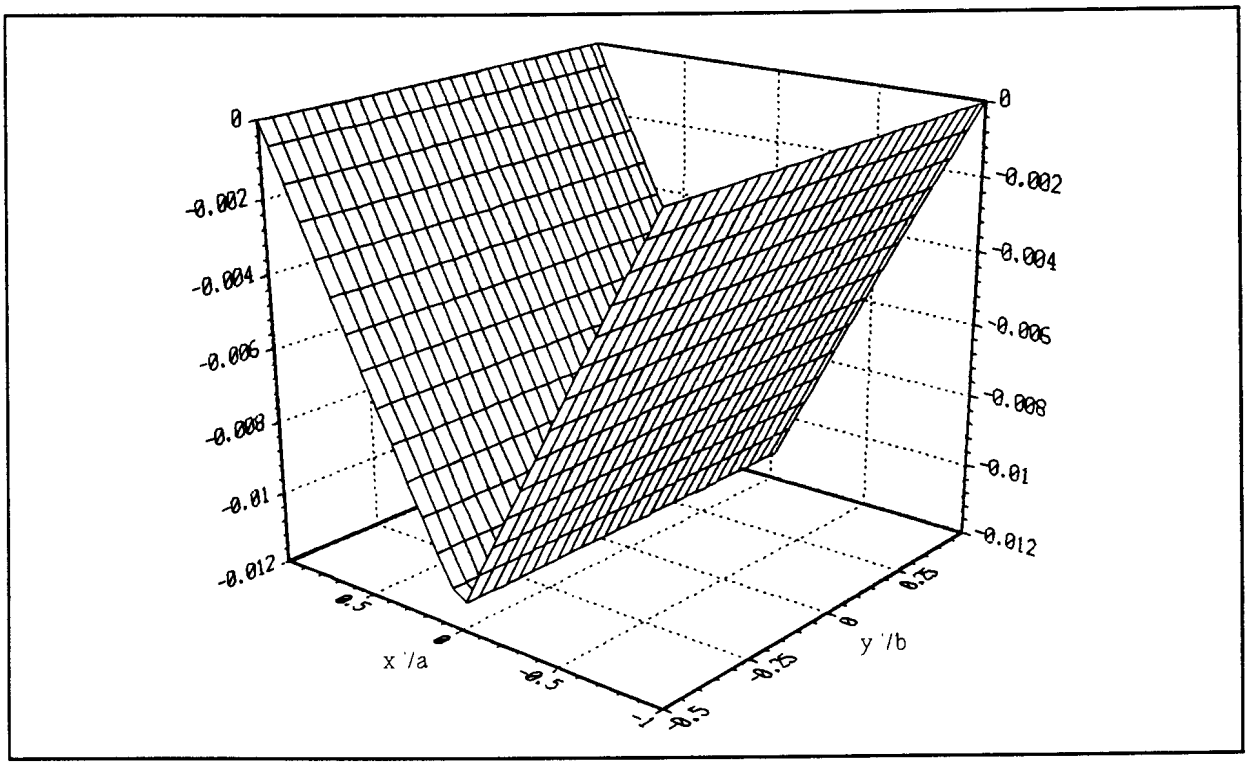

Figure 3.37 *Imaginary part of the integrand with the real part shown in Figure 3.36.*

3.4 MOMENT METHOD MATRIX EQUATION

The moment method matrix (defined in Section 2.3.5) is ill-conditioned[8] due to the fact that some rows are almost linear combinations of three other rows [2]. Therefore, careful evaluation of its elements is necessary to obtain results of sufficient accuracy. On the other hand, the moment method matrix is diagonally dominant [2], therefore less stringent accuracy requirements apply to the off-diagonal elements. Certain approximations may then be considered. Firstly, the discrete Green's functions (requiring double numerical integration) may be approximated by closed-form expressions; this was discussed in Section 3.3.

We consider here one additional closed-form approximation for a term involving the vector potential discrete Green's function. This is being done here rather than in Section 3.3 (where the other approximations were discussed) since arguments in favour of its adoption depend in part on its relative importance in the overall matrix element expression (2.22) as well as the comparison of its exact form to its approximate form. The approximation in question is

$$\int_{C_{xi}} \Gamma_A^{xx}(r/r_{xj})\, k_0\, dx \simeq k_0\, a\, \Gamma_A^{xx}(r_{xi}/r_{xj}) \qquad (3.32)$$

A similar expression holds for Γ_A^{yy}. Figure 3.38 shows a comparison between the real parts of the terms on either side of the equal signs in (3.32), while close correspondence between the imaginary parts can be seen from Figure 3.39. This

[8] A system of linear equations is said to be **ill-conditioned** if small errors in the coefficients or in the solving process have a large effect on the solution [21].

approximation, strictly speaking, does not apply for short distances between current cells S_{xi} ($\mathbf{r}_{xi}$) and S_{xj} ($\mathbf{r}_{xj}$). However, in these cases, the contribution of the vector potential to the value of the matrix element is overshadowed by that of the scalar potential, so that approximation (3.32) still applies. Consider, for example the case: f=1.206 GHz, ϵ_r=(4.34,-0.0868), h=0.8 mm and a=b=6.666 mm for which $k_0 a \Gamma_A^{xx}$ for an observer at $\mathbf{r}$=(1.5a,0) and a source cell centred at (0,0) is equal to (0.3018E−04,0.1038E−06), while the contribution of the scalar potential to the matrix element is (−0.7777E−01,−0.1481E−02); keep in mind that discrete Green's functions are dimensionless quantities. It can be seen that the contribution of the scalar potential overshadows that of the vector potential in the off-diagonal terms and the use of (3.32) will therefore not introduce a significant error. In fact, for the same reason, (3.32) may even be considered for the diagonal matrix elements, as has been confirmed by [16].

As outlined in Section 2.3.5 the moment method matrix is divided into four submatrices. It has also been pointed out in the afore-mentioned section that for charge cells of equal size C_{ij}^{xy} and C_{ji}^{yx} are equal. Under some circumstances however, it may not be possible (or desirable) to discretize the upper conductor with cells of equal size; in such cases C_{ij}^{xy} and C_{ji}^{yx} would not be equal.

The excitation vector is constructed according to (2.28) applying the same approximation for Γ_V as in the moment matrix case. Careful consideration should finally be given to the solution process. In this case, since matrix C is ill-conditioned, a *conjugate gradient method* [24] is used for the iterative solution of the moment method system of linear algebraic equations.

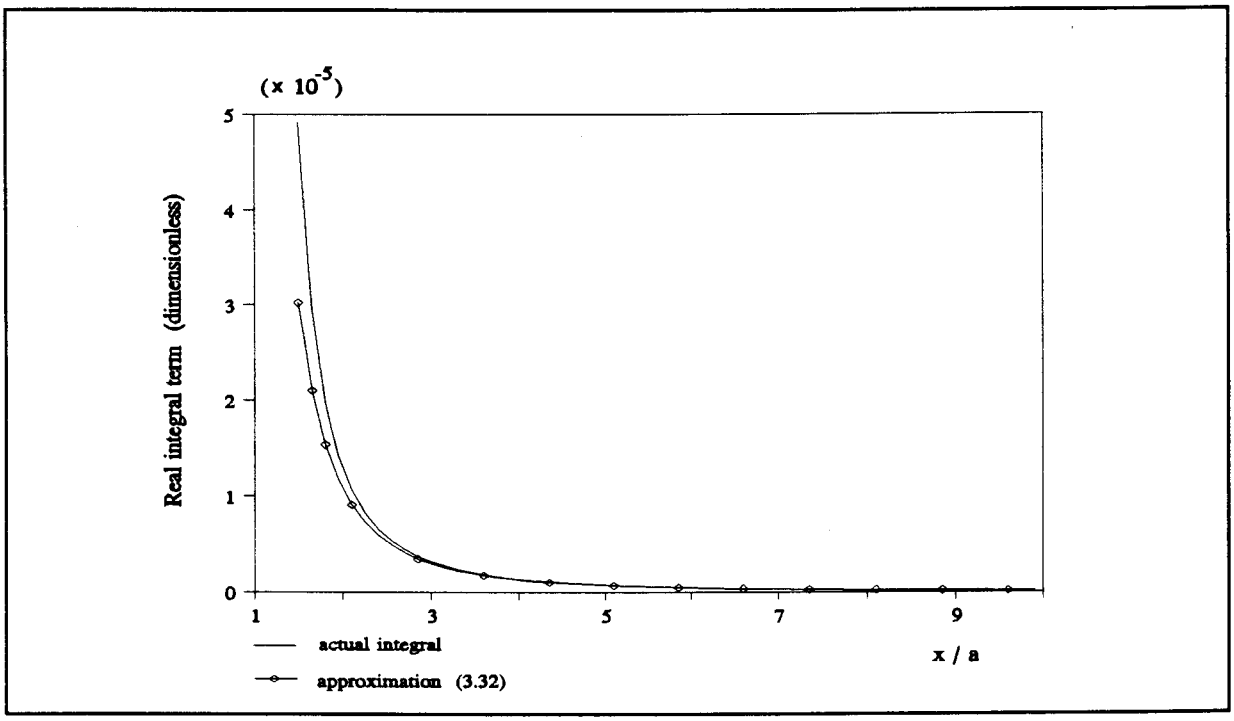

Figure 3.38 *Real parts of the actual integral and approximation (3.32) suggested by Mosig and Gardiol [2] for $f = 1.206$ GHz, $\epsilon_r = (4.34, -0.0868)$; $h = 0.8$mm and $a = b = 6.666$ mm.*

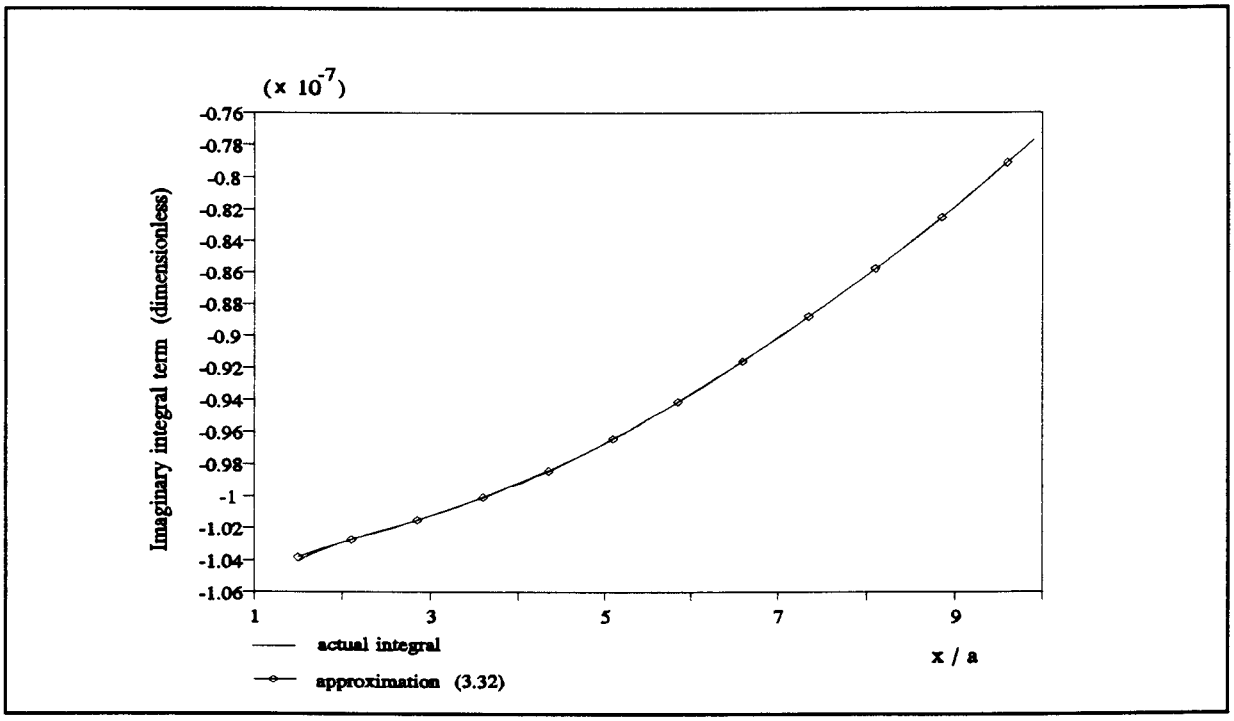

Figure 3.39 *Imaginary parts of the actual integral and an approximation with the corresponding real part shown in Figure 3.38.*

3.5 INTEGRATION

Because numerical integration is such an important part of the analysis, it is imperative that fast, accurate and reliable routines be used. The present author has found that the IMSL integration routines [20] comply with these requirements.

3.5.1 Single integration

Single integrals are numerically evaluated through the use of the IMSL routine QDAG [20] which is a general-purpose integrator that uses a globally adaptive scheme in order to reduce the absolute error. It subdivides the integration interval using a (2k+1)-point Gauss-Kronrod rule to estimate the integral over each sub-interval. The error for each sub-interval is estimated by comparison with the k-point Gauss quadrature rule. The sub-interval with the largest estimated error is then bisected and the same procedure is applied to both halves. The bisection process is continued until either the error criterion is satisfied, roundoff error is detected, the sub-intervals become too small, or the maximum number of sub-intervals allowed is reached. The subroutine QDAG is based on the subroutine QAG by Piessens et al [25].

3.5.2 Double integration

Double integration is numerically performed by the IMSL integration routine, TWODQ [20]. This routine approximates the two-dimensional integral by iterated calls to QDAG. Therefore this algorithm will share

many of the characteristics of the QDAG-routine: the absolute and relative error must be specified in addition to the Gauss-Kronrod pair which is denoted by an integer between 1 and 6. The lower-numbered rules are used for less smooth integrands, while the higher order rules are more efficient for smooth oscillatory integrands.

3.6 INTERPOLATION

For given material parameters and frequency, the Green's functions depend only on the absolute distance from source to observer, $R=|\mathbf{r}-\mathbf{r}'|$. This fact may be exploited through the use of an interpolation table to minimize computation time. Values of the Green's functions are tabulated against a discrete set of distances R_i ($i = 1..N$, where N is typically between 50 and 250[9]) varying from the maximum linear dimension of the antenna (R_{max}) to a minimum value (R_{min}). Interpolation may then be used to determine the Green's functions for any source-observer distances ranging from R_{max} to R_{min}. R_{min} may be chosen arbitrarily provided it is several orders of magnitude smaller than the dimensions of a charge cell. Tests performed by the author on discrete Green's function selfterms for a=b=6.666 mm and R_{min} values of 1.0E−04 m and 1.0E−11 m, respectively, showed relative differences in the selfterm values on the order of 0.1%. Since the Green's functions become singular at $R=|\mathbf{r}-\mathbf{r}'|=0$, evaluation points ($R_i$) for the interpolation table need to be concentrated around R_{min} to ensure accurate evaluation of the selfterms in the moment method matrix.

[9] Convergence tests may be performed to determine a value for N.

Consider for instance the case of a tabulation scheme based on equispaced points; hereby

$$R_i = R_{\min} + \frac{R_{\max} - R_{\min}}{(N-1)}(i-1) \tag{3.33}$$

For R_{min} = 1.0E-06 m, R_{max} = 1.0E-02 m and N = 100, the first two entries in the interpolation table, as shown in Table 3.2, will be at R_1 = 1.0E-06[10] and $R_2 \approx$ 1.02E-04; for N = 200 we have $R_2 \approx$ 5.1E-05. It is clear that for a reasonable amount of evaluation points, it is not possible to obtain a suitable distribution of these points close to the source. It is for this reason that this author proposes a tabulation scheme based on a *logarithmic distribution* of evaluation points. Hereby, R_i may be calculated according to

$$R_i = 10^{\left(\log_{10}(R_{\min}) + (i-1)\left[\frac{\log_{10}(R_{\max}) - \log_{10}(R_{\min})}{(N-1)}\right]\right)} \tag{3.34}$$

Now, for the case mentioned earlier with N = 100, we have, from Table 3.2: R_1 = 1.0E-06, $R_2 \approx$ 1.09E-06, $R_3 \approx$ 1.2E-06, ..., $R_{99} \approx$ 9.11E-03 and R_{100} = 1.0E-02. Therefore, compared to (3.33), expression (3.34) yields a better distribution of evaluation points close to the source; however, from Table 3.2 it follows that an equispaced (i.e. linear) scheme on its part yields a better distribution further away from the source point. Therefore, to include both these features in a tabulation

[10] Throughout this section, R will be given in terms of meters [m].

scheme, we may consider a combination of the logarithmic and equispaced schemes. For instance, we may make use of (3.34) for $R_{min} \leq R \leq R_{inter}$ and use (3.33) for $R_{inter} < R \leq R_{max}$ where, for example, R_{inter} is the maximum linear dimension of a charge cell: $R_{inter}=(a^2+b^2)^{1/2}$. Values of R_i for $R_{inter}=1.0E-03$ and $N_1=N_2=50$ are shown in Table 3.2. N_1 and N_2 are the total amount of evaluation points used by the logarithmic and equispaced schemes, respectively, so that $N_1 + N_2 = N$. It can be seen that the combination of logarithmic and equispaced schemes has a higher concentration of evaluation points close to the source and a comparable concentration further away from it.

Another possible tabulation scheme whereby a *parabolic distribution* of evaluation points is taken, was suggested by Mosig and Gardiol [4]. These evaluation points may be determined by

$$R_i = \frac{(R_{max} - R_{min})}{(N^2 - 1)}(i^2 - 1) + R_{min} \qquad (3.35)$$

With this suggestion, corresponding entries in the interpolation table for $N=100$ are shown in Table 3.2.

Now Mosig and Gardiol [3] suggested that the *regular part* $(G-G_s)$ of the Green's function in the expansion $G = (G-G_s) + G_s$ where G_s is the static Green's function, be tabulated against distances R_i. Interpolation is then used to determine $(G-G_s)$ at distances not listed in the table. The static part, therefore, has to be added to the interpolated value for all cases except where selfterm evaluation is considered. *Cublic spline interpolation* [27] has been found to be

particularly accurate for our purposes.

By means of proper interpolation, computation time may be reduced considerably, without significant loss in accuracy.

i	LINEAR (3.33)	LOGARITHMIC (3.34)	PARABOLIC (3.35)	COMBINING (3.33)&(3.34)
1	1.00E-06	1.00E-06	1.00E-06	1.00E-06
2	1.02E-04	1.09E-06	4.00E-06	1.15E-06
3	2.03E-04	1.20E-06	9.00E-06	1.32E-06
49	4.85E-03	8.69E-05	2.40E-03	8.69E-04
50	4.95E-03	9.54E-05	2.50E-03	1.00E-03
51	5.05E-03	1.04E-04	2.60E-03	1.18E-03
98	9.80E-03	8.30E-03	9.60E-03	9.64E-03
99	9.90E-03	9.11E-03	9.80E-03	9.82E-03
100	1.00E-02	1.00E-02	1.00E-02	1.00E-02

Table 3.2 R_i's determined according to the four tabulation schemes discussed in Section 3.6. All distances are given in terms of meters [m].

3.7 NUMERICAL ASPECTS IN THE COMPUTATION OF FAR-FIELD RADIATION

Far-field radiation by implication means that the observer is no longer bound to the air-dielectric interface described by $z = 0$ (Figure 2.1). Therefore the term $\exp(-u_0 z)$ appearing in the Green's function expressions (2.4) through (2.10) can

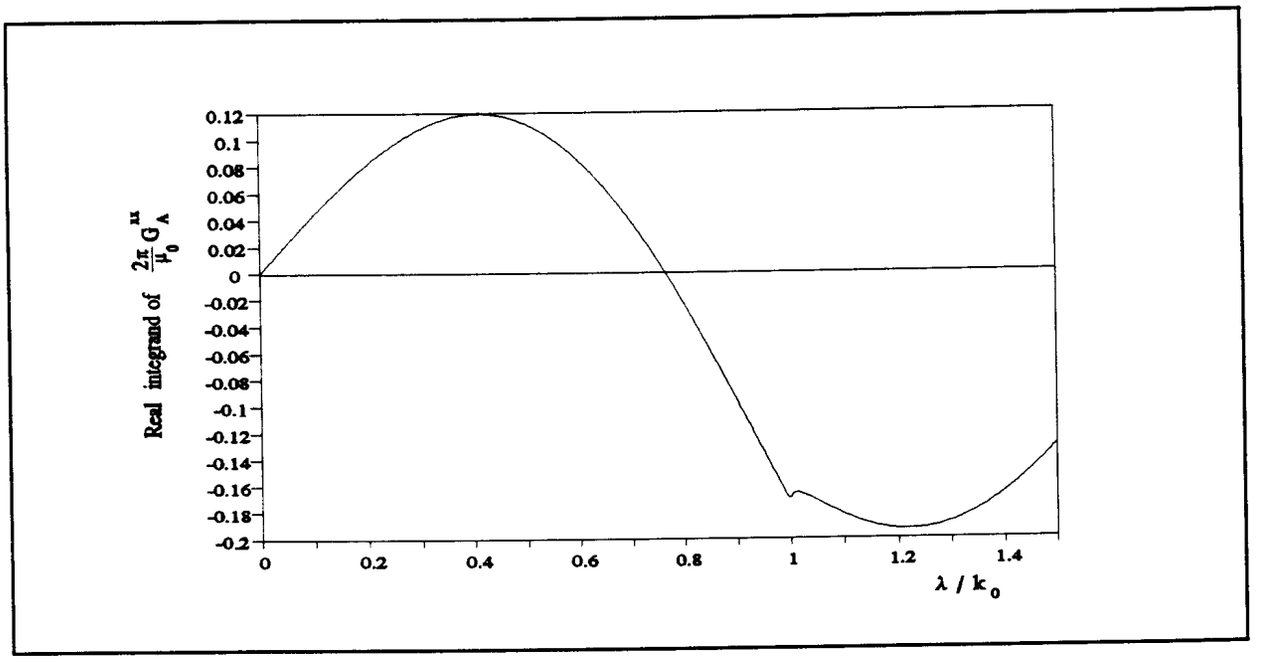

(a) *z = 0 m*

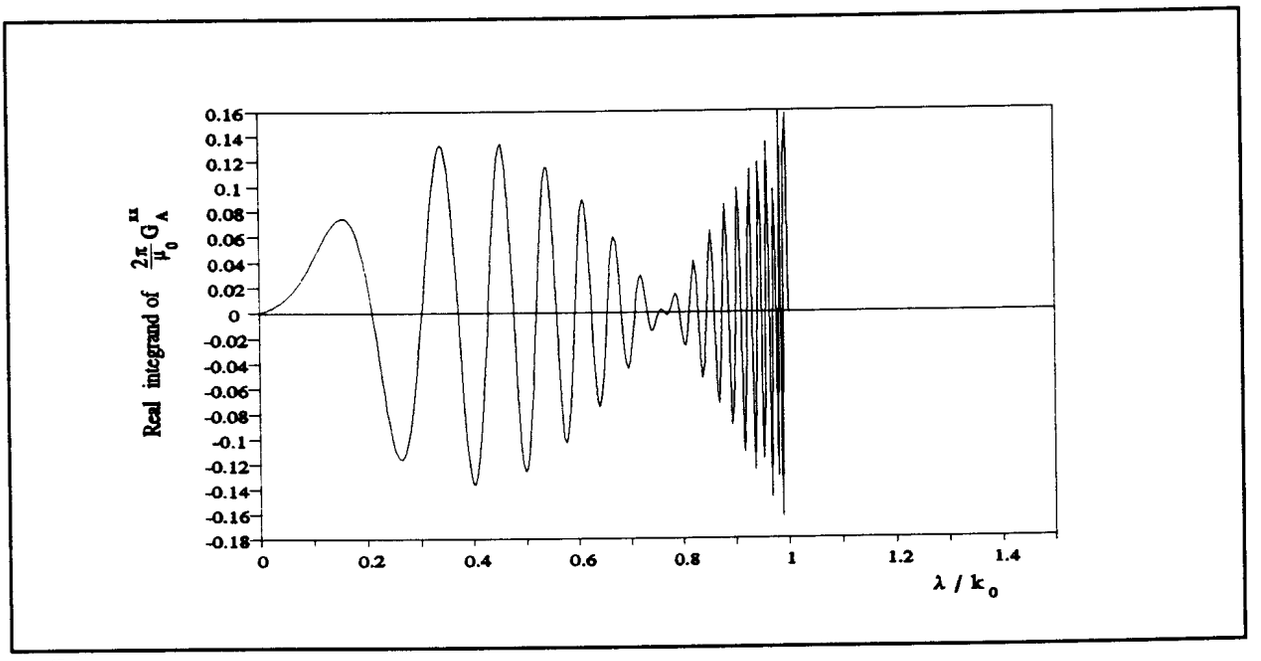

(b) *z = 5.0 m*

Figure 3.40: Normalised real integrands of G_A^{xx} (i.e. $J_0(\lambda R)\lambda \exp(-u_0 z)/D_{TE}$ for $R/\lambda_0=0.5$ and $h/\lambda_0=0.07$ at f=1.206 GHz and $\epsilon_r=(4.34,-0.0868)$) for z = 0.0 and 5.0 m.

no longer be set to unity. Consider the following situation: an observer is placed at (r, ϕ, θ = 90°) with the radiating antenna centred at the origin. For fixed values of r and ϕ, the observer is now rotated from θ = 90° towards θ = 0°. This implies that z now becomes large for θ < 90° if r is large (Figure 2.1), and the following situation arises: since u_0 is purely imaginary in the interval $0 \leq \lambda < k_0$, and z a very large real number, $\exp(-j(k_0^2 - \lambda^2)z)$ causes rapid sign changes in this interval. Furthermore, since u_0 is real for $\lambda \geq k_0$ we have $\exp(-u_0 z) \rightarrow 0$ and thus the integration interval in effect reduces to $0 \leq \lambda < k_0$. An example of a Green's function integrand for z = 5.0 m is shown in Figure 3.40(b). This figure illustrates the rapid sign changes and reduced integration interval just spoken of. From this we conclude that standard numerical integration routines are not capable of yielding accurate estimates of the Green's function integrals with large z values. We therefore resort to *asymptotic techniques* to obtain approximate analytic solutions to these integrals. Mosig and Gardiol [3] have found the *method of steepest descent* [28] to be particularly suited to integrals associated with microstrip structures. This method is based on the concept of deforming the integration path, within certain limits, without affecting the value of the integral, to such an extent that the main contribution to the integral can be attributed to small segments on the new path. The integrand can then be approximated by simpler functions over the important parts of the path, whilst the contribution over the other segments can be neglected. If in the deformation of the integration path, singularities are encountered, we must add (a) the residue when crossing a pole and (b) the integral when encountering a branch point [29]. The method of steepest descent

applies to integrals of type

$$I = \int_C F(w)\, e^{[\Omega\, q(w)]}\, dw \tag{3.36}$$

where F and q are analytic complex functions (except maybe for some isolated singularities), C is an arbitrary integration path in the complex w-plane and Ω a very large real number. Recall that the Green's function integrals may be written in the general form

$$I = \int_0^\infty J_n(\lambda R)\, \lambda^{n+1}\, g(\lambda)\, e^{-u_0(\lambda)z}\, d\lambda \tag{3.37}$$

Now *if $g(k_\rho)$ is always an even function of k_ρ* the following identity holds [30]:

$$\begin{aligned} &\int_0^\infty J_n(\lambda R)\, \lambda^{n+1} g(\lambda) e^{-u_0(\lambda)z} d\lambda \\ &= \frac{1}{2}\int_C H_n^{(2)}(k_\rho R) k_\rho^{n+1} g(k_\rho) e^{-u_0(k_\rho)z} dk_\rho \end{aligned} \tag{3.38}$$

As seen from (2.4)-(2.10), g may take on various forms. Consider for instance $g(k_\rho) = 1/D_{TE}(k_\rho)$, for which 3-D plots of the real and imaginary parts are shown in Figures 3.41 and 3.42, respectively. These figures serve to give a view of this particular function over a part of the k_ρ-plane. To draw conclusions on certain characteristics of the function however, these illustrations will not suffice

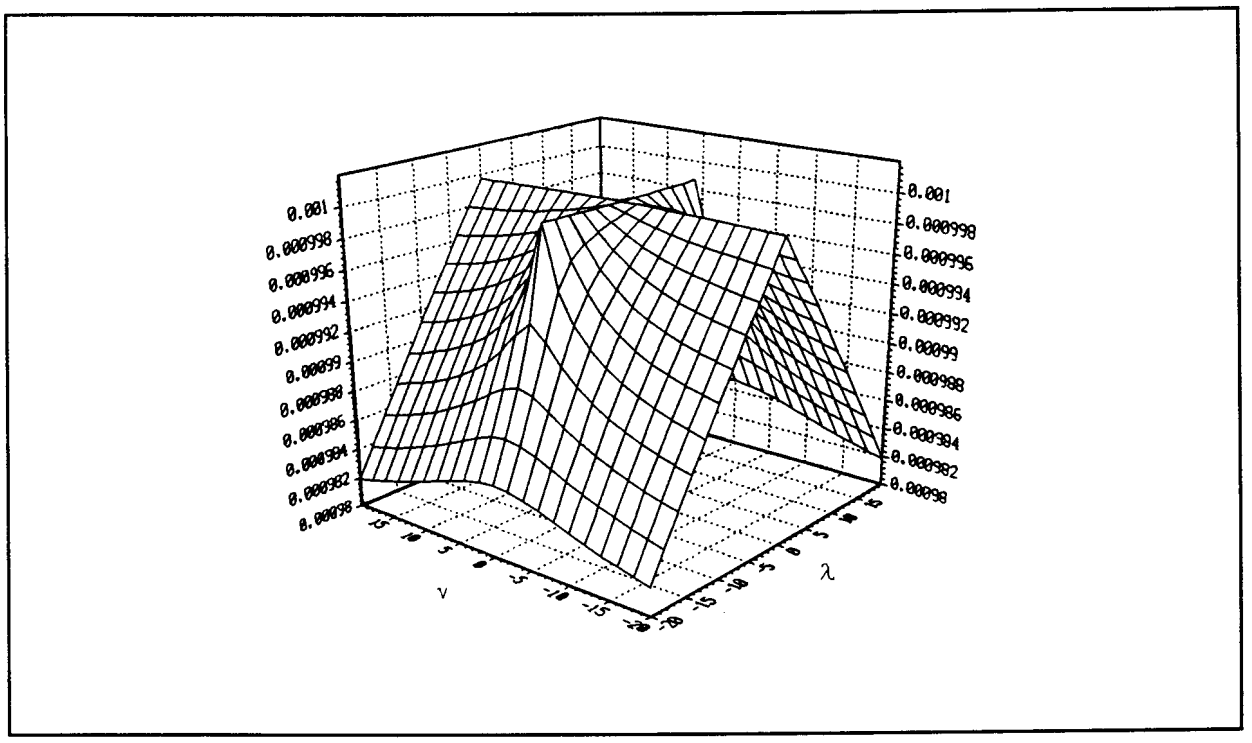

Figure 3.41 *Real part of* $1/D_{TE}(k_\rho)$ *where* $k_\rho = \lambda + j\nu$.

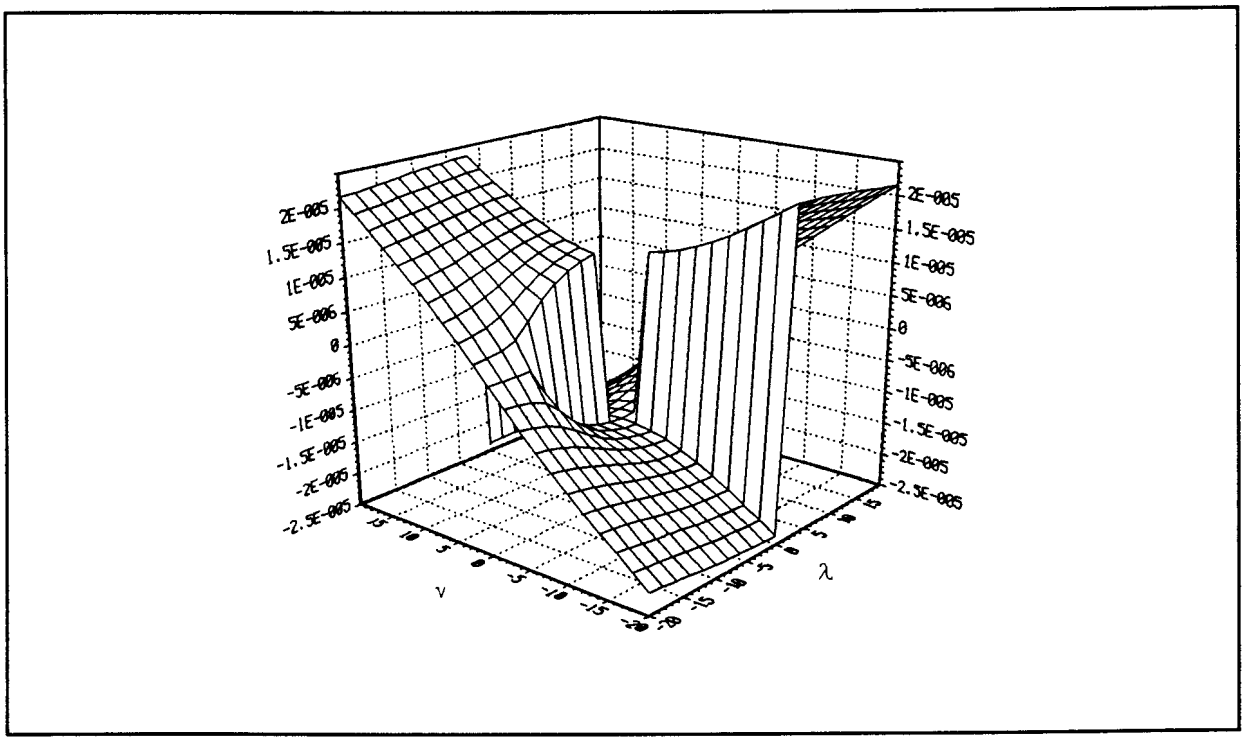

Figure 3.42 *Imaginary part of* $1/D_{TE}(k_\rho)$ *where* $k_\rho = \lambda + j\nu$

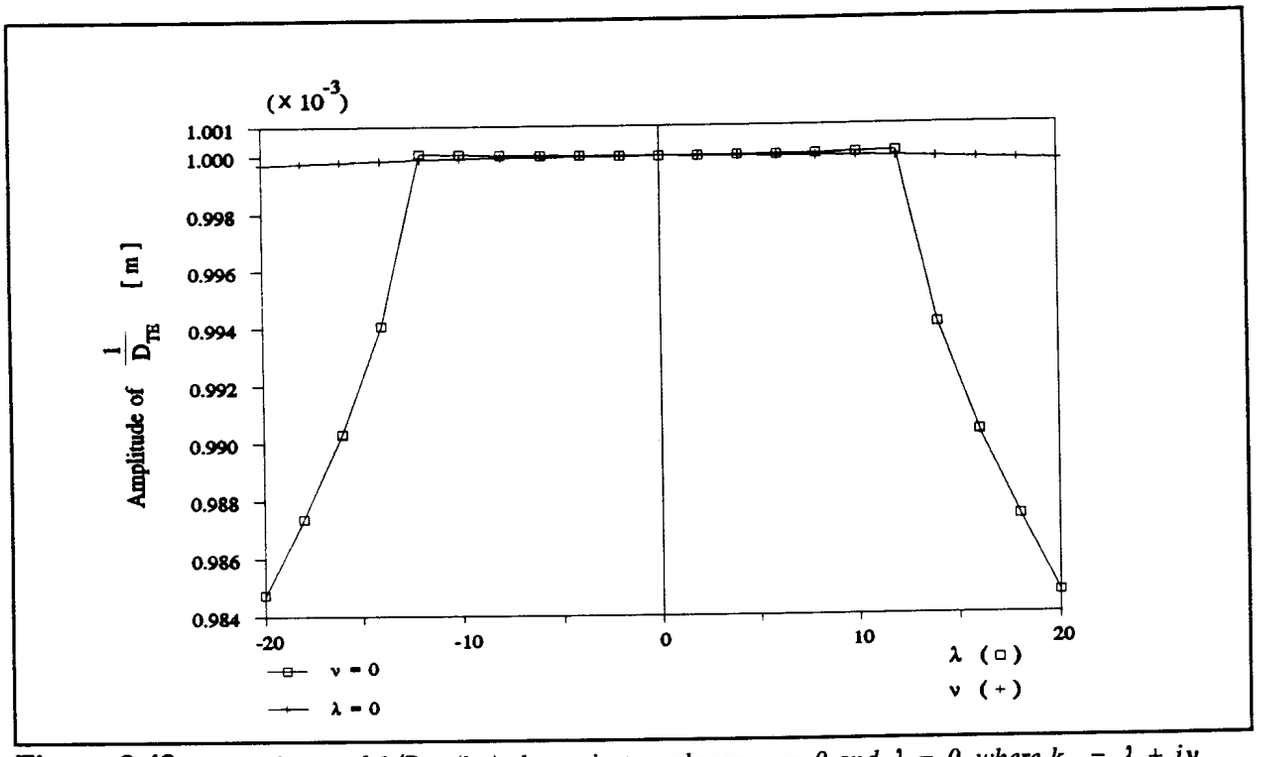

Figure 3.43 *The real part of $1/D_{TE}(k_\rho)$ shown in two planes: $\nu = 0$ and $\lambda = 0$, where $k_\rho = \lambda + j\nu$.*

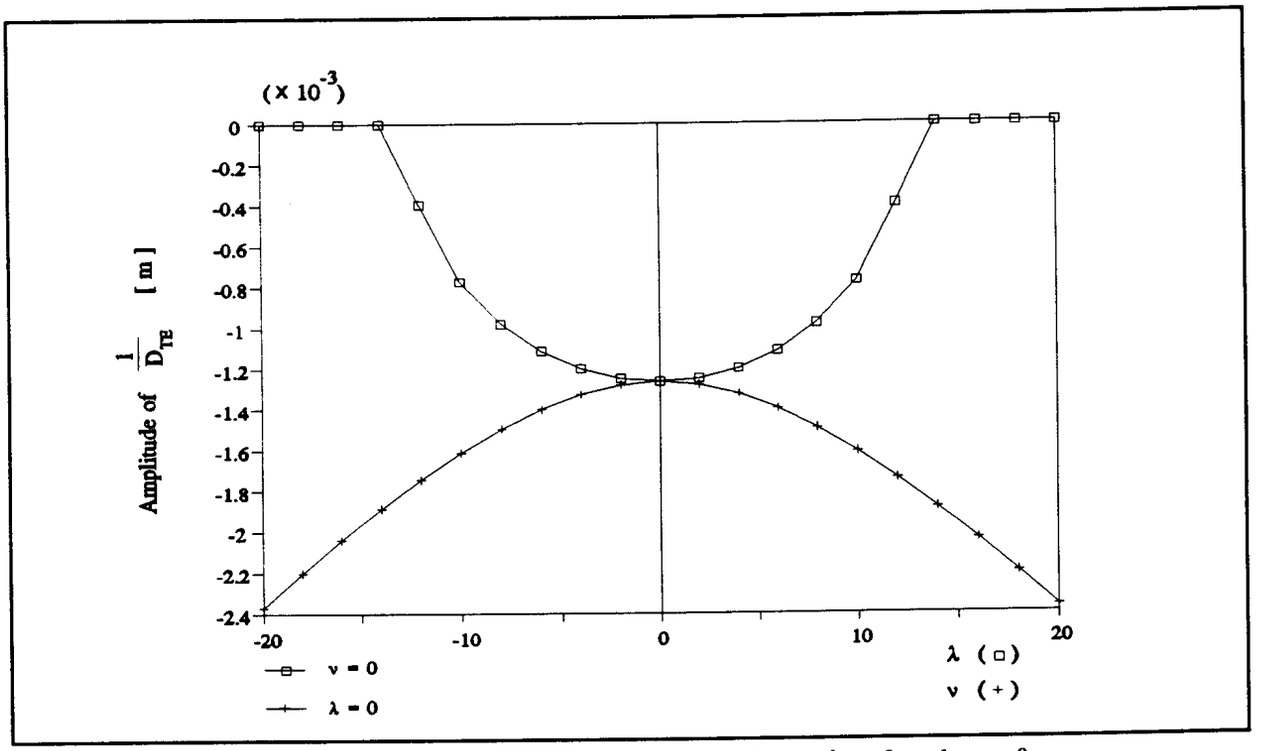

Figure 3.44 *The imaginary part of $1/D_{TE}(k_\rho)$ shown in two planes: $\lambda = 0$ and $\nu = 0$.*

and for this reason, Figures 3.43 and 3.44 are included. These figures give the real and imaginary parts of the function in two cut-planes: $\lambda = 0$ and $\nu = 0$ where $k_\rho = \lambda + j\nu$. From this, and keeping Figures 3.41 and 3.42 in mind, it may be concluded that $1/D_{TE}(k_\rho)$ is an even function of k_ρ. In similar fashion, the other forms of function g (that is $1/(D_{TE}D_{TM})$ and $N/(D_{TE}D_{TM})$) were confirmed to be even. It is for this reason that identity (3.38) is applicable in this case to integrals written in the general form of (3.37). Therefore we may now consider

$$I = \int_C H_n^{(2)}(k_\rho R) f(k_\rho)\, e^{-u_0(k_\rho)z}\, dk_\rho \qquad (3.39)$$

The method of steepest descent now requires that (3.39) be written in the general form of (3.36). In this regard, it is convenient to transform the complex k_ρ-plane into a new complex plane, w, by the relation: $k_\rho = k_0 \sin w$ [3]. Introducing spherical coordinates ($R = r\sin\theta$ and $z = r\cos\theta$) and applying this transformation (whereby $u_0 = jk_0 \cos w$), we have:

$$I = \int_{C^*} H_n^{(2)}(k_0 r \sin\theta \sin w) f(k_0 \sin w)\, e^{-jk_0 r \cos w \cos\theta} k_0 \cos w\, dw \qquad (3.40)$$

where C^* is the transformed integration path. Assuming that $f(k_\rho)$ has a pole at λ_p on the k_ρ-plane, then with the transformed path C^*, the pole is now located at $w_p = \pi/2 + j\cosh^{-1}(\lambda_p/k_0)$ [3] whilst the branch points at $k_\rho = \pm k_0$ disappear due to the transformation [3]. Provided $k_0 r \sin\theta \sin w >> 1$ we can make use of the following first order asymptotic approximation for $H_n^{(2)}$ [29]:

$$H_n^{(2)}(k_0 r\sin\theta\sin w) \simeq \sqrt{\frac{2}{\pi k_0 r\sin\theta\sin w}}\, e^{-j\left[k_0 r\sin\theta\sin w - \frac{n\pi}{2} - \frac{\pi}{4}\right]} \qquad (3.41)$$

Since we are interested in an expression valid in the far-field, we have $k_0 r >> 1$; the integration path can furthermore be deformed far from the origin (w=0) in order that sin w does not vanish, while it can be shown [3] that this asymptotic approximation will yield correct results even for the broadside direction $\theta=0$. Therefore, making use of (3.41) and noting that $e^{(jn\pi/2)}=j^n$, $e^{j\pi/4}=(j)^{1/2}$ and $\cos w\cos\theta+\sin\theta\sin w = \cos(w-\theta)$, yields for (3.40):

$$I \simeq \int_{C^*} j^n \sqrt{\frac{2j}{\pi\,\Omega\sin\theta\sin w}}\, f(k_0\sin w)\, e^{-j\Omega\cos(w-\theta)}\, k_0\sin w\, dw \qquad (3.42)$$

where $\Omega = k_0 r$. (3.39) has now been written in the general form of (3.36) where

$$F(w) = j^n \sqrt{\frac{2j}{\pi\,\Omega\sin\theta\sin w}}\, f(k_0\sin w)\, k_0\cos w \qquad (3.43)$$

$$q(w) = -j\cos(w-\theta)$$

and $\Omega = k_0 r$. The path C^* may now be transformed to a steepest descent path C_{SD} provided the contribution of the pole is added when it is crossed in the transformation. From the particularities of the steepest-descent path [11], it follows

[11] It is not within the scope of this text to derive these particularities; more details are given in [3].

that C_{SD} crosses the pole at w_p only when $\theta > \theta_p = \sin^{-1}(k_0/\lambda_p)$ [3]. The integral may then be written as

$$\int_{C^*} = \int_{C_{SD}} + U(\theta - \theta_p) \int_{C_p} \tag{3.44}$$

where U is the Heaviside unit step function[12] and C_p a path surrounding the pole at w_p. A first-order analytical approximation for the integral along path C_{SD} can now be obtained from general closed form solutions to (3.36) [28] while the integral around the pole is evaluated using the residue theorem [21]. An approximated solution to (3.39) may finally be written as

$$I \simeq 2 j^{n+1} \cot\theta f(k_0 \sin\theta) \frac{e^{-jk_0 r}}{r} - U(\theta - \theta_p) 2\pi j Res H_n^{(2)}(\lambda_\rho R) e^{-z\sqrt{\lambda_p^2 - k_0^2}} \tag{3.45}$$

where Res is the residue of function $f(k_\rho)$ at λ_p. It has been pointed out by Mosig and Gardiol [3] that this asymptotic approximation is only valid if the pole is located far enough from the saddle point, i.e. $(k_0 \sin\theta - \lambda_p)r >> 1$, otherwise a modified saddle-point method must be used whereby the contributions of the pole and saddle-point are not separated. Further warnings in this regard have been given by Hsu et. al. [26]. Assuming that this inequality holds, Appendix D makes

[12] $U(\theta) = 0$ for $\theta < 0$ while $U(\theta) = 1$ for $\theta \geq 0$.

use of the method of steepest descent to derive far-field radiation expressions for etched radiators given the surface current distribution as a set of discrete coefficients I_{xi} (i=1...M) and I_{yj} (j=1...N). Mosig and Gardiol [3], applying (3.45), have also derived far-field radiation expressions for a HED on microstrip from which the radiated fields of an arbitrarily shaped etched radiator may also be obtained. The radiator is replaced by an array of Hertz dipoles for which the radiated electric fields are given by [3]

$$E_\theta = G_E^{\theta x}(r/0)\sum_{i=1}^{M} aI_{xi}\, e^{jk_0 g_i} + G_E^{\theta y}(r/0)\sum_{j=1}^{N} bI_{yj}\, e^{jk_0 g_j} \tag{3.46}$$

$$E_\phi = G_E^{\phi x}(r/0)\sum_{i=1}^{M} aI_{xi}\, e^{jk_0 g_i} + G_E^{\phi y}(r/0)\sum_{j=1}^{N} bI_{yj}\, e^{jk_0 g_j} \tag{3.47}$$

where $g_k = x_k \sin\theta\cos\phi + y_k \sin\theta\sin\phi$ (k=i,j); x_k and y_k are the centre coordinates of the k'th current cell. We also have[13]

$$G_E^{\theta x}(r/0) = -j\left(\frac{Z_0}{\lambda_0}\right)\cos\phi\, f_\theta(\theta)\,\frac{\exp(-jk_0 r)}{r} \tag{3.48}$$

$$G_E^{\phi x}(r/0) = j\left(\frac{Z_0}{\lambda_0}\right)\sin\phi\, f_\phi(\theta)\,\frac{\exp(-jk_0 r)}{r} \tag{3.49}$$

[13] E_θ and E_ϕ for a HED are given in [3]. From this, $G_E^{\theta x}$ and $G_E^{\phi x}$ follow directly, while $G_E^{\theta y}$ and $G_E^{\phi y}$ follow from rotational symmetry about the z-axis.

$$G_E^{\theta y}(r/0) = -j\left(\frac{Z_0}{\lambda_0}\right)\sin\phi\, f_\theta(\theta)\,\frac{\exp(-jk_0 r)}{r} \tag{3.50}$$

$$G_E^{\phi y}(r/0) = -j\left(\frac{Z_0}{\lambda_0}\right)\cos\phi\, f_\phi(\theta)\,\frac{\exp(-jk_0 r)}{r} \tag{3.51}$$

with

$$f_\theta(\theta) = \frac{T\cos\theta}{\left[T - j\epsilon_r\cos\theta\, cotan(k_0 hT)\right]} \tag{3.52}$$

$$f_\phi(\theta) = \frac{\cos\theta}{\left[\cos\theta - jT\, cotan(k_0 hT)\right]} \tag{3.53}$$

and

$$T = \sqrt{(\epsilon_r - \sin^2\theta)} \tag{3.54}$$

Z_0, λ_0 and k_0 are the free-space characteristic impedance, wavelength and wavenumber, respectively. Although these expressions appear to be different from those derived in Appendix D (not surprising since two different approaches were used), both sets of expressions yield exact same results. The co- and cross-polarized E-fields may then be determined from these expressions as follows [31]:

$$E_{co}(\theta,\phi) = E_\theta(\theta,\phi)\sin\phi + E_\phi(\theta,\phi)\cos\phi \tag{3.55}$$

$$E_{cross}(\theta,\phi) = E_\theta(\theta,\phi)\cos\phi - E_\phi(\theta,\phi)\sin\phi \tag{3.56}$$

3.8 CONCLUDING REMARKS

The formal theoretical integral equation formulation of the microstrip antenna problem as presented in Section 2.3 is but a relatively small first step in the analysis problem. It is the numerical implementation of the analysis (and the associated computer code development) that is the most cumbersome and time-consuming part, and which requires substantial effort. Due to restrictions on their length, journal articles contain a very limited amount of detail to aid in the latter task. This chapter has provided such complete details required for direct implementation of the formulation of [2,3,4], has illustrated graphically where and why certain numerical difficulties arise, and how these may be handled. Such a "pictorial guide" (for which all graphs were computed by the author), and the finer points how to actually implement the numerical schemes, do not appear to be available in the same detail elsewhere. The contents of the present chapter can be summarized as follows: We saw that the required Green's functions, forming the kernel of the integral equation, posed distinct numerical difficulties. These were overcome by appropriate mathematical techniques, the applications of which were discussed and illustrated in complete detail. In the solution of the integral equation, it was mentioned that the introduction of discrete Green's functions eased the computational task. A singularity problem in the selfterm evaluations arose however, requiring the use of a pole extraction technique; the application of this technique was illustrated. Since the construction of the moment method matrix involves a large amount of computation, certain ways were described whereby computation time could be reduced. This was achieved through

interpolation and the use of approximate expressions for the discrete Green's functions. Illustrations were used to validate the use of these approximations. Finally, far-field computational techniques were discussed and appropriate expressions derived. Numerical techniques for the mixed-potential integral equation method of microstrip analysis have therefore been developed and implemented. This implementation is in the form of a computer code written in FORTRAN.

CHAPTER 4

THE ANALYSIS OF WIRE-GRID ANTENNA ARRAYS

4.1 INTRODUCTION

In Chapter 3 we discussed the numerical methods needed for the implementation of the mixed-potential integral-equation formulation. This implementation is now at our disposal for the analysis of arbitrarily shaped microstrip antennas. Firstly, we will analyse rectangular microstrip patches and give a comparison with known surface current distributions in order to verify the present implementation. The method will then be applied to etched wire-grid antenna arrays which have not yet been analysed rigorously. Theoretical results will be given and discussed. A comparison with measured results will then be given to verify the theoretical results.

4.2 VERIFICATION OF THE PRESENT ANALYSIS THROUGH COMPARISON WITH KNOWN RESULTS

Rectangular microstrip patch antennas have been analysed rigorously and the surface current distributions on these structures, at specific frequencies, are known [2]. Consider a rectangular microstrip patch antenna with dimensions 60×40 mm on a dielectric substrate of thickness 0.8 mm and relative permittivity $\epsilon_r = (4.34, -0.0868)$. An effective conductivity of $\sigma^* = \sigma_{Cu}/4$ was assumed. Rooftop subdomain basis functions will be used in the moment method expansion

and for this reason the patch is decomposed into 9 × 6 square cells referred to as charge cells in Chapter 2 (Figures 2.2 and 2.3). In this case, these charge cells all have equal size. A coaxial feed is used for the patch antenna and the coaxial probe is located at the centre of the (2,2) charge cell, its position being indicated by the bold dot in Figures 4.1 through 4.5. In [2], the surface current distributions on this patch are shown at four resonances, as well as an off-resonance frequency. According to numerical results given in [2], the first four resonance frequencies are at 1.206 GHz (TM_{10}), 1.783 GHz (TM_{01}), 2.177 GHz (TM_{11}) and 2.405 GHz (TM_{20}). Since microstrip patch computations were simply done in order to be able to validate the computer code through comparison with the patch data given in [2], the frequency was simply varied until the current distributions obtained agreed with those in [2]. Such agreements were found at 1.210 GHz, 1.793 GHz, 2.1876 GHz and 2.398 GHz; all within 0.56% of the values given in [2]. This discrepancy is often much less than what arises due to uncertainties in the fabrication process and material parameters [3]. The code can thus be considered validated. The real and imaginary parts of the surface current distributions on this patch at these frequencies are shown in Figures 4.1 through 4.5. Feedpoints are indicated and the numerical values given, correspond to the peak values of current represented by the longest arrows. When compared, close correspondence with published results [2] can be seen.

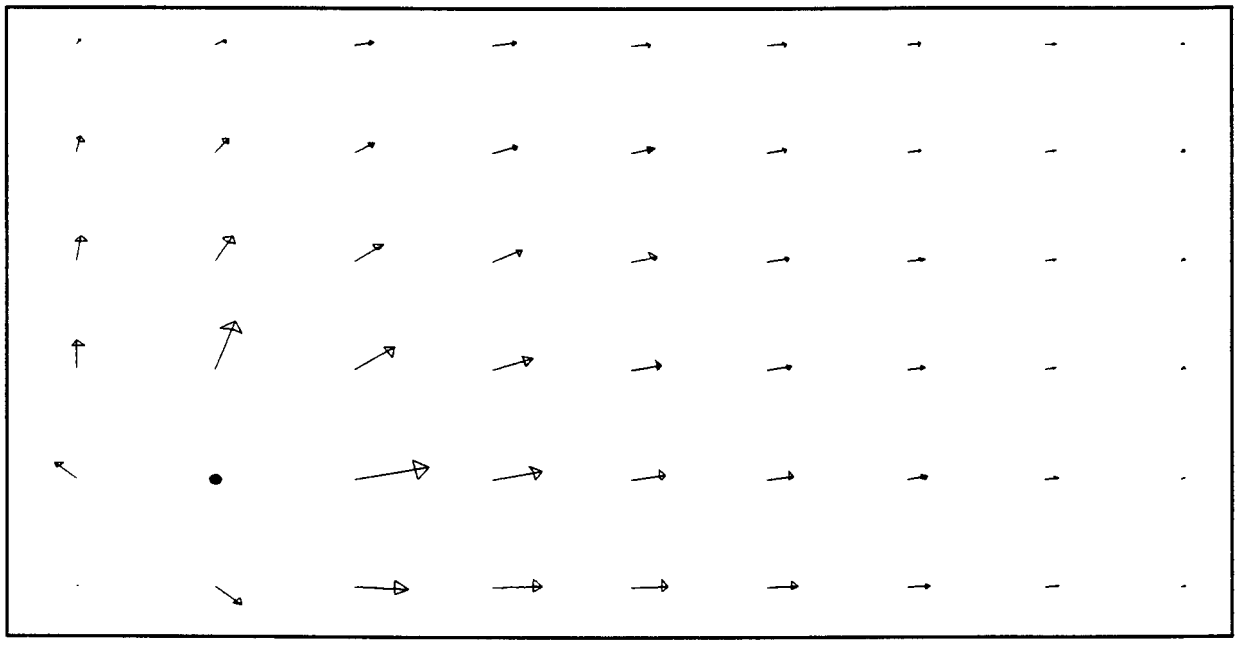

(a) *Real component. Maximum value = 0.280 A*

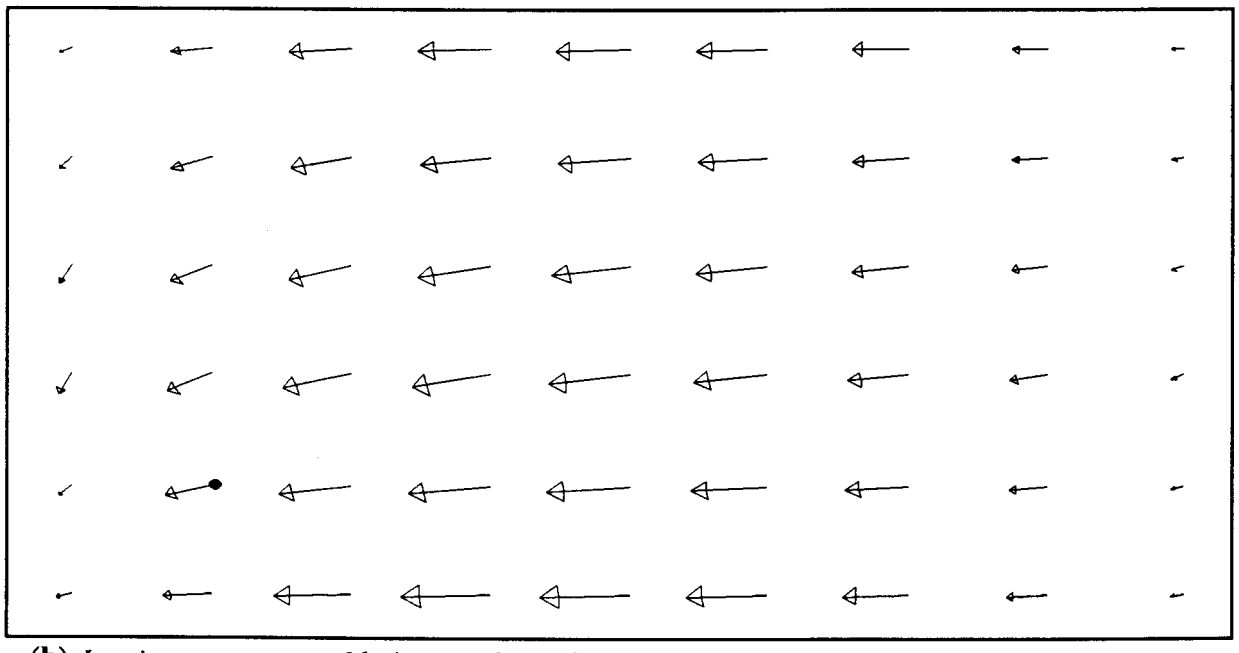

(b) *Imaginary component. Maximum value = 0.001 A*

Figure 4.1 *Real and imaginary parts of the surface currents on a coaxial-fed microstrip patch at 0.603 GHz*

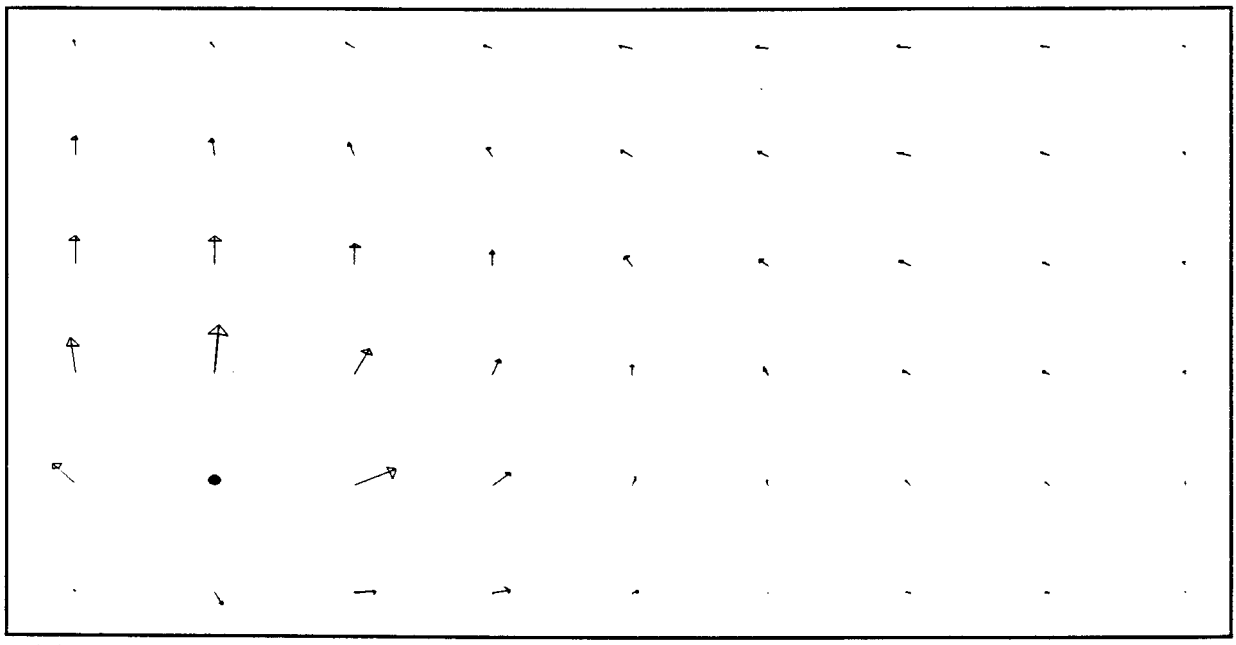

(a) *Real component. Maximum value = 0.286 A*

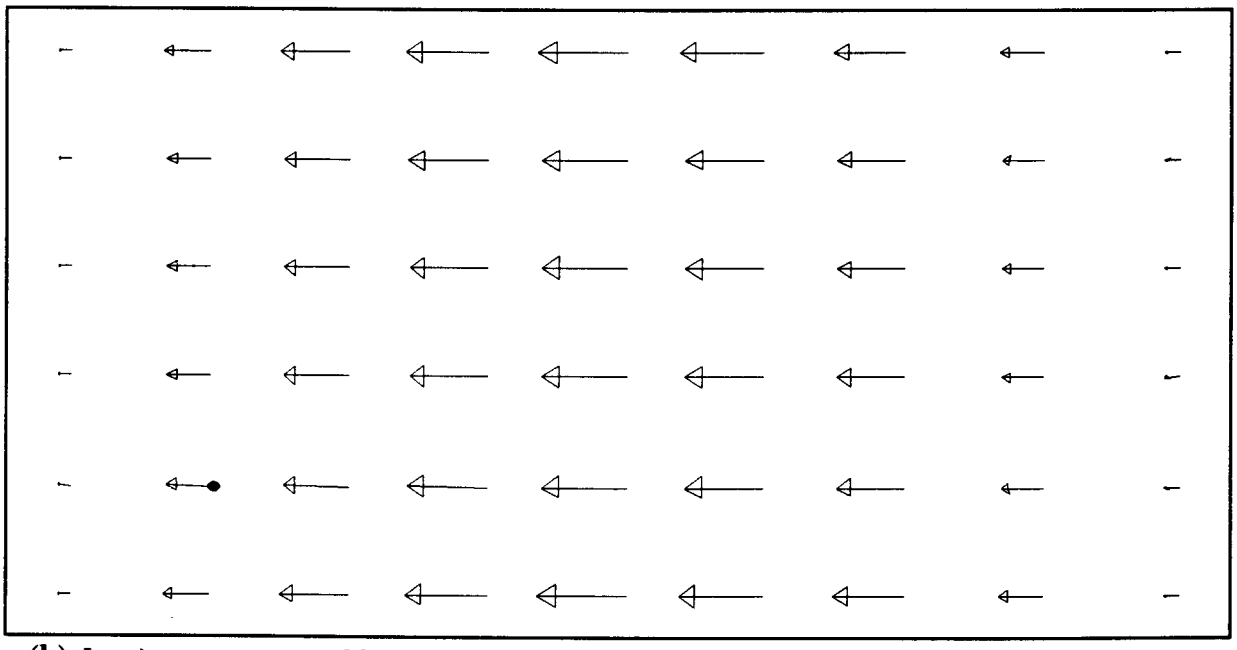

(b) *Imaginary component. Maximum value = 4.240 A*

Figure 4.2 *Real and imaginary parts of the surface currents on a coaxial-fed microstrip patch at 1.210 GHz*

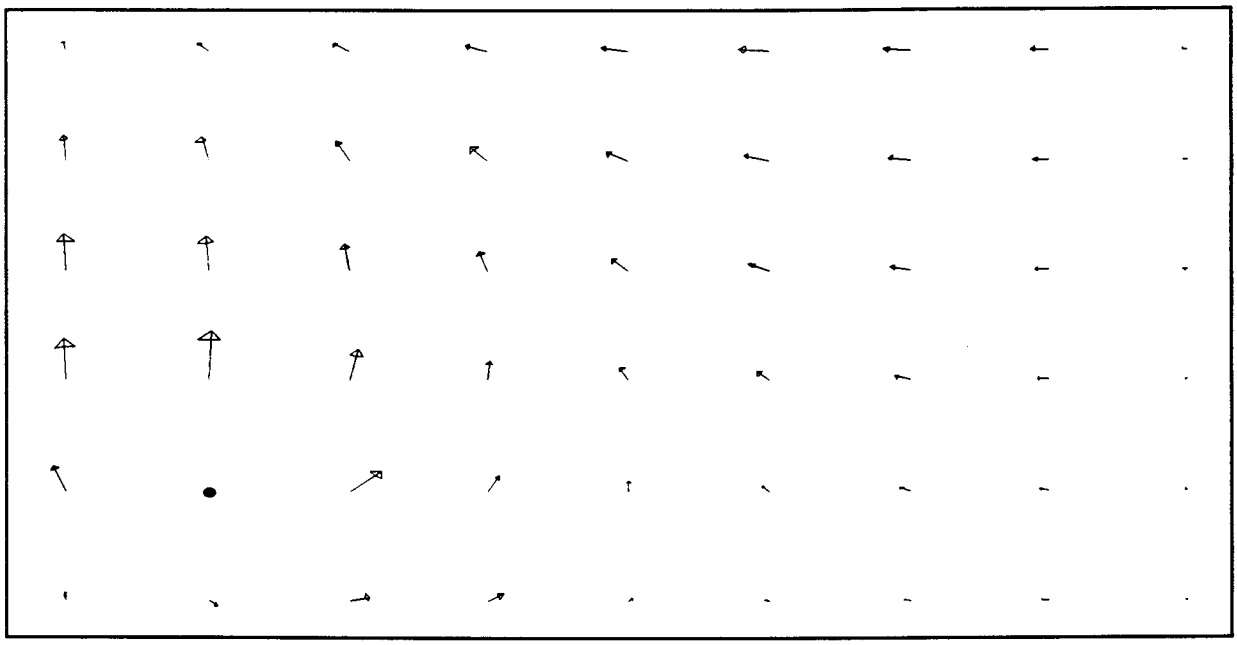

(a) *Real component. Maximum value = 0.421 A*

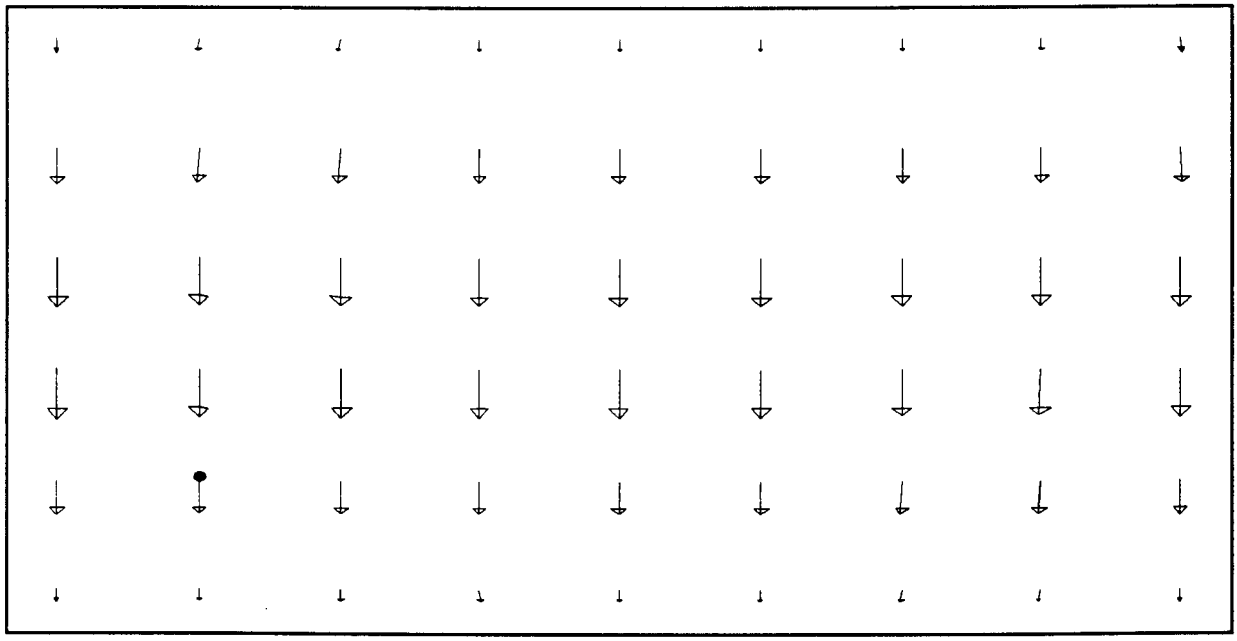

(b) *Imaginary component. Maximum value = 1.799 A*

Figure 4.3 *Real and imaginary parts of the surface currents on a coaxial-fed microstrip patch at 1.793 GHz*

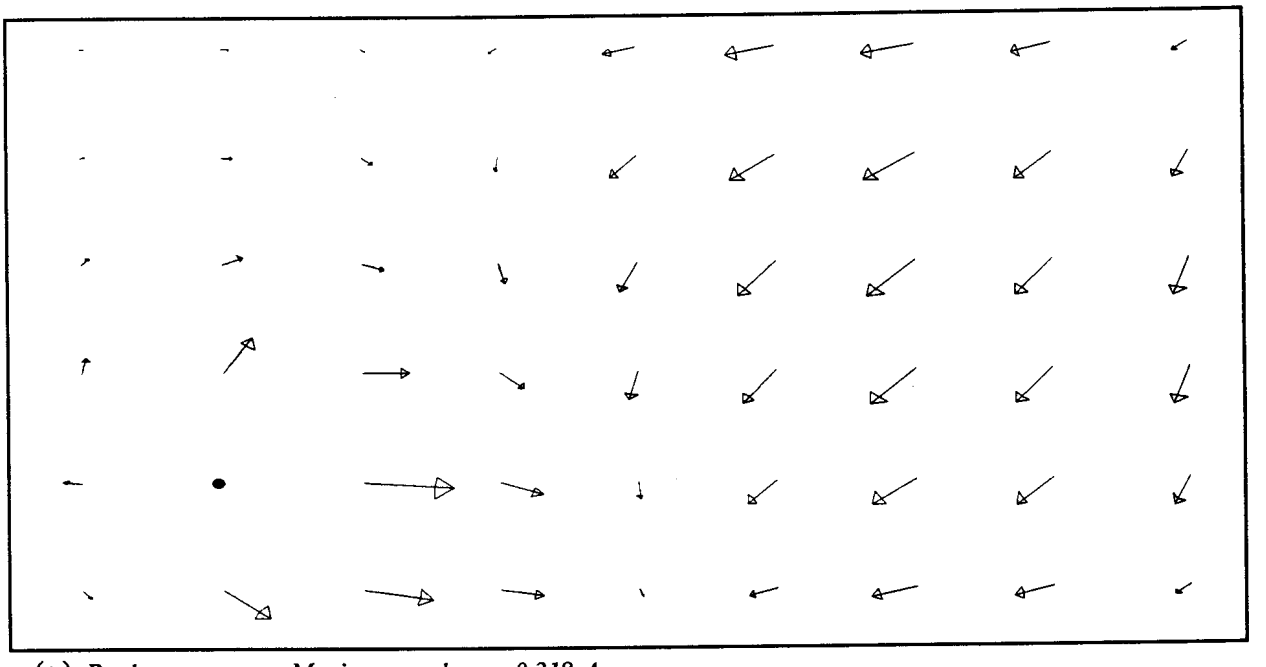

(a) *Real component. Maximum value = 0.318 A*

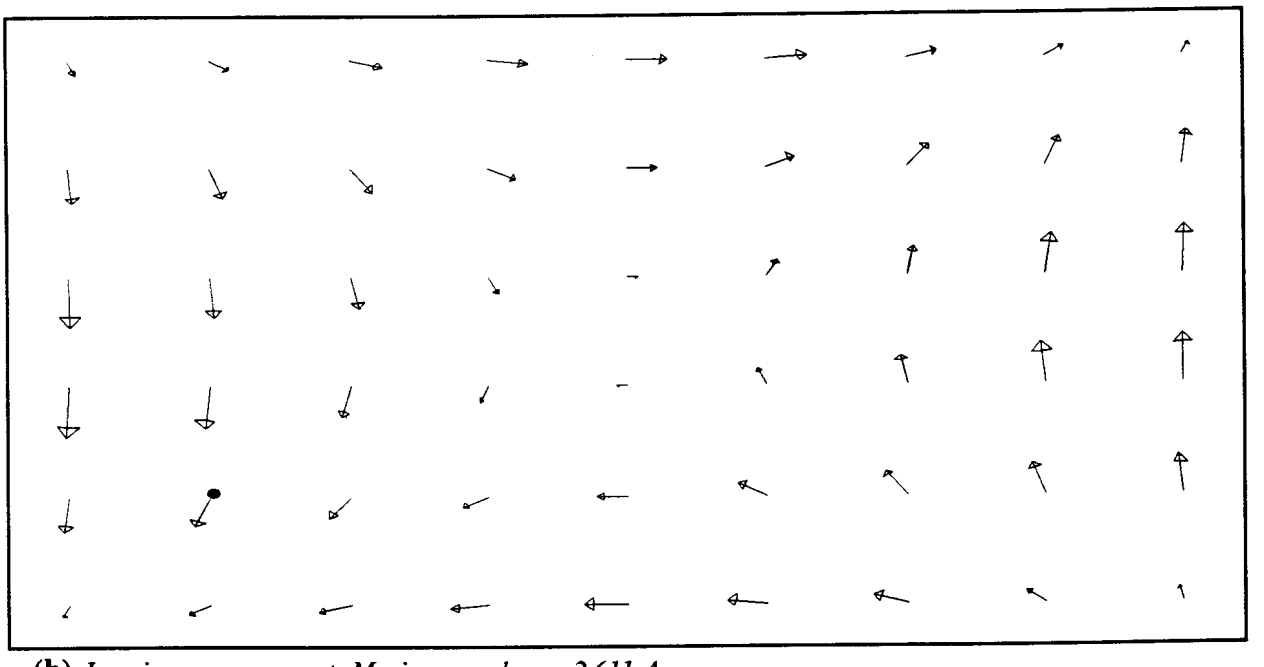

(b) *Imaginary component. Maximum value = 2.611 A*

Figure 4.4 *Real and imaginary parts of the surface currents on a coaxial-fed microstrip patch at 2.1876 GHz*

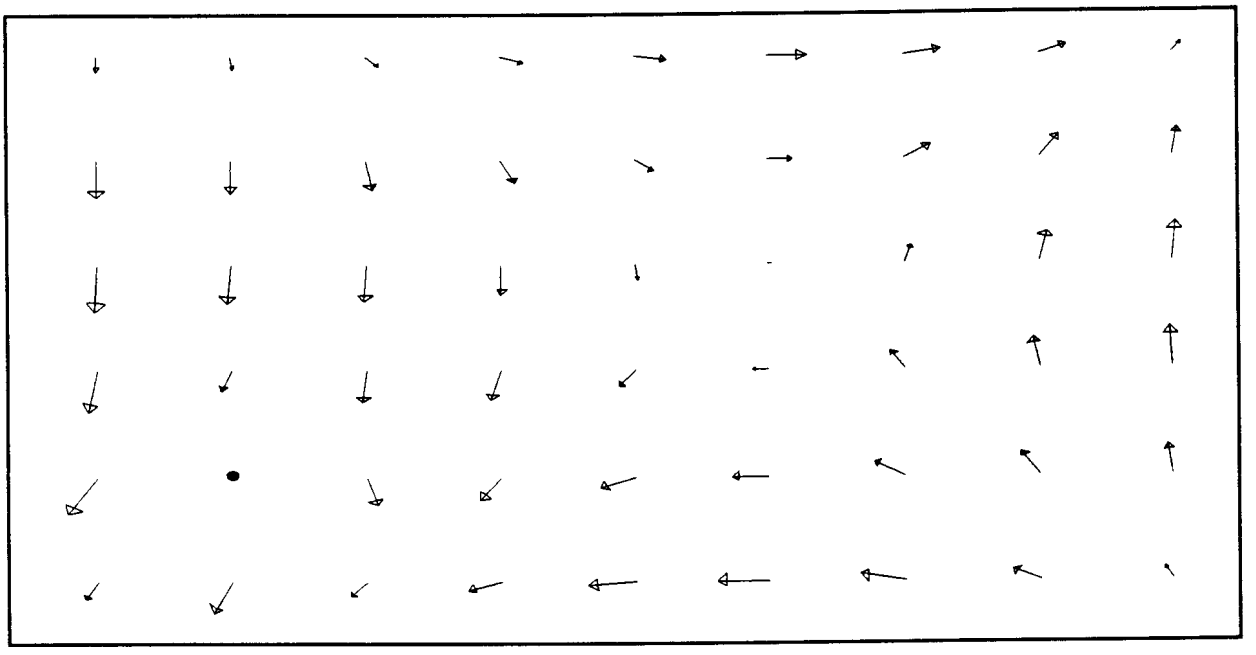

(a) *Real component. Maximum value = 0.292 A*

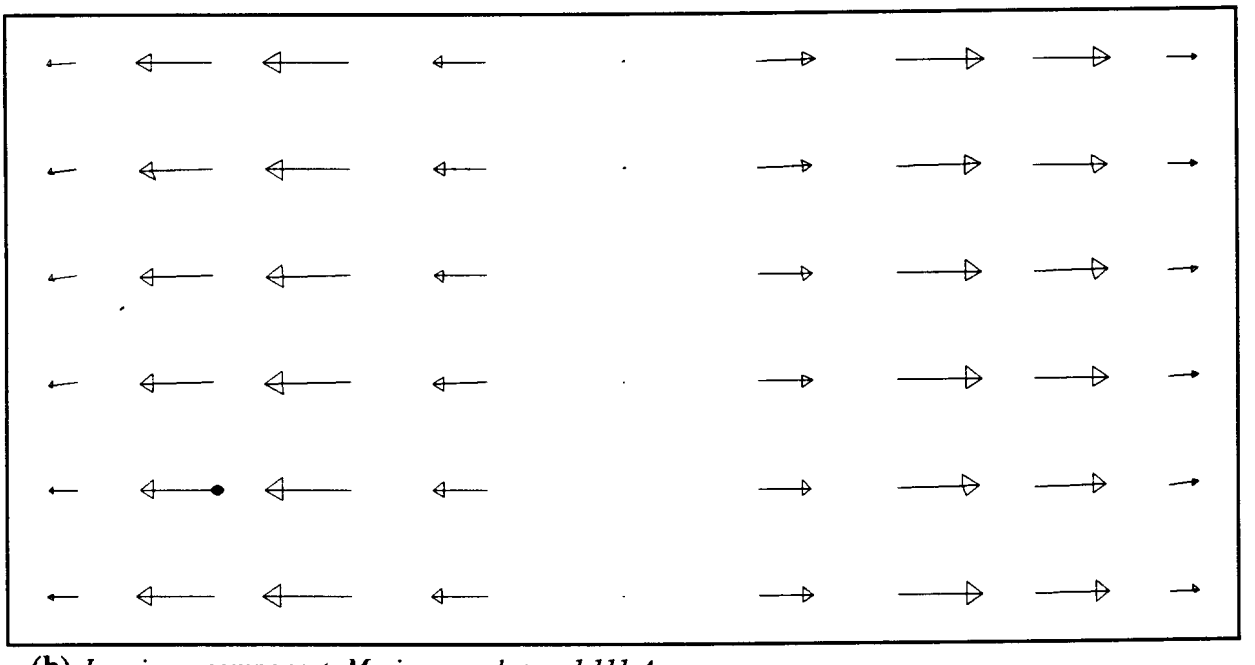

(b) *Imaginary component. Maximum value = 1.111 A*

Figure 4.5 *Real and imaginary parts of the surface currents on a coaxial-fed microstrip patch at 2.398 GHz*

4.3 THEORETICAL RESULTS FOR ETCHED WIRE-GRID ARRAYS

The implemented integral equation formulation is, of course, not restricted to the analysis of patch antennas and is applicable to larger and more complex microstrip structures such as etched wire-grid arrays. The purpose of this section is to examine the behaviour of these brick-wall arrays in order to come to a better understanding of their operation. We will examine current distributions on these structures (the relationship between the actual current distributions on the wire-grid structures and the coefficients which are solved for in the moment method matrix equation, is given in Appendix E) and show the effects on the far-field radiation patterns. Radiation patterns are determined directly from computed current distributions and are essentially exact, except for finite groundplane effects.

For the purposes of the analysis, the brick-wall arrays will be assumed placed on the xy-plane with x-directed horizontal segments (long segments) and y-directed vertical segments (short segments). Since the vertical segments radiate the dominant vertically polarized electric field, the zy-plane represents the E-plane (ϕ = 90° in Figure 4.6). The H-plane then coincides with the zx-plane (ϕ = 0°). Radiation patterns will be determined in these principal planes[1], as a function of the angle on either side of the z-axis in the appropriate plane. Theoretical results for specific antenna geometries will now be discussed.

[1] We are not restricted to these planes, however.

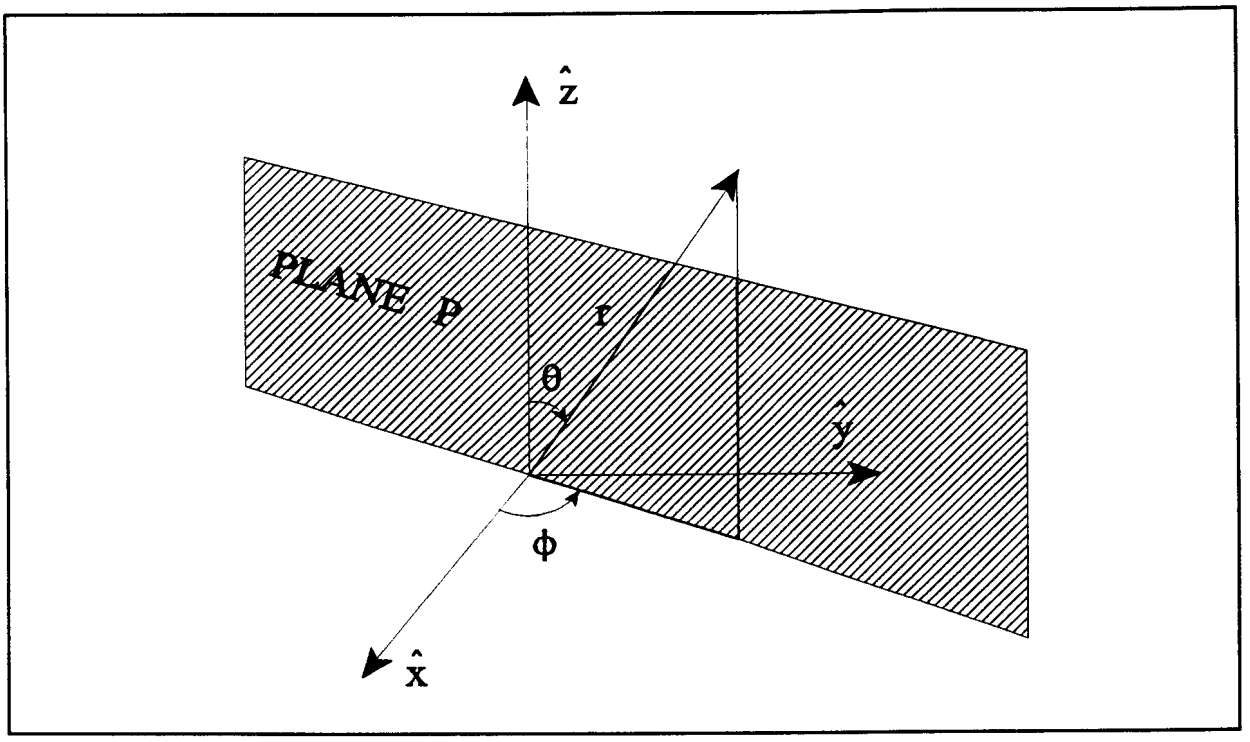

Figure 4.6 *The coordinate system which will be used in the analysis. The zx-plane (zy-plane) represents the H-plane (E-plane).*

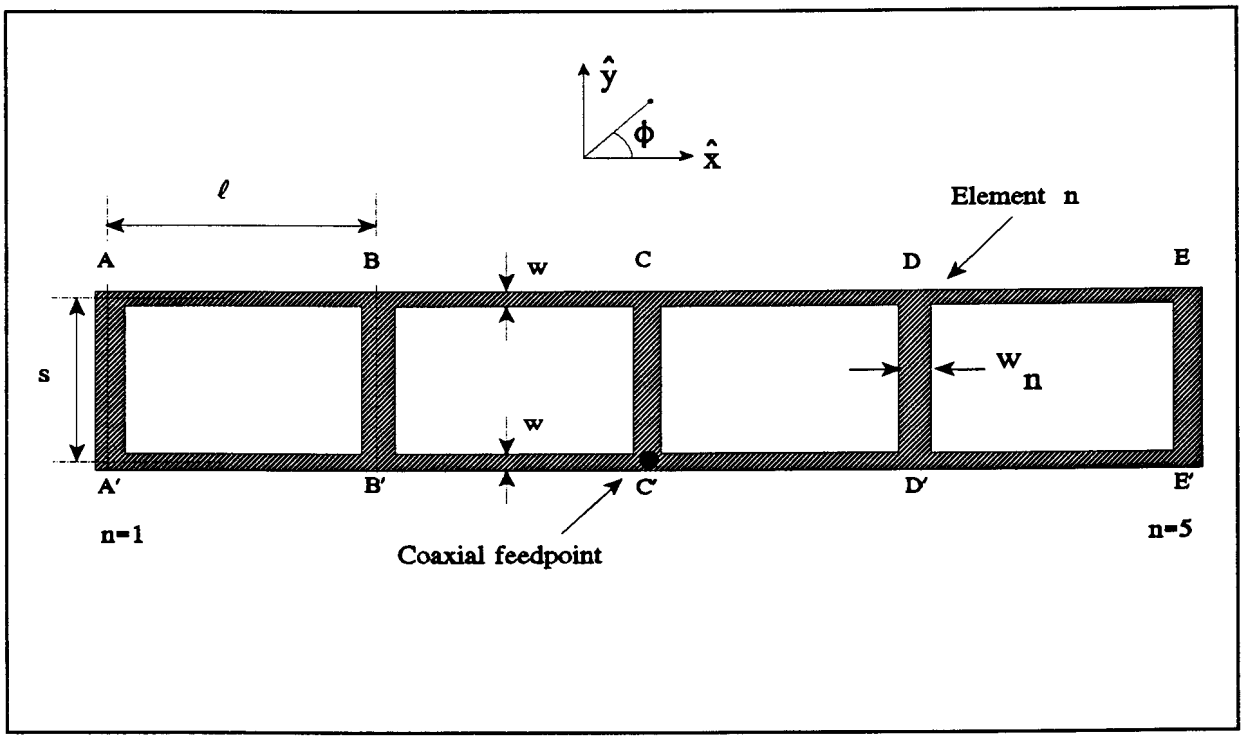

Figure 4.7 *Geometry of a 5-element linear brick-wall array.*

4.3.1 A 5-element uniformly excited linear array

Consider the linear array shown in Figure 4.7 with $\ell = 2s = \lambda_{eff}$ and equal vertical element widths $w_n = \lambda_{eff}/20$ (n=1,2,..5). λ_{eff} is the wavelength at some centre-frequency f_0 in the presence of the dielectric substrate and groundplane. The difficulty in determining λ_{eff} is of course that it is not only a function of ϵ_r, but also of the dielectric substrate thickness, frequency and specific line widths. Let us assume, for the moment, that we do not have access to a rigorous numerical method such as this one. We would then have to consider an approximation for λ_{eff} (ℓ), design and fabricate the antenna, measure the performance and redesign until optimum performance is obtained. This *trial-and-error* method may become time-consuming and expensive. To illustrate this, suppose we were to design and fabricate a 5-element linear brick-wall array with an approximate value for ℓ obtained by assuming $\lambda_{eff} \approx \lambda_0/\sqrt{\epsilon_r'}$ (which assumes the radiators are completely immersed in the dielectric). Use of the numerical method to examine the current distributions along horizontal segments AE and A′E′, as well as along the vertical segments of this structure for a dielectric substrate of thickness 0.8 mm and $\epsilon_r = (4.34, -0.0005)$, at a frequency of 10 GHz, reveals a distribution on the structure as shown in Figure 4.8. Note that this approximation for λ_{eff} does not give the desired 360° phase shift along the horizontal segments. The discontinuities in the current distributions occur at points where the vertical segments are attached to the horizontal ones. For this same case, the currents along the vertical segments are also shown in Figure 4.8.

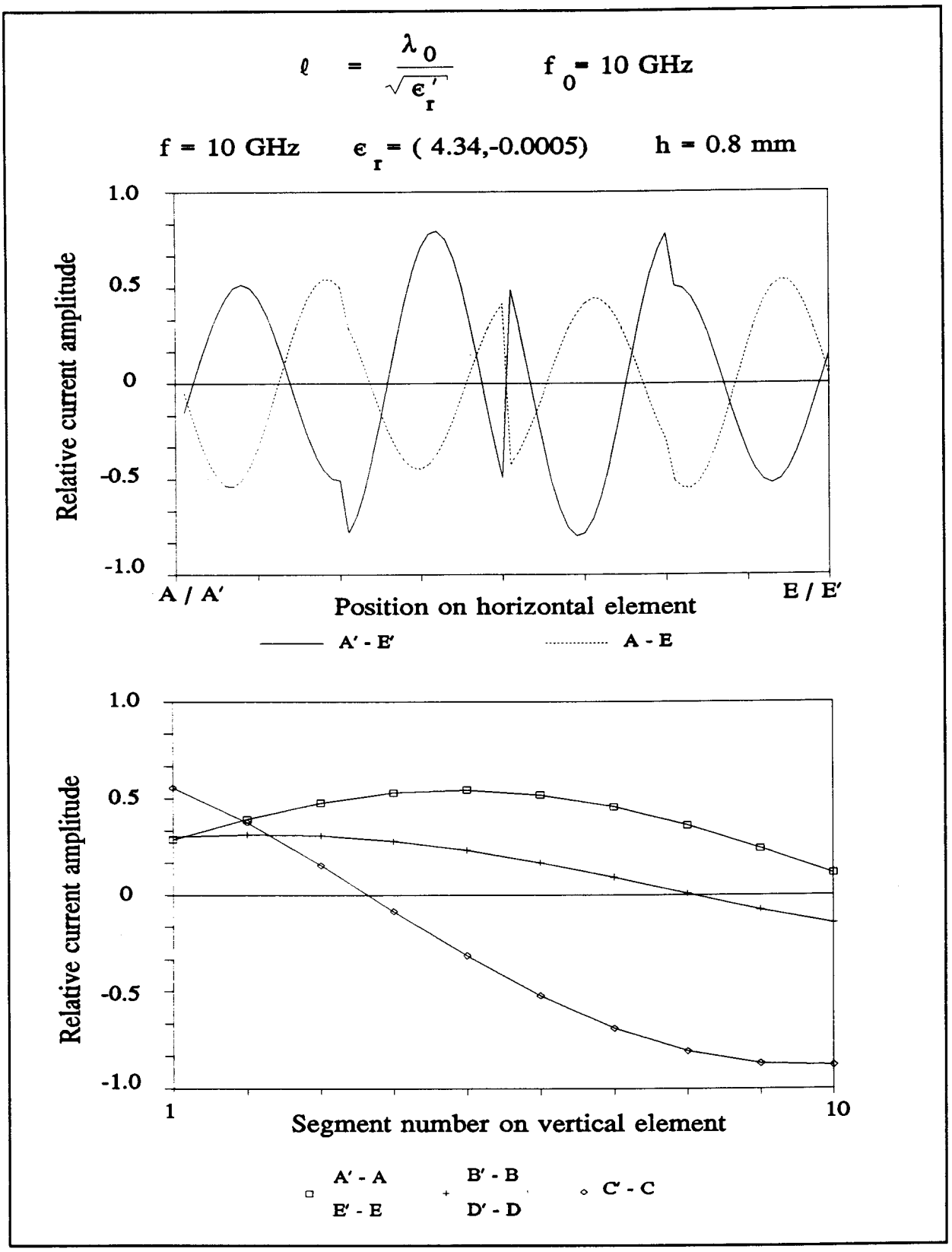

Figure 4.8 *Current distributions on the 5-element equal-segment-width linear array, with the approximation for* λ_{eff}.

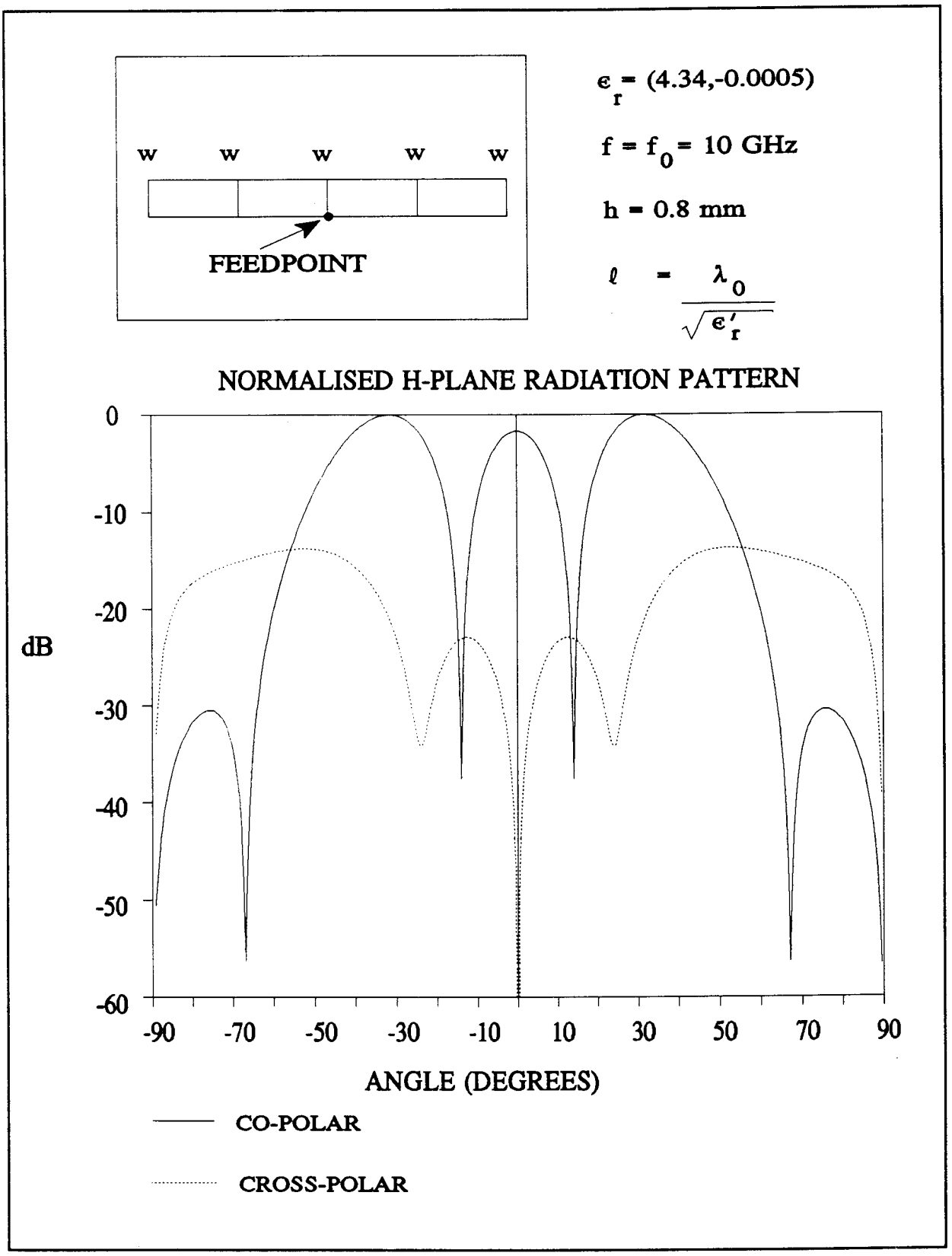

Figure 4.9 *Normalised H-plane radiation patterns for the 5-element array which was designed using the approximation for* ℓ

Note that due to structural symmetry, the currents on A′A would be the same as that on E′E; similarly for B′B and D′D. Despite the fact that the vertical elements have equal widths, their current amplitudes differ. This is due to the incorrect selection of ℓ. For these currents, the normalised H-plane radiation patterns are shown in Figure 4.9. It can be seen that this approximation for ℓ does not give a desired radiation pattern and another approximation has to be considered. If we had in fact fabricated the antenna, it would probably not have fulfilled our requirements. However, using an implementation of the rigorous integral-equation formulation, we can examine the performance of this antenna *before* fabrication. We therefore alter ℓ (λ_{eff}) and use the computer code to examine current distributions until they are as shown in Figure 4.10. This amounts to a value for λ_{eff} of 1.19 $\lambda_0/\sqrt{\epsilon_r'}$. (In this same way, values for λ_{eff} related to specific geometries will henceforth be determined.) We can now define a quantity, ϵ_{eff}, so that $\lambda_{eff} = \lambda_0/\sqrt{\epsilon_{eff}}$ where λ_0 is the free space wavelength. ϵ_{eff} is an effective relative dielectric constant accounting for the fact that the radiators are on the air-dielectric interface of the microstrip structure. $\epsilon_{eff} = 1.552$ for the present case, for which $\epsilon_r' = 2.2$. The horizontal currents now provide the correct "phasing" to the vertical elements and the latter have essentially equal amplitudes due to their equal widths. From Figure 4.10 we can also see that the currents along horizontal segments AE and A′E′ are equal in amplitude but 180 degrees out of phase. For this reason, radiation due to these currents interfere destructively in the far-field over a sector broadside to the array, the effectiveness thereof determining the cross-polarization levels over the main beam. The

associated normalised H-plane radiation patterns for the 5-element brick-wall are shown in Figure 4.11, with a beamwidth between first nulls (BWFN) of some 40° and a side lobe level of -13 dB, which is to be expected from a uniformly excited linear array. The cross-polarization level is below -55 dB for much of the main beam and below -40 dB throughout.

From Figure 4.10 we notice that (with the feedpoint at C′) when the horizontal currents provide the correct phasing to the vertical elements, there is a current minimum at the feedpoint. This implies a relatively high input impedance. We therefore next examine the effect on the radiation patterns of moving the feedpoint to an existing current maximum. The radiation patterns for this structure with a feedpoint moved $\lambda_{eff}/4$ along a horizontal segment, are shown in Figure 4.12. These radiation patterns, with rather high levels of cross-polarization, are highly undesirable. It was found that by moving the feedpoint the current distributions on the structure are disturbed to such an extent that the structure can no longer be considered resonant. A manifestation thereof can be seen in the radiation patterns shown in Figure 4.12.

One of the reasons for wanting to utilise these brick-wall arrays, is to obtain relatively broadband behaviour. In this regard, we examine the behaviour of this specific 5-element linear array over the frequency band 9 (f_l) to 11 GHz (f_u). H-plane radiation patterns at different frequencies in this band were determined and are shown in Figures 4.13 and 4.14. According to [34], an antenna is defined as broadband if the impedance and radiation patterns do not change significantly over about an octave ($f_u/f_l = 2$) or more; clearly from a radiation pattern

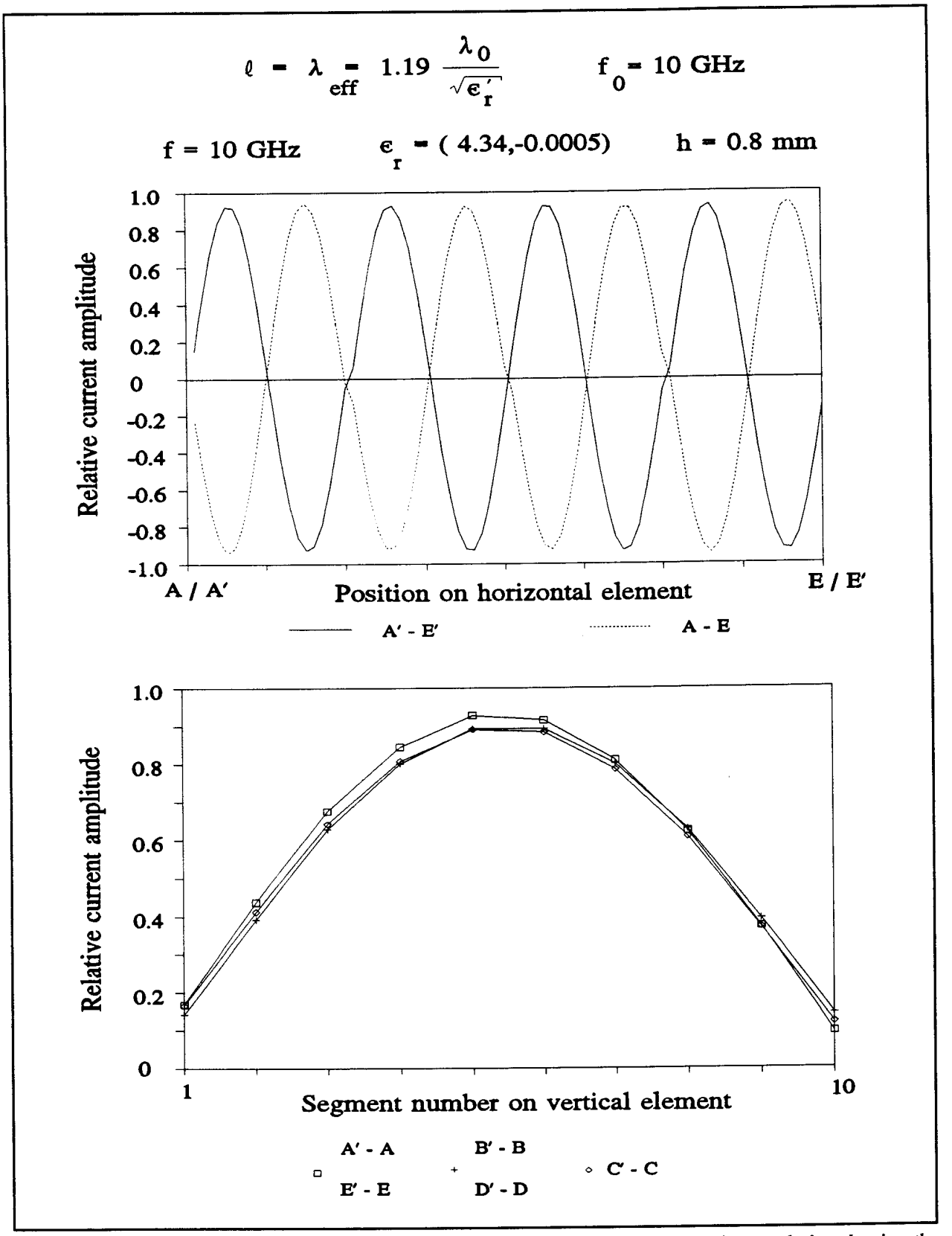

Figure 4.10 *Current distributions on the 5-element linear brick-wall array which was designed using the numerical analysis method.*

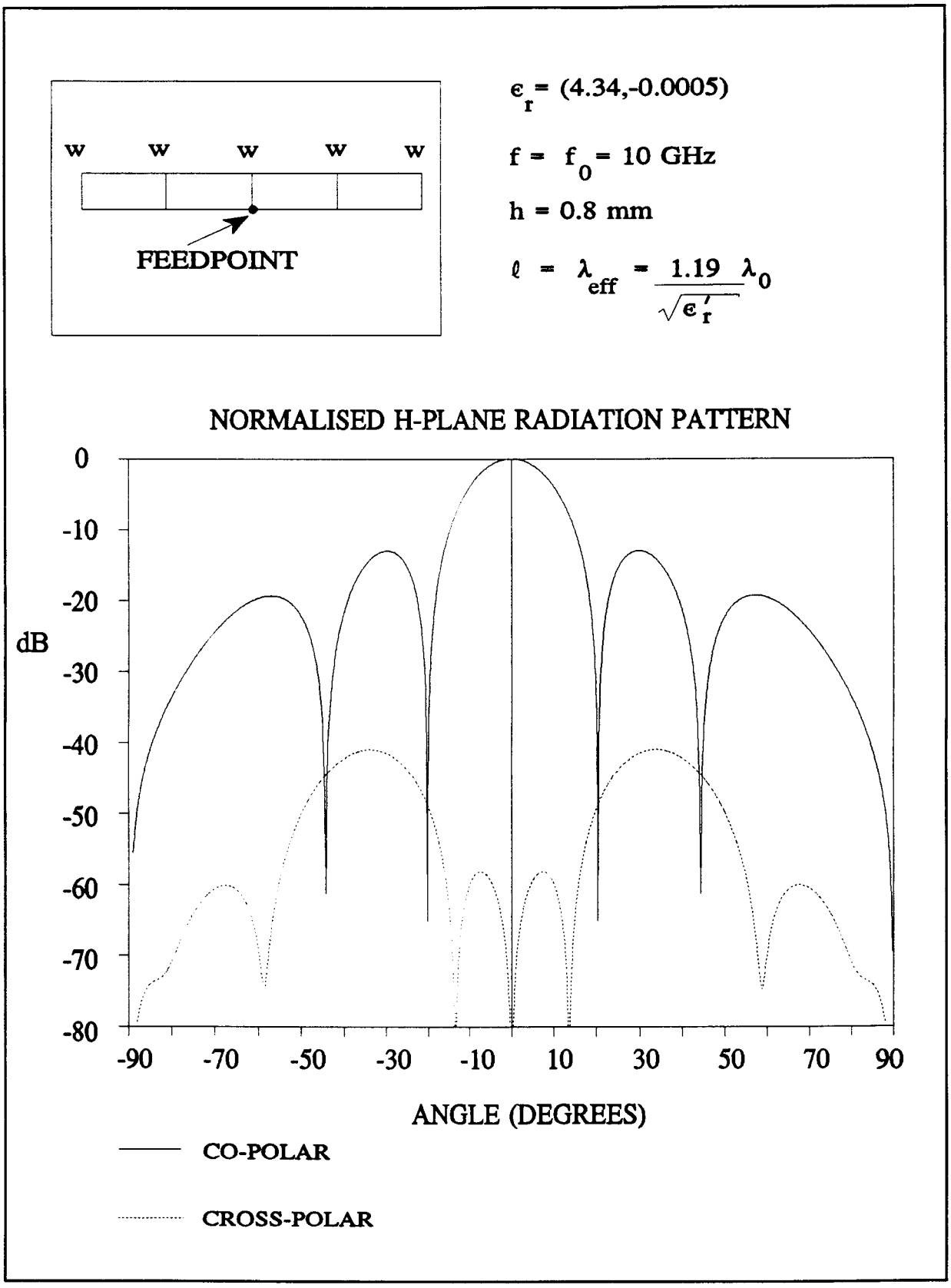

Figure 4.11 *Normalised radiation patterns for the optimized 5-element linear brick-wall array.*

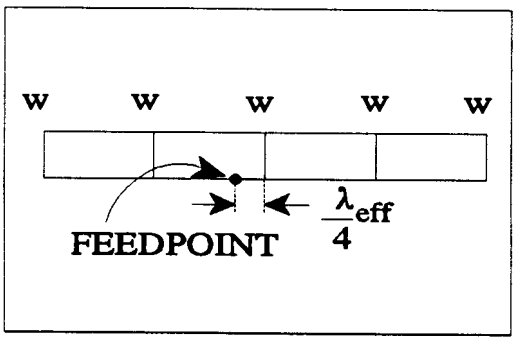

$\epsilon_r = (4.34, -0.0005)$

$f = f_0 = 10$ GHz

$h = 0.8$ mm

$\ell = \frac{1.19\ \lambda_0}{\sqrt{\epsilon'_r}}$

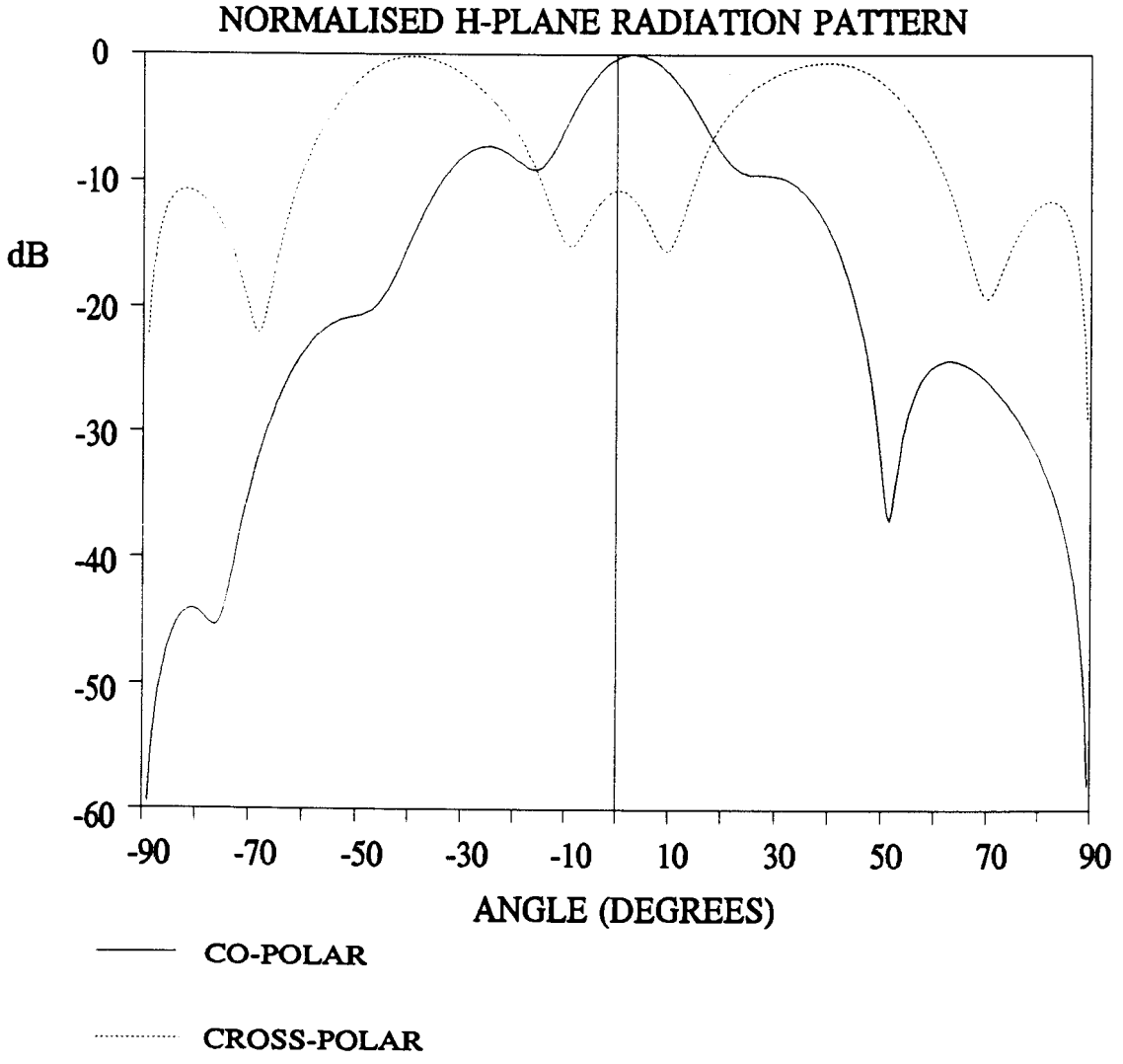

Figure 4.12 *Radiation patterns for the 5-element linear brick-wall array, with the feedpoint moved to a position where a feedpoint at C′ yielded a current maximum.*

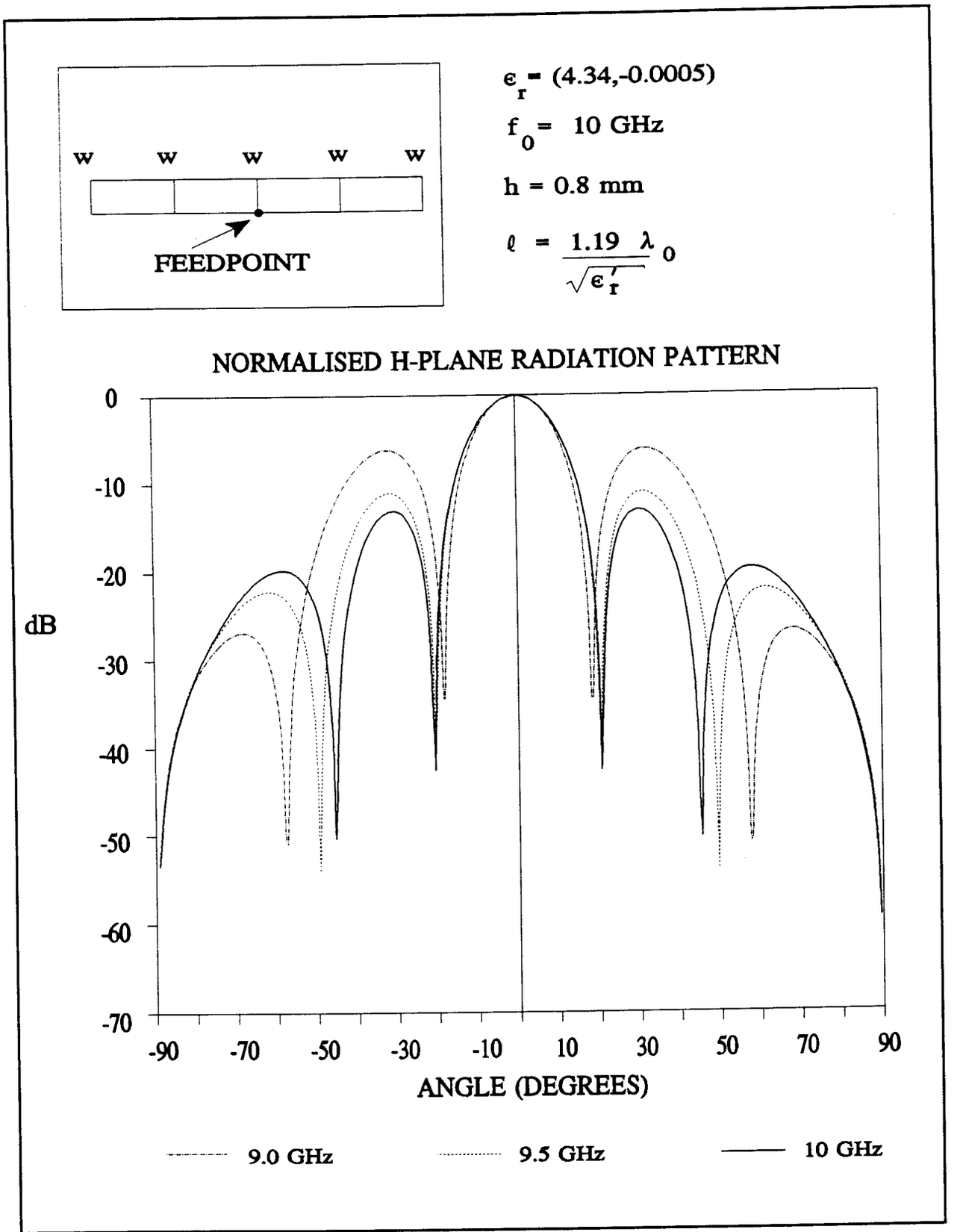

Figure 4.13 *Normalised H-plane radiation patterns for the 5-element linear array at 9, 9.5 and 10 GHz. This array was designed for a centre-frequency of 10 GHz.*

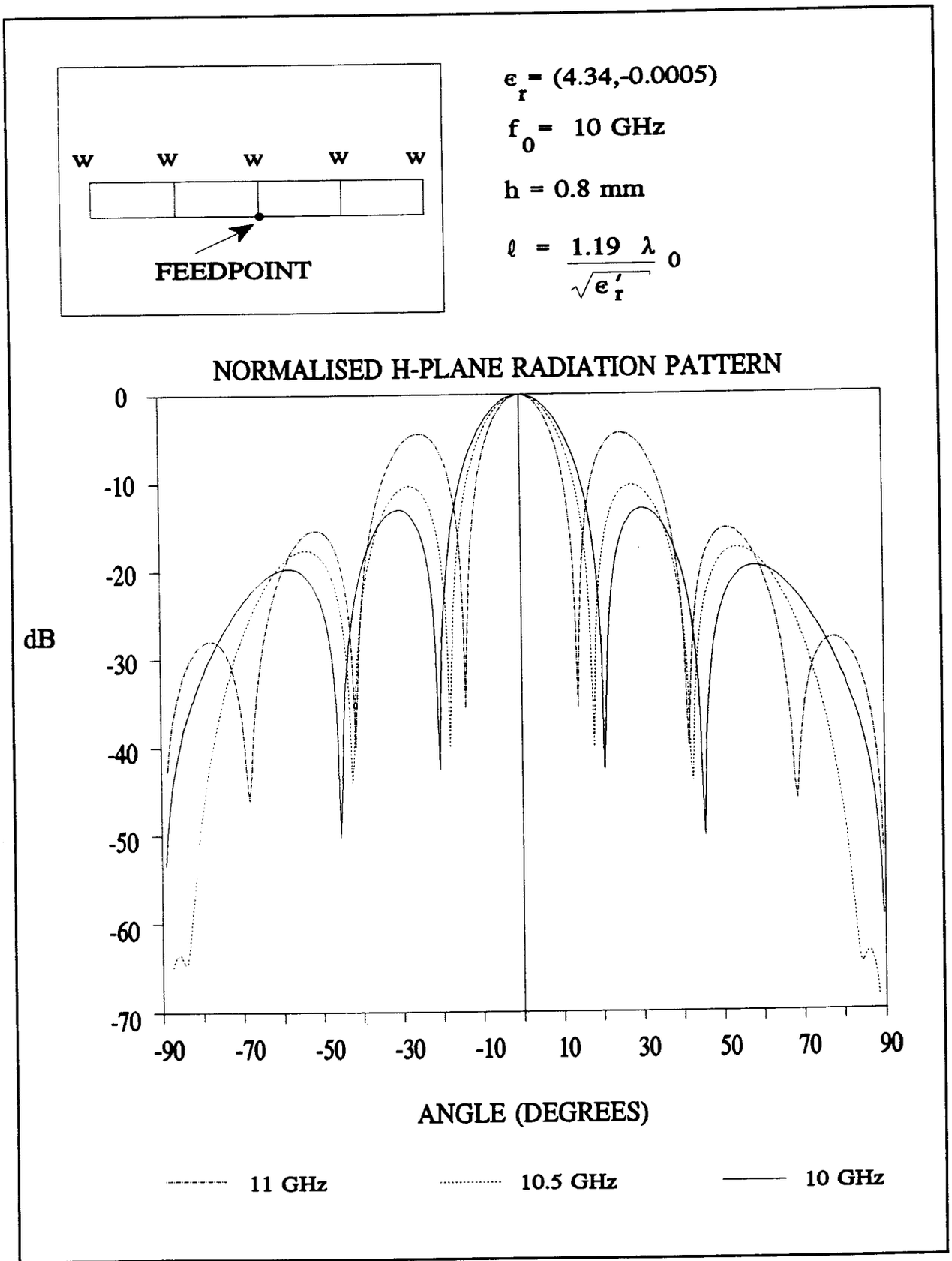

Figure 4.14 *Normalised H-plane radiation patterns for the 5-element linear array at 10, 10.5 and 11 GHz.*

viewpoint alone this specific structure cannot be considered broadband according to the above definition. However, with typical bandwidths of 6 to 12% [35], these arrays could well be considered *relatively broadband* [35] ones, especially when compared to the other structures in the menu of microstrip antennas.

4.3.2 A 7-element uniformly excited linear array

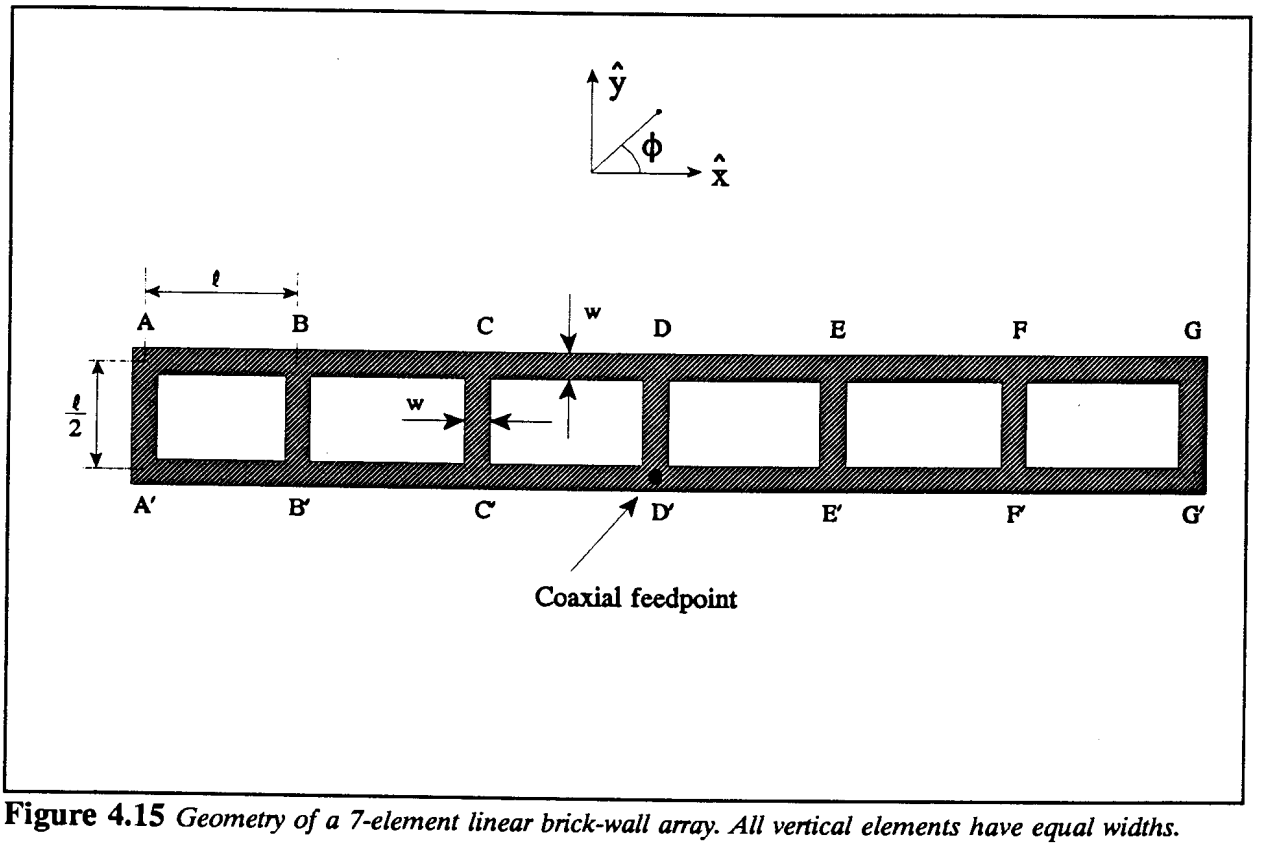

Figure 4.15 *Geometry of a 7-element linear brick-wall array. All vertical elements have equal widths.*

The BWFN for the 5-element linear array was found to be 40°. From array theory [34] we know that this beamwidth may be reduced by increasing the number of (vertical) elements. Consider now, for the same material parameters as in the previous example, the 7-element linear array shown in Figure 4.15. As was the case for the 5-element array, all segments have equal widths of $\lambda_{eff}/20$.

Using numerical experimentation a resonant structure was designed for which the current distributions are shown in Figure 4.16. In this case, $\lambda_{eff} = 1.195\ \lambda_0/\sqrt{\epsilon_r'}$ (in other words, the effective relative dielectric constant for this case is 1.541). Once again, the horizontal currents provide the correct phasing to the vertical elements, and the latter have essentially equal amplitudes, due to their equal widths. Normalised radiation patterns for this structure in both principal planes are shown in Figures 4.17 and 4.18. In the H-plane we now have a BWFN of some 30° and an increased number of side lobes. The side lobe level is still at -13 dB with predicted cross-polarized radiation below the -47 dB level (-60 dB over the main beam). In the E-plane, radiation is strongly affected by the groundplane and is similar to that for a rectangular microstrip patch antenna [2].

Up to this point we have only been able to attain side lobe levels of -13 dB. This is the lowest that can be achieved from uniformly excited linear arrays. From array theory [34], however, we know that the side lobe level of a linear antenna array may be reduced by introducing amplitude tapering in the element excitations. In some arrays, however, this requires a complex, and hence expensive, feeding network. On the other hand, the element excitations of these etched brick-wall arrays may be varied by simply varying the widths of the vertical elements: the wider the element, the higher the relative current amplitude therein. This is investigated next.

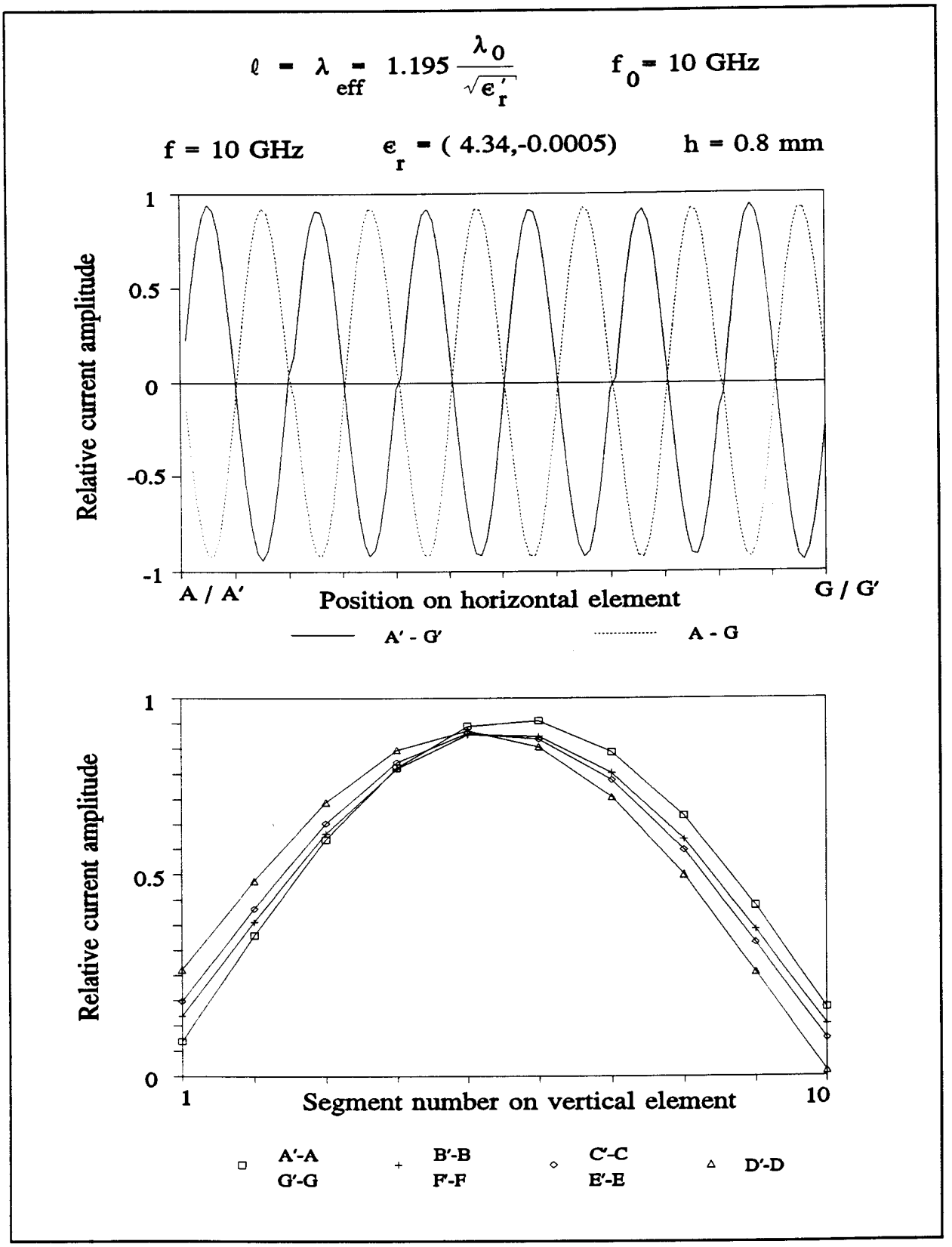

Figure 4.16 *Current distributions on the horizontal and vertical elements of the 7-element linear array discussed in Section 4.3.2.*

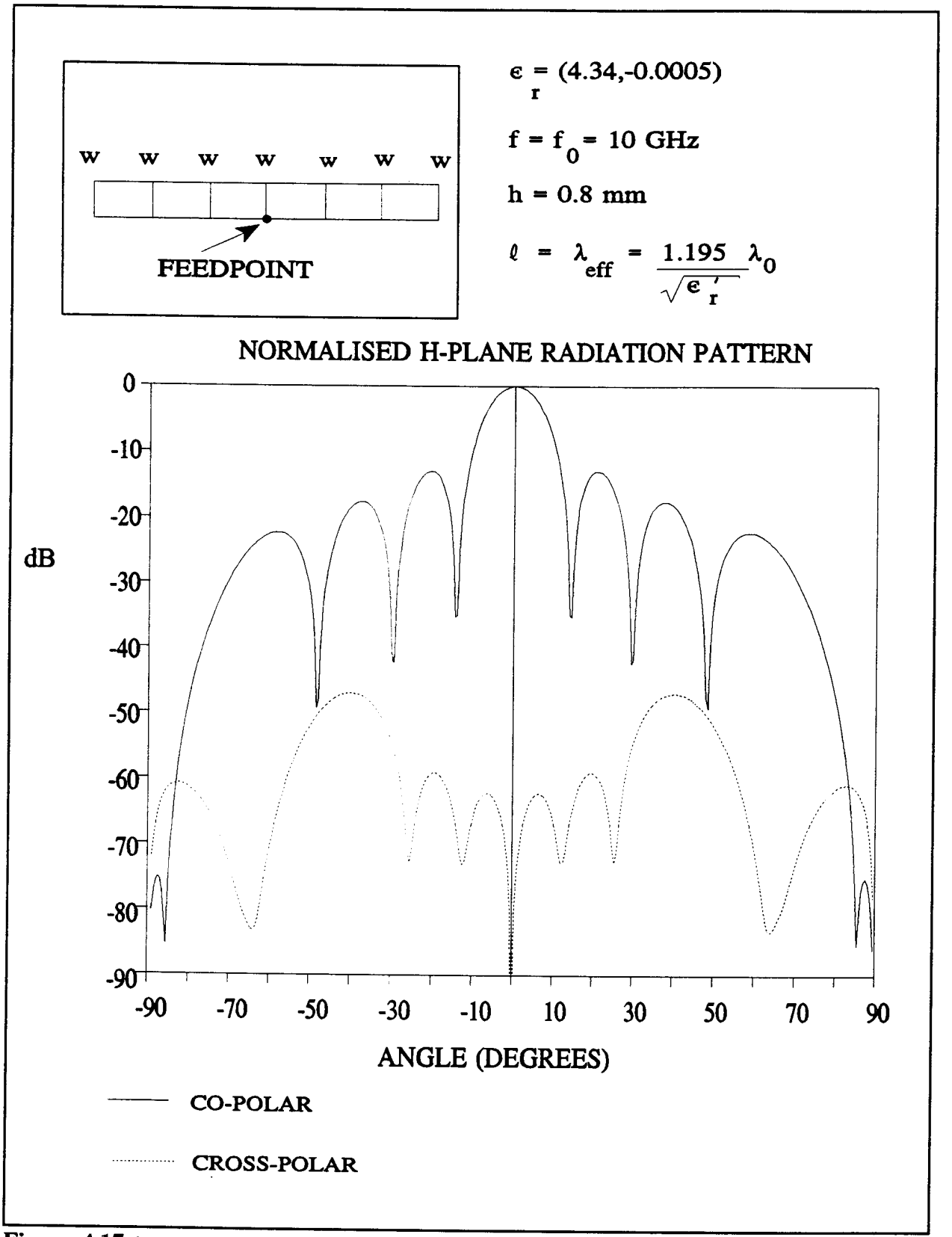

Figure 4.17 *Normalised H-plane radiation patterns for the 7-element linear brick-wall array with material parameters as indicated.*

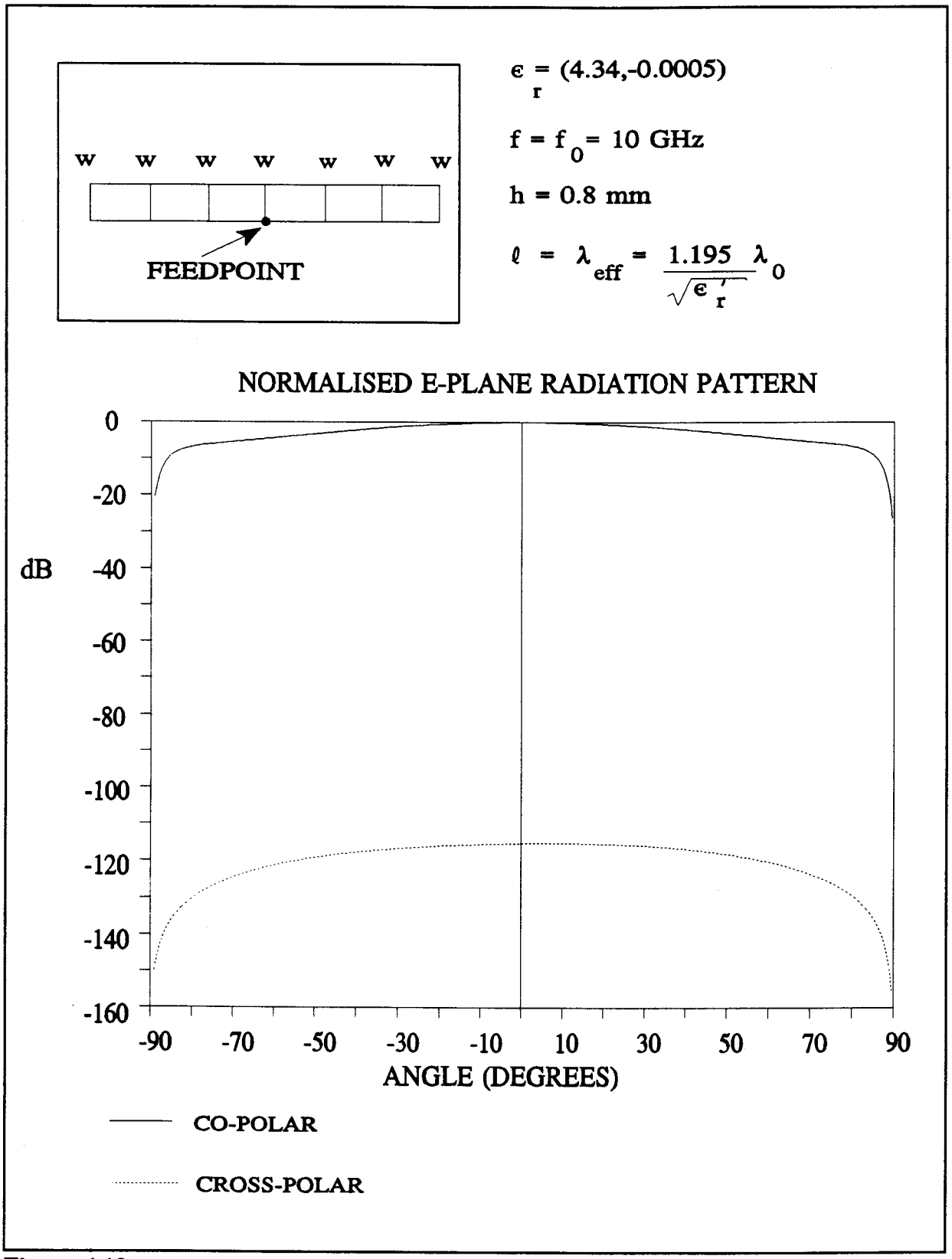

Figure 4.18 *Normalised E-plane radiation patterns for the 7-element linear brick-wall array discussed in Section 4.3.2.*

4.3.3 A 5-element linear tapered brick-wall array

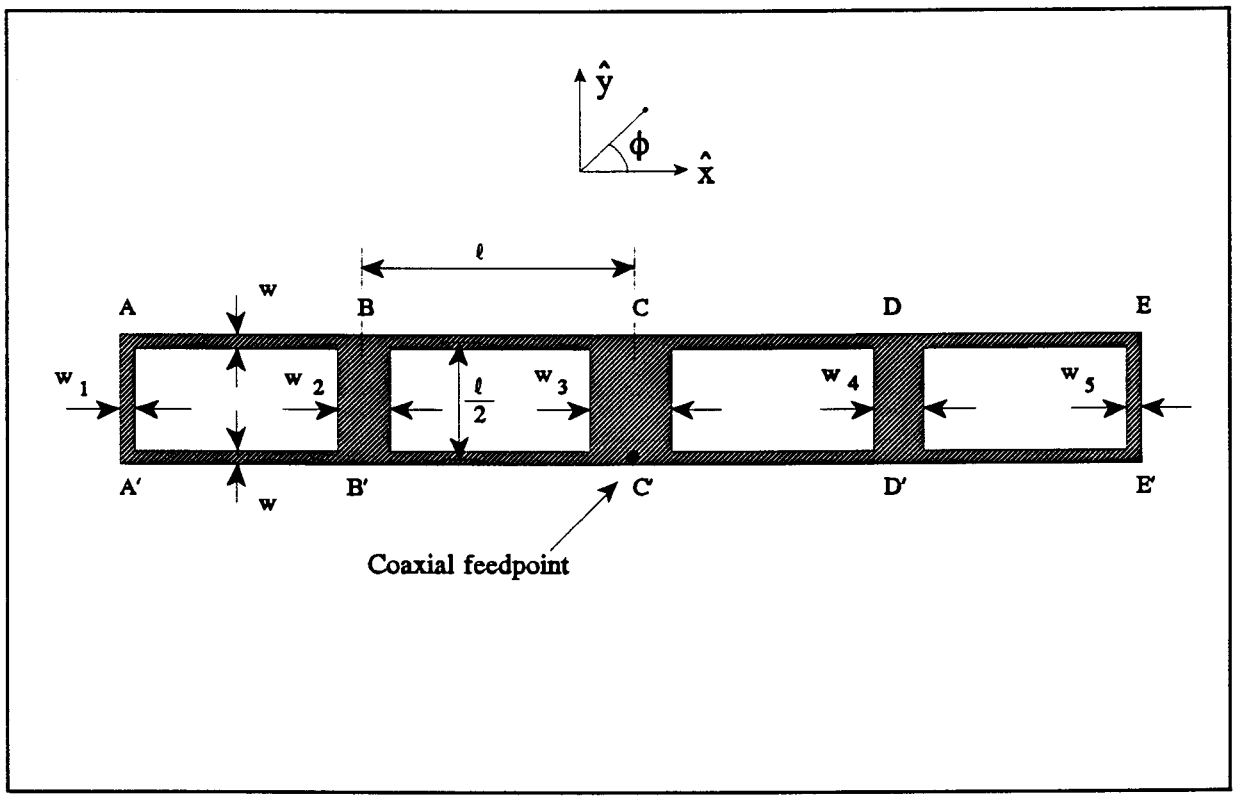

Figure 4.19 *Geometry of a 5-element linear tapered array with segment widths indicated.*

Consider the structure represented in Figure 4.19. This is the geometry of a tapered brick-wall array for which $w_1/w = w_5/w = 1$, $w_2/w = w_4/w = 3$ and $w_3/w = 5$, with w once again equal to $\lambda_{eff}/20$. For this structure the wider vertical elements are expected to have larger current amplitudes. Using numerical experimentation, it was found that $\ell = \lambda_{eff} = 1.12\ \lambda_0/\sqrt{\epsilon_r'}$ yields the expected current distributions (note that this is different from that required for the 5-element uniform-segment-width array of Section 4.3.1). These current distributions are shown in Figure 4.20. For these currents, on the structure represented in Figure 4.19, the H-plane radiation patterns are shown in Figure 4.21. The side lobe level is now at −23 dB: a full 10 dB improvement on the uniformly excited

case. This illustrates the ease with which the side lobe levels of these etched brick-wall arrays may be reduced.

To examine the effects of feedpoint placing on the radiation patterns of these tapered brick-wall arrays, a similar 5-element linear array was analysed. An *existing* array, which had not been designed with the help of the integral equation method, was used for this experiment. Although this antenna was initially designed for a centre-frequency of 10 GHz, measurements showed that the antenna had a minimum in $|S_{11}|$ at 10.37 GHz. For this reason, we also analyse this antenna at 10.37 GHz. Firstly, for the feedpoint at C′ (Figure 4.19), the H-plane radiation patterns are shown in Figure 4.22 (these patterns remind of the radiation patterns which were obtained for the array discussed in Section 4.3.1 using an incorrect value for λ_{eff} (Figure 4.9)). Now, by moving the feedpoint of this same array a distance of $\lambda_{eff}/4$ from C′ towards B′, the radiation patterns are modified to that shown in Figure 4.23. Thus, we have moved from a situation of a local maximum at $\theta = 0°$ to that of a minimum. This seems to suggest that by carefully selecting the feed position, some degree of radiation pattern synthesis might be possible.

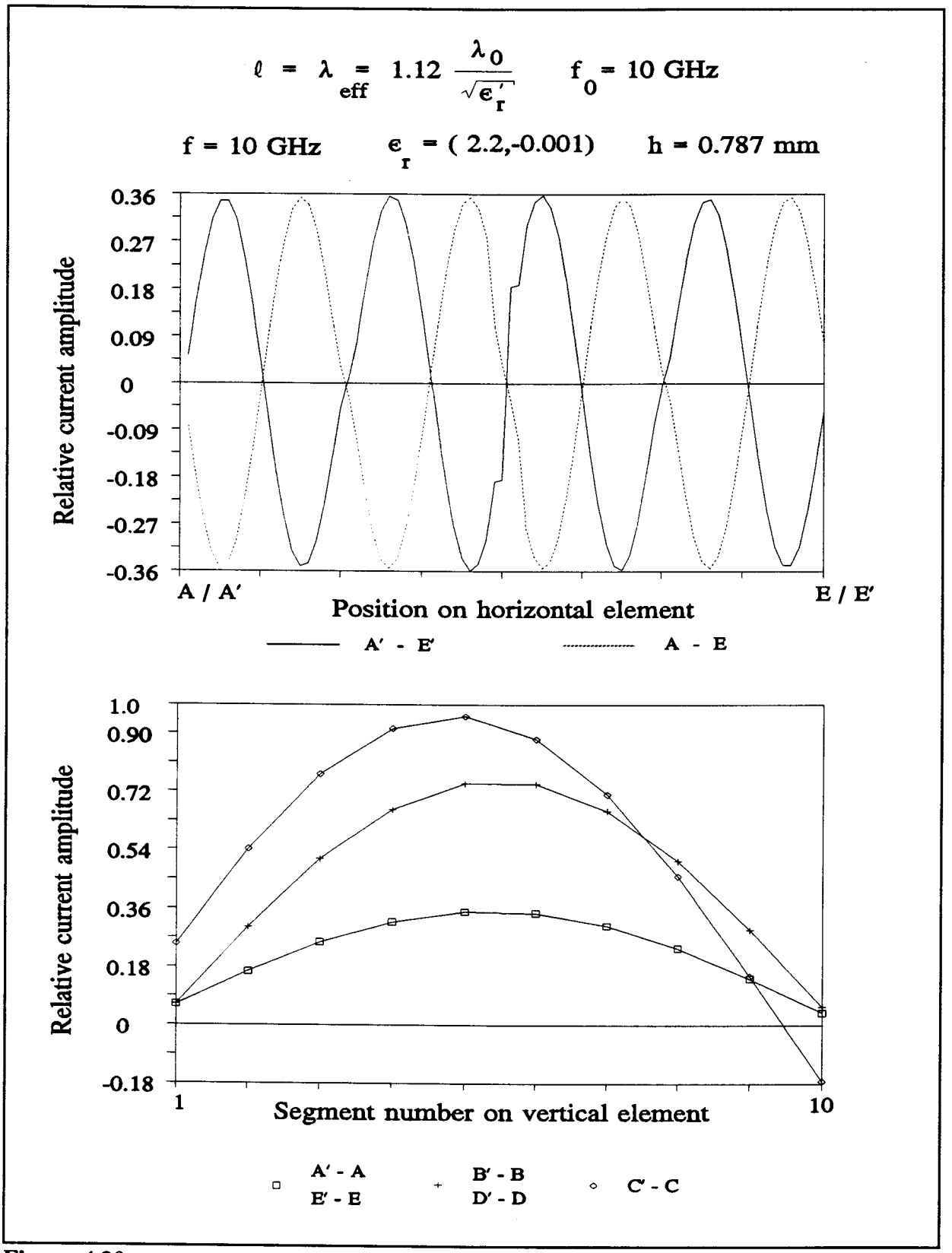

Figure 4.20 *Current distributions on the 5-element tapered brick-wall array discussed in Section 4.3.3 for* $\lambda_{eff} = 1.12\ \lambda_0/\sqrt{\epsilon_r'}$

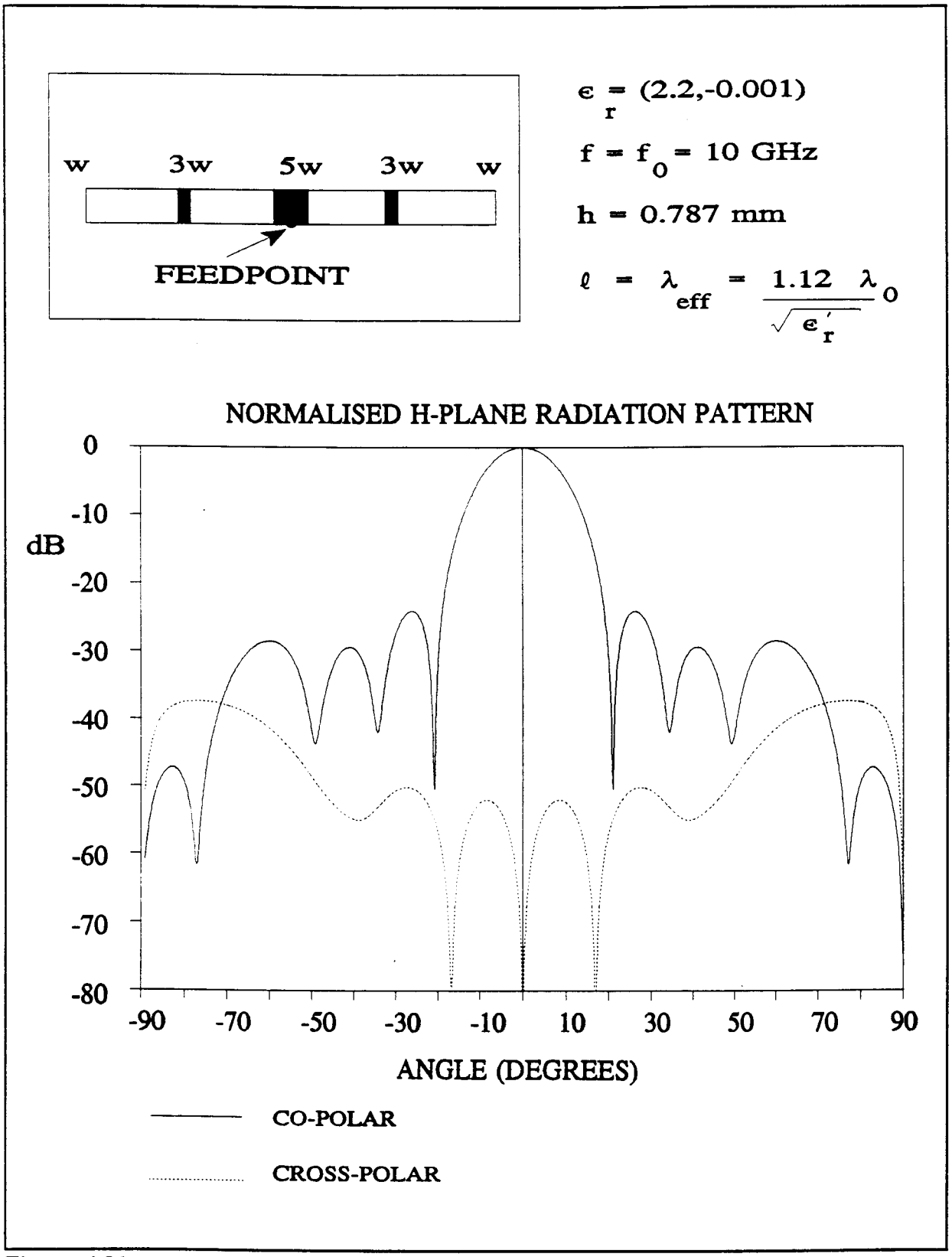

Figure 4.21 *Normalised H-plane cross- and co-polar radiation patterns for the 5-element linear brick-wall array with a 1:3:5:3:1 vertical-element-width taper.*

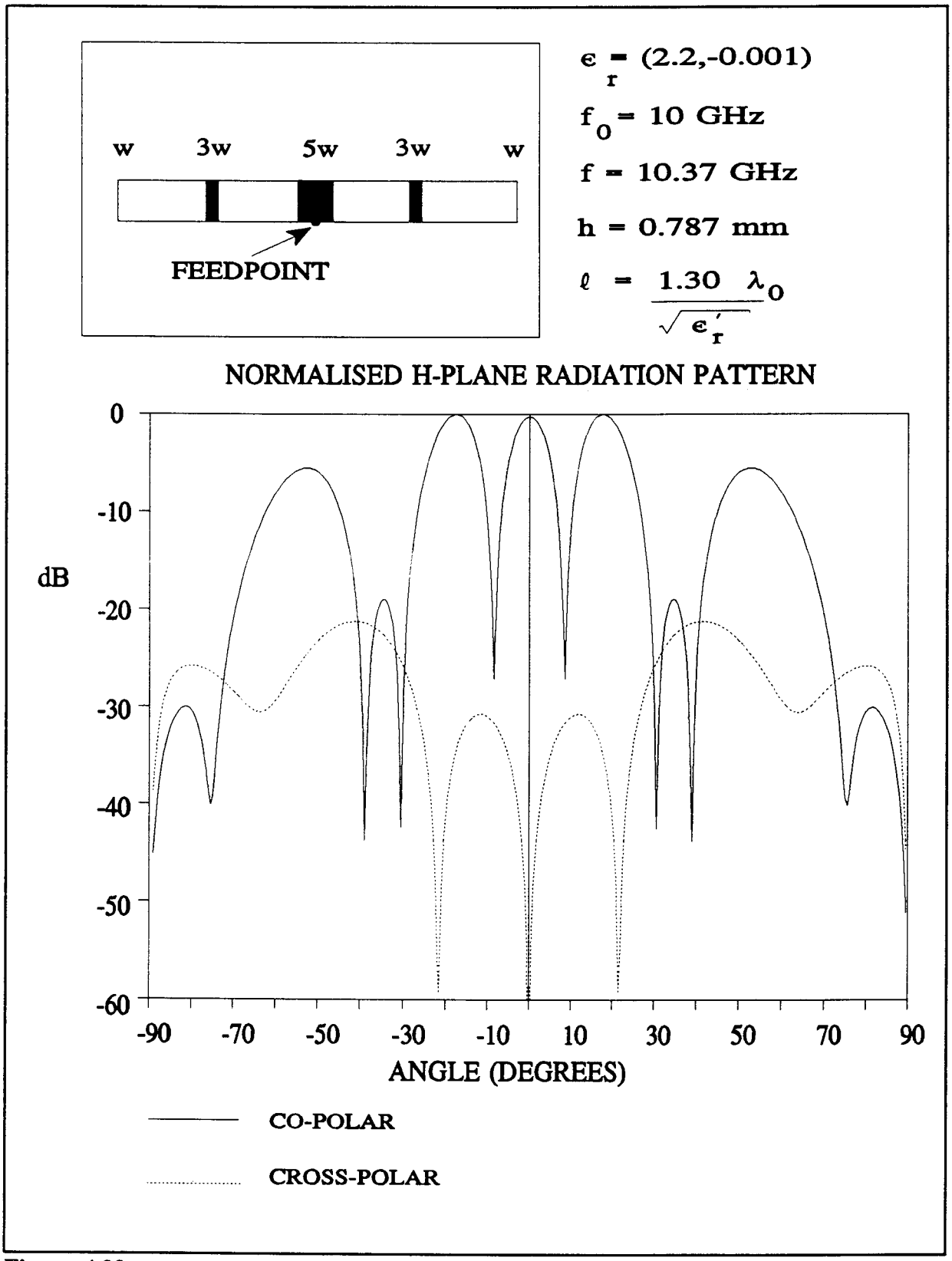

Figure 4.22 *Radiation patterns for the tapered array with an "incorrect" value for ℓ Material and antenna parameters are also indicated. The feedpoint for this case is at C'.*

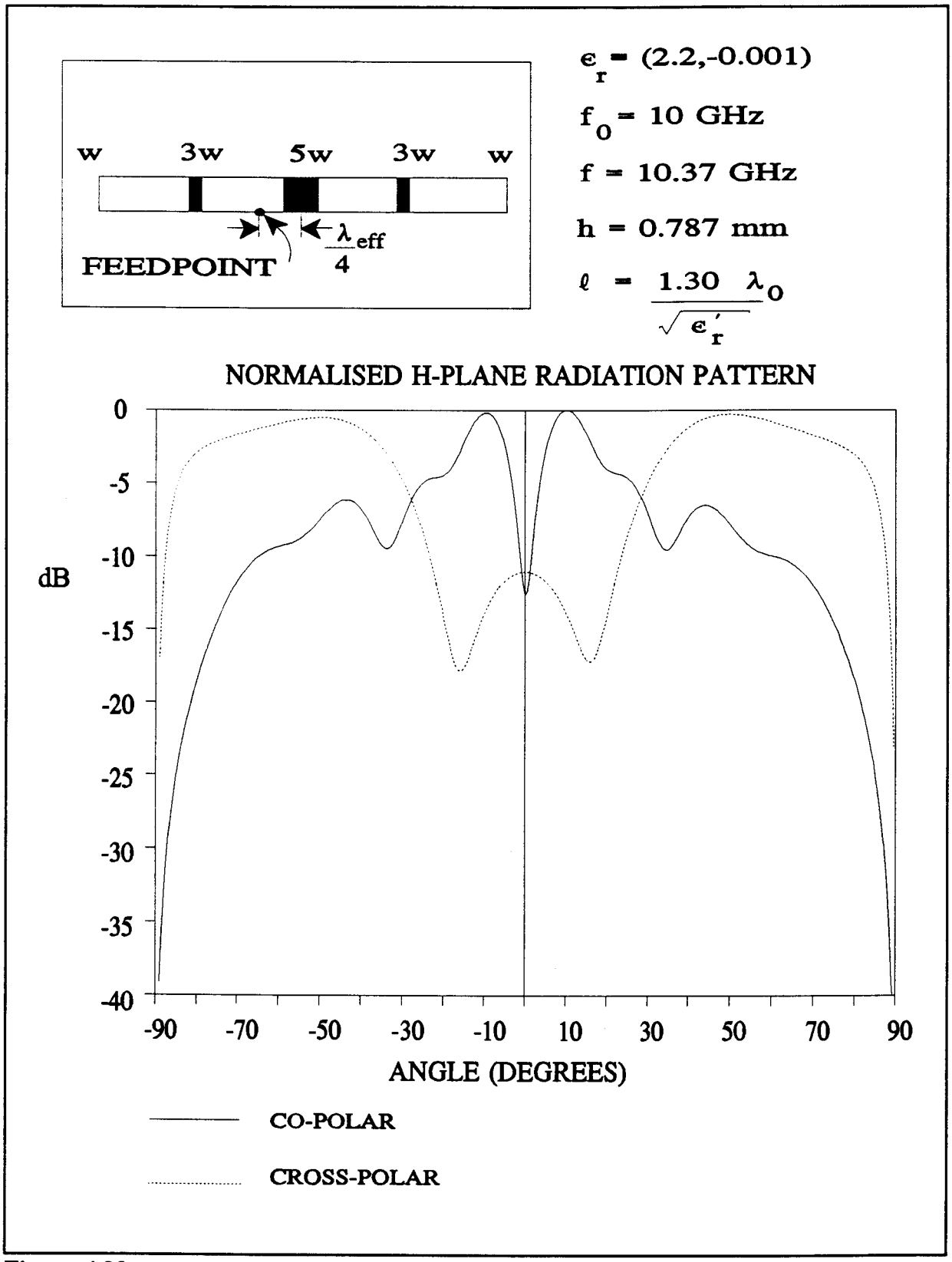

Figure 4.23 *Radiation patterns for the linear tapered array (ℓ = 1.30 $\lambda_0/\sqrt{\epsilon_r'}$) with the feedpoint moved to the position indicated on the insert.*

4.3.4 A 4-level brick-wall array

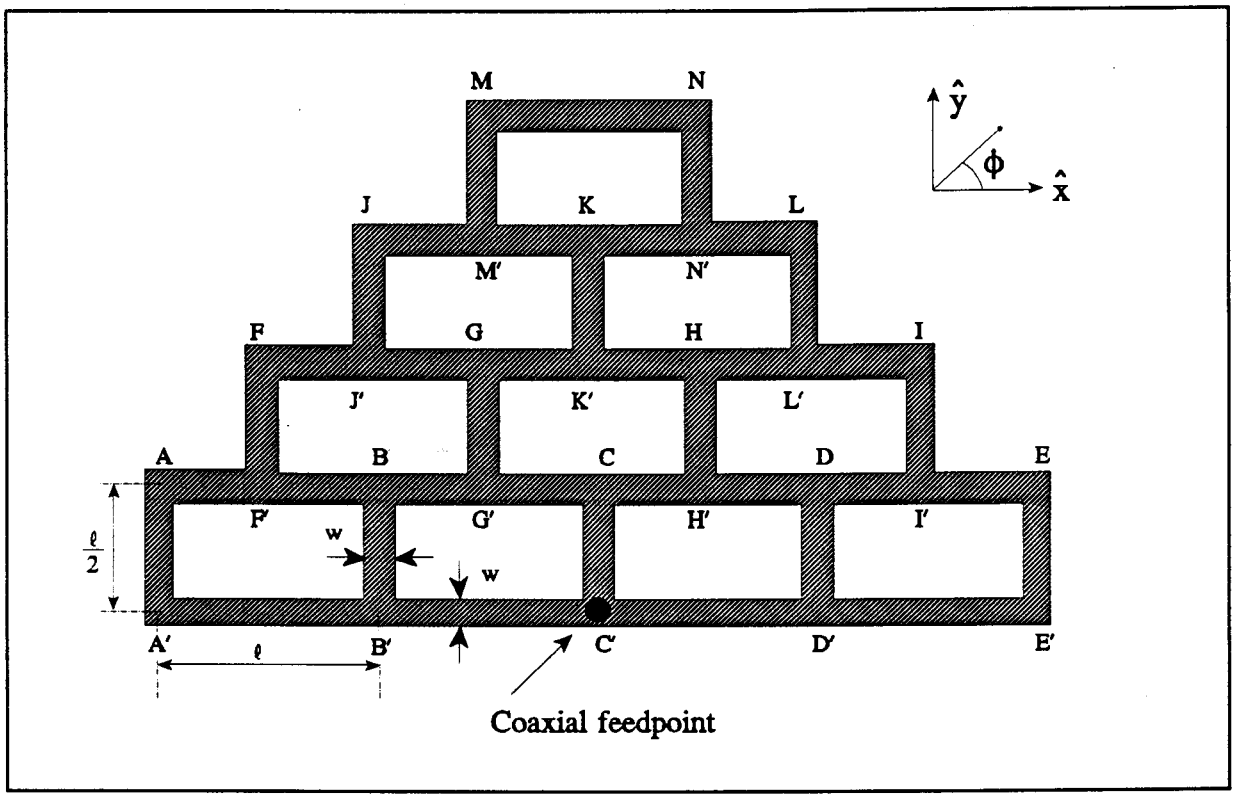

Figure 4.24 *Geometry of a brick-wall array which has been extended in the transverse directions. All segment widths are equal at $\lambda_{eff}/20$. We will refer to this as a "4-level brick-wall array".*

Up to this point, only *linear* brick-wall arrays have been considered. To examine the effects of extending the brick-wall array in the transverse directions, consider the array shown in Figure 4.24. We will refer to this structure as a *4-level brick-wall.* This is simply due to the fact that the physical appearance is that of a brick-wall with 4 levels; it does **not** refer to multiple dielectric layers in the substrate. The structure represented in Figure 4.24 was analysed at 10 GHz for $\epsilon_r = (4.34, -0.0005)$ and h = 0.8 mm. The current distributions on this antenna array are shown in Figures 4.25 and 4.26. The radiation patterns in both principal planes, with these currents, are shown in Figures 4.27 and 4.28. From the H-plane

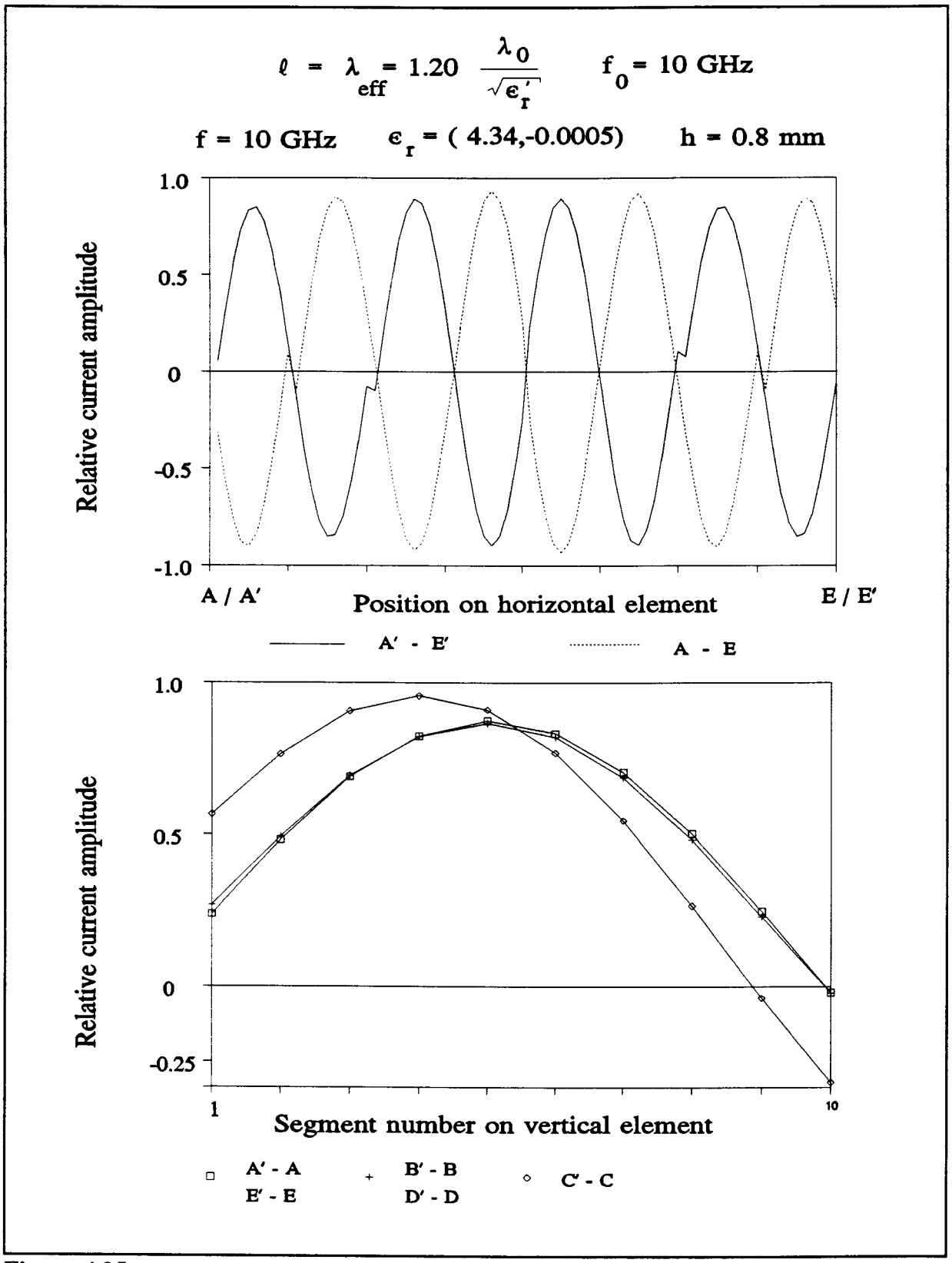

Figure 4.25 *Current distributions on several elements of the 4-level brick-wall array represented in Figure 4.24. The current distributions on the remainder of the array elements are shown in Figure 4.26.*

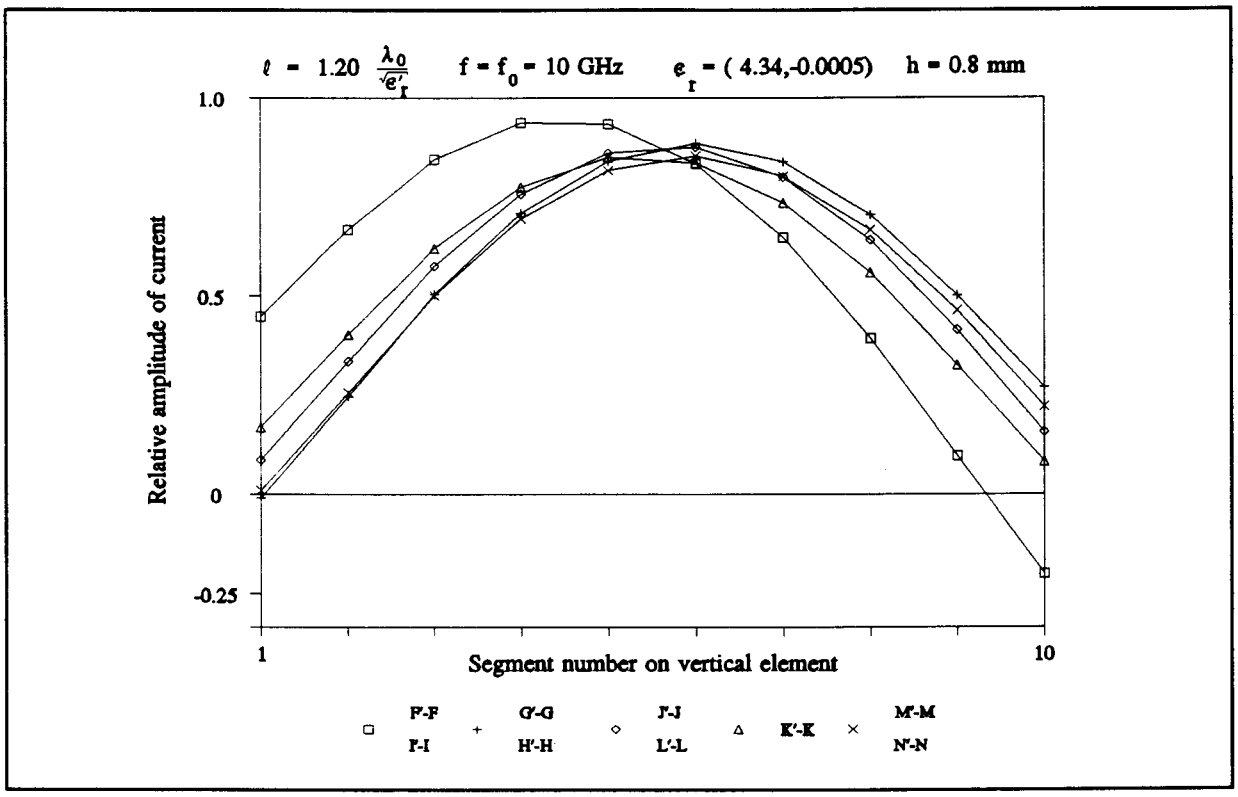

Figure 4.26 *Current distributions on several vertical elements of the 4-level brick-wall array shown in Figure 4.24*

co-polar radiation pattern, it is interesting to note that without having introduced tapering in the vertical element widths, the side lobe level of this array has dropped to -23 dB. This lowering of the sidelobes is due to the fact that the "collapsed distribution" of the array, in the H-plane, is tapered due to the array lattice not being completely filled (such a completely filled case is discussed in Section 4.3.5). The BWFN has also increased from 40° to almost 60° which is the expected beam broadening which accompanies any lowering of sidelobe levels. However, this array exhibits a rather high level of cross-polarization. This is due to the fact that the current distribution on the structure is such that radiation due to the currents on the horizontal segments cancel less effectively in the far-field.

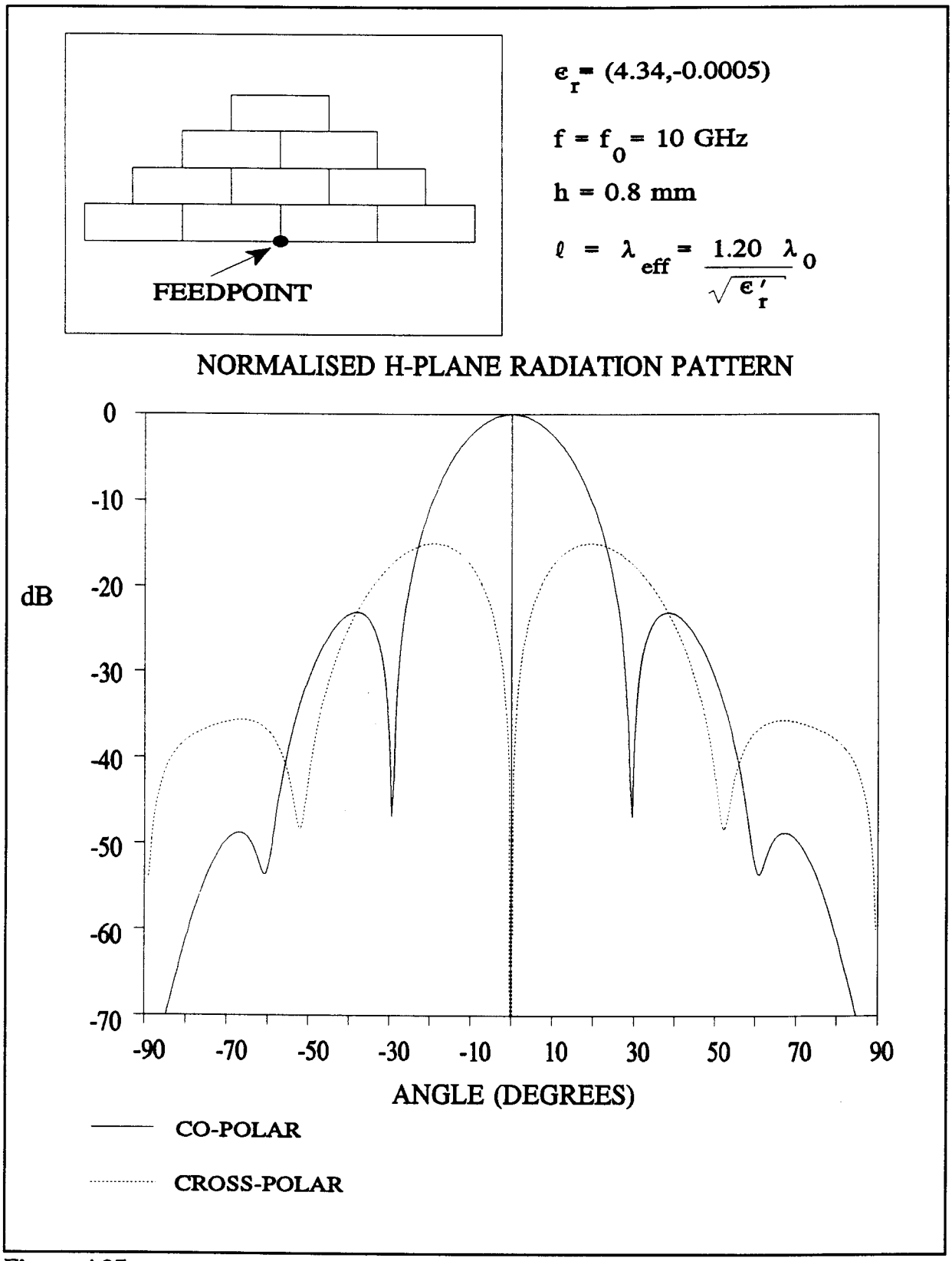

Figure 4.27 *Normalised H-plane radiation patterns for the current distributions shown in Figures 4.25 and 4.26 on the 4-level etched brick-wall array represented in Figure 4.24*

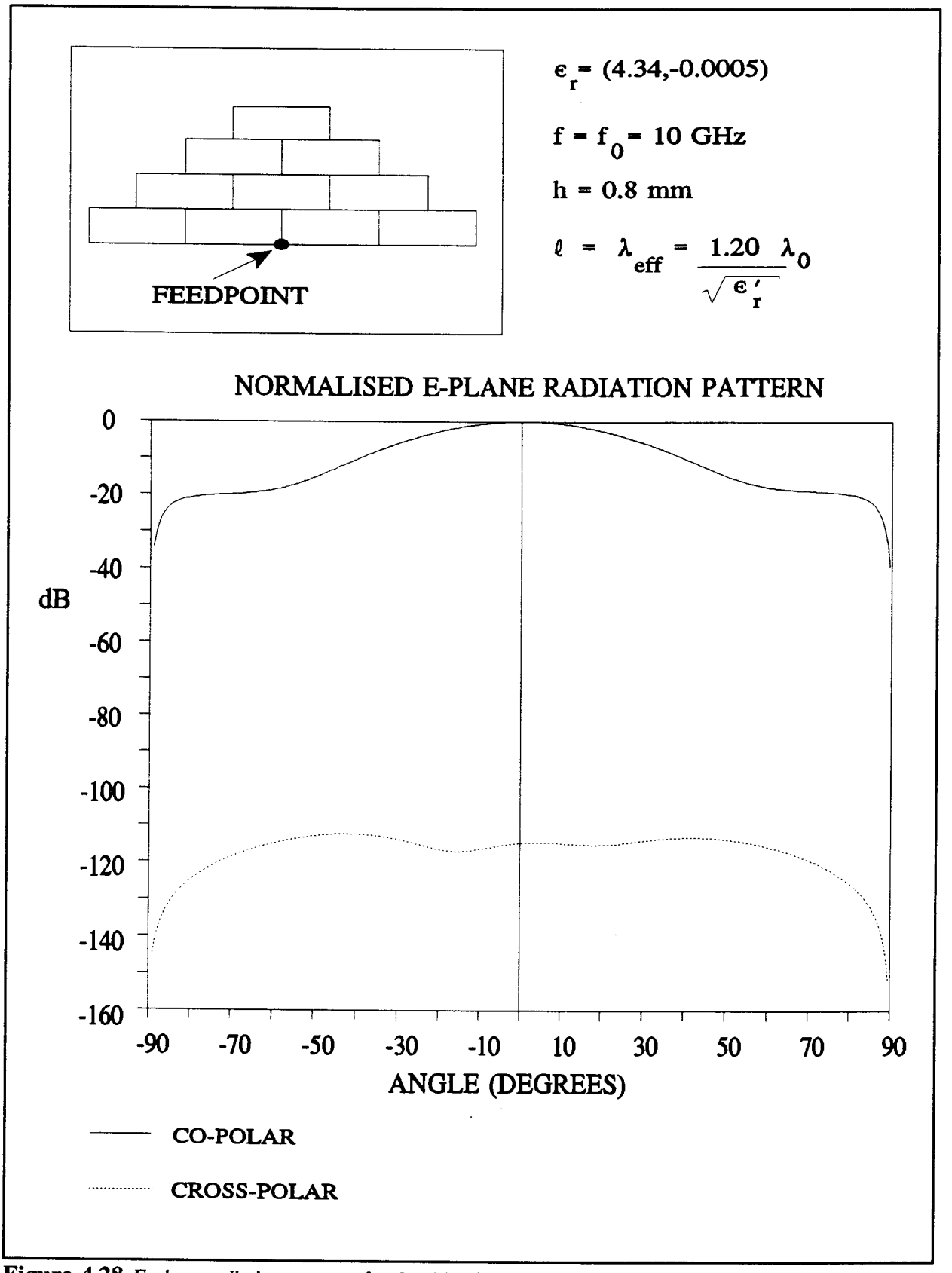

Figure 4.28 *E-plane radiation patterns for the 4-level etched brick-wall array shown in Figure 4.24.*

The far-field cross-polar radiation patterns of brick-wall arrays are dependent on the geometry of the structure itself (the layout of horizontal segments) and on the value of ℓ. However, after consideration of the current distribution on this particular array (Figures 4.25 and 4.26), one comes to the conclusion that the main reason for the high cross-polarization shown by this array, lies in the geometry of the brick-wall itself. This should be clear from Section 4.3.5 which discusses a planar array with lower cross-polarization.

4.3.5 A 3-level brick-wall array

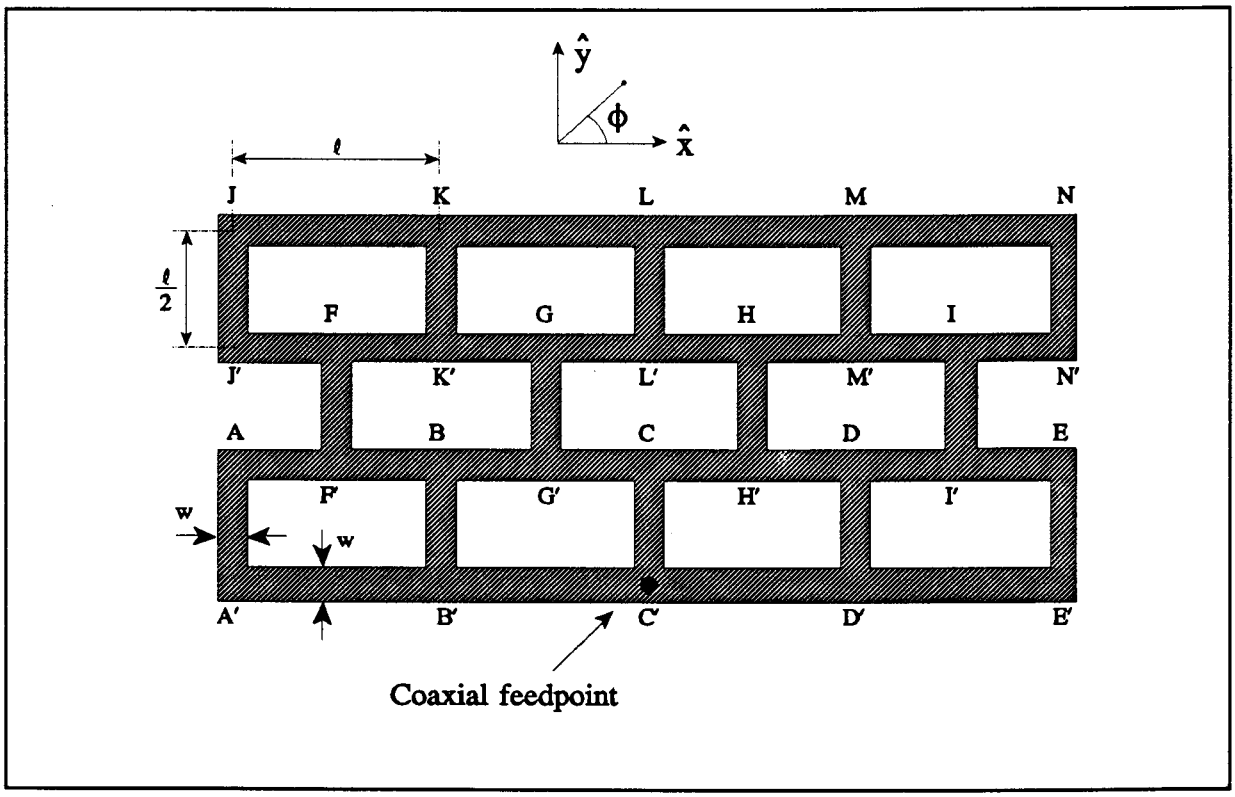

Figure 4.29 *Geometry of a 3-level brick-wall array with equal segment widths and coaxial feedpoint indicated.*

The 4-level brick-wall array discussed in Section 4.3.4, exhibits undesirable cross-polarization characteristics. In an attempt to find a planar array which improves on those characteristics, the structure shown in Figure 4.29 was analysed.

The current distribution on this structure, for a given set of material parameters, is shown in Figures 4.30 and 4.31. From these figures, it can be seen that the horizontal currents correctly feed the vertical elements and the latter have essentially equal current amplitudes because of their equal widths. The E- and H-plane far-field radiation patterns for these currents, on the structure represented in Figure 4.29, are shown in Figures 4.32 and 4.33. From the H-plane radiation patterns of this array, we notice that the cross-polarization characteristics have improved from that shown by the 4-level array (Figure 4.27). We also note that the side lobe level has increased from -23 dB to -13 dB, since the collapsed distribution in the H-plane is now effectively uniform (because the array lattice is completely filled). The increase in the sidelobe levels is accompanied by a decrease in the BWFN (compared to the previous case) to some 30°. The BWFN in the E-plane has become approximately 100°, and a sidelobe at -19 dB has formed. The behaviour is different from that observed for the linear arrays simply because for the present planar array case the array aperture transverse dimension is larger. This observation leads naturally to consideration of the even larger planar array in Section 4.3.6.

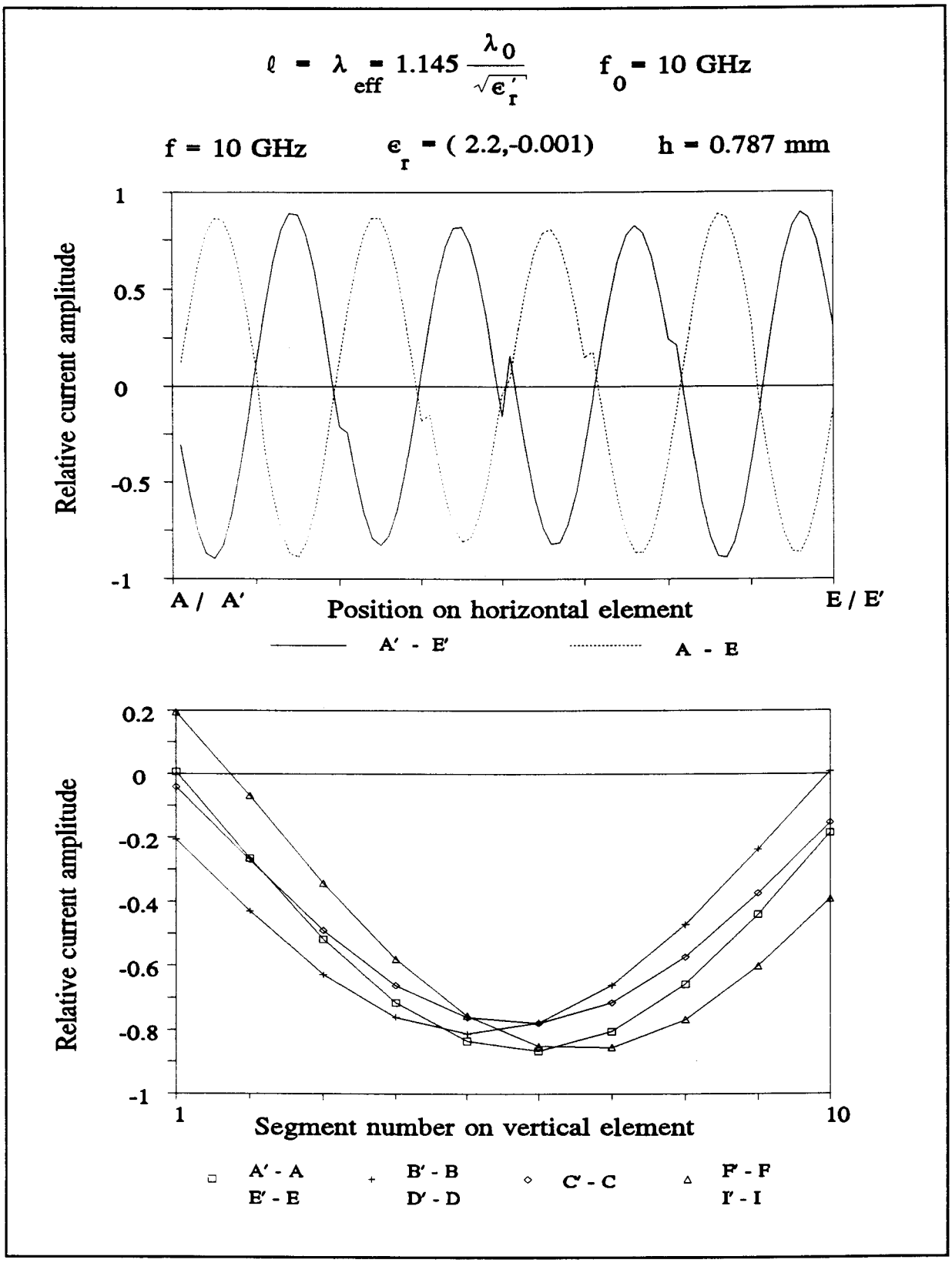

Figure 4.30 *Current distributions on several elements of the 3-level brick-wall array shown in Figure 4.29. The current distributions on the remainder of the elements are shown in Figure 4.31.*

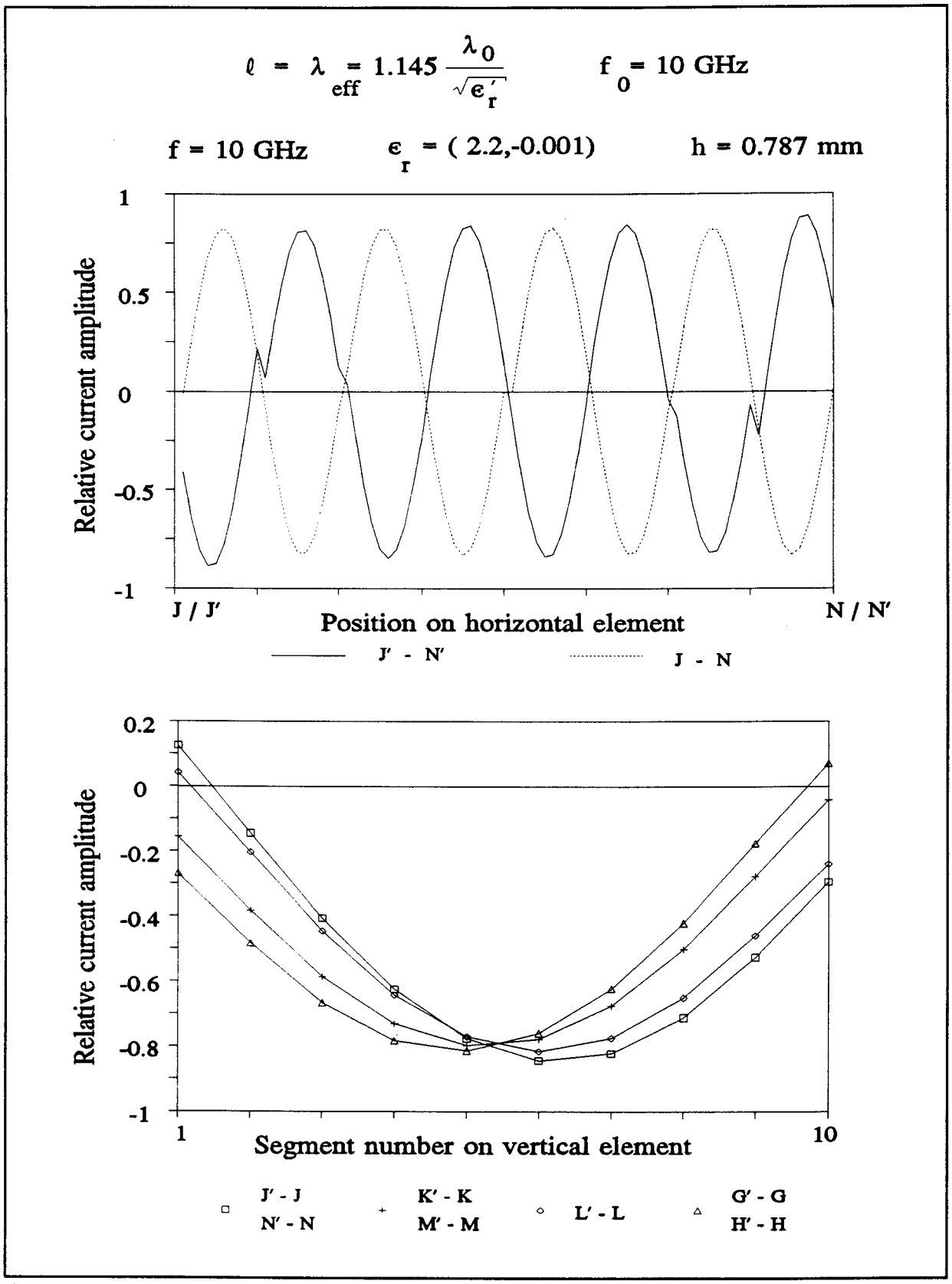

Figure 4.31 *Current distributions on several elements of the 3-level brick-wall array shown in Figure 4.29.*

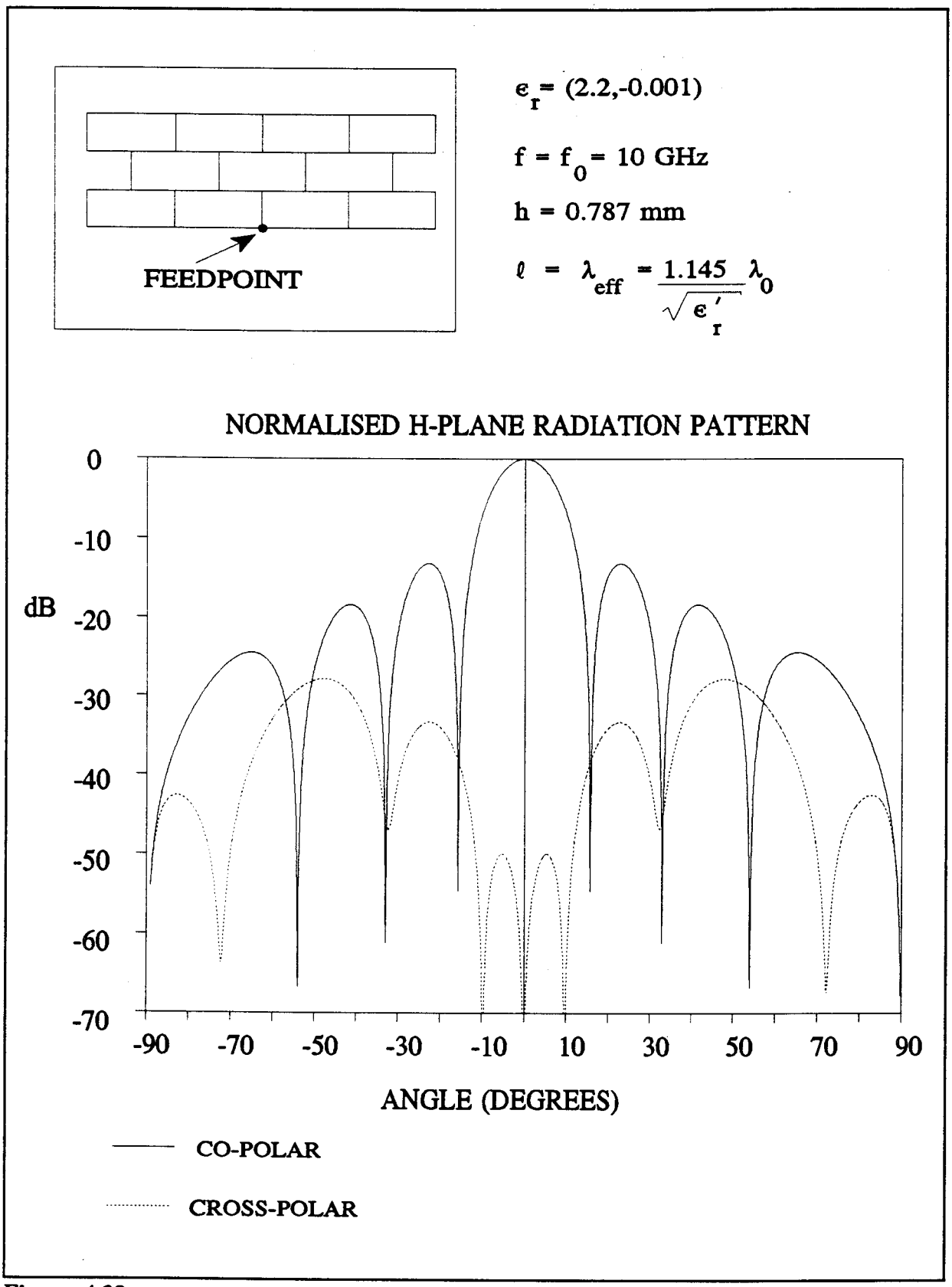

Figure 4.32 *Normalised H-plane radiation patterns for the 3-level brick-wall array shown in Figure 4.29.*

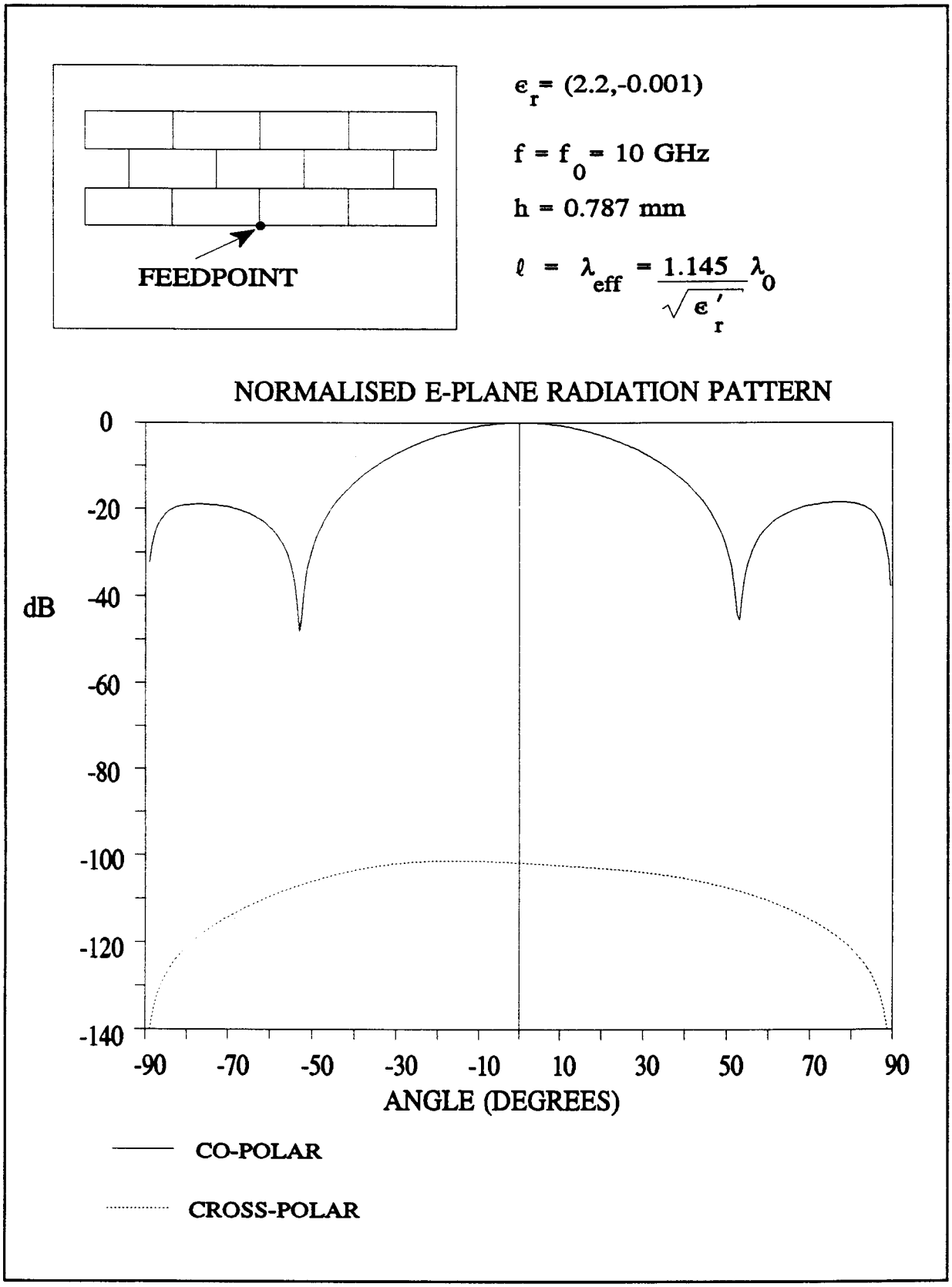

Figure 4.33 *Normalised E-plane radiation patterns for the 3-level brick-wall array.*

4.3.6 A 5-level brick-wall array

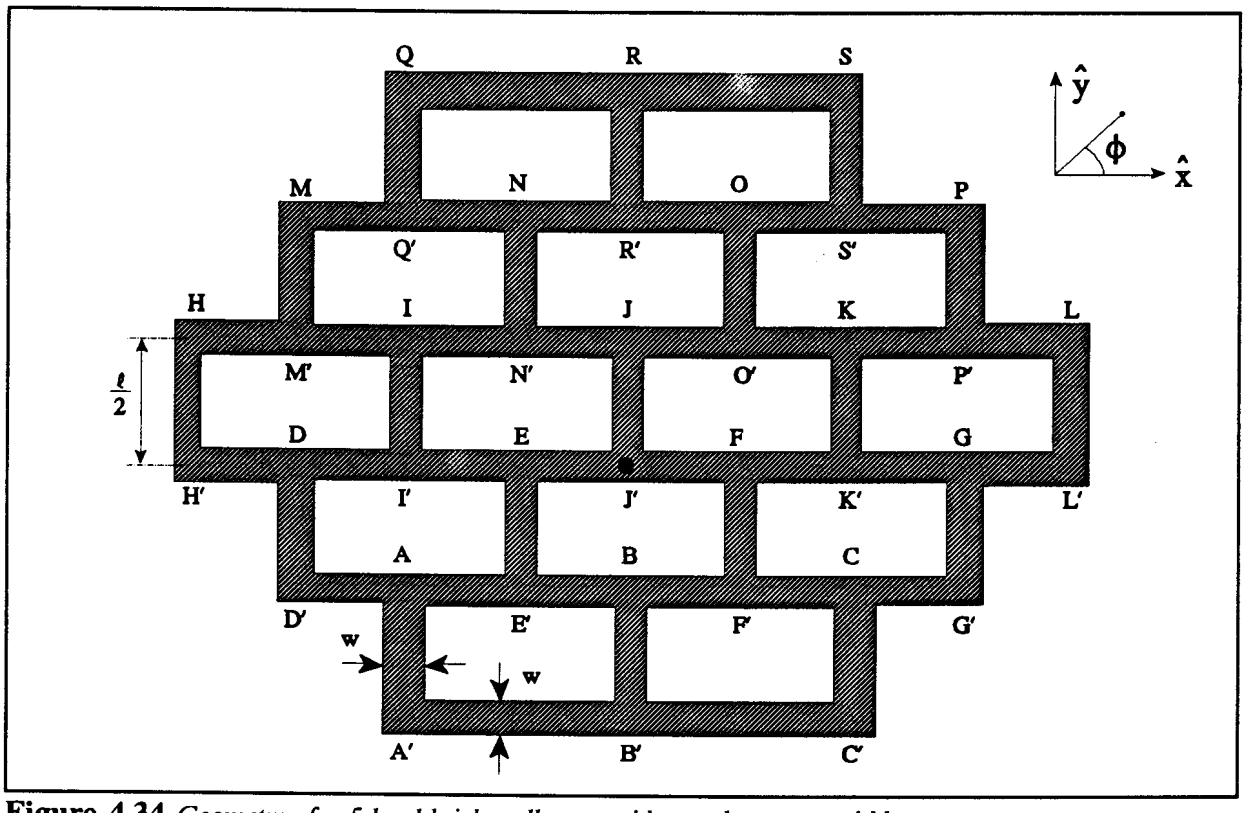

Figure 4.34 *Geometry of a 5-level brick-wall array with equal segment widths.*

The 5-level brick-wall array shown in Figure 4.34, was also analysed using the integral-equation method. The radiation patterns in both principal planes are shown in Figures 4.35 and 4.36. This geometry yields particularly good cross-polarization characteristics in both principal planes. In the E-plane, the BWFN has decreased from that shown by the 3-level array (discussed in Section 4.3.5) to approximately 80°.

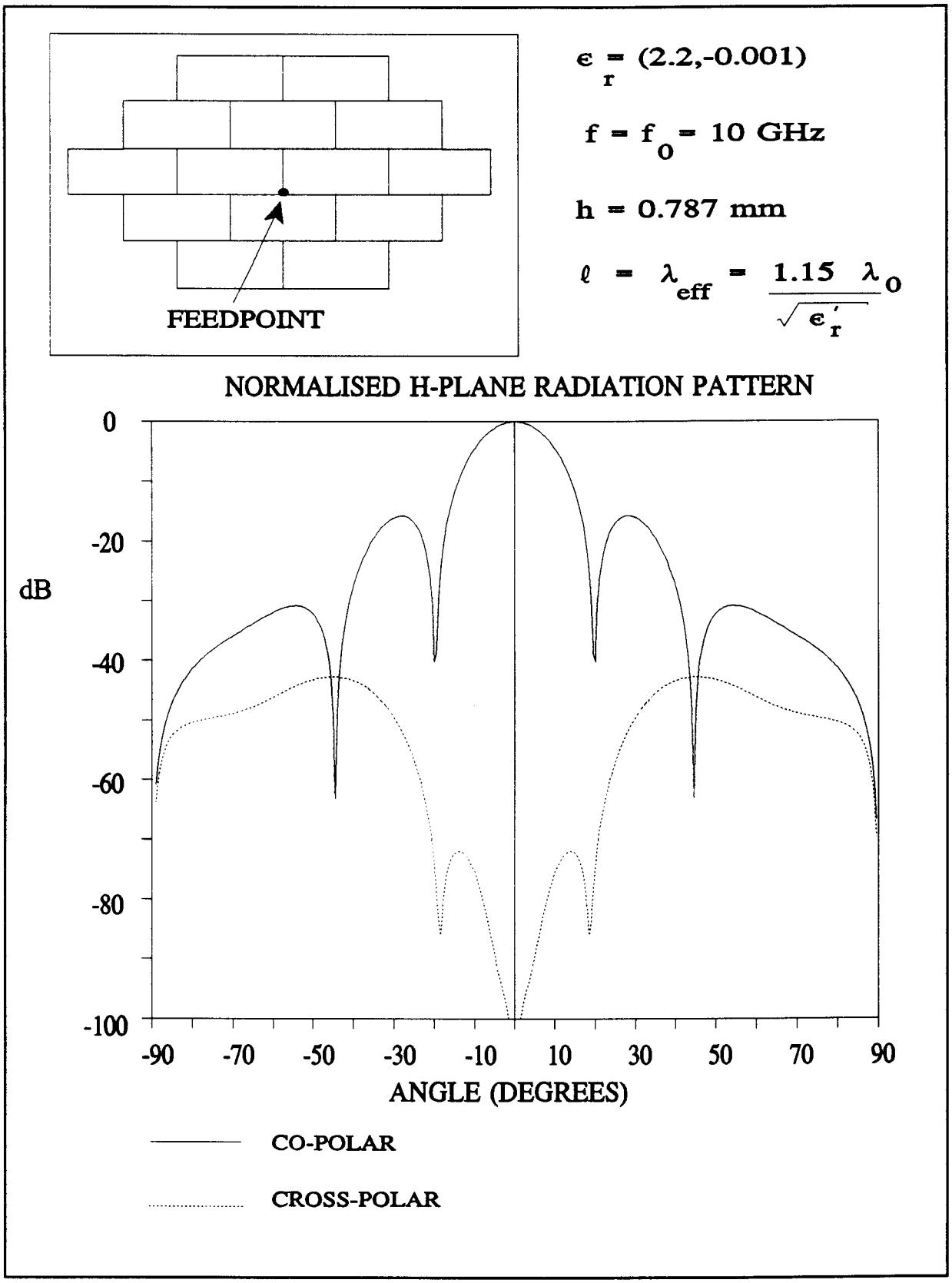

Figure 4.35 *H-plane radiation patterns for the 5-level brick-wall array shown in Figure 4.34.*

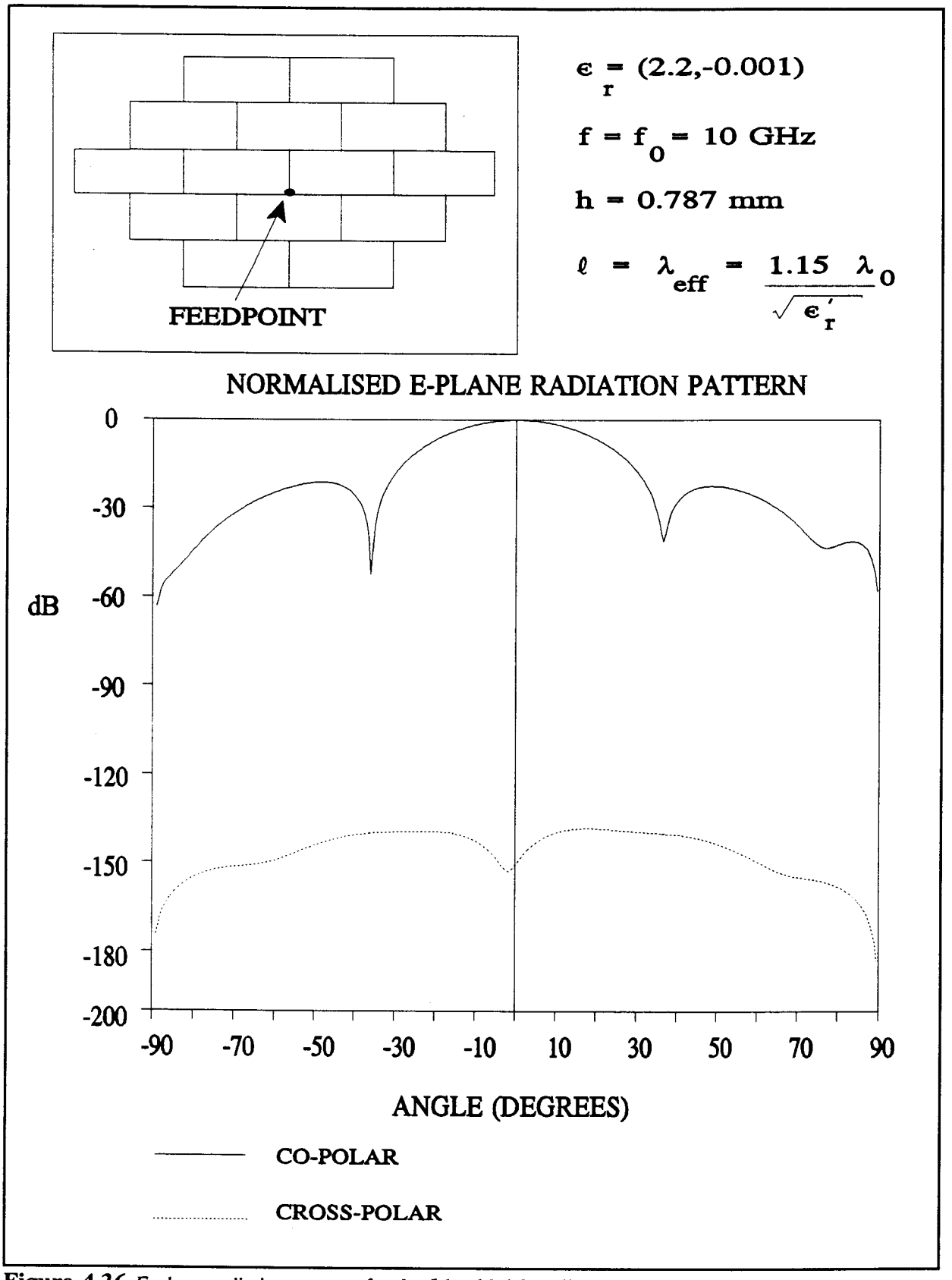

Figure 4.36 *E-plane radiation patterns for the 5-level brick-wall array shown in Figure 4.34.*

4.4 MEASURED RESULTS FOR ETCHED WIRE-GRID ARRAYS

In order to verify theoretically predicted results, a number of etched brick-wall arrays were designed and fabricated. A printed circuit technique package was used to generate the artwork and for etching purposes, the substrate/groundplane material used was either Taconic [37] or RT/duroid [38]. Radiation patterns were measured on the compact range at the University of Pretoria, while theoretical predictions were obtained from code execution on a Persetel 890/3 mainframe computer. Comparisons between measured and predicted results will be given in this section for four different arrays.

As mentioned in Section 2.3, the mixed-potential integral equation formulation assumes the dielectric substrate and groundplane[2] to extend to infinity in the transverse directions. This, of course, is not attainable in practice. For a rectangular groundplane, there are several orientations by which the conductors can be deposited on the dielectric substrate. In this regard, we make use of the two orientations shown in Figures 4.37 and 4.38. Unless stated otherwise, all arrays will be oriented as shown in Figure 4.37. A simple experiment has been performed to examine the effect of the finite groundplane on the radiation pattern of an etched brick-wall array; its results are next discussed.

[2] Unless stated otherwise, the dielectric substrate and metallic groundplane have the same transverse dimensions

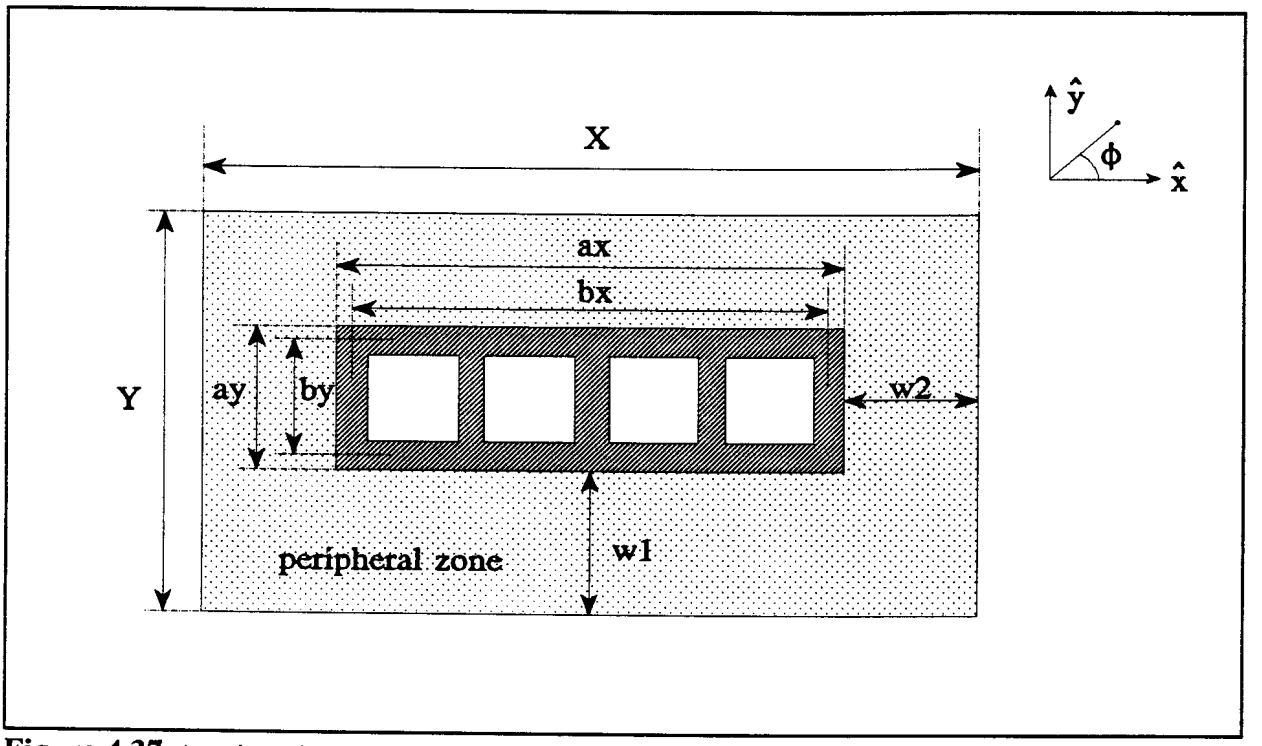

Figure 4.37 *An orientation by which the conductors of the etched antenna may be deposited on the dielectric sheet. This figure also seems to define what is meant by the term peripheral zone.*

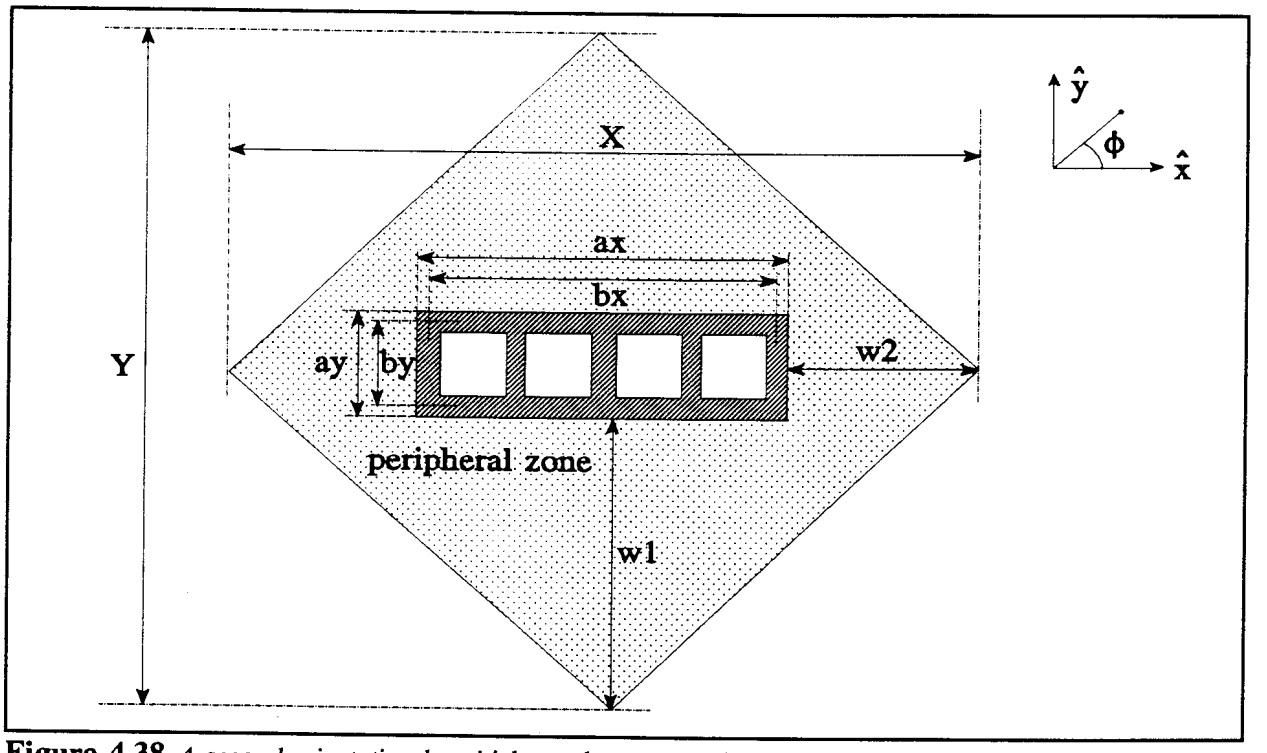

Figure 4.38 *A second orientation by which conductors may be deposited on the dielectric substrate.*

4.4.1 A 5-element linear tapered etched brick-wall array with $\ell \neq \lambda_{eff}$

The geometry of this array is shown in Figure 4.19 and theoretical results are discussed in Section 4.3.3. An existing array which had been etched on RT/duroid dielectric substrate backed by a metallic groundplane with transverse dimensions (according to Figure 4.37) of X = 7.47 λ_{eff} and Y = 3.18 λ_{eff} was used for this experiment. Since this 5-element array itself has transverse dimensions of ax = 4.7 λ_{eff} and ay = 0.64 λ_{eff} (in other words, ax = 4.05 ℓ and ay = 0.55 ℓ since $\ell \neq \lambda_{eff}$ for this specific array[3]), the structure has a *peripheral zone* with widths w1 = 1.27 λ_{eff} and w2 = 1.385 λ_{eff}. This is certainly an electrically small groundplane. The H-plane co-polar radiation pattern of this structure was measured at 10 GHz and a comparison between measured and predicted results is shown in Figure 4.39. The comparison is surprisingly good when considering the limited dimensions of the groundplane and dielectric substrate. In order to more accurately predict the radiation patterns of this array, one would need to considerably increase the transverse dimensions of the dielectric substrate and groundplane. Although it would be difficult to enlarge *both* the dielectric substrate and metallic groundplane of this "already-fabricated array", it is possible to enlarge the groundplane portion only. This was accomplished by simply using domestic tin foil to carefully cover a large non-conducting sheet, and securing the microstrip antenna on the conducting tin foil. The important matter is that there be electrical contact between the metallic groundplane of the original microstrip structure and the tin foil. The groundplane now has dimensions of X = 24.21 λ_{eff}

[3] Also bx = 4.0 λ_{eff} and by = 0.5 λ_{eff}.

and Y = 19.13 λ_{eff}. One must of course, keep in mind that this is not the ideal setup since the dielectric substrate still has not been enlarged. Nevertheless, the H-plane co-polar radiation pattern of this antenna was measured and a comparison with predicted results is given in Figure 4.40. It is interesting to note that even for the array secured on this "home-made" groundplane, the correspondence is much closer than that shown in Figure 4.39. This seems to suggest that finite groundplane effects are primarily responsible for the deviation between measured patterns for structures with electrically small groundplanes and their computed patterns (which assume infinitely large groundplanes).

In general, the cross-polarized radiation pattern of a microstrip antenna is very difficult to predict accurately and is sensitive in practice to the size of the groundplane. Nevertheless, the H-plane cross-polarized radiation pattern of this array on the large groundplane was measured and a comparison with predicted results is shown in Figure 4.41. The overall angular behaviour of the cross-polarization is correctly predicted, but not the details.

For this 5-element linear tapered etched brick-wall array, 5 megabytes of memory was needed with approximately 22 hours of CPU execution time.

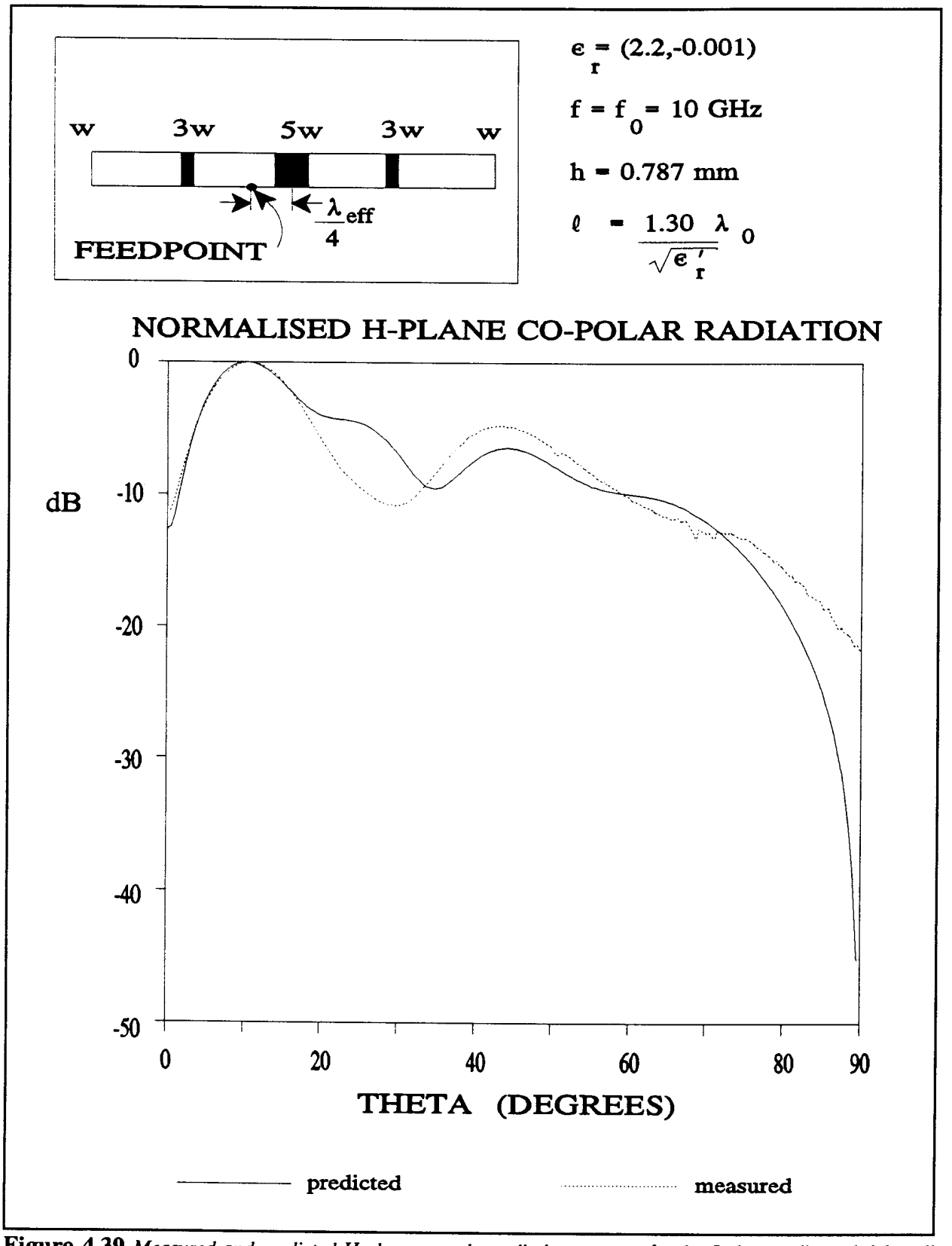

Figure 4.39 *Measured and predicted H-plane co-polar radiation patterns for the 5-element linear brick-wall array (ℓ = 1.3 $\lambda_0/\sqrt{\epsilon_r'}$) on the small groundplane (Section 4.4.1).*

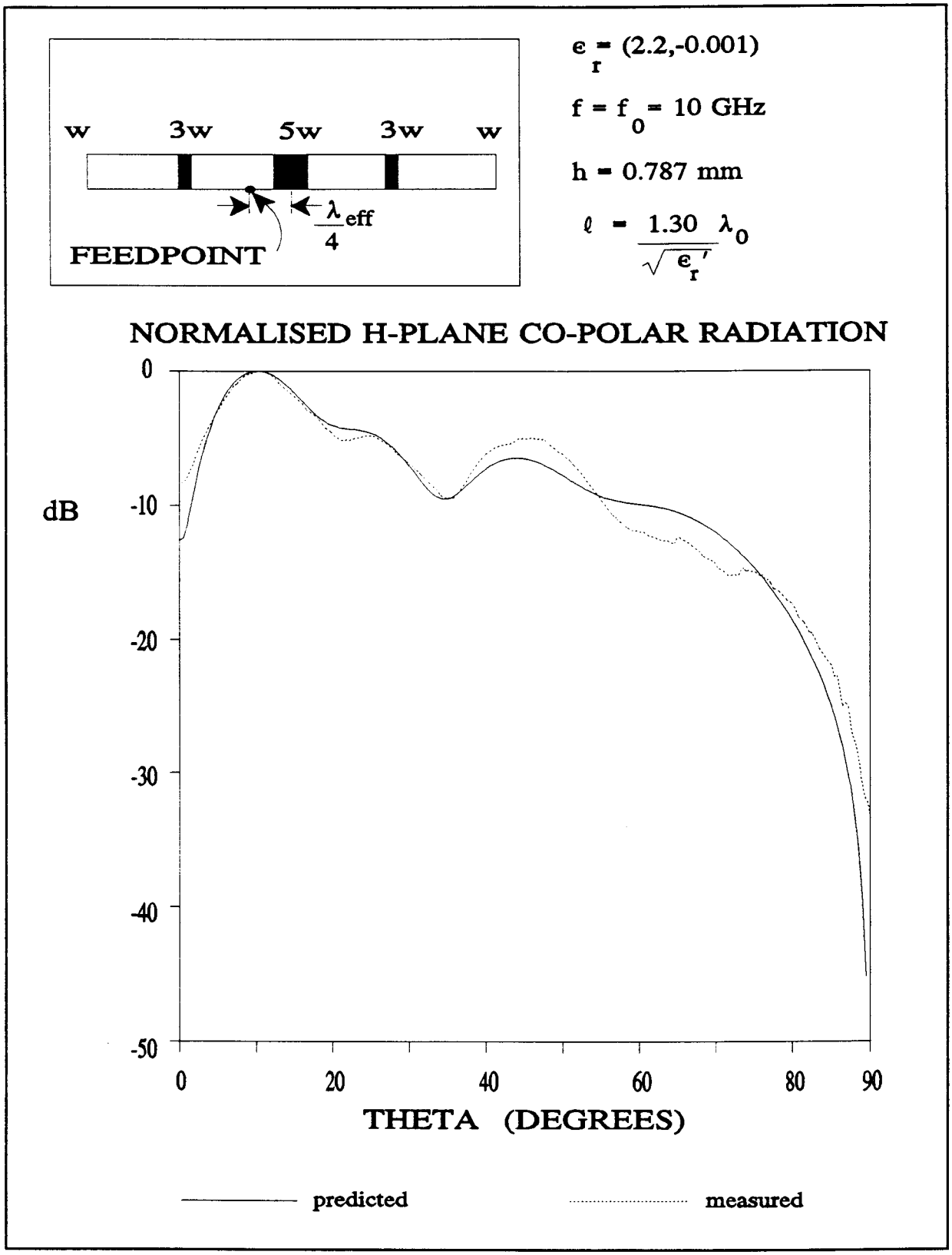

Figure 4.40 *Measured and predicted H-plane co-polar radiation patterns for the 5-element linear brick-wall array ($\ell = 1.3\ \lambda_0/\sqrt{\epsilon_r'}$) on an enlarged metallic groundplane.*

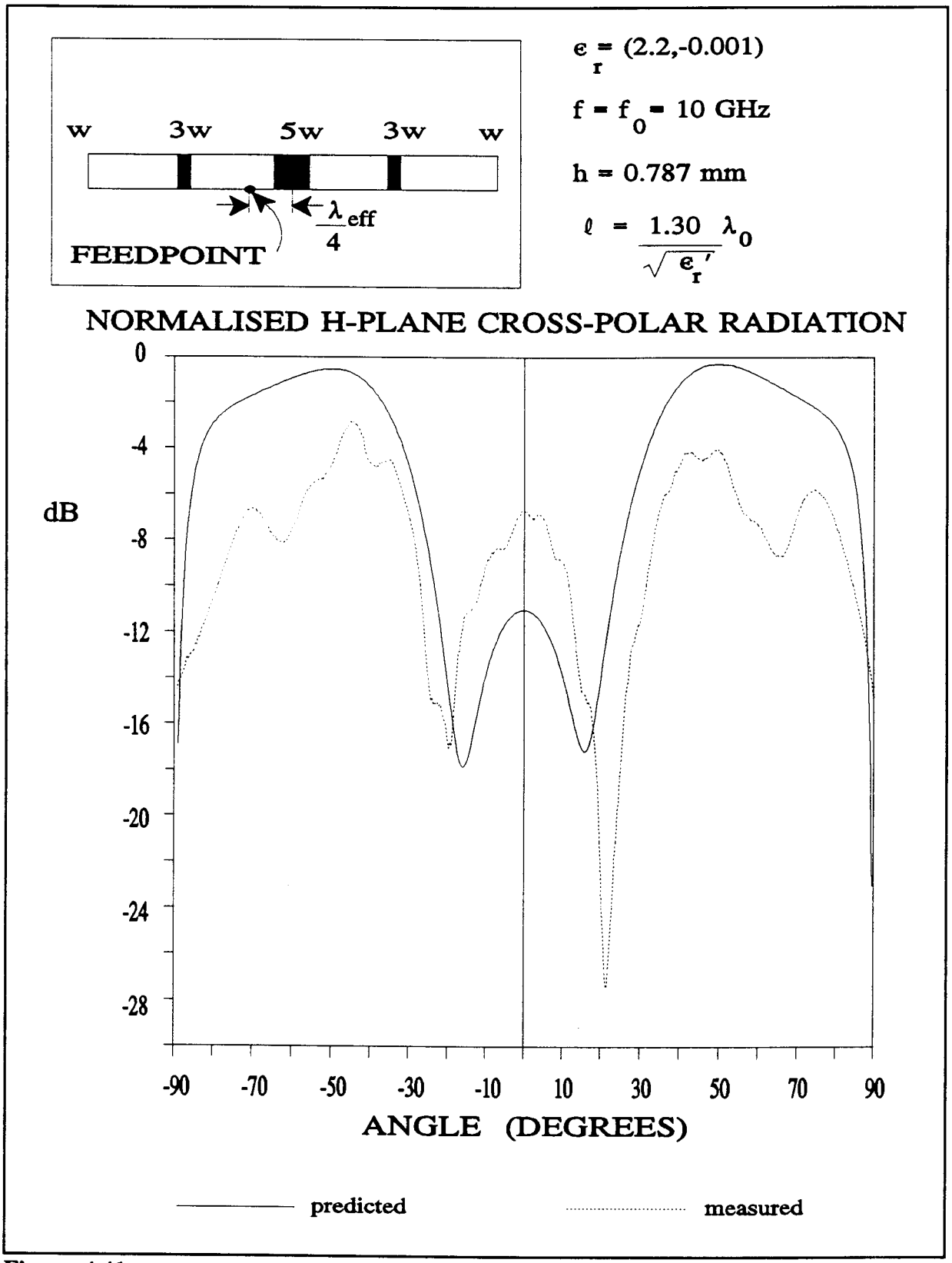

Figure 4.41 *Measured and predicted cross-polar radiation patterns in the H-plane for the tapered array on the large groundplane.*

4.4.2 A 5-element linear tapered etched brick-wall array with $\ell = \lambda_{eff}$

This array which is described theoretically in Section 4.3.3 was etched according to Figure 4.37 on a groundplane with dimensions of X = 13.47 λ_{eff} and Y = 9.85 λ_{eff}, so that w1 = 4.65 λ_{eff} and w2 = 4.71 λ_{eff}. Taconic [37] substrate with ϵ_r' = 2.2 and h = 0.787 mm was used for this array. The H-plane co-polar radiation pattern is shown in Figure 4.42. Close correspondence between measured and predicted results is observed for this array, especially at smaller angles: finite groundplane effects become greater at larger angles. The encouraging fact about these results is that the first side lobe level at -23 dB is closely predicted. Figure 4.43 shows the measured and predicted E-plane co-polar radiation patterns. Since the E-plane pattern is broad, and there is "hard" diffraction from the groundplane edge in this plane, one expects the groundplane to have a strong effect on this pattern (as for the case of rectangular microstrip patches [2]). This expectation is borne out in Figure 4.43.

The H-plane cross-polar radiation pattern of this tapered array was measured and a comparison with computed results is given in Figure 4.44. Due to finite groundplane effects, however, the correspondence between theoretical and practical results is not entirely satisfactory.

Measured and predicted radiation patterns for this array at a frequency of 11 GHz are shown in Figure 4.45. Even though this is not the centre-frequency good correspondence between measured and predicted results is observed. This illustrates the fact that the numerical method is accurate at frequencies other than the centre-frequency. This is important, considering that one is interested in examining broadband behaviour of these brick-wall arrays.

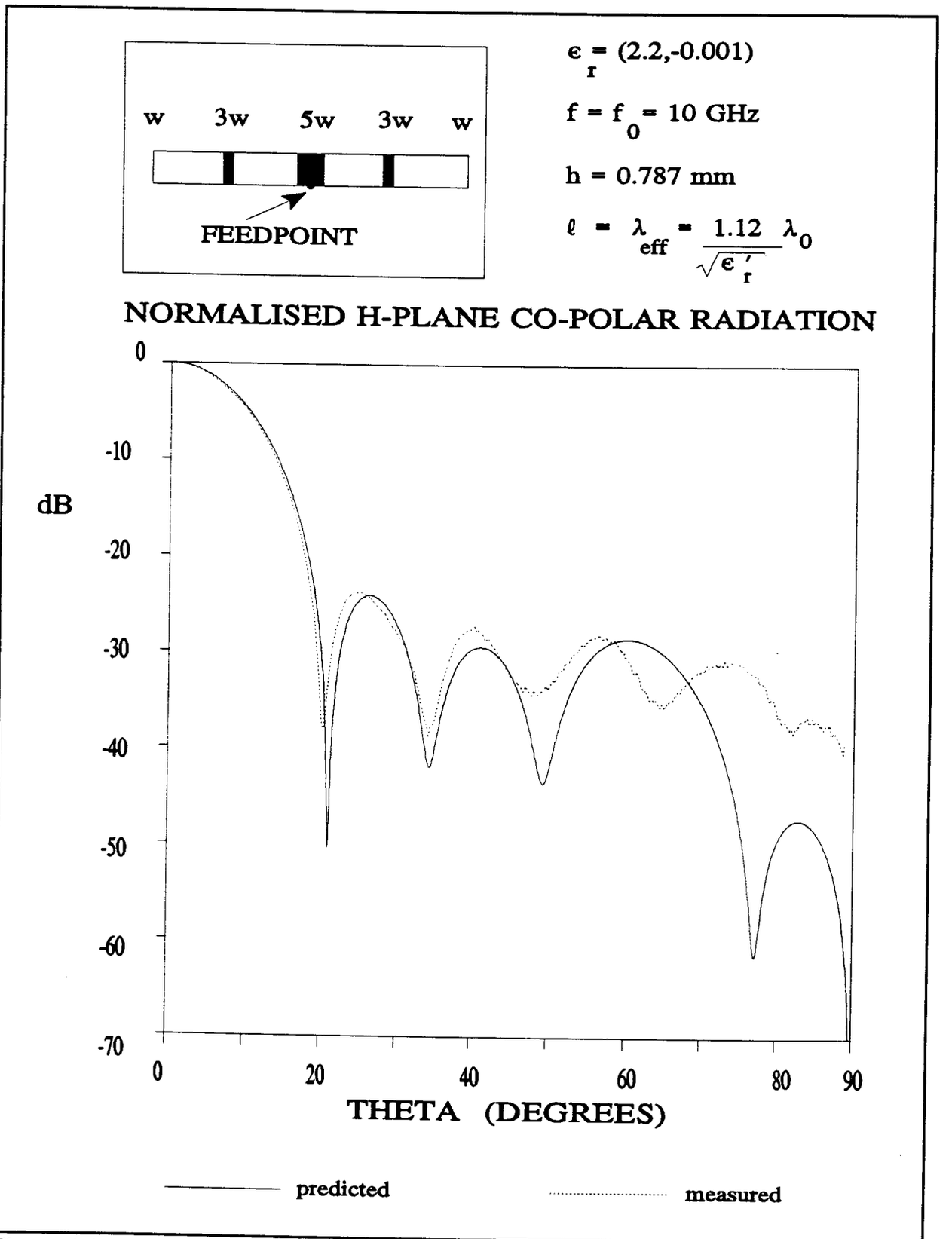

Figure 4.42 *Measured and predicted H-plane co-polar radiation patterns of the 5-element linear tapered brick-wall array with* $\ell = \lambda_{eff}$

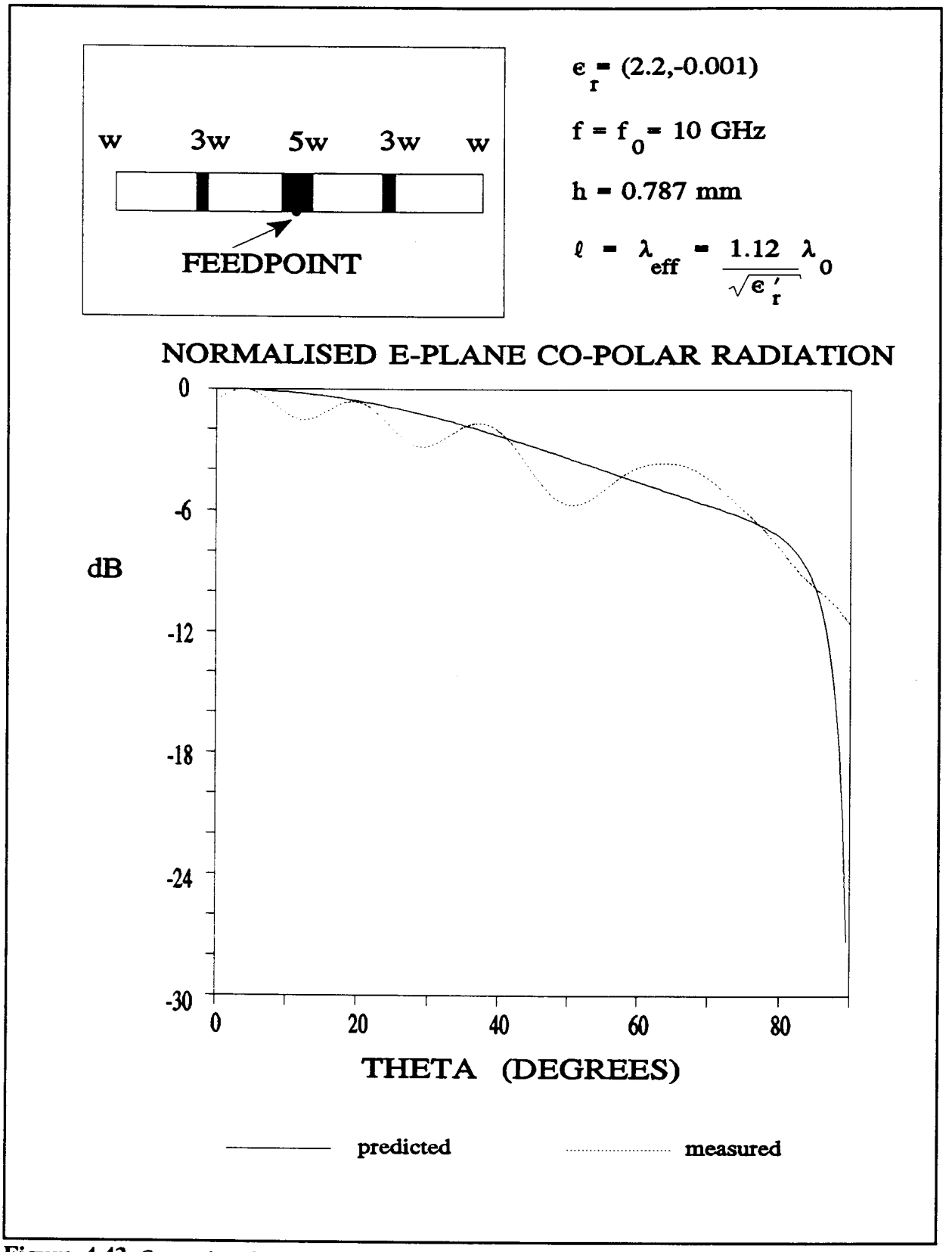

Figure 4.43 *Comparison between measured and predicted E-plane co-polar radiation patterns for the 5-element linear tapered array.*

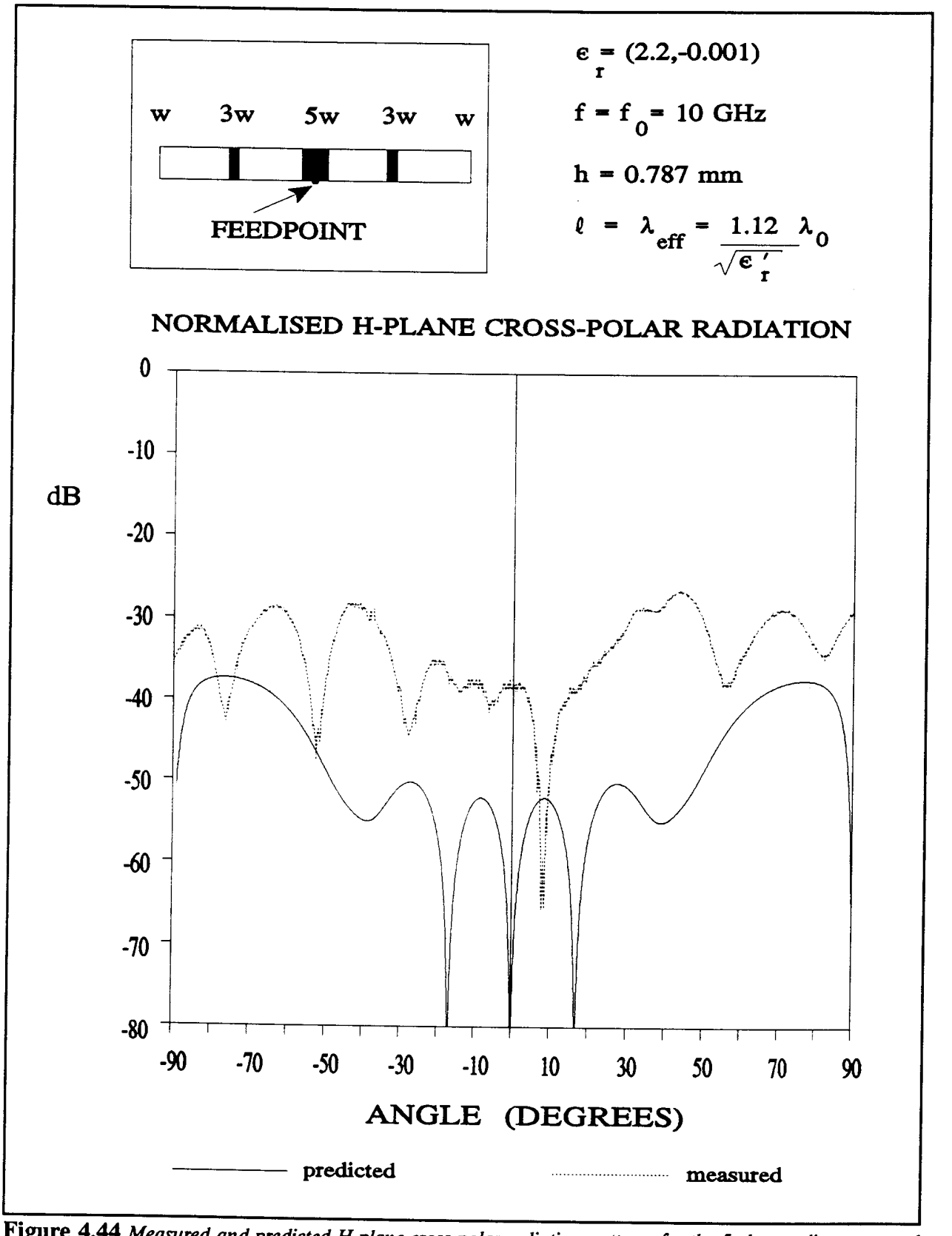

Figure 4.44 *Measured and predicted H-plane cross-polar radiation patterns for the 5-element linear tapered brick-wall array.*

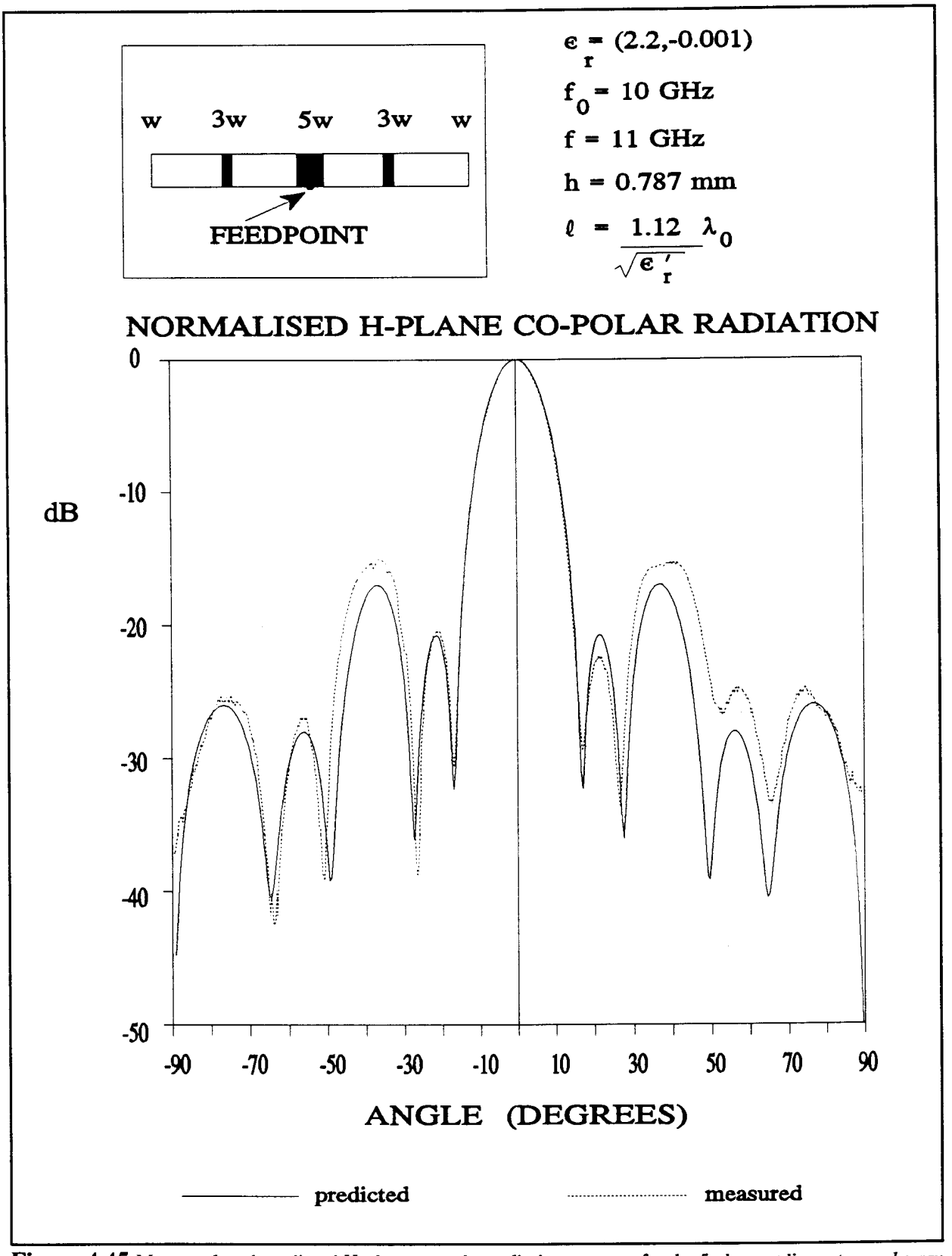

Figure 4.45 *Measured and predicted H-plane co-polar radiation patterns for the 5-element linear tapered array at 11 GHz. The centre-frequency for this array is 10 GHz.*

4.4.3 A 3-level brick-wall array

The geometry of this array is shown in Figure 4.29 and theoretical results are given in Section 4.3.5. In that section we saw that for the given material parameters and resonant behaviour at 10 GHz, that structure requires $\ell = \lambda_{eff} = 1.145\ \lambda_0/\sqrt{\epsilon_r'}$. However, in order to increase the variety of arrays for which computations were performed, an array was etched with $\ell = 1.072\ \lambda_0/\sqrt{\epsilon_r'}$ - this will be off-resonance at 10 GHz. This brick-wall array was etched on RT/duroid [38] substrate (h = 0.787 mm and $\epsilon_r = (2.2, -0.001)$) with the orientation shown in Figure 4.38. In other words, the array is deposited on the diagonal of a rectangular groundplane of dimensions $X = Y = 15\ \lambda_{eff}$. This implies that the widths of the peripheral zone are $w1 = 6.725\ \lambda_{eff}$ and $w2 = 5.475\ \lambda_{eff}$. Measurements are now carried out in the two principal planes: the H-plane ($\phi = 0°$) and the E-plane ($\phi = 90°$). Measured and predicted H-plane co-polar radiation patterns for this 3-level brick-wall array are shown in Figure 4.46. Close correspondence can be seen, even at large angles, and this despite the fact that $\ell \neq \lambda_{eff}$ and the structure therefore not resonant. This supports the usefulness and generality of the numerical method.

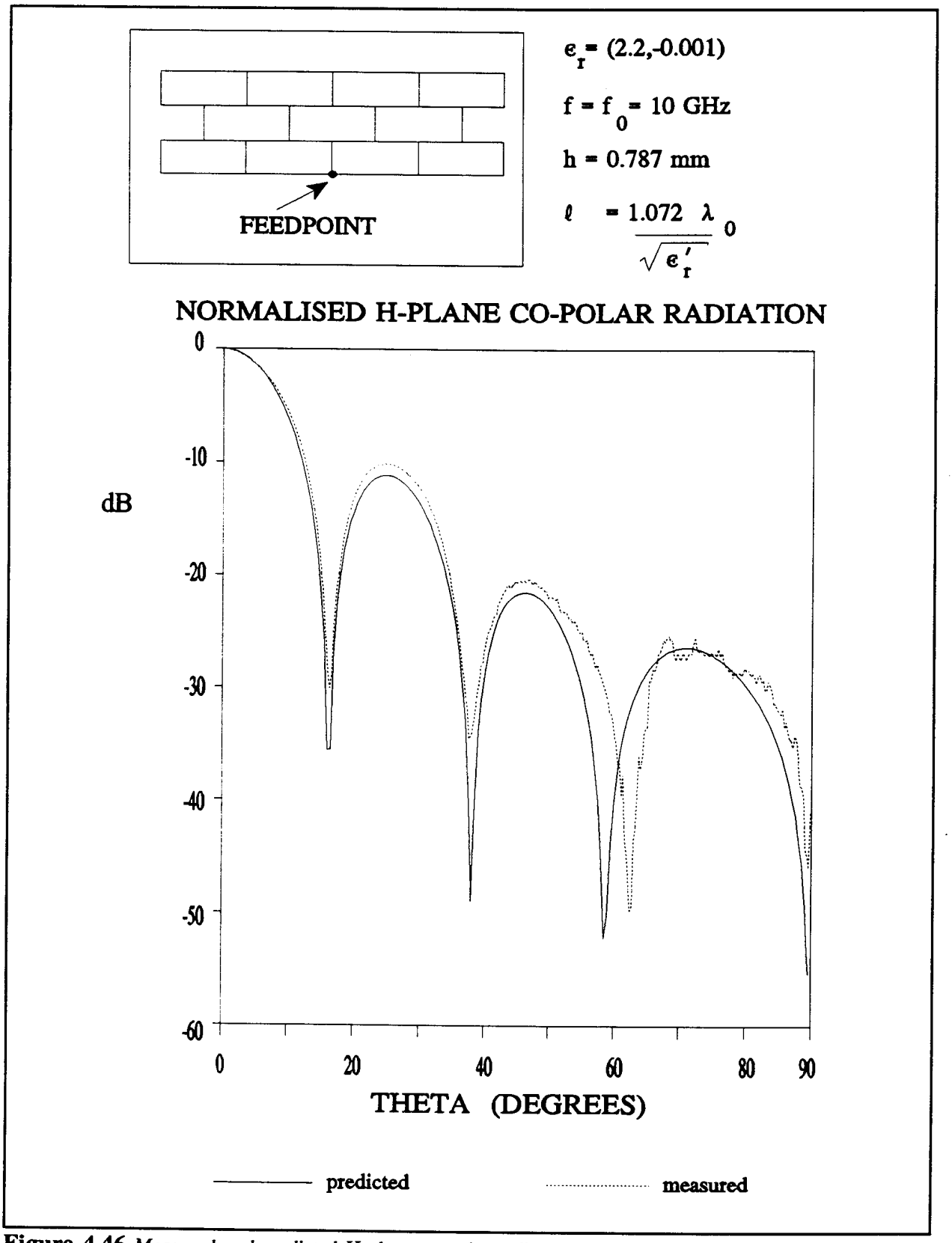

Figure 4.46 *Measured and predicted H-plane co-polar radiation patterns for a 3-level brick-wall array with* $\ell = 1.072\ \lambda_0/\sqrt{\epsilon_r'}$ *at 10 GHz.*

4.4.4 A 5-level brick-wall array

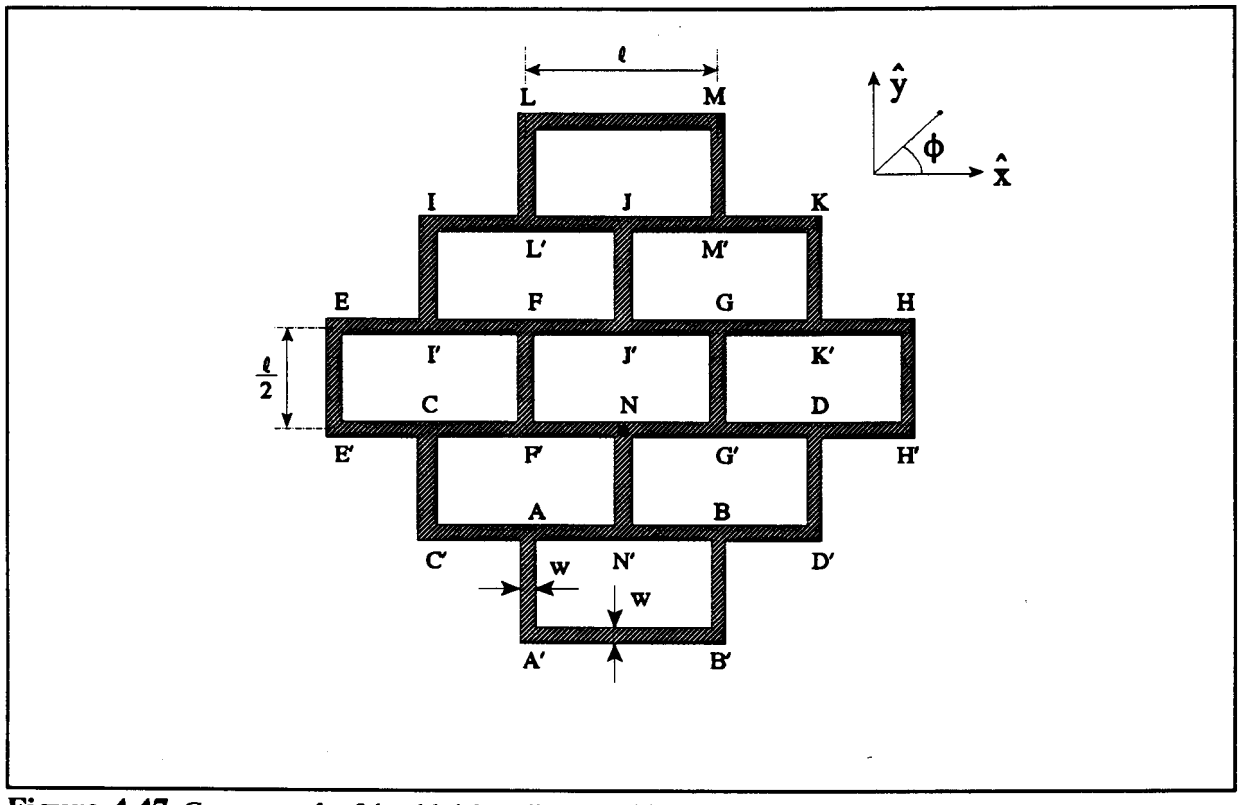

Figure 4.47 *Geometry of a 5-level brick-wall array with equal element widths.*

Finally, consider the array represented in Figure 4.47. As in the previous case, RT/duroid [38] substrate was used in the fabrication process. The groundplane for this array has dimensions (according to Figure 4.37) of X = 13.92 λ_{eff} and Y = 10.36 λ_{eff}, so that w1 = 3.905 λ_{eff} and w2 = 5.435 λ_{eff}. Measured and predicted results for the co-polar H-plane radiation pattern are shown in Figure 4.48. Although close correspondence can be seen over the main beam, the side lobes are not well predicted. However, the unexpected ripple in the measured side lobe shapes suggest that this lack of agreement is due to groundplane effects. The normalised cross-polar radiation pattern in the H-plane is shown in Figure 4.49, where the normalisation is with respect to the maximum value of the

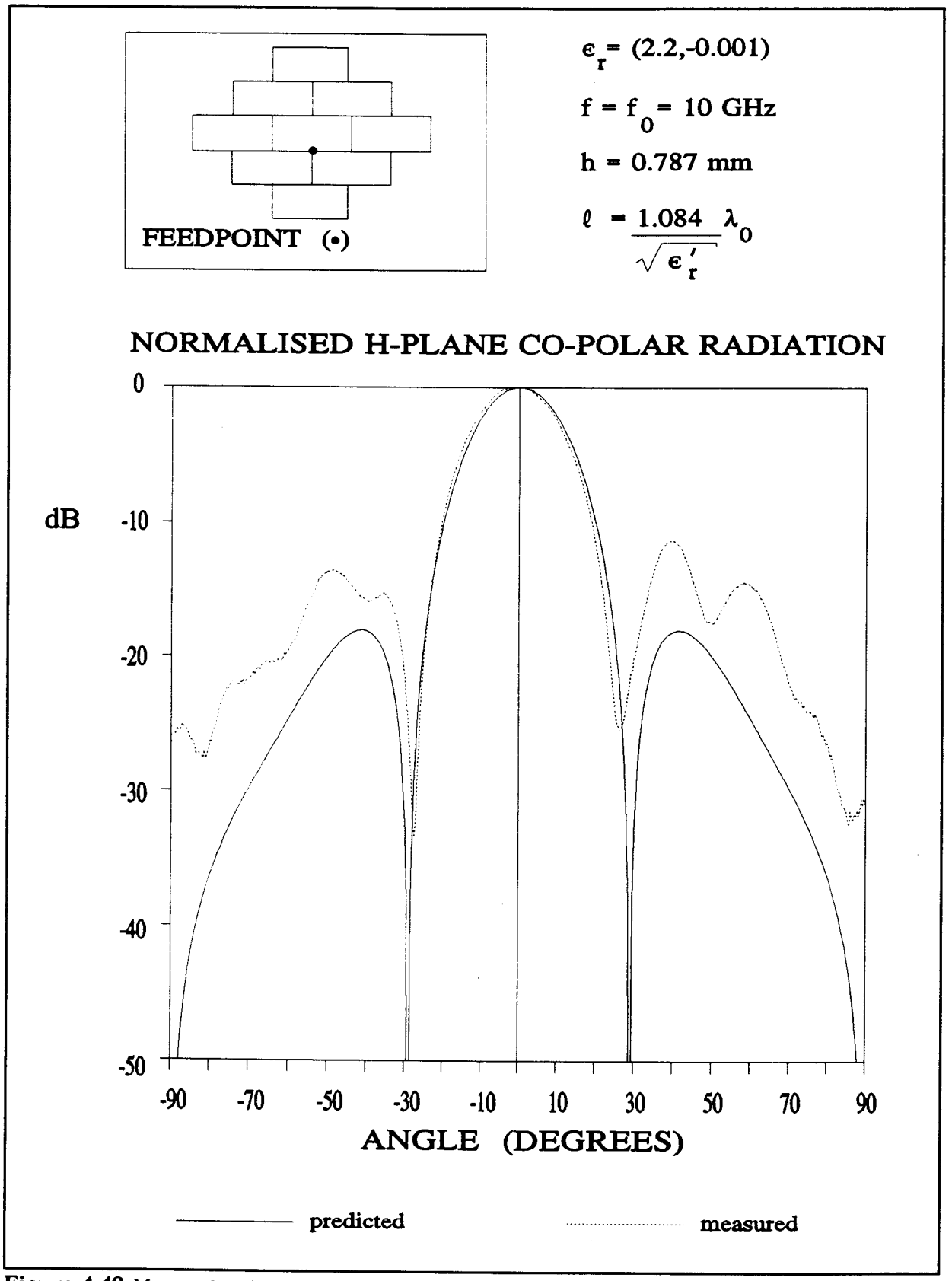

Figure 4.48 *Measured and predicted H-plane co-polar radiation patterns for the array shown in Figure 4.47.*

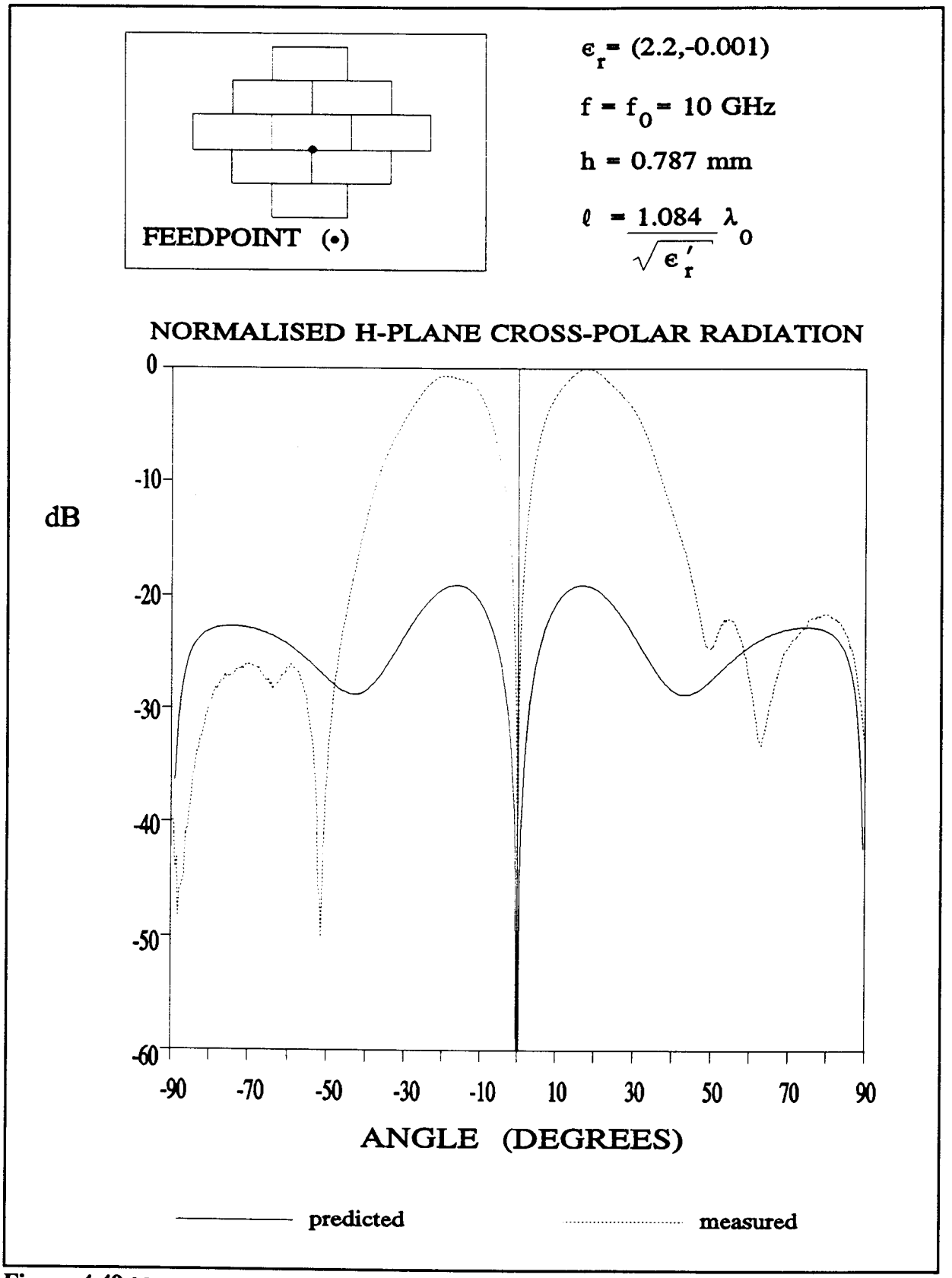

Figure 4.49 *Measured and predicted cross-polar radiation patterns for the 5-level array shown in Figure 4.47.*

measured co-polarization pattern shown in Figure 4.48. The level of the measured cross-polarization is some 20 dB above the value predicted.

4.5 CONCLUDING REMARKS

The general integral equation formulation of Section 2.3, implemented as described in Chapter 3, was used in this chapter to examine the operation of etched brick-wall antenna arrays. In order to validate the implementation developed by the author, computed current distributions for a rectangular microstrip patch were satisfactorily compared to previously published results. In the design of wire-grid antenna arrays, dimensions are selected in terms of λ_{eff}. The difficulty in determining values for λ_{eff} is that it is not only a function ϵ_r but also of the dielectric substrate thickness, frequency and specific line widths. It was also shown how the numerical method can be used to determine values for λ_{eff} related to specific geometries. Current distributions on several specific geometries were examined, and the radiation patterns determined directly from these computed current distributions (these are essentially exact, given a current distribution, except for finite groundplane effects).

Several brick-wall arrays were fabricated and close correspondence between measured and predicted co-polar radiation patterns was found. This essentially validates the use of the present analysis for the design of brick-wall arrays. Cross-polar radiation patterns are very difficult to predict accurately, and are dependent on the actual size of the groundplane, an aspect not included in the numerical model. Through a simple experiment, we showed that by increasing the transverse

dimensions of the metallic groundplane, closer correspondence between measured and predicted radiation patterns could be observed. We also investigated, theoretically, the effects on radiation patterns, of moving coaxial feedpoints. These effects seemed to be very much case dependent. This numerical method is equally valid at off-centre frequencies (important in determining the pattern bandwidth of the antenna), and this was illustrated by the close correspondence between measured and computed radiation patterns at 11 GHz for a 5-element linear tapered array which had been designed for a centre-frequency of 10 GHz.

The fact that numerical experimentation can be performed on etched wire-grid antenna arrays to examine current distributions, means that it is now possible to carefully design for some desired aperture distribution and hence radiation pattern.

CHAPTER 5

GENERAL CONCLUSIONS

The versatility of array antennas has been known for many years but their widespread use was prevented by their relatively high cost compared to alternative antenna types. More recently the realisation of arrays in microstrip has altered such considerations - not only are microstrip antennas relatively in-expensive, but they can be directly integrated with printed feed networks and active circuits. While many microstrip antenna geometries have been proposed and investigated experimentally, only a few of these (and the microstrip wire-grid array is not one of these) have enjoyed a rigorous theoretical analysis. One reason for this is probably the very substantial and time-consuming effort involved between the integral equation analysis formulation and its actual numerical implementation in practice - the numerical analysis of layered structures is fraught with difficulties, the finer details of whose solution is seldom readily available. The principal contributions of this thesis therefore are:

(a) Chapter 3, which gives an illustrative guide to the numerical "pitfalls" encountered in the application of the spatial domain integral equation analysis of microstrip antennas (which guide shows such aspects in a form more easily understandable than has heretofore been the case), and which provides information down to the finest detail on the numerical implementation of the analysis. Such detail was previously not readily available.

(b) Chapter 4, which applies a rigorous full-wave integral equation analysis to microstrip wire-grid arrays in order to achieve desired aperture distributions. This does not appear to have been done previously, and the design of such arrays through numerical experimentation is now possible.

APPENDIX A

DEFINITION OF THE SPATIAL FOURIER TRANSFORM; THE SPECTRAL DOMAIN

The Fourier transformation and its inverse are defined as follows [3]:

$$\tilde{f}(k_x, k_y) = \frac{1}{2\pi} \int_{-\infty}^{+\infty} \int_{-\infty}^{+\infty} f(x,y) \exp(-j k_x x - j k_y y)\, dx\, dy \tag{A.1}$$

$$f(x,y) = \frac{1}{2\pi} \int_{-\infty}^{+\infty} \int_{-\infty}^{+\infty} \tilde{f}(k_x, k_y) \exp(j k_x x + j k_y y)\, dk_x\, dk_y$$

where x and y are spacial domain variables; k_x and k_y representing their spectral domain counterparts.

The **spectral domain method** is a very powerful tool in electromagnetic radiation, propagation, and scattering problems. This method allows for considerable simplification of moment method calculations involving planar surfaces, because it effectively removes the singularity in the spatial Green's function [46]. Spatial domain integral expressions or integral equations, furthermore, convert to algebraic and differential equations in the spectral domain, hence the spatial convolution of the surface current and the Green's function, reduces to simple multiplication in the spectral domain.

The application of the spectral domain method in electromagnetics was developed and refined by Mittra [41] and numerous coworkers, beginning in the 1970's. Only recently some examples of the application of this method to microstrip structures have appeared in the technical literature. The first paper dealing with the full wave approach to microstrip problems was presented in 1981 by Itoh [32]. Several authors have since proposed spectral domain methods as viable alternatives to their spatial domain counterparts [41,42,43,44,45,46,47,48].

APPENDIX B

DERIVATION OF THE GREEN'S FUNCTIONS FOR A GROUNDED DIELECTRIC SLAB

In the construction of the Green's functions for a grounded dielectric slab, it is necessary to determine the potentials created by a horizontal electric dipole (HED) on the air-dielectric interface of the structure. Although a similar derivation of these potentials is given in [3], several details of the derivation reveal concepts important to the implementation of the method, and for this reason it is included in this appendix.

Consider an x-directed HED placed at the origin on the air-dielectric interface (Figure 2.1). A solution to the *homogeneous* Helmholtz equation for the vector potential will yield an expression for the potential due to the HED, in an *infinite homogeneous* medium. Consider the homogeneous Helmholtz equation for the vector potential in the spectral domain [3]:

$$\left(\frac{d^2}{dz^2} + u_i^2\right)\tilde{A} = 0 \qquad \textbf{(B.1)}$$

where $u_i^2 = k_x^2 + k_y^2 - k_i^2 = k_\rho^2 - k_i^2$ and k_i is the wavenumber of medium i. Since (B.1) is written in its spectral domain form, a general solution thereof is easily recognized to be of form

$$\tilde{A}_s = a e^{-u_i z} + b e^{+u_i z} \quad ; \quad s = (x, y, z) \tag{B.2}$$

where a and b are unknowns (they may be functions of the spectral variables k_x and k_y) which are to be determined through application of the boundary conditions. Now, in the case of an x-directed dipole embedded in an infinite homogeneous medium, the vector potential is given by [3]

$$\tilde{A} = \hat{x} \frac{\mu_0}{4\pi} \frac{\exp(-u_0 z)}{u_0} \tag{B.3}$$

where $u_0^2 = k_\rho^2 - k_0^2$ and k_0 the wavenumber in free space. In the case of an x-directed dipole on a *microstrip structure*, on the other hand, **two** components of the vector potential are needed to satisfy the boundary conditions [30]. These boundary conditions being [33]

$$\left.\begin{aligned} V_1 &= V_2 \\ A_1 &= A_2 \\ \frac{\partial A_{x1}}{\partial z} - \frac{\partial A_{x2}}{\partial z} &= -\mu_0 J_x \end{aligned}\right\} \quad on \; z = 0 \tag{B.4}$$

$$\left.\begin{aligned} V_2 &= 0 \\ A_{x2} &= 0 \\ \frac{\partial A_{z2}}{\partial z} &= 0 \end{aligned}\right\} \quad on\ z = -h \tag{B.5}$$

Hence, let $\mathbf{A} = \hat{\mathbf{x}}A_x + \hat{\mathbf{z}}A_z$. Choosing now for $\tilde{A}_x$ and $\tilde{A}_z$ general expressions of the form of (B.2) and applying the boundary conditions, leads to the following expressions [3]:

$$\tilde{A}_x = \frac{\mu_0}{2\pi}\left(\begin{array}{c} \dfrac{\exp(-u_0 z)}{D_{TE}} \\ \\ \dfrac{\sinh u(z+h)}{(D_{TE}\sinh uh)} \end{array}\right) \tag{B.6}$$

$$\tilde{A}_z = \frac{\mu_0}{2\pi}(\epsilon_r - 1)jk_x\left(\begin{array}{c} \dfrac{\exp(-u_0 z)}{D_{TE}\,D_{TM}} \\ \\ \dfrac{\cosh u(z+h)}{D_{TE}\,D_{TM}\cosh uh} \end{array}\right) \tag{B.7}$$

where $D_{TE} = u_0 + u\coth uh$, $D_{TM} = \epsilon_r u_0 + u\tanh uh$, $u^2 = k_\rho^2 - \epsilon_r k_0^2$, $\epsilon_r = \epsilon_r'(1-j\tan\delta)$ and h the substrate thickness. The upper and lower expressions inside symbols () correspond, respectively, to observers in the upper semi-infinite medium (free space: $z > 0$) and in the substrate ($-h < z < 0$). $z = 0$ represents an observer on the air-dielectric interface for which both expressions inside these symbols simplify to yield similar expressions. The Lorentz gauge [29] may now be used to obtain an expression for the scalar potential of a HED located on the air-dielectric interface of

a microstrip structure in the spectral domain [3]. Thus

$$\tilde{V} = \frac{-jk_x}{2\pi j\omega\epsilon_0}\begin{pmatrix} \dfrac{N\exp(-u_0 z)}{D_{TE}D_{TM}} \\ \\ \dfrac{N\sinh u(z+h)}{D_{TE}D_{TM}\sinh uh} \end{pmatrix} \tag{B.8}$$

with $N = u_0 + u \tanh uh$. The continuity equation applied to an electric dipole implies the existence of two point charges $q = \pm I/j\omega$ at both ends of the dipole [3]. Assuming $Idx = 1$, the moment of this pair of charges is $qdx = 1/j\omega$. In the spectral domain, the scalar potential of an electrostatic dipole ($\tilde{V}$) of moment $1/j\omega$ is related to the scalar potential of a single unit point charge ($\tilde{V}_q$) by the well-known expression [3]

$$\tilde{V} = -\frac{jk_x}{j\omega}\tilde{V}_q \tag{B.9}$$

Therefore, from (B.8) and (B.9) it follows that

$$\tilde{V}_q = \frac{1}{2\pi\epsilon_0}\begin{pmatrix} \dfrac{N\exp(-u_0 z)}{D_{TE}D_{TM}} \\ \\ \dfrac{N\sinh u(z+h)}{D_{TE}D_{TM}\sinh uh} \end{pmatrix} \tag{B.10}$$

Appropriate expressions for the vector potential ($\tilde{\mathbf{A}}$) due to a HED, and the scalar potential ($\tilde{V}_q$) due to a single unit point charge, have now been determined in the

spectral domain ((B.6),(B.7) and (B.10)). The formulation used in this thesis, however, is in the spatial domain, which implies that an inverse transformation has to be applied. Since D_{TE} and D_{TM} depend on k_x and k_y only through the radial spectral variable $k_\rho^2 = k_x^2 + k_y^2$, the inverse Fourier transform can be written as a Hankel transform [3]:

$$\mathcal{F}^{-1}[\tilde{f}(k_\rho)] = \int_0^\infty J_0(k_\rho R)\, k_\rho \tilde{f}(k_\rho)\, dk_\rho \qquad \text{(B.11)}$$

and

$$\mathcal{F}^{-1}[j k_x \tilde{f}(k_\rho)] = -\cos\phi \int_0^\infty J_1(k_\rho R)\, k_\rho^2\, \tilde{f}(k_\rho)\, dk_\rho \qquad \text{(B.12)}$$

where R and ϕ are polar co-ordinates and J_n the Bessel function of n'th order and first kind. The spatial domain expressions for the potentials are therefore given by

$$A_x(r/r') = \frac{\mu_0}{2\pi} \int_0^\infty J_0(k_\rho R)\, \frac{k_\rho}{D_{TE}} \exp(-u_0 z)\, dk_\rho \qquad \text{(B.13)}$$

$$A_z(r/r') = -\frac{\mu_0}{2\pi} \cos\phi\, (\epsilon_r - 1) \int_0^\infty J_1(k_\rho R)\, \frac{k_\rho^2}{D_{TE} D_{TM}} \exp(-u_0 z)\, dk_\rho \qquad \text{(B.14)}$$

$$V_q(r/r') = \frac{1}{2\pi\epsilon_0} \int_0^\infty J_0(k_\rho R)\, \frac{k_\rho N}{D_{TE} D_{TM}} \exp(-u_0 z)\, dk_\rho \qquad \text{(B.15)}$$

with $\mathbf{r} = \hat{\mathbf{x}}\,x + \hat{\mathbf{y}}\,y + \hat{\mathbf{z}}\,z$, $R = |\,\mathbf{r} - \mathbf{r}'\,|$ and $\phi = \tan^{-1}[(y-y')/(x-x')]$. The integrals above are line integrals on the complex k_ρ-plane where $k_\rho = \lambda + j\nu$. Mosig and Gardiol [3] have found that *integration along the contour described by the real positive λ-axis*, provides the most efficient means of evaluating these integrals. In this regard, we set $k_\rho = \lambda$ in the expressions above. Therefore

$$A_x(r/r') = \frac{\mu_0}{2\pi}\int_0^\infty J_0(\lambda R)\,\frac{\lambda}{D_{TE}}\exp(-u_0 z)\,d\lambda \qquad \textbf{(B.16)}$$

$$A_z(r/r') = -\frac{\mu_0}{2\pi}\cos\phi\,(\epsilon_r - 1)\int_0^\infty J_1(\lambda R)\,\frac{\lambda^2}{D_{TE}\,D_{TM}}\exp(-u_0 z)\,d\lambda \qquad \textbf{(B.17)}$$

$$V_q(r/r') = \frac{1}{2\pi\epsilon_0}\int_0^\infty J_0(\lambda R)\,\frac{\lambda\,N}{D_{TE}\,D_{TM}}\exp(-u_0 z)\,d\lambda \qquad \textbf{(B.18)}$$

At this point, we have derived expressions from which the required Green's functions for $z \geq 0$ follow directly: $G_V = V_q$[1], $G_A^{xx} = A_x$ and $G_A^{zx} = A_z$. The other terms of the dyadic Green's function are either zero ($G_A^{xy} = G_A^{yx} = 0$), not important for the purposes of this analysis (G_A^{xz}, G_A^{yz}, G_A^{zz}) or may be obtained from symmetry (G_A^{yy}, G_A^{zy}). In the determination of the *surface current distribution (as opposed to far-field radiation), we are interested in the potentials on the air-dielectric interface (z = z' = 0)*. Expressions (B.16)-(B.18) therefore reduce to

[1] The Green's function G_V is viewed as the scalar potential created by an *isolated point charge* on the air-dielectric interface. Since these charges do not exist in the real world, *G_V is rather considered to be a useful mathematical device*.

$$A_x(r/r') = \frac{\mu_0}{2\pi}\int_0^{\infty} J_0(\lambda R)\frac{\lambda}{D_{TE}}d\lambda \qquad \textbf{(B.19)}$$

$$A_z(r/r') = -\frac{\mu_0}{2\pi}\cos\phi\,(\epsilon_r - 1)\int_0^{\infty} J_1(\lambda R)\frac{\lambda^2}{D_{TE}D_{TM}}d\lambda \qquad \textbf{(B.20)}$$

$$V_q(r/r') = \frac{1}{2\pi\epsilon_0}\int_0^{\infty} J_0(\lambda R)\frac{\lambda N}{D_{TE}D_{TM}}d\lambda \qquad \textbf{(B.21)}$$

In conclusion, expressions for the vector potential (**A**) due to a HED, and the scalar potential (V_q) due to a single unit point charge, have now been determined in the spatial domain ((B.16) through (B.18)). These expressions are valid for $z \geq 0$; however, for surface current computation the special case $z = 0$ is to be considered. Far-field radiation calculations on the other hand, require knowledge of the potentials for $z > 0$. It was also shown that the Green's function expressions for a grounded dielectric slab follow directly from the expressions for these potentials.

APPENDIX C

ANALYTICAL INTEGRATION OF THE SINGULAR PART IN VECTOR POTENTIAL DISCRETE GREEN'S FUNCTION SELFTERM EVALUATIONS

In the evaluation of the discrete Green's function selfterms the situation arises where the observer and a source cell coincide. This leads to singularities in the discrete Green's function integrands due to the presence of the Green's functions therein. It was then suggested by Mosig and Gardiol [3] that the singular parts of the Green's functions be extracted as follows: $G = G_s + (G - G_s)$, where G represents the Green's functions and G_s the static values given by [3]

$$G_{As}^{xx}(r/r') = \frac{\mu_0}{4\pi\,|r-r'|} \tag{C.1}$$

for the vector potential, and

$$G_{Vs}(r/r') = \frac{1}{2\pi\epsilon_0(\epsilon_r+1)\,|r-r'|} \tag{C.2}$$

for the scalar potential; ϵ_r is the complex relative permittivity which takes into account dielectric losses. The discrete Green's function integrands with the difference terms $(G-G_s)$ are well-behaved functions and can be integrated numerically, while the integrands with the static parts, although being singular for $\mathbf{r} = \mathbf{r}'$, are analytically integrable. It is the purpose of this appendix to perform such an analytical surface integration.

The discrete Green's functions are defined as follows:

$$\Gamma_A^{xx}(r/r_{xj}) = \int_{S_{xj}} \frac{1}{\mu_0 k_0} G_A^{xx}(r/r') T_x(r' - r_{xj}) k_0^2 dS' \qquad \text{(C.3)}$$

$$\Gamma_V(r/r_{oj}) = \int_{S_{oj}} \frac{\epsilon_0}{k_0} G_V(r/r') \Pi(r' - r_{oj}) k_o^2 dS' \qquad \text{(C.4)}$$

Since only an expression for $\Gamma_{Vs}(\mathbf{r}/\mathbf{r})$[1] is given in [3], it is the purpose of this appendix to derive analytically an expression for $\Gamma_{As}^{xx}(\mathbf{r}/\mathbf{r}_{xj})$, where $\mathbf{r}$ lies within the boundaries of the x-directed current cell centred at $\mathbf{r}_{xj}$. In the construction of the C_{ij}^{xx} submatrix, Γ_A^{xx} appears in the term

$$\int_{C_{xi}} \Gamma_A^{xx}(r/r_{xj})\, dx \qquad \text{(C.5)}$$

For i = j, the single integral in (C.5) implies that the observer $\mathbf{r}$ may be situated at any point along the test segment C_{xi} placed within the source current cell at $\mathbf{r}_{xj}$. Surface integration for Γ_A^{xx} over the current cell, now leads to the point $\mathbf{r}' = \mathbf{r}$ being included within S_0 which on its turn leads to a singularity in the Green's function (and therefore the Γ_A^{xx} integrand) at that point. From (C.3), with the basis functions selected in Section 2.3.3, it follows that

[1] The subscript *s* indicates that the Green's function, appearing in the discrete Green's function integrand, has been replaced by it's static part.

$$\Gamma_A^{xx}(r/r_{xj}) = \int_{S_{xj}} \frac{1}{\mu_0 k_0} G_A^{xx}(r/r') \left[1 - \frac{|x' - x_{xj}|}{a}\right] k_0^2 \, dS' \qquad \text{(C.6)}$$

Since $\mathbf{r}_{xj}$ has no effect on the final expression (a correct choice does however simplify mathematical manipulation), we may conveniently suppose that the source current cell is centred at $\mathbf{r}_{xj} = (0,0)$. Therefore

$$\Gamma_A^{xx}(r/0) = \int_{S_0} \frac{1}{\mu_0 k_0} G_A^{xx}(r/r') \left[1 - \frac{|x'|}{a}\right] k_0^2 \, dS' \qquad \text{(C.7)}$$

S_0 is now the surface occupied by the x-directed current cell centred at (0,0). Application of the pole extraction technique described above, leads to the following expression:

$$\Gamma_A^{xx}(r/0) = \int_{S_0} \frac{1}{\mu_0 k_0} \left[G_{As}^{xx}(r/r') + \left(G_A^{xx}(r/r') - G_{As}^{xx}(r/r')\right)\right] \left[1 - \frac{|x'|}{a}\right] k_0^2 \, dS' \qquad \text{(C.8)}$$

Let us introduce Γ_{As}^{xx} by retaining the singular part of this expression. Now

$$\Gamma_{As}^{xx}(r/0) = \int_{S_0} \frac{k_0}{\mu_0} G_{As}^{xx}(r/r') \left[1 - \frac{|x'|}{a}\right] dS' \qquad \text{(C.9)}$$

Subsequent substitution of (C.1) into (C.9) leads to

$$\Gamma_{As}^{xx}(r/0) = \frac{k_0}{4\pi} \int_{S_0} \frac{1}{|r - r'|} \, dS' - \frac{k_0}{4\pi a} \int_{S_0} \frac{|x'|}{|r - r'|} \, dS' \qquad \text{(C.10)}$$

Since S_0 is centred at the origin, the x-directed test segment therein extends along the x-axis and therefore we know that the singularity is bound to this axis (Figure C.1). Also, because the integrands of (C.10) are symmetric around this axis, integration may be performed over the first two quadrants ($y > 0$) and the result doubled to account for the contribution of the third and fourth quadrants ($y < 0$). Therefore, it follows that

$$\Gamma_{As}^{\infty}(r/0) = \frac{k_0}{2\pi}\int_{S_0'}\frac{1}{|r-r'|}dS' - \frac{k_0}{2\pi a}\int_{S_0'}\frac{|x'|}{|r-r'|}dS' \qquad \textbf{(C.11)}$$

where S_0' is now the area occupied by the *first and second quadrants* of the current cell centred at (0,0). Let us suppose that $\mathbf{r} = r_x\hat{\mathbf{x}}$ where $0 \le r_x \le a/2$; we also have $\mathbf{r}' = x'\hat{\mathbf{x}} + y'\hat{\mathbf{y}}$. Thus $|\mathbf{r} - \mathbf{r}'| = [(r_x-x')^2 + y'^2]^{1/2}$. Analytical integration may be simplified by application of the substitution $x'' = x' - r_x$ and $y'' = y'$. This implies that $dx'' = dx'$, $dy'' = dy'$ and $dS'' = dx''dy'' = dS'$, while the integration limits are altered accordingly. S_0'' is now the area on the x"y"-plane described by $-b/2 \le y'' \le b/2$ and $-(a+r_x) \le x'' \le (a-r_x)$. We now have

$$\Gamma_{As}^{\infty}(\hat{x}\,r_x/0) = \frac{k_0}{2\pi}\int_{S_0''}\frac{1}{\sqrt{x''^2+y''^2}}dS'' - \frac{k_0}{2\pi a}\int_{S_0''}\frac{|x''+r_x|}{\sqrt{x''^2+y''^2}}dS'' \qquad \textbf{(C.12)}$$

The introduction of cylindrical coordinates further simplifies integration, hence let $r'' = [x''^2+y''^2]^{1/2}$ and $dS'' = r''dr''d\phi''$. Then

$$\Gamma_{As}^{xx}(\hat{x}\, r_x/0) = \frac{k_0}{2\pi}\int_{S_{0c}''} dr''d\phi'' - \frac{k_0}{2\pi a}\int_{S_{0c}''} |\, r''\cos\phi'' + r_x \,|\, dr''d\phi'' \qquad \text{(C.13)}$$

where the integration limits have also changed with S_{0c}'' representing S_0'' in cylindrical coordinates. From Figure C.1 it can be seen that if the integration interval (S_{0c}'') is carefully divided into sub-intervals, simple expressions may be obtained for the integration limits in terms of cylindrical coordinates. Consider therefore the following subdivisions:

SUB-INTERVAL 1: $\alpha_1 = \tan^{-1}[b/(2(a-r_x))]; \quad 0 \le \phi'' \le \alpha_1;$

$0 \le r'' \le (a-r_x)\sec(\phi'')$

SUB-INTERVAL 2: $\alpha_3 = \tan^{-1}[b/(2r_x)]; \quad \alpha_1 \le \phi'' \le \pi - \alpha_3;$

$0 \le r'' \le b/2\ \mathrm{cosec}(\phi'')$

SUB-INTERVAL 3: $\alpha_2 = \tan^{-1}[b/(2(a+r_x))]; \quad \pi - \alpha_3 \le \phi'' \le \pi - \alpha_2;$

$0 \le r'' \le b/2\ \mathrm{cosec}(\phi'')$

SUB-INTERVAL 4: $\pi - \alpha_2 \le \phi'' \le \pi; \quad 0 \le r'' \le -(a+r_x)\sec\phi''$

Let us consider the two terms in (C.13) separately. For the first term, integration may be performed over *three* sub-intervals since the derivative of the argument is not discontinuous in the transition from $x'' \ge -r_x$ to $x'' < -r_x$. This is the case for the integrand in the second term of (C.13) and therefore integration is performed over all *four* sub-intervals. Consider, firstly

$$I_1 = \frac{k_0}{2\pi}\int_{S''_{0c}} dr''d\phi'' = \frac{k_0}{2\pi}\left(\int_0^{\alpha_1}\int_0^{(a-r_x)\sec\phi''} dr''d\phi'' + \int_{\alpha_1}^{\pi-\alpha_2}\int_0^{b/2\operatorname{cosec}\phi''} dr''d\phi'' + \int_{\pi-\alpha_2}^{\pi}\int_0^{-(a+r_x)\sec\phi''} dr''d\phi''\right)$$

$$= \frac{k_0}{2\pi}\left((a-r_x)\ln\tan\left(\frac{\phi''}{2}+\frac{\pi}{4}\right)\Big|_0^{\alpha_1} + \frac{b}{2}\ln\tan\left(\frac{\phi''}{2}\right)\Big|_{\alpha_1}^{\pi-\alpha_2} - (a+r_x)\ln\tan\left(\frac{\phi''}{2}+\frac{\pi}{4}\right)\Big|_{\pi-\alpha_2}^{\pi}\right) \quad \textbf{(C.15)}$$

$$= \frac{k_0}{2\pi}\left((a-r_x)\ln\tan\left(\frac{\alpha_1}{2}+\frac{\pi}{4}\right) + \frac{b}{2}\ln\left[\frac{\tan\left(\frac{\pi}{2}-\frac{\alpha_2}{2}\right)}{\tan\left(\frac{\alpha_1}{2}\right)}\right] - (a+r_x)\ln\left[\frac{\tan\left(\frac{3}{4}\pi\right)}{\tan\left(\frac{3}{4}\pi-\frac{\alpha_2}{2}\right)}\right]\right) \quad \textbf{(C.16)}$$

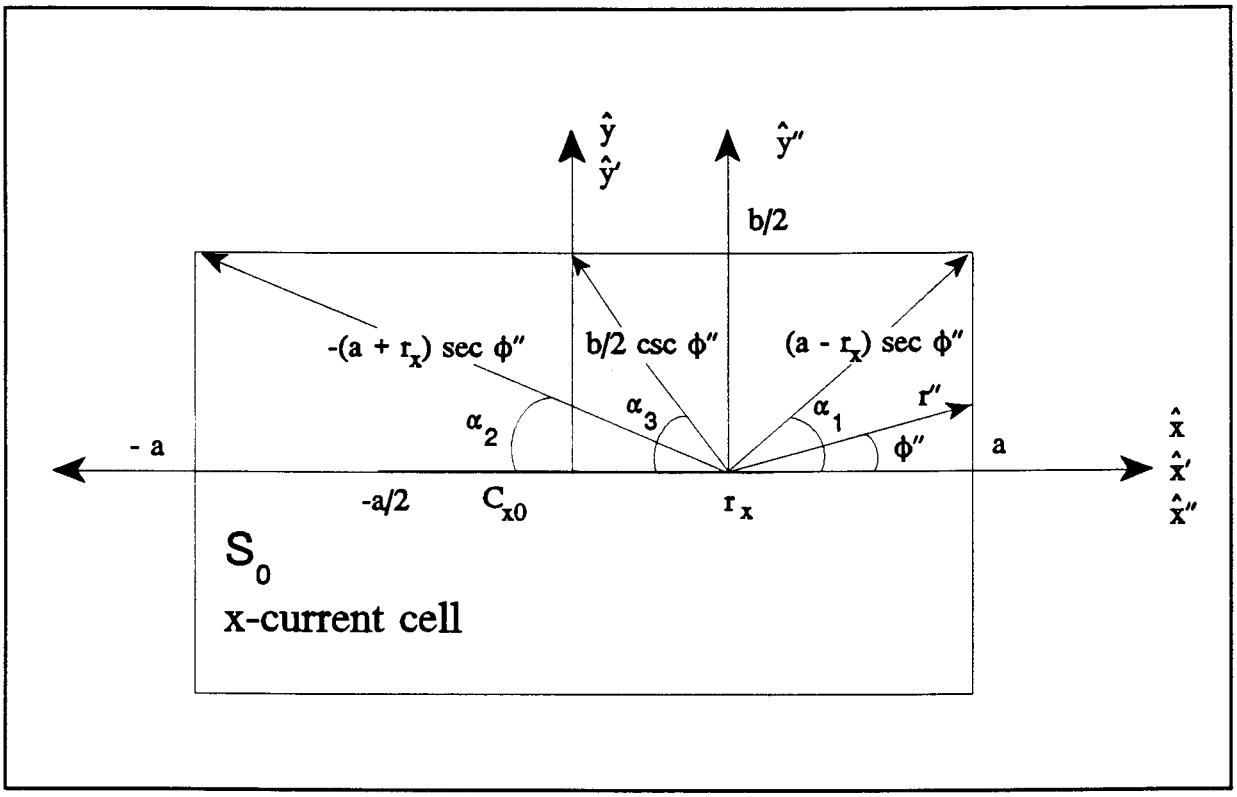

Figure C.1: *X-directed current cell with test segment C_{x0}. The observer (singularity) is situated on the x-axis at r_x. Sub-intervals with integration limits on ϕ'' and r'' are indicated.*

We note from (C.16) that $\tan(3\pi/4) = -1$ appears in the argument of the natural logarithm !. However, for $0 \le r_x \le a/2$ we have $\alpha_2/2 < \pi/4$, and therefore $\pi/2 < 3\pi/4 - \alpha_2/2 < \pi$. This implies that the denominator will always be negative, bringing about a positive argument for the logarithm. This argument may be rewritten as

$$\frac{\tan(\frac{3}{4}\pi)}{\tan(\frac{3}{4}\pi - \frac{\alpha_2}{2})} = \frac{-\tan(\pi - \frac{3}{4}\pi)}{-\tan(\pi - \frac{3}{4}\pi + \frac{\alpha_2}{2})} = \left[\tan(\frac{\alpha_2}{2} + \frac{\pi}{4})\right]^{-1} \qquad \textbf{(C.17)}$$

leading to a simplified expression for I_1:

$$I_1 = \frac{k_0}{2\pi}\left((a-r_x)\ln\tan\left(\frac{\alpha_1}{2}+\frac{\pi}{4}\right) + \frac{b}{2}\ln\left[\frac{\tan\left(\frac{\pi}{2}-\frac{\alpha_2}{2}\right)}{\tan\left(\frac{\alpha_1}{2}\right)}\right] + (a+r_x)\ln\tan\left(\frac{\alpha_2}{2}+\frac{\pi}{4}\right)\right) \qquad \textbf{(C.18)}$$

This has been the evaluation of the first term in (C.13). Consider now the second term in that expression. This integrand consists of $| r''\cos\phi'' + r_x |$ which transforms to $| x'' + r_x |$ in rectangular coordinates. This implies that

$$|x''+r_x| = \begin{cases} x''+r_x & for \quad x'' \ge -r_x \\ -(x''+r_x) & for \quad x'' < -r_x \end{cases} \qquad \textbf{(C.19)}$$

Thus, once $\phi'' > \pi - \alpha_3$, integration over r'' must be performed in two parts: from 0 to

$x=x'=0$ and secondly from there on to the edges of the current cell (Figure C.1). Therefore we define I_2 as

$$I_2 = -\frac{k_0}{2\pi a}\int_{S''_{0c}} |r''\cos\phi'' + r_x|\,dr''d\phi'' = -\frac{k_0}{2\pi a}\int_0^{\alpha_1(a-r_x)\sec\phi''}\int_0 (r''\cos\phi'' + r_x)\,dr''d\phi''$$

$$-\frac{k_0}{2\pi a}\int_{\alpha_1}^{\pi-\alpha_3}\int_0^{b/2\operatorname{cosec}\phi''} (r''\cos\phi'' + r_x)\,dr''d\phi'' - \frac{k_0}{2\pi a}\int_{\pi-\alpha_3}^{\pi}\int_0^{-r_x\sec\phi''} (r''\cos\phi'' + r_x)\,dr''d\phi''$$

$$+\frac{k_0}{2\pi a}\int_{\pi-\alpha_3}^{\pi-\alpha_2}\int_{-r_x\sec\phi''}^{b/2\operatorname{cosec}\phi''} (r''\cos\phi'' + r_x)\,dr''d\phi'' + \frac{k_0}{2\pi a}\int_{\pi-\alpha_2}^{\pi}\int_{-r_x\sec\phi''}^{-(a+r_x)\sec\phi''} (r''\cos\phi'' + r_x)\,dr''d\phi'' \qquad \textbf{(C.20)}$$

Through the use of integration tables [23] the individual terms in (C.20) may be simplified as follows:

$$\int_0^{\alpha_1(a-r_x)\sec\phi''}\int_0 (r''\cos\phi'' + r_x)\,dr''d\phi'' = \left(r_x(a-r_x) + \frac{1}{2}(a-r_x)^2\right)\ln\tan\left(\frac{\alpha_1}{2}+\frac{\pi}{4}\right) \qquad \textbf{(C.21)}$$

$$\int_{\alpha_1}^{\pi-\alpha_3}\int_0^{b/2\operatorname{cosec}\phi''} (r''\cos\phi'' + r_x)\,dr''d\phi'' = r_x\frac{b}{2}\ln\left(\frac{\operatorname{cotan}\left(\frac{\alpha_3}{2}\right)}{\tan\left(\frac{\alpha_1}{2}\right)}\right) - \frac{b^2}{8}\left[\operatorname{cosec}(\pi-\alpha_3) - \operatorname{cosec}(\alpha_1)\right]$$

(C.22)

$$\int_{\pi-\alpha_3}^{\pi}\int_{0}^{-r_x\sec\phi''}(r''\cos\phi''+r_x)\,dr''d\phi'' = \frac{r_x^2}{2}\ln\tan\left(\frac{\alpha_3}{2}+\frac{\pi}{4}\right) \tag{C.23}$$

$$\int_{\pi-\alpha_3}^{\pi-\alpha_2}\int_{-r_x\sec\phi''}^{b/2\operatorname{cosec}\phi''}(r''\cos\phi''+r_x)\,dr''d\phi'' = \frac{b^2}{8}\left[\operatorname{cosec}(\pi-\alpha_3)-\operatorname{cosec}(\pi-\alpha_2)\right]$$

$$+\frac{r_x b}{2}\ln\left[\frac{\tan(\frac{\alpha_3}{2})}{\tan(\frac{\alpha_2}{2})}\right]-\frac{r_x^2}{2}\ln\tan\left(\frac{\alpha_2}{2}+\frac{\pi}{4}\right)+\frac{r_x^2}{2}\ln\tan\left(\frac{\alpha_3}{2}+\frac{\pi}{4}\right) \tag{C.24}$$

$$\int_{\pi-\alpha_2}^{\pi}\int_{-r_x\sec\phi''}^{-(a+r_x)\sec\phi''}(r''\cos\phi''+r_x)\,dr''d\phi'' = -\frac{a^2}{2}\ln\tan\left(\frac{\alpha_2}{2}+\frac{\pi}{4}\right) \tag{C.25}$$

Now I_2 may be written as

$$I_2 = -\frac{k_0 a}{4\pi}\ln\tan\left(\frac{\alpha_2}{2}+\frac{\pi}{4}\right)+\frac{k_0 b^2}{16\pi a}\left[\operatorname{cosec}(\alpha_3)-\operatorname{cosec}(\alpha_2)\right]$$

$$-\frac{k_0 r_x^2}{4\pi a}\ln\tan\left(\frac{\alpha_2}{2}+\frac{\pi}{4}\right)+\frac{k_0 r_x b}{4\pi a}\ln\left[\frac{\tan(\frac{\alpha_3}{2})}{\tan(\frac{\alpha_2}{2})}\right]$$

$$-\frac{k_0}{4\pi a}(a-r_x)^2\ln\tan\left(\frac{\alpha_1}{2}+\frac{\pi}{4}\right)+\frac{k_0 b^2}{16\pi a}\left[\operatorname{cosec}(\alpha_3)-\operatorname{cosec}(\alpha_1)\right] \tag{C.26}$$

$$-\frac{k_0 r_x}{2\pi a}(a-r_x)\ln\tan\left(\frac{\alpha_1}{2}+\frac{\pi}{4}\right)-\frac{k_0 r_x b}{4\pi a}\ln\left[\frac{\operatorname{cotan}(\frac{\alpha_3}{2})}{\tan(\frac{\alpha_1}{2})}\right]$$

Finally, $\Gamma_{As}^{xx}(\hat{x}r_x/0) = I_1 + I_2$, where I_1 is given by (C.18) and I_2 by (C.26). Therefore

$$\Gamma_{As}^{xx}(\hat{x}r_x/0) = \frac{k_0}{2\pi}\left[(a-r_x)\ln\tan\left(\frac{\alpha_1}{2}+\frac{\pi}{4}\right)+\frac{b}{2}\ln\left[\frac{\tan\left(\frac{\pi}{2}-\frac{\alpha_2}{2}\right)}{\tan\left(\frac{\alpha_1}{2}\right)}\right]+(a+r_x)\ln\tan\left(\frac{\alpha_2}{2}+\frac{\pi}{4}\right)\right]$$

$$-\frac{k_0 a}{4\pi}\ln\tan\left(\frac{\alpha_2}{2}+\frac{\pi}{4}\right) + \frac{k_0 b^2}{16\pi a}\left[\operatorname{cosec}(\alpha_3)-\operatorname{cosec}(\alpha_2)\right]$$

$$-\frac{k_0 r_x^2}{4\pi a}\ln\tan\left(\frac{\alpha_2}{2}+\frac{\pi}{4}\right) + \frac{k_0 r_x b}{4\pi a}\ln\left[\frac{\tan\left(\frac{\alpha_3}{2}\right)}{\tan\left(\frac{\alpha_2}{2}\right)}\right]$$

$$-\frac{k_0}{4\pi a}(a-r_x)^2\ln\tan\left(\frac{\alpha_1}{2}+\frac{\pi}{4}\right) + \frac{k_0 b^2}{16\pi a}\left[\operatorname{cosec}(\alpha_3)-\operatorname{cosec}(\alpha_1)\right]$$

$$-\frac{k_0 r_x}{2\pi a}(a-r_x)\ln\tan\left(\frac{\alpha_1}{2}+\frac{\pi}{4}\right) - \frac{k_0 r_x b}{4\pi a}\ln\left[\frac{\operatorname{cotan}\left(\frac{\alpha_3}{2}\right)}{\tan\left(\frac{\alpha_1}{2}\right)}\right] \qquad \textbf{(C.27)}$$

This expression was derived for the case of an x-directed current cell with $0 \le r_x \le a/2$. The case of a y-directed current cell follows similarly, and the derivation is therefore not repeated. In fact, when $a = b$ the expressions for Γ_{As}^{xx} and Γ_{As}^{yy} are identical. The case $-a/2 \le r_x \le 0$ is a mirror-image of $0 \le r_x \le a/2$ and therefore $\Gamma_{As}^{xx}(-\hat{x}r_x/0) = \Gamma_{As}^{xx}(\hat{x}r_x/0)$.

APPENDIX D

DETERMINATION OF THE RADIATED ELECTRIC FIELDS OF A MICROSTRIP ANTENNA GIVEN THE SURFACE CURRENT DISTRIBUTION

In this appendix we will derive expressions for the radiated electric fields of a microstrip antenna once the surface current distribution is known. Although final expressions for the radiated fields of a HED on microstrip are given in [3], no derivation is included and since the author is of the opinion that insight can be gained from such an exercise, it is performed in this appendix.

A general expression[1] for the electric field in terms of vector and scalar potentials is [49]

$$\boldsymbol{E} = -j\omega \boldsymbol{A} - \nabla V \tag{D.1}$$

where the vector potential is defined by

$$\boldsymbol{A}(\boldsymbol{r}) = \int_{S_0} \bar{\boldsymbol{G}}_{\boldsymbol{A}}(\boldsymbol{r}/\boldsymbol{r}') \cdot \boldsymbol{J}_s(\boldsymbol{r}')\, dS' \tag{D.2}$$

$\bar{\mathbf{G}}_{\mathbf{A}}$ is the Green's function associated with $\mathbf{A}(\mathbf{r})$ while $\mathbf{J}_s$ is the surface current distribution. Since this is a mixed-potential formulation, the scalar potential due to the surface current distribution (related to the charge distribution through the continuity

[1] This is a **general expression** not unique to microstrip.

equation) has to be determined. Applying the Lorentz gauge [49] to $\mathbf{A(r)}$ and making use of the equality $\nabla.\bar{\mathbf{G}}_{\mathbf{A}}(\mathbf{r}/\mathbf{r}') = \mu\epsilon\nabla\mathbf{G}_{\mathbf{V}}(\mathbf{r}/\mathbf{r}')$ [3] leads to an expression for the scalar potential in terms of $\mathbf{J}_s$ [3]:

$$V(r) = -\frac{1}{j\omega}\int_{S_0} \nabla G_V(r/r').J_s(r')\,dS' \qquad \textbf{(D.3)}$$

G_V is the Green's function associated with the scalar potential V. Substituting the expressions for the potentials into (D.1) results in

$$E(r) = -j\omega\int_{S_0} \bar{G}_A(r/r').J_s(r')\,dS' + \frac{1}{j\omega}\int_{S_0} \nabla\nabla G_V(r/r').J_s(r')\,dS' \qquad \textbf{(D.4)}$$

This expression may also be written as

$$E(r) = \int_{S_0} \bar{G}_E(r/r').J_s(r')\,dS' \qquad \textbf{(D.5)}$$

where

$$\bar{G}_E(r/r') = -j\omega\,\bar{G}_A(r/r') + \frac{\nabla\nabla G_V(r/r')}{j\omega} \qquad \textbf{(D.6)}$$

is a dyadic Green's function associated with the electric field. In (D.5) we now have an expression for the electric field in terms of the surface current distribution and the Green's function $\bar{\mathbf{G}}_{\mathbf{E}}$. This Green's function will now be expanded. The three-dimensional

dyadic Green's function $\bar{\mathbf{G}}_{\mathbf{A}}$ may be written as

$$\bar{G}_A = \begin{array}{c} \\ \hat{x} \\ \hat{y} \\ \hat{z} \end{array} \begin{array}{c} \begin{array}{ccc} \hat{x} & \hat{y} & \hat{z} \end{array} \\ \begin{bmatrix} G_A^{xx} & 0 & G_A^{xz} \\ 0 & G_A^{yy} & G_A^{yz} \\ G_A^{zx} & G_A^{zy} & G_A^{zz} \end{bmatrix} \end{array} \tag{D.7}$$

We also have

$$\nabla\nabla G_V = \begin{array}{c} \\ \hat{x} \\ \hat{y} \\ \hat{z} \end{array} \begin{array}{c} \begin{array}{ccc} \hat{x} & \hat{y} & \hat{z} \end{array} \\ \begin{bmatrix} \frac{\partial^2}{\partial x^2} G_V & \frac{\partial^2}{\partial x\,\partial y} G_V & \frac{\partial^2}{\partial x\,\partial z} G_V \\ \frac{\partial^2}{\partial y\,\partial x} G_V & \frac{\partial^2}{\partial y^2} G_V & \frac{\partial^2}{\partial y\,\partial z} G_V \\ \frac{\partial^2}{\partial z\,\partial x} G_V & \frac{\partial^2}{\partial z\,\partial y} G_V & \frac{\partial^2}{\partial z^2} G_V \end{bmatrix} \end{array} \tag{D.8}$$

Therefore $\bar{\mathbf{G}}_{\mathbf{E}}$ may be written as

$$\begin{array}{c} \\ \hat{x} \\ \hat{y} \\ \hat{z} \end{array} \begin{array}{c} \begin{array}{ccc} \hat{x} & \hat{y} & \hat{z} \end{array} \\ \begin{bmatrix} \frac{1}{j\omega}\frac{\partial^2}{\partial x^2} G_V - j\omega G_A^{xx} & \frac{1}{j\omega}\frac{\partial^2}{\partial x\,\partial y} G_V & \frac{1}{j\omega}\frac{\partial^2}{\partial x\,\partial z} G_V - j\omega G_A^{xz} \\ \frac{1}{j\omega}\frac{\partial^2}{\partial y\,\partial x} G_V & \frac{1}{j\omega}\frac{\partial^2}{\partial y^2} G_V - j\omega G_A^{yy} & \frac{1}{j\omega}\frac{\partial^2}{\partial y\,\partial z} G_V - j\omega G_A^{yz} \\ \frac{1}{j\omega}\frac{\partial^2}{\partial z\,\partial x} G_V - j\omega G_A^{zx} & \frac{1}{j\omega}\frac{\partial^2}{\partial z\,\partial y} G_V - j\omega G_A^{zy} & \frac{1}{j\omega}\frac{\partial^2}{\partial z^2} G_V - j\omega G_A^{zz} \end{bmatrix} \end{array} \tag{D.9}$$

In the moment method analysis, the surface current distribution $\mathbf{J_s}$ is given in terms of a set of discrete coefficients I_{xi} (i=1...M) and I_{yj} (j=1...N) each related to a charge cell of dimensions a and b. With this in mind, Mosig and Gardiol [3] have shown that in the far-field we can approximate the radiated electric field of the etched radiator by replacing it with an array of Hertz dipoles, for which the radiated electric field is given by

$$E_\theta = G_E^{\theta x}(r/0)\sum_{i=1}^{M} aI_{xi}\, e^{jk_0 g_i} + G_E^{\theta y}(r/0)\sum_{j=1}^{N} bI_{yj}\, e^{jk_0 g_j} \qquad \textbf{(D.10)}$$

$$E_\phi = G_E^{\phi x}(r/0)\sum_{i=1}^{M} aI_{xi}\, e^{jk_0 g_i} + G_E^{\phi y}(r/0)\sum_{j=1}^{N} bI_{yj}\, e^{jk_0 g_j} \qquad \textbf{(D.11)}$$

where $g_k = x_k\sin\theta\cos\phi + y_k\sin\theta\sin\phi$ (k=i,j) and $k_0 = \omega(\mu_0\epsilon_0)^{1/2}$; x_k and y_k are the coordinates of the k'th Hertz dipole. Since $\bar{\mathbf{G}}_E$, according to (D.9), is defined purely in terms of rectangular coordinates, a coordinate transformation has to be performed to determine $G_E^{\theta x}$, $G_E^{\theta y}$, $G_E^{\phi x}$ and $G_E^{\phi y}$. To illustrate such a transformation, consider for a moment a general dyadic

$$\bar{D} = D^{(x)}\hat{x} + D^{(y)}\hat{y} + D^{(z)}\hat{z} \qquad \textbf{(D.12)}$$

with

$$\begin{aligned} \boldsymbol{D}^{(x)} &= D^{xx}\hat{x} + D^{yx}\hat{y} + D^{zx}\hat{z} \\ \boldsymbol{D}^{(y)} &= D^{xy}\hat{x} + D^{yy}\hat{y} + D^{zy}\hat{z} \\ \boldsymbol{D}^{(z)} &= D^{xz}\hat{x} + D^{yz}\hat{y} + D^{zz}\hat{z} \end{aligned} \tag{D.13}$$

Now with a rectangular-to-spherical coordinate transformation, $\mathbf{D}^{(x)}$ becomes

$$\boldsymbol{D}^{(x)} = D^{rx}\hat{r} + D^{\theta x}\hat{\theta} + D^{\phi x}\hat{\phi} \tag{D.14}$$

where

$$\begin{aligned} D^{rx} &= D^{xx}\sin\theta\cos\phi + D^{yx}\sin\theta\sin\phi + D^{zx}\cos\theta \\ D^{\theta x} &= D^{xx}\cos\theta\cos\phi + D^{yx}\cos\theta\sin\phi - D^{zx}\sin\theta \\ D^{\phi x} &= -D^{xx}\sin\phi + D^{yx}\cos\phi \end{aligned} \tag{D.15}$$

In similar fashion, a coordinate transformation for $\bar{\mathbf{G}}_E(\mathbf{r}/0)$ yields

$$G_E^{\theta x}(r/0) = G_E^{xx}(r/0)\cos\theta\cos\phi + G_E^{yx}(r/0)\cos\theta\sin\phi - G_E^{zx}(r/0)\sin\theta \tag{D.16}$$

$$G_E^{\phi x}(r/0) = -G_E^{xx}(r/0)\sin\phi + G_E^{yx}(r/0)\cos\phi \tag{D.17}$$

$$G_E^{\theta y}(r/0) = G_E^{xy}(r/0)\cos\theta\cos\phi + G_E^{yy}(r/0)\cos\theta\sin\phi - G_E^{zy}(r/0)\sin\theta \tag{D.18}$$

$$G_E^{\phi y}(r/0) = -G_E^{xy}(r/0)\sin\phi + G_E^{yy}(r/0)\cos\phi \tag{D.19}$$

Let us now, for example, expand $G_E^{\theta x}(r/0)$. From (D.9) it follows that

$$G_E^{\theta x} = \left(\frac{1}{j\omega}\frac{\partial^2}{\partial x^2}G_V - j\omega G_A^{xx}\right)\cos\theta\cos\phi + \left(\frac{1}{j\omega}\frac{\partial^2}{\partial y\partial x}G_V\right)\cos\theta\sin\phi$$
$$-\left(\frac{1}{j\omega}\frac{\partial^2}{\partial z\partial x}G_V - j\omega G_A^{zx}\right)\sin\theta \qquad \textbf{(D.20)}$$

Since we are interested in the *radiated fields*, our observation point is no longer on the interface z = z′ = 0 and the expressions for $\bar{G}_A$ and G_V given in Appendix B of this thesis must be used. For the sake of this discussion, the relevant expressions are summarized below.

$$G_A^{xx}(r/r') = \frac{\mu_0}{2\pi}\int_0^\infty J_0(\lambda R)\frac{\lambda}{D_{TE}}e^{-u_0 z}d\lambda \qquad \textbf{(D.21)}$$

$$G_A^{zx}(r/r') = \frac{-\mu_0}{2\pi}\cos\phi\,(\epsilon_r - 1)\int_0^\infty J_1(\lambda R)\frac{\lambda^2}{D_{TE}D_{TM}}e^{-u_0 z}d\lambda \qquad \textbf{(D.22)}$$

$$G_A^{yy}(r/r') = G_A^{xx}(r/r') \qquad \textbf{(D.23)}$$

$$G_A^{zy}(r/r') = \frac{-\mu_0}{2\pi}\sin\phi\,(\epsilon_r - 1)\int_0^\infty J_1(\lambda R)\frac{\lambda^2}{D_{TE}D_{TM}}e^{-u_0 z}d\lambda \qquad \textbf{(D.24)}$$

$$G_V(r/r') = \frac{1}{2\pi\epsilon_0}\int_0^\infty J_0(\lambda R)\frac{\lambda}{D_{TE}}e^{-u_0 z}d\lambda \qquad \textbf{(D.25)}$$

The partial derivatives in (D.9) (some of which appear in (D.20)) may be obtained

through straightforward, albeit lengthy, algebra. These partial derivatives are given below.

$$\frac{\partial^2}{\partial x^2} G_V(r/r') = -\frac{1}{2\pi\epsilon_0} \int_0^\infty \left(\frac{J_1(\lambda R)}{R} - \lambda \left[\frac{x-x'}{R} \right]^2 J_2(\lambda R) \right) \frac{\lambda^2 N}{D_{TE} D_{TM}} e^{-u_0 z} d\lambda \quad \textbf{(D.26)}$$

$$\frac{\partial^2}{\partial y \partial x} G_V(r/r') = \frac{1}{2\pi\epsilon_0} \int_0^\infty \frac{(x-x')(y-y')}{R^2} J_2(\lambda R) \frac{\lambda^3 N}{D_{TE} D_{TM}} e^{-u_0 z} d\lambda \quad \textbf{(D.27)}$$

$$\frac{\partial^2}{\partial z \partial x} G_V(r/r') = \frac{1}{2\pi\epsilon_0} \int_0^\infty \frac{(x-x')}{R} J_1(\lambda R) \frac{\lambda^2 N}{D_{TE} D_{TM}} u_0 e^{-u_0 z} d\lambda \quad \textbf{(D.28)}$$

$$\frac{\partial^2}{\partial x \partial y} G_V(r/r') = \frac{\partial^2}{\partial y \partial x} G_V(r/r') \quad \textbf{(D.29)}$$

$$\frac{\partial^2}{\partial y^2} G_V(r/r') = -\frac{1}{2\pi\epsilon_0} \int_0^\infty \left(\frac{J_1(\lambda R)}{R} - \lambda \left[\frac{y-y'}{R} \right]^2 J_2(\lambda R) \right) \frac{\lambda^2 N}{D_{TE} D_{TM}} e^{-u_0 z} d\lambda \quad \textbf{(D.30)}$$

$$\frac{\partial^2}{\partial z \partial y} G_V(r/r') = \frac{1}{2\pi\epsilon_0} \int_0^\infty \frac{(y-y')}{R} J_1(\lambda R) \frac{\lambda^2 N}{D_{TE} D_{TM}} u_0 e^{-u_0 z} d\lambda \quad \textbf{(D.31)}$$

Therefore we have for $G_E^{\theta x}(\mathbf{r}/\mathbf{0})$, from (D.20):

$$G_E^{\theta x}(r/0) = -\left[\frac{1}{j\omega 2\pi\epsilon_0}\int_0^\infty\left(\frac{J_1(\lambda R)}{R} - \lambda(\frac{x}{R})^2 J_2(\lambda R)\right)\frac{\lambda^2 N}{D_{TE}D_{TM}}e^{-u_0 z}d\lambda\right]\cos\theta\cos\phi$$

$$-\left[\frac{j\omega\mu_0}{2\pi}\int_0^\infty J_0(\lambda R)\frac{\lambda}{D_{TE}}e^{-u_0 z}d\lambda\right]\cos\theta\cos\phi$$

$$+\left[\frac{1}{j\omega 2\pi\epsilon_0}\int_0^\infty \frac{xy}{R^2}J_2(\lambda R)\frac{\lambda^3 N}{D_{TE}D_{TM}}e^{-u_0 z}d\lambda\right]\cos\theta\sin\phi$$

$$-\left[\frac{1}{j\omega 2\pi\epsilon_0}\int_0^\infty \frac{x}{R}J_1(\lambda R)\frac{\lambda^2 N}{D_{TE}D_{TM}}u_0 e^{-u_0 z}d\lambda\right]\sin\theta$$

$$-\left[-\frac{\mu_0}{2\pi}\cos\phi(\epsilon_r - 1)\int_0^\infty J_1(\lambda R)\frac{\lambda^2}{D_{TE}D_{TM}}e^{-u_0 z}d\lambda\right]\sin\theta \qquad \textbf{(D.32)}$$

By expanding $G_E^{\theta y}$, $G_E^{\phi x}$ and $G_E^{\phi y}$ in similar fashion and defining

$$I_0 = \int_0^\infty J_0(\lambda R)\frac{\lambda}{D_{TE}}e^{-u_0 z}d\lambda \qquad \textbf{(D.33)}$$

$$I_1 = \int_0^\infty J_1(\lambda R)\frac{\lambda^2 N}{D_{TE}D_{TM}}e^{-u_0 z}d\lambda \qquad \textbf{(D.34)}$$

$$I_2 = \int_0^{\infty} J_2(\lambda R)\frac{\lambda^3 N}{D_{TE}D_{TM}} e^{-u_0 z} d\lambda \qquad \textbf{(D.35)}$$

$$I_3 = \int_0^{\infty} J_1(\lambda R)\frac{\lambda^2}{D_{TE}D_{TM}} e^{-u_0 z} d\lambda \qquad \textbf{(D.36)}$$

$$I_4 = \int_0^{\infty} J_1(\lambda R)\frac{\lambda^2 N}{D_{TE}D_{TM}} u_0 e^{-u_0 z} d\lambda \qquad \textbf{(D.37)}$$

we can write for (D.10) and (D.11):

$$E_\theta = \Bigg(\left[\frac{-j\omega\mu_0}{2\pi} I_0 - \frac{I_1}{j\omega 2\pi\epsilon_0 R} + \frac{I_2}{j\omega 2\pi\epsilon_0}\left(\frac{x}{R}\right)^2 \right] \cos\theta\cos\phi + \left[\frac{I_2}{j\omega 2\pi\epsilon_0}\frac{xy}{R^2} \right] \cos\theta\sin\phi -$$

$$\left[\frac{j\omega\mu_0}{2\pi}(\epsilon_r - 1)\cos\phi I_3 + \frac{I_4}{j\omega 2\pi\epsilon_0}\frac{x}{R} \right] \sin\theta \Bigg) \sum_{i=1}^{M} aI_{xi} e^{jk_0 g_i} +$$

$$\Bigg(\left[\frac{-j\omega\mu_0}{2\pi} I_0 - \frac{I_1}{j\omega 2\pi\epsilon_0 R} + \frac{I_2}{j\omega 2\pi\epsilon_0}\left(\frac{y}{R}\right) \right] \cos\theta\sin\phi + \left[\frac{I_2}{j\omega 2\pi\epsilon_0}\frac{xy}{R^2} \right] \cos\theta\cos\phi +$$

$$\left[\frac{j\omega\mu_0}{2\pi}(\epsilon_r - 1)\sin\phi I_3 + \frac{I_4}{j\omega 2\pi\epsilon_0}\frac{y}{R} \right] \sin\theta \Bigg) \sum_{j=1}^{N} bI_{yj} e^{jk_0 g_j} \qquad \textbf{(D.38)}$$

$$E_\phi = \left(\left[\frac{j\omega\mu_0}{2\pi} I_0 + \frac{I_1}{j\omega 2\pi\epsilon_0 R} - \frac{I_2}{j\omega 2\pi\epsilon_0} \left(\frac{x}{R}\right)^2 \right] \sin\phi \quad + \right.$$

$$\left. \left[\frac{I_2}{j\omega 2\pi\epsilon_0} \frac{xy}{R^2} \right] \cos\phi \right) \sum_{i=1}^{M} a I_{xi} e^{jk_0 g_i} \quad +$$

$$\left(\left[\frac{-j\omega\mu_0}{2\pi} I_0 - \frac{I_1}{j\omega 2\pi\epsilon_0 R} + \frac{I_2}{j\omega 2\pi\epsilon_0} \left(\frac{y}{R}\right)^2 \right] \cos\phi \quad - \right. \tag{D.39}$$

$$\left. \left[\frac{I_2}{j\omega 2\pi\epsilon_0} \frac{xy}{R^2} \right] \sin\phi \right) \sum_{j=1}^{N} b I_{yj} e^{jk_0 g_j}$$

Closer inspection[2] of the integrands in (D.33) through (D.37) leads one to the conclusion that straightforward integration will not suffice for these integrals and therefore we make use of the *method of steepest descent* [28]. Then we have for the integrals in (D.33) through (D.37):

$$I_0 \sim j\,cotan\theta\, f_0(k_0 \sin\theta) \frac{e^{-jk_0 r}}{r} \; ; \qquad f_0(x) = \frac{x}{D_{TE}(x)} \tag{D.40}$$

$$I_2 \sim -j\,cotan\theta\, f_2(k_0 \sin\theta) \frac{e^{-jk_0 r}}{r} - U(\theta - \theta_p) 2\pi j Res_2 H_2^{(2)}(\lambda_p \rho)\, e^{-z\sqrt{\lambda_p^2 - k_0^2}}$$

$$f_2(x) = \frac{x^3 N(x)}{D_{TE}(x)\, D_{TM}(x)} \tag{D.41}$$

[2] Section 3.7 gives further detail.

$$I_3 \approx -cotan\theta\, f_3(k_0 \sin\theta)\frac{e^{-jk_0 r}}{r} - U(\theta-\theta_p)2\pi j Res_3 H_1^{(2)}(\lambda_p \rho)\, e^{-z\sqrt{\lambda_p^2-k_0^2}} \qquad \textbf{(D.42)}$$

$$f_3(x)=\frac{x^2}{D_{TE}D_{TM}}$$

$$I_4 \approx -cotan\theta\, f_4(k_0 \sin\theta)\frac{e^{-jk_0 r}}{r} - U(\theta-\theta_p)2\pi j Res_4 H_1^{(2)}(\lambda_p \rho)\, e^{-z\sqrt{\lambda_p^2-k_0^2}} \qquad \textbf{(D.43)}$$

$$f_4(x) = \frac{x^2 u_0(x) N(x)}{D_{TE}(x) D_{TM}(x)}$$

where Res_i is the residue of function f_i (i=2,3,4) at λ_p. Since I_1 only appears in terms with "R" in the denominator (D.38 and D.39), and because these terms tend to zero in the far-field, it is not necessary to evaluate I_1. By replacing "x" and "y" in (D.38) and (D.39) with R cos ϕ and R sin ϕ, respectively, the final expressions for the electric fields are now given by

$$\begin{aligned} E_\theta = (& \left[-A_0 I_0 + A_2 \cos^2\phi\, I_2\right]\cos\theta\cos\phi + \left[A_2 \cos\phi \sin\phi\, I_2\right]\cos\theta\sin\phi - \\ & \left[A_0(\epsilon_r - 1)\cos\phi\, I_3 + A_2 \cos\phi\, I_4\right]\sin\theta\ ) \sum_{i=1}^{M} aI_{xi}\, e^{jk_0 g_i} \quad + \\ (& \left[-A_0 I_0 + A_2 \sin^2\phi\, I_2\right]\cos\theta\sin\phi + \left[A_2 \cos\phi \sin\phi\, I_2\right]\cos\theta\cos\phi - \\ & \left[A_0(\epsilon_r - 1)\sin\phi\, I_3 + A_2 \sin\phi\, I_4\right]\sin\theta\ ) \sum_{j=1}^{N} bI_{yj}\, e^{jk_0 g_j} \end{aligned} \qquad \textbf{(D.44)}$$

$$E_\phi = \left(\left[A_0 I_0 - A_2 \cos^2\phi I_2 \right] \sin\phi + \left[A_2 \cos\phi \sin\phi I_2 \right] \cos\phi \right) \sum_{i=1}^{M} a I_{xi} e^{jk_0 g_i} + \left(\left[-A_0 I_0 + A_2 \sin^2\phi I_2 \right] \cos\phi - \left[A_2 \cos\phi \sin\phi I_2 \right] \sin\phi \right) \sum_{j=1}^{N} b I_{yj} e^{jk_0 g_j} \quad \textbf{(D.45)}$$

where

$$A_0 = \frac{j\omega\mu_0}{2\pi} \quad \textbf{(D.46)}$$

and

$$A_2 = \frac{1}{j\omega 2\pi\epsilon_0} \quad \textbf{(D.47)}$$

APPENDIX E

THE RELATIONSHIP BETWEEN THE COEFFICIENTS I_{xi} AND I_{yi} AND ELECTRICAL CURRENT FLOWING ON THE ELEMENTS OF WIRE-GRID ARRAYS

The solution to the moment matrix equation yields the coefficients I_{xi} and I_{yi}. The aim of this appendix is to examine the relationship between these coefficients and the electrical current flowing on the elements of wire-grid arrays.

In the integral equation formulation discussed in Chapter 2, the unknown surface current distribution on the upper conductor of an etched radiator is expanded over rooftop basis functions as follows (Section 2.3.3):

$$J_{sx} = \frac{1}{b} \sum_{i=1}^{M} I_{xi} T_x(r - r_{xi}) \qquad \left(\frac{A}{m}\right) \tag{E.1}$$

$$J_{sy} = \frac{1}{a} \sum_{i=1}^{N} I_{yi} T_y(r - r_{yi}) \qquad \left(\frac{A}{m}\right) \tag{E.2}$$

where

$$T_x(r) = \begin{cases} 1 - |x|/a & ; \quad |x| < a \ , \quad |y| < b/2 \\ 0 & ; \quad \textit{elsewhere} \end{cases} \tag{E.3}$$

and a similar expression holds for $T_y(\mathbf{r})$. These expressions give the relationship between coefficients I_{xi} and I_{yi}, and the surface current *density* existing on the radiator. From these

expressions it also follows that coefficients I_{xi} and I_{yi} have dimensions of current (A). To relate these coefficients to the total current flowing on an element of an etched wire-grid array, consider an x-directed segment of width w_s; Figure E.1 shows part of this segment after decomposition of the upper conductor into charge cells of dimensions a and b. Rooftop basis functions of which the coefficients I_{xi} (i=1..m) are known through the solution of the moment method matrix equation, are also shown on the figure. To calculate the total x-directed current $I_{tot}(x)$ flowing along the segment past a given position along the segment, the contributions of the S x-directed strips comprising the element of width w_s (w_s = S × b) have to be added. Thus

$$I_{tot}(x) = \sum_{i=1}^{S} I_i(x) \qquad (A) \tag{E.4}$$

so that the calculation of $I_{tot}(x)$ requires knowledge of the individual contributions $I_i(x)$. Consider for example the calculation of $I_4(x_1)$ in Figure E.1. At x_1 two rooftop distributions of current density exist and both have to be included in the calculation of $I_4(x_1)$. The x-directed current density at x_1 is given by

$$J_{sx}(x_1) = \frac{I_{x1}}{b}\left\{1-\frac{x_1}{a}\right\} + \frac{I_{x2}}{b}\left\{1+\frac{x_1-a}{a}\right\} \qquad \left(\frac{A}{m}\right) \tag{E.5}$$

The total current flowing across an element of width dy at x_1 (Figure E.1) is then $J_{sx}(x_1)$ dy. Therefore the total current flowing along a strip of width b past x_1 is

$$I_4(x_1) = \int_0^b J_{sx}(x_1)\, dy = I_{x1}\left\{1-\frac{x_1}{a}\right\} + I_{x2}\left\{1+\frac{x_1-a}{a}\right\} \qquad (A) \qquad \textbf{(E.6)}$$

In the same way, values for $I_i(x)$ may be determined for any x and i=1 to S. With this and (E.4) it is now possible to calculate the total x-directed current flowing along the segment of width w_s past any position along the segment. This is given in terms of the coefficients I_{xi}. Similar expressions hold for y-directed segments.

Consider the following special case: from (E.6) and $x_1=0$ ($x_1=a$) it follows that the total current flowing across the common boundary of the two charge cells is given by I_{x1} (I_{x2}). From this it follows that the total current flowing across all the charge cell boundaries at $x=x_2$ in Figure E.1 will be

$$I_{tot}(x_2) = \sum_{i=4}^{m} I_{xi} \qquad (A) \qquad \textbf{(E.7)}$$

(E.7) gives an expression in terms of coefficients I_{xi} for the total current flowing along a segment past a given position which coincides with charge cell boundaries in the decomposition of the segment. If the position along the segment at which total current has to be calculated does not coincide with charge cell boundaries, expressions (E.4) and (E.6) have to be used.

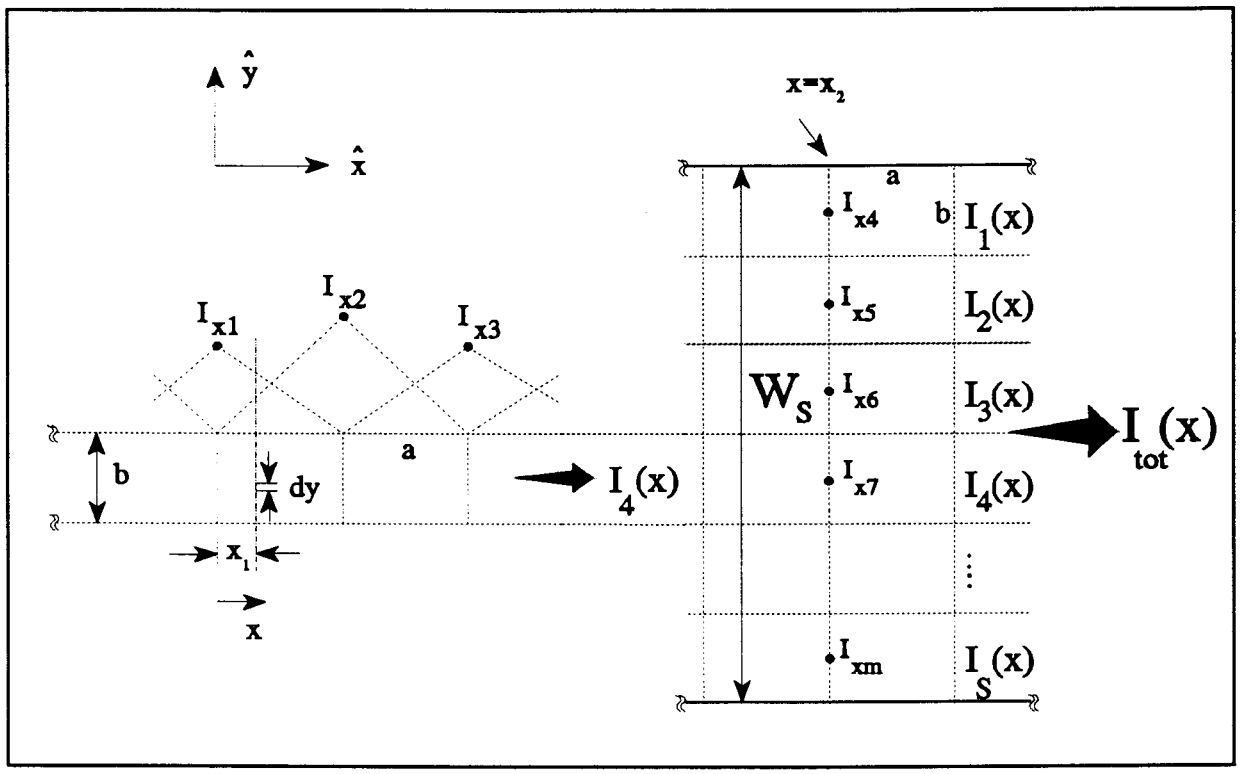

Figure E.1: *Decomposition of an x-directed segment on an etched radiator to calculate the total current flowing along the segment. Rooftop basis functions are used in the moment method solution.*

REFERENCES

[1] J.D. Kraus, "A backward angle-fire array antenna", *IEEE Trans.*, vol. AP-12, no. 1, pp. 48-50, Jan. 1964.

[2] J.R. Mosig and F.E. Gardiol, "General integral equation formulation for microstrip antennas and scatterers," *IEE Proc.*, vol. 132, Pt.H, no. 7, Dec. 1985.

[3] J.R. Mosig and F.E. Gardiol, "Numerical analysis of microstrip patch antennas" in: J.R. James and P.S. Hall (Edits.), *Handbook of microstrip antennas* (Peter Peregrinus, vol. 1, Chapter 8, 1989).

[4] J.R. Mosig and F.E. Gardiol, "A dynamical radiation model for microstrip structures," in P. Hawkes (Edit) *Advances in electronics and electron physics* (Academic Press, 1982) pp. 139-237.

[5] L. Lier, "Improved formulas for input impedance of coax-fed microstrip patch antennas," *IEE Proc.*, Pt.H, 129, pp. 161-164, 1982.

[6] W.F. Richards, Y.T. Lo and D.D. Harrison, "An improved theory for microstrip antennas and applications," *IEEE Trans.*, vol. AP-29, pp. 38-46, 1981.

[7] R.F. Harrington, *Field Computation by Moment Methods* (MacMillan, 1968).

[8] D.M. Pozar, "Microstrip antennas", *Proc.IEEE*, vol. 80, no. 1, pp. 79-91, Jan. 1992.

[9] K.A. Michalski and D. Zheng, "Analysis of microstrip resonators of arbitrary shape", *IEEE Trans. Microwave Theory Tech.*, vol. MTT-40, no. 1, pp. 112-119, Jan. 1992.

[10] M. Marin, S. Barkeshli and P.H. Pathak, "Efficient analysis of planar microstrip geometries using a closed-form asymptotic representation of the grounded dielectric slab Green's function", *IEEE Trans. Microwave Theory Tech.*, vol. MTT-37, no. 4, pp. 669-678, April 1989.

[11] R.F. Harrington, *Time Harmonic Electromagnetic Fields* (McGraw-Hill, 1961).

[12] P.J. Davies and P. Rabinowitz, *Methods of Numerical Integration* (Academic Press, 1975).

[13] L.M. Delves, *Comput.J.*, vol. 10, p.389, 1967.

[14] J.R. Mosig and F.E. Gardiol, "Analytic and numerical techniques in the Green's function treatment of microstrip antennas and scatterers," IEE Proc., vol. 130,

Pt.H, no. 2, pp. 175-182, March 1983.

[15] A.W. Glisson and D.R. Wilton, "Simple and efficient numerical methods for problems of electromagnetic radiation and scattering from surfaces," *IEEE Trans. Antennas Propagat.*, vol. AP-29, pp. 593-603, 1981.

[16] J.R. Mosig, Laboratoire d'Electromagnetisme et d'Acoustique, Ecole Polytechnique Federale de Lausanne, Lausanne, Switzerland. Personal communication.

[17] R.C. Hall, J.R. Mosig and F.E. Gardiol, "Analysis of microstrip antenna arrays with thick subtrates", *Proc. 17 th European Microwave Conf.*, Rome, 1987.

[18] J.T. Aberle, D.M. Pozar and C.R. Birtcher, "Evaluation of input impedance and radar cross section of probe-fed microstrip patch elements using an accurate feed model," *IEEE Trans. Antennas Propagat.*, vol. 39, pp. 1691-1696, Dec. 1991.

[19] D.E. Müller, "A method for solving algebraic equations using an automatic computer", *Math. Tables Aids Comput.*, vol. 10, pp. 208-215, 1956.

[20] IMSL Inc., Houston, Texas, USA. Library of Fortran Routines for Mathematical Application, Version 1.0, April 1989.

[21] E. Kreyszig, *Advanced Engineering Mathematics* (John Wiley & Sons, 1988).

[22] H. Hurwitz and P.F. Zweifel, "Numerical quadrature of Fourier transform integrals," *Math. Tables Aids Comput.*, vol. 10, pp. 140-149, 1956.

[23] M.R. Spiegel, *Mathematical handbook* (McGraw-Hill, 1968).

[24] M. Hestenes and E. Stiefel, "Method of conjugate gradients for solving linear systems," *J. Res. Natl. Bur. Stand.*, vol. 49, pp. 409-436, 1952.

[25] R.E. Piessens, de Doncker-Kapenga, C.W. Űberhuber and D.K. Kahaner, QUADPAK (Springer-Verlag, 1983).

[26] C.G. Hsu, R.F. Harrington, J.R. Mautz and T.K. Sarkar, "On the location of leaky wave poles for a grounded dielectric slab", *IEEE Trans. Microwave Theory Tech.*, vol. 39, no. 2, pp. 346-349, Feb. 1991.

[27] W.H. Press et.al.,*Numerical Recipes* (Cambridge University Press, 1989).

[28] L.B. Felsen and N. Marcuvitz, *Radiation Scattering of Waves* (Prentice_Hall, 1973).

[29] C.A. Balanis, *Advanced Engineering Electromagnetics* (John Wiley & Sons, 1989).

[30] A. Sommerfeld, *Partial Differential Equations in Physics* (Academic Press, 1949).

[31] A.C. Ludwig, "The definition of cross-polarization," *IEEE Trans. Antennas Propagat.*, vol. AP-21, pp. 116-119, Jan. 1973.

[32] T. Itoh and W. Menzel, "A full wave analysis method for open microstrip structures," *IEEE Trans. Antennas Propagat.*, vol. AP-29, pp. 63-68, Jan. 1981.

[33] J.R. Mosig and T.K. Sarkar, "Comparison of quasi-static and exact electromagnetic fields from a horizontal electric dipole above a lossy dielctric backed by an imperfect ground plane," *IEEE Trans. Microwave Theory Tech.*, vol. MTT-34, no. 4, April 1986.

[34] W.L. Stutzman and G.A Thiele, *Antenna Theory and Design* (John Wiley & Sons, 1981).

[35] R. Conti, J. Toth, T. Dowling and J. Weiss, "The wire-grid microstrip antenna", *IEEE Trans. Antennas Propagat.*, vol. AP-29, no. 1, pp. 157-166, Jan. 1981.

[36] M.D. Deshpande and M.C. Bailey, "Input impedance of microstrip antennas", *IEEE Trans. Antennas. Propagat.*, vol. AP-30, no. 4, July 1982.

[37] Taconic is marketed by Taconic Plastics Ltd, Petersburg, NA, 1213, USA.

[38] RT/duroid is a registered trademark of Rogers Corporation, and marketed by Rogers Corporation Microwave Materials Division, 100 S.Roosevelt Avenue, Chandler, AZ 85226, USA.

[39] N. Faché and D. de Zutter, "Rigorous full-wave space-domain solution for dispersive microstrip lines," *IEEE Trans. Microwave Theory Tech.*, vol. MTT-36, no. 4, April 1988.

[40] L. Beyne and D. de Zutter, "Green's function for layered lossy media with special application to microstrip antennas," *IEEE Trans. Microwave Theory Tech.*, vol. MTT-36, no. 5, May 1988.

[41] R. Mittra, "Spectral domain methods for analyzing frequency selective surfaces (FSS)" in: *Lectures on Computational Methods in Electromagnetics* (SCEEE Press, St. Cloud, Florida, 1981)

[42] C.H. Tsao and R. Mittra, "A spectral-iteration approach for analyzing scattering from frequency selective surfaces," *IEEE Trans. Antennas Propagat.*, vol. AP-30, no. 2, pp. 303-308, March 1982.

[43] C.H. Tsao and R. Mittra, "Spectral domain analysis of frequency selective surfaces comprised of periodic arrays of cross dipoles and Jerusalem crosses," *IEEE Trans. Antennas Propagat.*, vol. AP-32, no. 5, May 1984.

[44] T.A. Cwik and R. Mittra, "Scattering from a periodic array of free-standing arbitrarily shaped perfectly conducting or resistive patches," *IEEE Trans. Antennas Propagat.*, vol. AP-35, no. 11, pp. 1226-1234, Nov. 1987.

[45] D.M. Pozar, "Input impedance and mutual coupling of rectangular microstrip antennas", *IEEE Trans. Antennas Propagat.*, vol. AP-30, no. 6, Nov. 1982.

[46] C. Scott, *The Spectral Domain Method in Electromagnetics* (Artech House, 1989).

[47] L. Vegni, R. Cicchetti and P. Capece, "Spectral dyadic Green's function formulation for planar integrated structures," *IEEE Trans. Antennas Propagat.*, vol. 36, no. 8, Aug. 1988.

[48] D.M. Pozar, "Radiation and scattering from a microstrip patch on a uniaxial substrate," *IEEE Trans. Antennas Propagat.*, vol. AP-35, no. 6, June 1987.

[49] R.E. Collin, *Foundations for Microwave Engineering* (McGraw-Hill, 1966).